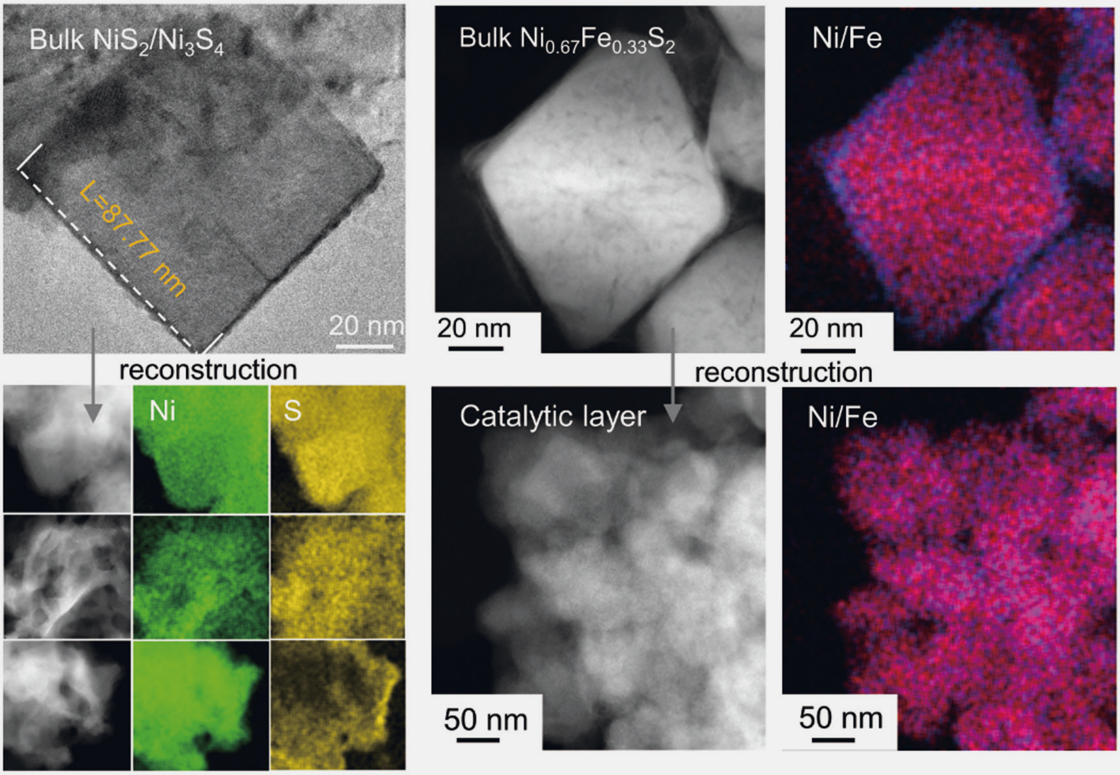

Nanostructures of Transition Metal Sulfides for Anion Exchange Membrane Water Electrolysis

Lu Xia

Energie & Umwelt / Energy & Environment
Band / Volume 597
ISBN 978-3-95806-670-0

Mitglied der Helmholtz-Gemeinschaft

JÜLICH
Forschungszentrum

Schriften des Forschungszentrums Jülich
Reihe Energie & Umwelt / Energy & Environment Band / Volume 597

Forschungszentrum Jülich GmbH
Institut für Energie- und Klimaforschung
Elektrochemische Verfahrenstechnik (IEK-14)

Nanostructures of Transition Metal Sulfides for Anion Exchange Membrane Water Electrolysis

Lu Xia

Schriften des Forschungszentrums Jülich
Reihe Energie & Umwelt / Energy & Environment Band / Volume 597

ISSN 1866-1793 ISBN 978-3-95806-670-0

Bibliografische Information der Deutschen Nationalbibliothek.
Die Deutsche Nationalbibliothek verzeichnet diese Publikation in der
Deutschen Nationalbibliografie; detaillierte Bibliografische Daten
sind im Internet über http://dnb.d-nb.de abrufbar.

Herausgeber und Vertrieb:	Forschungszentrum Jülich GmbH Zentralbibliothek, Verlag 52425 Jülich Tel.: +49 2461 61-5368 Fax: +49 2461 61-6103 zb-publikation@fz-juelich.de www.fz-juelich.de/zb
Umschlaggestaltung:	Grafische Medien, Forschungszentrum Jülich GmbH
Druck:	Grafische Medien, Forschungszentrum Jülich GmbH

Schriften des Forschungszentrums Jülich
Reihe Energie & Umwelt / Energy & Environment, Band / Volume 597

D 82 (Diss. RWTH Aachen University, 2022)

ISSN 1866-1793
ISBN 978-3-95806-670-0

Abstract

Anion exchange membrane (AEM) water electrolysis is an emerging technology for potentially large-scale hydrogen generation owing to the low cost of catalysts based on transition metals. To date, it is still in the laboratory stage for single-cell tests due to the stability issues from the membrane, cathodic and anodic catalysts. Particularly, the anodic catalyst for oxygen evolution reactions (OER) is highly unstable under such strong polarization. Recently, transition metal sulfides (TMS) have been widely used as anodic catalysts for their promising activity and stability. However, research on TMS focuses on *in-situ* growth on nickel foams and the corresponding half-cell performance, which leads to uncontrollable mass loading, poor repeatability, and low practicality. Moreover, matrix-free synthesis of sulfides with three-dimensional (3D) nanostructures and their morphological and structural evolutions during OER processes are rarely reported.

To address the above issues from *in-situ* grown TMS, NiS_2/Ni_3S_4 nano-cubes were synthesized and exhibited enhanced OER performance after electrochemical activation. This is attributed to the improved electrochemical active surface area (ECSA) and surface reconstruction of sulfides to more active (oxy)-hydroxides. A water splitting cell based on NiS_2/Ni_3S_4 exhibits 1800 mA cm^{-2} at 2.0 V and 60°C and long-term stability of 500 h at 1000 mA cm^{-2}. However, single-metal-based catalyst (NiS_2/Ni_3S_4) shows high ohmic resistance and sluggish kinetics.

Continuously, $Ni_{0.67}Fe_{0.33}S_2$ nano-octahedrons were further synthesized and exhibited ten times higher ECSA and a low overpotential of 288 mV at 10 mA cm^{-2} after sulfur leaching. It is proved that Ni/FeOOH acts as active species and the Ni/Fe (oxy)-hydroxides evolved from $Ni_{0.67}Fe_{0.33}S_2$ consist of ultra-fine particles with a diameter of about 2-5 nm. A water splitting cell based on $Ni_{0.67}Fe_{0.33}S$ exhibits a current density of 2200 mA cm^{-2} at 2.0 V and long-term stability of 550 h at 1000 mA cm^{-2}. To further boost cell performance, mechanical pressure optimization was utilized through a well-controlled thicknesses gap between PTFE and electrodes (Δd). The mechanical pressure-optimized $Ni_{0.67}Fe_{0.33}S_2$ based cell performance was up to 2515 mA cm^{-2} (315 mA cm^{-2} higher than the mechanical pressure-free cells at 2.0 V and 60°C).

These results demonstrate that TMS nanostructures are promising OER pre-catalysts and exhibit high activity and stability, which are suitable for large-scale applications. This study provides a general strategy and activation method for the efficient utilization of TMS as OER catalysts.

Zusammenfassung

Die Wasserelektrolyse mit Anionenaustauschermembran (AEM) ist aufgrund der niedrigen Kosten von Katalysatoren auf der Basis von Übergangsmetallen eine aufstrebende Technologie für die potenziell großtechnische Wasserstofferzeugung. Bisher befindet es sich aufgrund der Stabilitätsprobleme der Membran-, Kathoden- und Anodenkatalysatoren noch im Laborstadium für Einzelzelltests. Insbesondere der anodische Katalysator für Sauerstoffentwicklungsreaktionen (OER) ist unter solch starker Polarisierung höchst instabil. In letzter Zeit wurden Übergangsmetallsulfide (TMS) weithin als Katalysatoren für die Sauerstoffentwicklungsreaktion (OER) verwendet. Die Forschung zu TMS konzentriert sich jedoch auf das In-situ-Wachstum auf Nickelschäumen und die entsprechende Halbzellenleistung, was zu unkontrollierbarer Massenbeladung, schlechter Wiederholbarkeit und geringer Praktikabilität führt. Darüber hinaus wird selten über die matrixfreie Synthese von Sulfiden mit dreidimensionalen (3D) Nanostrukturen und ihre morphologischen und strukturellen Entwicklungen während OER-Prozessen berichtet.

So wurden NiS_2/Ni_3S_4-Nanowürfel synthetisiert, die nach elektrochemischer Aktivierung eine verbesserte OER-Leistung zeigten. Dies wird der verbesserten elektrochemisch aktiven Oberfläche (ECSA) und der Oberflächenrekonstruktion von Sulfiden zu aktiveren (Oxy)-Hydroxiden zugeschrieben. Eine Wasserspaltungszelle auf Basis von NiS_2/Ni_3S_4 weist eine Stromdichte von 1800 mA cm^{-2} bei 2.0 V und 60°C und eine Langzeitstabilität von 500 h bei 1000 mA cm^{-2} auf. Katalysatoren auf Einzelmetallbasis (NiS_2/Ni_3S_4) zeigen jedoch einen hohen ohmschen Widerstand und eine träge Kinetik.

Kontinuierlich wurden $Ni_{0.67}Fe_{0.33}S_2$-Nanooktaeder weiter synthetisiert und zeigten eine zehnmal höhere ECSA und eine niedrige Überspannung von 288 mV bei 10 mA cm^{-2} nach der Schwefelauswaschung. Es wurde bewiesen, dass Ni/FeOOH als aktive Spezies fungiert und die aus $Ni_{0.67}Fe_{0.33}S_2$ entwickelten Ni/Fe-Oxyhydroxide aus ultrafeinen Partikeln mit einem Durchmesser von etwa 2-5 nm bestehen. Eine auf $Ni_{0.67}Fe_{0.33}S_2$ basierende Wasserspaltungszelle weist eine Stromdichte von 2200 mA cm^{-2} bei 2.0 V und eine Langzeitstabilität von 550 h bei 1000 mA cm^{-2} auf. Um die Zellleistung weiter zu steigern, wird eine mechanische Druckoptimierung durch einen gut kontrollierten Dickenabstand zwischen PTFE und Elektroden (Δd) verwendet. Die druckoptimierte $Ni_{0.67}Fe_{0.33}S_2$-basierte Zellenleistung betrug bis zu 2515 mA cm^{-2} (315 mA cm^{-2} höher ist als die der drucklosen Zellen bei 2.0 V und 60°C).

Diese Ergebnisse zeigen, dass TMS-Nanostrukturen vielversprechende OER-Präkatalysatoren sind und eine hohe Aktivität und Stabilität aufweisen, die für eine großtechnische Anwendung geeignet sind. Diese Studie bietet eine allgemeine Strategie und Aktivierungsmethode für die effiziente Nutzung von TMS als OER-Katalysatoren.

1 Introduction and highlights of the work

1.1 State of the art

Hydrogen is considered an ideal energy carrier, which not only has an advantage of a huge amount of resources from organic compounds and water,[1, 2] but also a high energy density of ca. 39.4 kWh kg^{-1},[3] and practicable transportability (gas, liquid, metal hydride), etc.[4, 5] It can be produced on large scale by three main routes, namely, steam reforming of natural gas and methanol,[6-8] and water electrolysis.[9-12] Thereof, water electrolysis shows unique highlights compared to the formers: First, water splitting involving only hydrogen and oxygen evolution reaction (HER and OER) has no pathway to produce carbon dioxide, which mitigates the impact of greenhouse gas;[13] Second, it is better than thermal processes to produce ultra-pure hydrogen ca. 99.9999 vol% without carbon impurities (e.g. CO, CO_2, CH_4);[14] Third, electrolysis devices can be flexibly installed and hydrogen can be produced at low temperature (<100°C).[15] Forth, both H_2 and O_2 are important industrial raw materials, which are widely used in metallurgy and chemical industries.[1] However, the high cost or low performance of newly developed technologies of both acidic and alkaline water electrolysis hinders their further commercialization .[16, 17] Therefore, researchers proposed a “green hydrogen” routine: water electrolysis powered by inexhaustible energy, which is dominant in environmental friendliness (de-carbonization, non-toxicity) and economic viability, providing new vitality for the research of water electrolysis.[13, 18, 19]

1.2 Research progress and bottlenecks

1.2.1 Classification of water electrolysis systems

Hydrogen generation by electrolysis can be achieved by high-temperature solid oxide electrolysis (SOEC) and low-temperature water electrolysis, and this thesis is focused on the latter technology. To date, low-temperature electrolysis technologies can be divided into acidic, alkaline, and acid-alkaline mixed systems by different electrolytes.[20-25] In addition, different membranes can also be used for classification, such as proton exchange membrane (PEM),[24, 26] diaphragms,[19, 27] and anion exchange membrane (AEM).[9, 28] Thereof, the PEM (Figure 1.1A) consists of the main chains and negatively charged functional groups that exhibit high ionic conductivity and stability.[24, 26, 29] However, PEMWE is strongly hindered by low scalability, due to the high cost of platinum group metal (PGM) based catalysts and their scarcity.[24, 30, 31]

Additionally, the diaphragm in classical alkaline water electrolysis (Figure 1.1 B) consists of the solid part, large-area tiny pores and is advantageous in low cost and high stability. However, its large thickness to mitigate hydrogen permeation leads to high resistance/polarization and low operating current density.[12, 27, 32] Then, the AEM with functional channels (Figure 1.1C) consists of main chains and positively charged functional groups (PEM-like structure) and has a much smaller thickness than the diaphragm and good combinability with low-cost transition metal (TM) based catalysts.[10, 11, 33-35] Furthermore, channel-free AEMs (Figure 1.1D) with a dense structure were referred as ion-solvating membranes by Aili et al, which exhibits improved ion conductivity and higher single-cell current density than channel-based AEM and even comparable to PEM, which however is still limited by long-term stability.[27, 36-39]

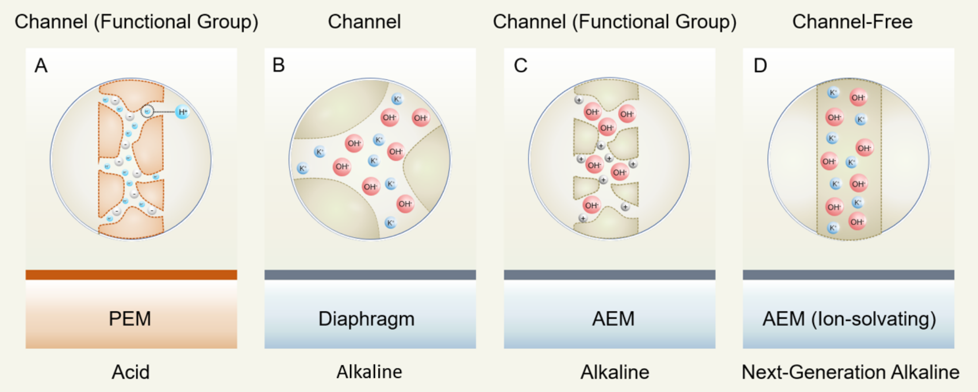

Figure 1.1 Ion-conducting mechanisms of (A) PEM, (B) Diaphragm, (C) AEM (functional group) and (D) AEM (ion-solvating) for acidic, classic alkaline, alkaline, and next-generation alkaline water electrolysis respectively.

1.2.2 Alkaline water electrolysis (AWE)

AWE is a commercialized technology for large-scale hydrogen production, which is derived from classic alkaline water electrolysis with large gaps to zero-gap electrolysis. The zero-gap electrolyzer consists of two transition-metal based electrodes separated by a porous diaphragm, supported by high-concentration KOH ca. 32.5 wt.% (~7.5 M). Miller et al. summarized that AWE is one of the most stable electrolysis technologies with lifetime of 60000-1000000 h,[11, 12] and the keys to promote successful commercialization are its scalability and low capital cost. As shown in Figure 1.2A, cheap transition metal (e.g. Ni, Fe, Co, Mo…) based compounds as anode and cathode catalysts, and cheap diaphragm as a separator greatly reduce the cost of key materials.

However, high-concentration KOH is sensitive to carbon dioxide (CO_2) and corrosive to tanks, pumps. The by-product potassium carbonate (K_2CO_3) and potassium bicarbonate ($KHCO_3$) have very low solubility in alkaline solution, which will precipitate on the membrane/electrode/bipolar plate interface and increase the internal resistance, thereby deteriorating cell performance.[40] Moreover, large thickness of ca. 500 μm is needed for the diaphragm to suppress hydrogen crossover, causing low ion conductivity. In addition, to ensure decent energy efficiency, the operating current density of AWE is limited to the range of only 200-400 mA cm^{-2}.[41, 42]

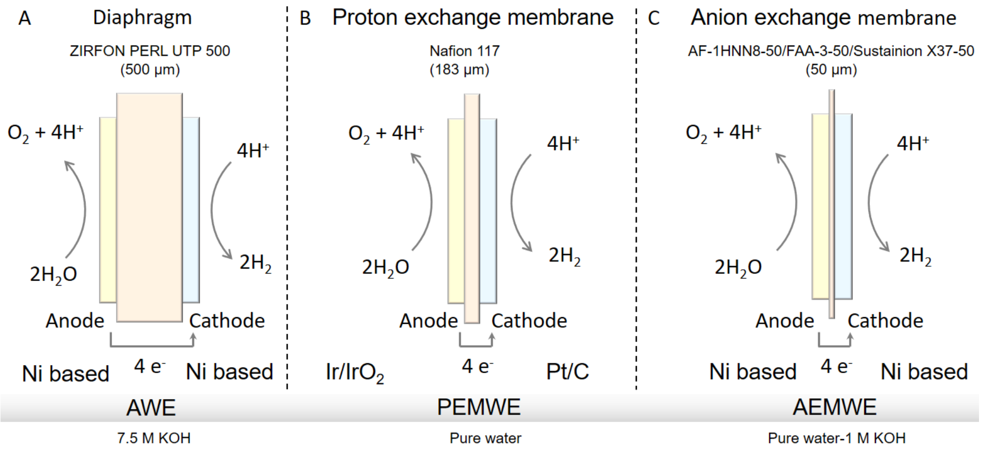

Figure 1.2 Technologies of water electrolysis: (A) Alkaline water electrolysis (AWE), (B) proton exchange membrane water electrolysis (PEMWE), (C) anion exchange membrane water electrolysis (AEMWE).

1.2.3 Proton exchange membrane water electrolysis (PEMWE)

To address the drawbacks of AWE, PEMWE has been developed by utilizing highly conductive PEM with ion transport channels as the electrolyte to replace porous diaphragm, thus enabling pure water electrolysis (Figure 1.2B).[24] Miller et al. summarized that the stability of PEMWE is comparable to AWE, with stack lifetime from 20000 to 60000 h.[11] Also, PEMWE exhibits numerous of advantages, such as fast response that enables combination with renewable energy, high operating current density/mechanical pressure, ultra-high purity of H_2, thus being promising for large-scale application from the perspective of performance.[31]

However, from the point of cost analysis, only scarce, high-cost noble metal based catalysts (e.g. platinum/carbon and iridium black/oxide) can survive in such a harsh acidic condition provided by PEM, causing high material and stack cost.[24] Additionally, the cost of PEM itself is also an issue, which is much more expensive than diaphragm.[43]

1.2.4 Anion exchange membrane water electrolysis (AEMWE)

In the last 10 years, a developing zero-gap technology of anion exchange membrane (AEM) electrolysis has been proposed and studied (Figure 1.2C). It combines the advantages of AWE and PEMWE, including the use of platinum group metal (PGM) free catalysts without much performance loss.[9, 10] AEMWE is an extended application of ion exchange membrane from PEMWE to alkaline electrolysis with an AEM as the separator that also consists of ion transport channels, but positively charged functional groups. Representative products are FAA-3-50 from FuMA-Tech, AF1-HNN8-50 from Ionomr Innovations, and Sustainion X37-50 from Dioxide Material.[9] Among them, the PTFE-reinforced Sustainion membrane, coupling with Pt/C and IrO_2, was tested in an electrolyzer for 12000 h, which is the highest durability of AEMWE until now.[44]

However, AEM electrolysis is still much less mature than AWE or PEMWE (e.g. i) durability is still an order of magnitude lower than AWE and PEMWE, ii) trade-off between conductivity and water management cost). Additionally, the activity and stability of PGM-free catalysts are still not comparable to PGM catalysts.[45-50] More investigations concerning these issues should be done to promote its commercialization.

1.3 Basic knowledge of AEMWE

1.3.1 Configuration of AEMWE system

As shown in Figure 1.3, AEMWE is achieved by a complex cell system under specific i) current density or voltage controlled by testing system, ii) electrolyte flowing rate by electrolyte system, and iii) concentration of KOH by water refilling system. Meanwhile, generated H_2 should be treated during the test to ensure safety, and the H_2 permeation through the membrane to the anodic tank will be tested by a gas crossover system.

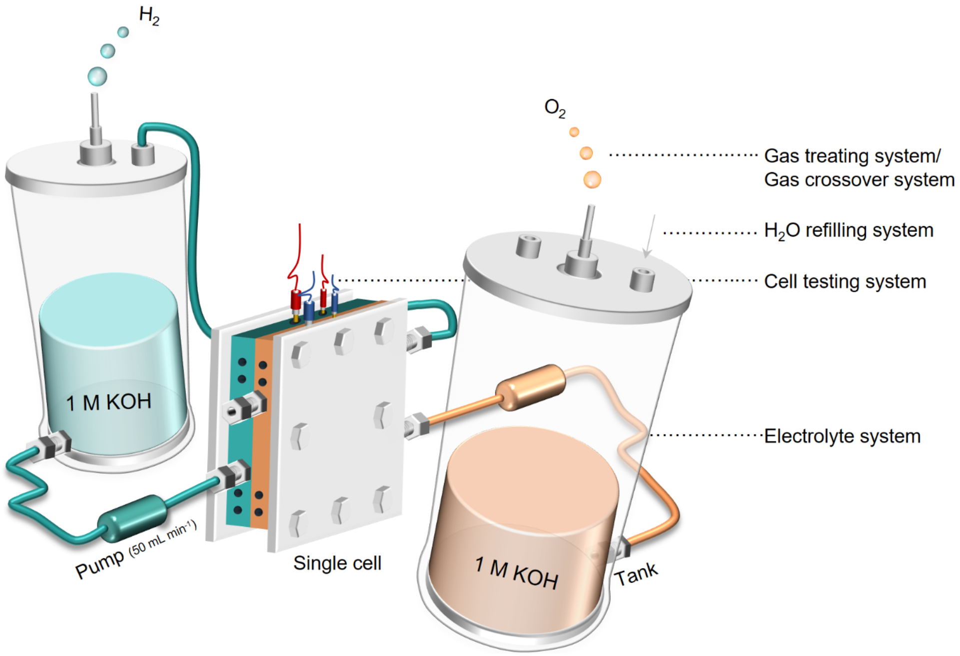

Figure 1.3 Water electrolysis systems consist of a single cell, two electrolyte tanks with 1 M KOH and pumps with the pumping rate of 50 mL min^{-1}, and other auxiliary systems (e.g. water refilling, gas crossover, and gas treating systems).

Specifically, the testing system consists of potentiostatic, galvanostatic, and AC impedance components. The electrolyte system is composed of tanks, pumps, tubes and insulation materials covered on the tanks and tubes. The water refilling system is of crucial importance to ensure the concentration of KOH during long-term tests, which is achieved by a water level sensor and refilling pump. When the electrolyte level is lower than the initial scale, the sensor delivers this information to the control system, and the control system opens the refilling pump for water compensation up to the initial level. Then the water-level sensor senses the electrolyte level position and transmits information to the control system to shut down the pump.

As for the generated H_2 and O_2, they will be pumped out together from the testing window and it is safe to mix together due to relatively low concentration of H_2 in O_2. The gas from the anodic tank will be filtered by water-absorbent material and analyzed by a gas crossover system to test H_2 concentration in O_2. When the H_2 concentration is higher than 2% (mass percentage), then the cell testing should be stopped due to safety reasons.

1.3.2 Single cell configuration

In addition to the auxiliary system, the core component is the single cell. As shown in Figures 1.4A-C, it consists of two end plates, two bipolar plates with serpentine channels, an anode/membrane/cathode, and corresponding two polytetrafluoroethylenes (PTFE) gaskets among them. The material of both bipolar plates is nickel so that the bipolar plate of the anode will be oxidized to nickel oxides after the cell tests, which will affect the contact resistance between the electrode and the bipolar plate, thus it is necessary to remove the surface oxide before the next cell test.

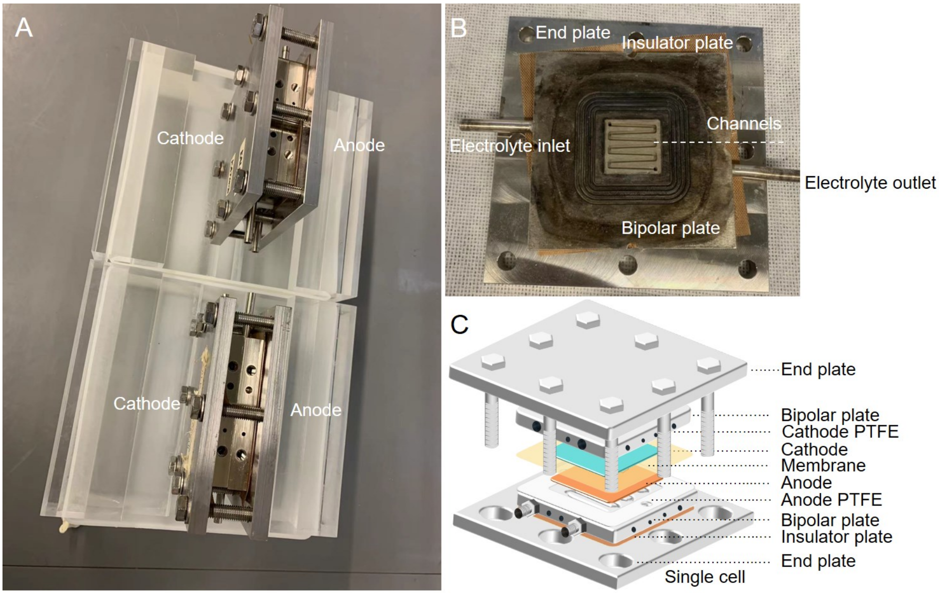

Figure 1.4 Single cell configuration for AEMWE: (A, B) photos of single cells and components, (C) schematic illustration of all crucial materials (Polytetrafluoroethylene, PTFE).

To insulate the external circuit, two pieces of plastic paper behind the end plates act as the insulating plate. The area of the insulating plate should be large enough to prevent short circuits in micro-areas. There are 4 holes on both sides of the pipe of the cell for heating rods and thermocouples to measure the temperature of the outlet and inlet, while another 6 holes on the top, perpendicular to the sides, are used for the i) current and ii) voltage input of the cathode/anode and iii) temperature measurement. Therefore, temperature tests are conducted on the top and side of the cell to ensure that the temperature distribution is repeatable and the error is controlled within 1-2°C.

1.3.3 Thermodynamics and kinetics

Water electrolysis involves energy conversion of both electrical energy from power supply and heat energy from environment to chemical energy in hydrogen. The reactions on the anode and cathode side and the overall reaction of alkaline water electrolysis are described from equation 1.1 to 1.3, respectively.[11, 24]

$$\text{Anode:} \quad 2\ OH^- \rightarrow 1/2\ O_2 + H_2O + 2\ e^- \qquad (1.1)$$

$$\text{Cathode:} \quad 2\ H_2O + 2\ e^- \rightarrow H_2 + 2\ OH^- \qquad (1.2)$$

$$\text{Overall:} \quad H_2O \rightarrow H_2 + 1/2\ O_2 \qquad (1.3)$$

The required energy to drive the water electrolysis reaction is noted as enthalpy (ΔH) that can be calculated by equation 1.4 (assume a reversible reaction under an isothermal condition), which consists of i) electrical supply (Gibbs free energy change, ΔG) and ii) heat supply ($T\Delta S$, T: temperature, ΔS: entropy change). The standard values of enthalpy and entropy at 1.013 bar, 25°C for splitting 1 mol water, noted as ΔH^0 and ΔS^0, is 285840 J and 163 J/mol/K, and thus the standard electrical work can be calculated as ΔG^0=237230 J/mol. Under a constant-pressure and constant-temperature condition, the electricity supplied energy can be calculated by equation 1.5. Therefore, the standard thermodynamic voltage (E_0) to split liquid water can be calculated as 1.23 V. It is noteworthy that the Gibbs free energy is dependent on temperature and pressure, thus 1.18 V is calculated for water vapor electrolysis. When water electrolysis is conducted under thermoneutral (TN) condition without heat supply from the environment, the thermoneutral voltage (E_{TN}) can be calculated as ca. 1.48 V by equation 1.6.[51]

$$\Delta H = \Delta G + T\Delta S \qquad (1.4)$$

$$\Delta G = -nFE_{\text{cell}} \qquad (1.5)$$

$$E_{TN} = \Delta H / nF \qquad (1.6)$$

(F: Faraday constant (96485 J); n: the number of exchanged (one water molecule with n=2).

In general, the thermodynamic cell voltage (E_{Nernst}) needs to be calculated by equation 1.7 (R: gas constant, 8.314 J/mol/K) by considering the effects of temperature (T), normalized partial pressures of H_2 (P_{H_2}) and O_2 (P_{O_2}) and the activity of water (a_{H_2O}). More generally, the extra electrical energy is needed to overcome the ohmic losses due to bulk resistances of all the key materials and contact resistance among them. Therefore, the practical cell voltage under a specific current density (i) can be described by equation 1.8, which is further normalized by the total activation overpotential from both anode and cathode sides ($\sum\eta$) and the ohmic polarizations (iR).[51]

$$E_{Nernst} = E_0 + RT\ 2F \ln (P_{H_2} \cdot P_{O_2}{}^{1/2} / a_{H_2O}) \qquad (1.7)$$

$$E_{General} = E_{Nernst} + \sum\eta + iR \qquad (1.8)$$

A typical polarization curve of the water electrolyzer is shown in Figure 1.5. The initial cell voltage is always above 1.23 V, which is caused by temperature and product partial pressure and water activity in non-standard conditions. Additionally, the mass transfer polarization will also affect the cell voltage, especially at high current density.

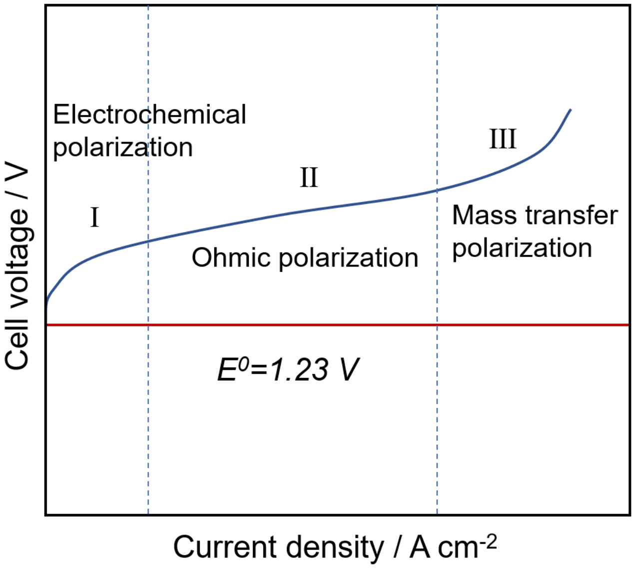

Figure 1.5 Typical polarization curve of water electrolysis cell and thermodynamically reversible voltage.

1.3.4 Membrane electrode assembly (MEA)

The MEA can be fabricated through catalyst-coated membrane (CCM) or catalyst-coated substrate (CCS).[11, 12] The CCM approach is achieved by blade or spray coating of the catalyst ink, consisting of ionomer/catalyst/solvent, onto the membrane. In this way, the great advantage lies in intimate catalyst-AEM contact, enhancing ionic conductivity. However, one trade-off is that the contact resistance between the porous transport electrode (PTE) and bipolar plate is high. Therefore, a mixed configuration with CCS on the anode side and CCM on the cathode side is developed to suppress the contact resistance and improve the cell performance. Meanwhile, the CCS approach results in the catalyst layer with higher roughness and robustness due to 3D-structured substrates as supporting materials, which means higher specific surface area and mechanical stability.[11] The substrate enables low contact resistance with bipolar plate, fast electron transfer, and enhances gas diffusion in porous channels.

CCS can be further classified as “self-standing or self-supporting electrodes” by *in-situ* growth and “post-coated electrodes” by blade/spraying. In half cells, the former has a large specific surface area without organic binders and is easy to prepare, thus being widely used in OER tests; while in full cells, the latter is widely used due to its feasibility in accurately controlling the catalyst mass loading. It is difficult to compare the performance between CCM and CCS due to different testing protocols As shown in Figure 1.6, Miller et al. used a statistical evaluation method and conclude that the results from CCS and CCM are approximately equal,[11] which agrees well with preliminary results from Irina Galkina et al. in IEK-14 (Forschungszentrum Jülich).

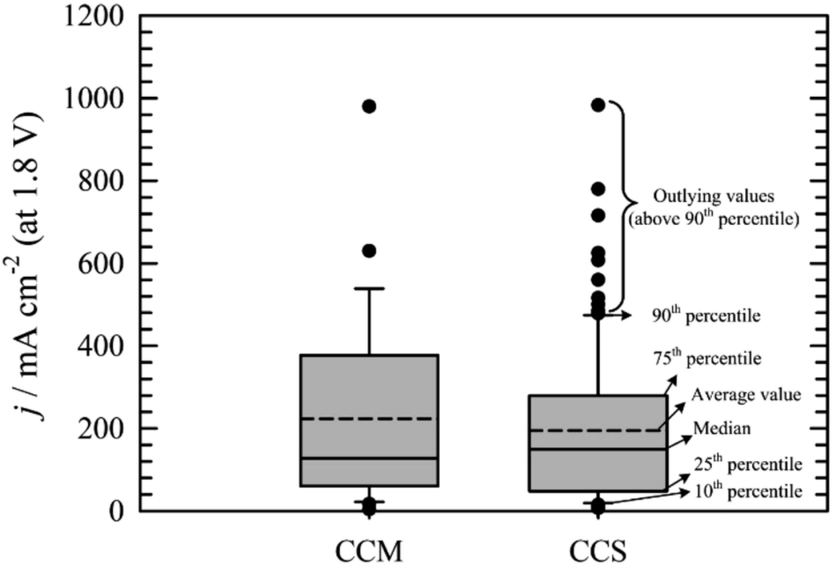

Figure 1.6 Cell performance (current density) of catalyst-coated membrane (CCM) and substrate (CCS) at the voltage of 1.8 V.[11] *Reprinted from ref. 11 with permission from Royal Society of Chemistry.*

1.3.5 Hydrogen evolution reaction (HER)

The interpretation of HER in alkaline conditions can be described as two electron-transfer processes in equations (1.9-1.11) as follows:[52, 53]

$$H_2O + e^- \rightarrow H^* + OH^- \qquad \text{(Volmer)} \qquad (1.9)$$

$$H_2O + e^- + H^* \rightarrow H_2 + OH^- \qquad \text{(Heyrovsky)} \qquad (1.10)$$

$$\text{or } 2H^* \rightarrow H_2 \qquad \text{(Tafel)} \qquad (1.11)$$

First, a water molecule combines with an electron to form the intermediate (H^*) with the release of an OH^-, as the “Volmer” step. Second H^* further reacts with another water molecule to form H_2 with the release of the second OH^-, as the “Heyrovsky” step. Alternatively, two H^* directly combine to form H_2, as the “Tafel” step.

Notably, HER under alkaline condition is 2 orders of magnitude slower than that under acidic condition. It can be explained by three theories, namely, water dissociation theory (WDT), hydrogen binding energy theory (HBET), and interface water/anion transfer theory (IW/AT).

First, WDT acclaims that due to the presence of a large amount of OH^- in the solution, the adsorption of OH^* occupies the sites for H^*, resulting in the difficulty of H_2 evolution. Second, HBET proposed that the activity for HER is highly related to the interaction of catalyst-H, which is similar to that under acidic condition. Moreover, IW/AT considers that at different pH, the arrangement of water molecules on the catalyst surface, and the electric double layer are different, which in turn affect the overall performance of the electrocatalyst.[54]

1.3.6 Oxygen evolution reaction (OER)

The interpretation of OER in alkaline conditions can be roughly divided into two categories, namely, adsorbate evolution mechanism (AEM^*) and lattice-oxygen-mediated mechanism (LOM). As shown in Figure 1.7A, traditional explanation of AEM involves four electron-transfer steps, which are described in equations (1.4-1.7) as follows:[54-56]

$$OH^- + {}^* \rightarrow HO^* + e^- \qquad (1.12)$$

$$HO^* \rightarrow O^* + e^- + H^+ \qquad (1.13)$$

$$O^* + OH^- \rightarrow HOO^* + e^- \qquad (1.14)$$

$$HOO^* \rightarrow {}^* + O_2\,(g) + e^- + H^+ \qquad (1.15)$$

First, OH^- diffuses and adsorbs on the surface oxygen active site ($*$) with the release of an electron in equation 1.12. Second, the adsorbed species (HO^*) deprotonate to form the first intermediate (O^*) with the release of the second electron in equation 1.13. Third, O^* reacts with another OH^- to form the second intermediate (HOO^*) with the release of the third electron in equation 1.14. Finally, O_2 evolves through further deprotonation from HOO^* with the regeneration of the active site ($*$) and the release of the fourth electron in equation 1.15. Therefore, any of the above four steps may limit the OER reaction rate, depending on the most sluggish one.[55]

Additionally, there are also some mechanisms beyond traditional AEM framework, represented by LOM. As shown in Figure 1.7B, LOM steps can be described as follows: i) Two adsorbed species (HO^*) at the metal sites deprotonate to generate two metal-oxygen species. ii) two metal-oxygen species combine with each other to form O-O bonds instead of combining with OH^- to form HOO^* intermediates in AEM steps. iii) The active sites in the lattice are then re-exposed for the next cycles with the release of oxygen.[55]

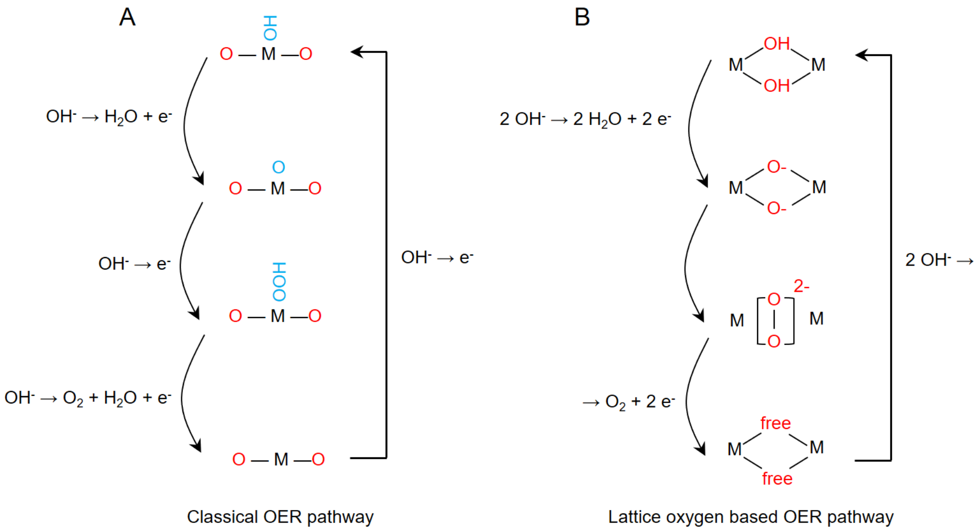

Figure 1.7 Two explanations for the mechanism of OER: (A) adsorbate evolution mechanism (AEM), (B) lattice-oxygen-mediated mechanism (LOM).*

1.4 Developments of OER catalysts in AEMWE

1.4.1 Catalysts for AEMWE

Highly stable bi-functional PGM-free catalysts used in full cells are still scarce, with strong incompatibility between HER and OER catalysts. Researchers configured different HER and OER catalysts to achieve better overall activity/stability, and only very few used the so-called "bi-functional" catalyst ($Fe_2P_2S_6$), developed by Chang et al. They synthesized this catalyst by combing chemical vapor deposition with solvent-thermal treatment and used it in the cell $Fe_2P_2S_6$||YAB membrane||$Fe_2P_2S_6$||1 M KOH, testing at 300 mA cm^{-2}, 50°C for 24 h with the cell-voltage increase rate of ~0.628 mV h^{-1}, which was much better than the control group of IrO_2||YAB membrane||Pt black||1 M KOH, with the voltage increase rate of ~5.833 mV h^{-1}.[57]

For the most high-performance PGM-free compounds, Ni-Fe-Co alloys/oxides/hydroxides, Ni/CeO_2-La_2O_3/C, Ni-Al-Mo alloy as HER catalysts, and Cu-Co oxides, Ni-Fe and Ni-Co oxides Ni-Al alloy as OER catalysts are preferred.[16, 47, 50, 58-64] For example, Liu et al used Nafion as a binder and NiFeCo nano-particles (US Nano) as the cathode catalyst with the mass loading of 2 mg cm^{-2}, depositing onto a carbon paper, while 2 mg cm^{-2} of $NiFe_2O_4$ particles

(Sigma Aldrich) as the anode coated on the stainless-steel fiber felt (Bekaert) and achieved the best catalyst durability in the cell $NiFe_2O_4$||Sustainion®X37-50||NiFeCo||1 M KOH, with one of the lowest cell-voltage increases of 0.005 mV h^{-1} for 2000 h at 1000 mA cm^{-2} and 60°C.[64] Therefore, the HER catalyst NiFeCo nano-particles from US Nano and OER catalyst $NiFe_2O_4$ particles from Sigma Aldrich is highly stable.

Additionally, commercial catalysts Acta 4030 (Ni/CeO_2-La_2O_3/C) and Acta 3030 ($CuCoO_x$) (Acta SpA, Italy) were also relatively stable HER and OER catalysts for 1000 h, supported by Pavel et al. who used the above two catalysts in the cell $CuCoO_3$||A-201, Tokuyama||Ni/CeO_2-La_2O_3/C ||1 wt.% $KHCO_3/K_2CO_3$, testing at 470 mA cm^{-2}, 43°C, 3 MPa for 1000 h, with the cell-voltage increase rate of 0.148 mV h^{-1}.[65] Meanwhile, Zeng et al. used them in the cell $CuCoO_3$||Mg/Al LDHs||Ni/CeO_2-La_2O_3/C||0.1 M NaOH at 80 mA cm^{-2}, 50°C for 600 h, with the cell-voltage increase rate of 0.132 mV h^{-1},[66] and Vincent et al. used them in the cells $CuCoO_x$||A-901, Tokuyama||Ni/CeO_2-La_2O_3/C||1 wt.% K_2CO_3 at 500 mA cm^{-2}, 50°C for 200 h, with the cell-voltage increase rate of 0.200 mV h^{-1}.[25]

Ni-Co and Ni-Fe oxides also are active and stable OER catalysts. For example, Zeng et al. used Ni-Co oxide in the cell $NiCo_2O_4$@MnO_x||QAPPO ||Ni/CeO_2-La_2O_3/C||D.I. water, testing at 400 mA cm^{-2}, 60°C for 100 h and the cell-voltage increase rate was only 0.007 mV h^{-1},[67] while Li et al. used Ni-Fe oxide in the cell Ni/Fe oxide ||AEM from ITM Power||Pt||4 M NaOH, testing at 1000 mA cm^{-2}, 50°C for 200 h,[49] with the cell-voltage increase rate of 0.287 mV h^{-1}. However, Ni-Co and Ni-Fe oxides are still lacking data support for ultra-long-term stability (~1000 h). Moreover, Ni-Al-Mo and Ni-Al alloys are also relatively stable catalysts with the support of Razmjooei et al. who used them in the cell NiAl||NEOSEPTA, Astom||NiAlMo||1 M KOH, testing at 500 mA cm^{-2}, 20°C for 112 h,[68] with the cell-voltage rate of 0.350 mV h^{-1}. They prepared electrodes by spraying NiAl/NiAlMo powder (HC Stack) on porous stainless steel and proved the stability of catalysts by SEM/EDX analysis for that the sponge porous morphology of NiAl and NiAlMo electrodes were well-retained after 112 h. Recently, Xiao et al. used dissolved oxygen and galvanic corrosion method to synthesize fluoride-incorporated Fe_xNi_yOOH-20F nanosheet that was assembled into the cell that simplified as follows: Fe_xNi_yOOH-20F||PAP-TP-85||Pt/C|| pure water, testing at 200 mA cm^{-2}, 80°C for 160 h,[69] with the voltage increase rate of 0.560 mV h^{-1}.

To summarize, bimetallic catalysts are scarce for single-cell stability tests and transition metal-based sulfides/phosphides are potential bifunctional candidates, while Ni-Fe-Co, Ni/CeO_2-La_2O_3/C are promising for HER coupling with Cu-Co, Ni-Fe, oxides for OER.

1.4.2 Transition metal sulfides (TMS) as OER catalysts

TMS have been widely used as OER catalysts in half cells but rarely in full cells of AEMWE. TMS are always fabricated by *in-situ* growth on porous substrates, which exhibits specific challenges. For example, Shang et al. prepared Ni_xS_y catalyst by *in-situ* growth on nickel foam, which exhibits fast degradation after 1000 CVs.[39] Overall, *in-situ* fabricated catalysts exhibit high activity for OER, but are strongly hindered by the following challenges for full-cell applications: First, it is hard to ensure repeatability of cell performance by using *in-situ* grown catalysts due to their random distribution and uncontrollable loading; Second, without binder reinforcement, the surface catalyst exhibits low stability under flow mode and will be washed away to a large extent[30-31]; Compared with uncontrollable self-supported structures, catalyst coating layers with more controllable ink dispersion, catalyst mass loading exhibit high reproducibility and stability due to binder strengthening.[17, 40-43] However, metal sulfides are unstable during strong-polarization OER processes in alkaline solution, especially for single-cell tests at a high current density of 1000 mA cm^{-2}, which will be continuously oxidized to oxides/(oxy)hydroxides. Therefore, the evolution mechanism of sulfides needs to be further studied to maximize activity/ stability, and their single-cell performance is urgently needed.

1.4.3 Advantages, challenges and strategies of TMS

Sulfides and oxides are very similar, and they can be interconverted at different temperatures and sulfur/oxygen atmospheres. At normal temperature and mechanical pressure, the stability of oxides is greater than that of sulfides so that sulfides will be slowly oxidized to corresponding oxides. Sulfides are chemically less stable than oxides, but it is a pre-catalyst capable of producing highly active catalysts. As shown in Figure 1.8, Yin et al., summarized that TMS are advantageous in various phases, lattices, and unique electronic structures (MS, MS_2, M_2S_3, M_3S_4, etc., M represents transition metal). The above feature enables TMS as a highly active catalyst with abundant defect sites, a large number of complex morphologies and electron transitions. Additionally, TMS can achieve self-adaptive surface reconstruction to (oxy)-hydroxides during OER processes, which is unique in defect chemistry, electrochemical active surface area (ECSA) and different from directly synthesized hydroxides. However, monometallic sulfides show low electrical conductivity and activity, which could be addressed by serval strategies such as heterogeneous atom doping, phase engineering, and optimized microstructure, etc. [70]

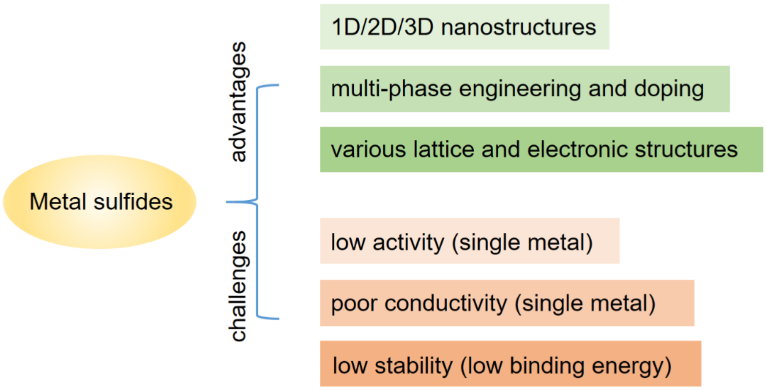

Figure 1.8 Advantages and challenges of metal chalcogenides as OER catalyst and synthesis, and note: 1/2/3 dimension (1D/2D/3D).

1.5 Highlights of the thesis

i) The strategies of phase engineering and morphology optimization were applied to synthesize NiS_2/Ni_3S_4 nano-cubes with the size of 80±20 nm. **(Chapter 5)**

ii) NiS_2/Ni_3S_4 activated by sulfur leaching with the surface reconstruction of sulfides/polysulfides to form highly active multiphase heterostructures of $NiS_x/Ni(OH)_2/NiOOH$ that exhibit greatly enhanced electrochemical active surface area (ECSA), increasing the OER performance from 365 to 339 mV at 10 mA cm^{-2} in half cells and from 1200 to 1800 mA cm^{-2} at 2.0 V in full cells. **(Chapter 5)**

iii) The strategy of doping engineering was further applied to synthesize the $Ni_{0.67}Fe_{0.33}S_2$ based nano-octahedrons with the size of (90±20) * (70±20) nm. **(Chapter 6)**

iv) $Ni_{0.67}Fe_{0.33}S_2$ nano-octahedron sacrifices its morphology and show 10 times higher ECSA after sulfur leaching, and further refined size to 2-5 nm. *In-situ* Raman spectra show that the obtained catalyst is $NiFeS_x/NiFe(OH)_2/NiFeOOH$ with multi-structures and rich interfaces captured by high-resolution transmission electron microscopy (HRTEM). **(Chapter 6)**

v) The activity order is as follows: monometallic heterostructure with two phases (NiS_2/Ni_3S_4, 339 mV) < bimetallic heterostructure with two phases (NiS_2/FeS_2-2:1, 323 mV) < bimetallic heterostructure with single phases ($Ni_{0.67}Fe_{0.33}S_2$, 288 mV at 10 mA cm^{-2}). **(Chapter 6)**

vi) The $Ni_{0.67}Fe_{0.33}S_2$ based cell exhibits 2200 mA cm^{-2}, while a cost-free mechanical pressure optimization further boosts the cell performance to 2515 mA cm^{-2} at 2.0 V. **(Chapter 7)**

1.6 Outline of the thesis

Chapter 1: Introduction and highlights of this work.

Chapter 2: Preparation of NiS_2/Ni_3S_4 nano-cubes by one-step vulcanization and various characterization techniques involved.

Chapter 3: Preparation of $Ni_{0.67}Fe_{0.33}S_2$ nano-octahedrons by two-step vulcanization via first co-precipitation and then recrystallization, and corresponding characterization techniques.

Chapter 4: Experimental methods for mechanical pressure control, quantification and details for single-cell tests.

Chapter 5: Characterizations of NiS_2/Ni_3S_4 nano-cubes before and after sulfur leaching and corresponding single-cell performance.

Chapter 6: Characterizations of $Ni_{0.67}Fe_{0.33}S_2$ nano-octahedrons before and after sulfur leaching and corresponding single-cell performance.

Chapter 7: Benchmarking mechanical pressure of iridium black//AEM//platinum/carbon based cells and extended application of optimized mechanical pressure for $Ni_{0.67}Fe_{0.33}S_2$based cells.

Chapter 8: A comprehensive discussion.

Chapter 9: Conclusion and outlook.

2 Experimental methods for NiS_x

2.1 Chemicals and materials

Nickel chloride hexahydrate ($NiCl_2·6H_2O$) as the cation precursor, thioacetamide (C_2H_5NS) as the sulfur source, and sodium hydroxide (NaOH) as the anion precursor were used as received from Sigma-Aldrich without further purification. The molar mass of the above chemicals and their purities were shown in Table 2.1.

Table 2.1 Synthesis information involved in NiS_x based catalysts.

Chemicals	Molar mass	purity
$NiCl_2·6H_2O$	237.69 g/mol	99.90%
TAA	75.13 g/mol	99.90%
NaOH	40.00 g/mol	98.00%

2.2 Catalyst synthesis

3.5 mmol $NiCl_2·6H_2O$ was fully dissolved in 60 mL deionized (D.I.) water, thus forming a uniform green solution, denoted as "solution A" (avoid long-term strong sonication to prevent from its hydrolysis). 1 mL KOH solution with the concentration of 10 mmol L^{-1} was add into the "solution A" under vigorous stirring to keep the mixture in a moderately alkaline condition. C_2H_5NS (TAA) was added into the above mixture under vigorous stirring for ca. half an hour. The mixture was further stirred and kept at 160±2°C for 2, 4, and 6 h in an oil bath assisted flask (not fully sealed). Thus, water will be slightly and gradually evaporated from the flask during the high-temperature period, which will be renewed every half an hour. The main processes were summarized in Figure 2.1.

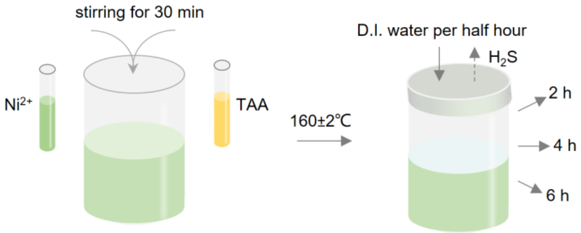

Figure 2.1 Vulcanization processes of $Ni^{2+}$by TAA for different time from 2, 4 to 6 h.

The above resulted black precipitates with different synthesis time were respectively marked as NiS_x-2 h, NiS_x-4 h, and NiS_x-6 h, which were further washed with deionized (D.I.) water and ethanol for at least three times to remove sulfur residues and organic precursor until the supernatant became completely clear. All three dark precipitates/catalysts were naturally dried in a vacuum oven at room temperature ca. 25°C for 1-2 days and then ground into fine powder for characterizations and tests.

The $Ni(OH)_2$ was prepared by a co-precipitation method by direct mixing of 3.5 mM $NiCl_2$ and 7.0 mM KOH under strong stirring, and the mixture was aged for 4 h at 160±2°C, which was under same conditions as that of NiS_x synthesis. Finally, green precipitates can be obtained with consistent collection, cleaning and drying processes as that of NiS_x based catalysts. All synthesis information of based catalysts was summarized in Table 2.2.

Table 2.2 Synthesis information involved in NiS_x based catalysts.

Catalyst#	Cation precursor	Anion precursor	Temperature / °C	Time / h	Denoted
NiS_x-#1	Ni^{2+}	TAA	160±2°C	2	NiS_x-2 h
NiS_x-#2	Ni^{2+}	TAA	160±2°C	4	NiS_x-4 h
NiS_x-#3	Ni^{2+}	TAA	160±2°C	6	NiS_x-6 h
$Ni(OH)_2$	Ni^{2+}	OH^-	160±2°C	4	$Ni(OH)_2$

2.3 Materials characterizations

2.3.1 X-ray diffraction (XRD)

X-ray diffraction is an analytical method for identifying phases by linking the periodicity of crystals with the wave nature of X-rays. When the wavelength of the incident X-rays is of the same magnitude order as the atomic spacing, the X-rays scattered by different atoms will interfere with each other, thus strengthening or counteracting. Therefore, the geometric properties of the diffracted X-rays are related to the structure of the periodically arranged material. Particularly, constructive interference follows Bragg equation that is illustrated in Figure 2.2A. And it is also possible for the scattered X-rays to cancel each other without diffraction peaks, which will be introduced in the part of diffraction intensity.[71]

Conversely, when a diffraction database of common crystalline materials is established, their phase composition can be inferred by testing the spatial geometric distribution (angles and intensity) of diffracted X-rays. However, there are two major difficulties in the operation of the X-ray diffraction for angle detecting: i) The X-ray emitter will generate multiple X-rays; ii) The angle detector needs to accurately correspond to the incident X-rays. To overcome the above issues, the X-rays produced in the X-ray tube can be filtered prior to X-ray diffraction. Then precise angle control needs to be achieved by the following special design. In Figure 2.2B, practically, an ingenious design of θ-2θ linkage is applied to the entire optical path to enable better detection of diffracted X-rays, which ensure that the sample surface is always tangent to the focusing circle.

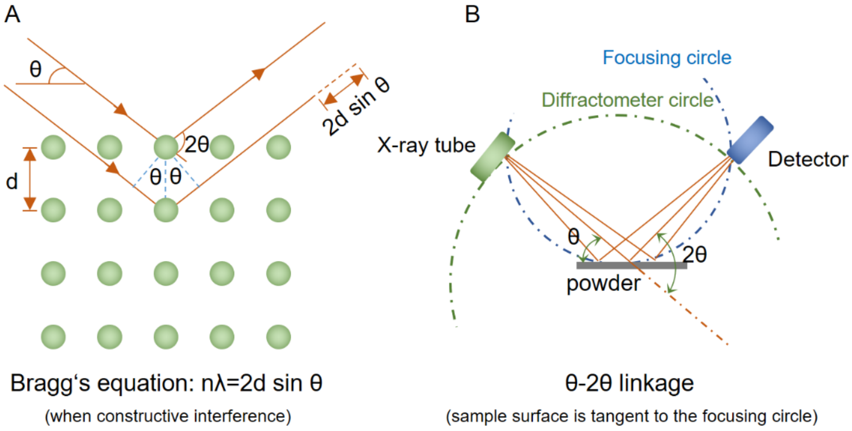

Figure 2.2 (A) Diffraction law of Bragg's equation and (B) construction of a diffractometer.

Other than diffraction angle, the calculation of diffraction intensity for polycrystals are extremely complicated. As shown in Figure 2.3, step-by-step approximation is summarized below: diffraction synthesis of electrons to one atom, of atoms to one unit cell, of unit cells to small crystals, of small crystals to polycrystals.

During each synthesis process, a corresponding factor will be introduced (e.g. structure, temperature factors etc.) Among all factors, the influence of structure factor is the most significant. Planes of different crystal structures may result in zero of "structure factor" and eventually zero diffraction intensity, which is called extinction effect. Taking the body-centered cubic unit cell as an example, when the sum of the crystal plane indices (h, k, l) is an odd number (h+k+l=odd), the diffraction intensity is zero.

Meanwhile, the effects of temperature, absorbance, and equivalent-plane number, intensity per unit arc length and small-crystal number should also be considered. Actually, the absolute intensity is uncommonly used, and the relative intensity between the diffraction lines is more practical. And for relative intensity, the approximation method is frequently used according to the influence degree of different factors.

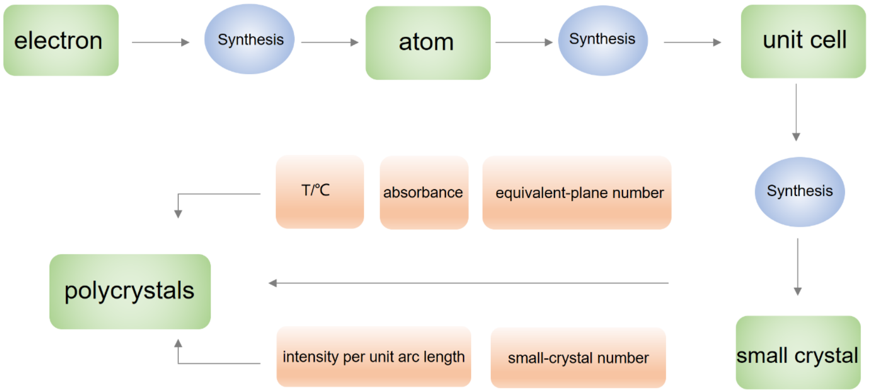

Figure 2.3 Step-by-step approximation of diffracted intensity from an electron, atom, unit cell, to small crystal, and then to crystals.

For the NiS_x based catalysts herein, their phase composition was unknown. Therefore, by measuring the diffraction intensity curve corresponding to the diffraction angle, and comparing with the XRD database of sulfide or polysulfide, the phase structures of the synthesized catalysts can be determined. The crystal/phase information of all NiS_x catalysts was studied by X-ray diffraction (D8 DISCOVER, Bruker) with X-ray emission from Cu-K_α target in both IEK-14 by Andreas Everwand and IEK-4 by Wulyu Jiang. First, the catalyst was ground to fine powder and then pressed onto an amorphous substrate, such as glass to avoid the background. Second, program of sweep speed, step size and ranges were set accordingly. Thirdly, the voltage was activated to accelerate the particles that will be blocked suddenly, and filtered to get monochromatic X-ray. Then, monochromatic X-rays were emitted, while the angle and intensity of diffracted X-rays were detected by the θ-2θ linkage setup. Finally, the outputs of angle-intensity curves were compared with the PDF card from Joint Committee on Powder Diffraction Standards (JCPDS) to determine corresponding phases.[72]

2.3.2 Scanning electron microscope (SEM)

SEM is a characterization method used to observe surface microstructure of conductive materials such as powder, solid substrate etc., which scans the sample with a narrow focused high-energy electron beam, thus obtaining various surface information through the interaction between incident beam and samples. As shown in Figure 2.4, detected signals can be divided into secondary electrons, backscattered electrons, Auger electrons, and characteristic X-rays etc., which are utilized for different characterizations. For example, signals from secondary and back-scattered electrons are used for surface morphology after collecting, amplifying, and imaging. Due to the lower energy of the secondary electrons, only the most superficial information can be obtained; while the back-scattered electrons have higher energy, and deeper structural information can be obtained. Additionally, Auger electrons and characteristic X-rays are used for X-ray Photoelectron Spectroscopy (XPS) and Energy Dispersive Spectroscopy (EDS), respectively.[73, 74]

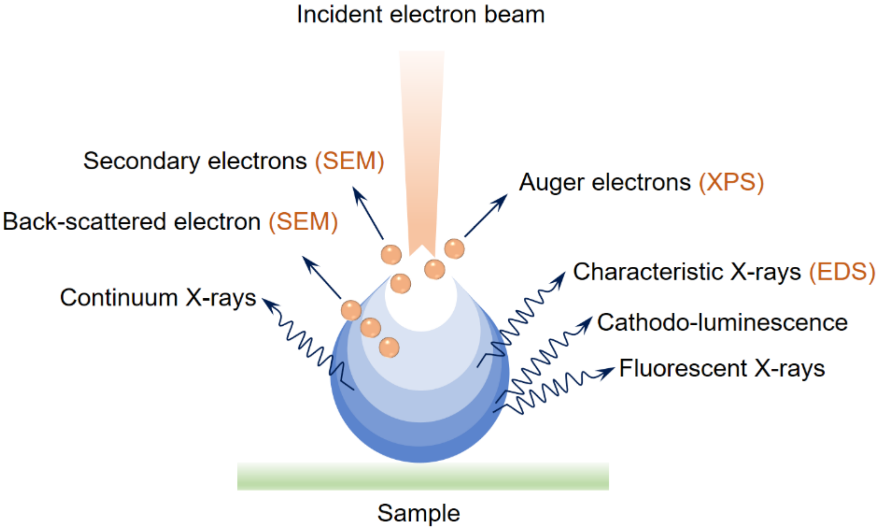

Figure 2.4 Fundamentals of Scanning Electron Microscopy (SEM): interaction of the electron beam with the surface of the sample.

At present, the common SEM uses field emission electrons, which means that the electrons move at high speed under the action of electric field force. As shown in Figure 2.5, the output high-energy electron beam is concentrated by the condenser lenses and then passed through the electromagnetic lens with scanning coil to interact with the surface of the sample. The excited electrical signals at different depths are collected by a detection probe located above the sample, then treated by an amplifier and subsequent re-imaging processes.

SEM (ZEISS LEO 1550 VP) in HNF was used to study the initial morphologies of NiS_x catalysts (Birgit Schumacher in IEK-14 also tested some important samples). Powder samples were coated on a conductive carbon substrate, and then gold was sprayed to prevent charging effects due to the poor conductivity of NiS_x. Meanwhile, the morphologies of NiS_x catalyst coated on carbon paper or nickel substrates before and after electrochemical tests, were also compared via SEM. This CCS sample was directly used for SEM observation without gold spraying due to the porous structure and high conductivity of nickel substrates. Particularly, the above samples were prepared first, then the vacuum was turned off and the sample was placed in the sample compartment and then started vacuum pump and voltage. Adjust the distance between the sample compartment and the probe and focus. Finally, some details could be adjusted to obtain high-quality images.

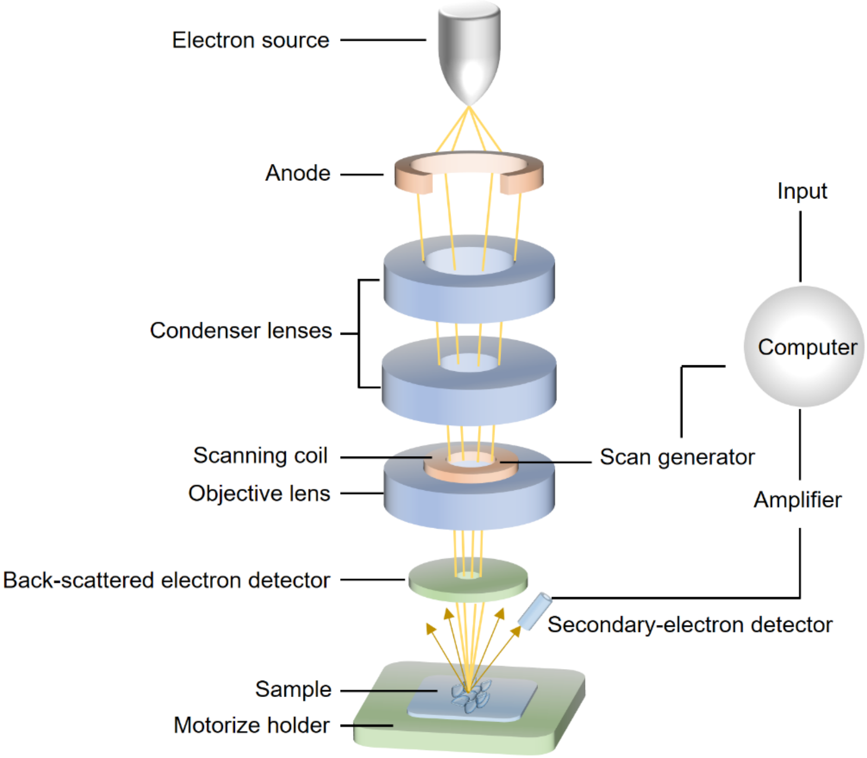

Figure 2.5 Structure of SEM: From high-energy electron beam emission to interaction with the sample surface, to signal collection and imaging processes.

2.3.3 Transmission Electron Microscopy (TEM)

TEM, similar in principle to SEM, but achieves higher resolution (<1 nm). The most essential difference between TEM and SEM lies in different signals. SEM prefers signals that are excited at the surface, while TEM detects transmitted or scattered electron signals.

As shown in Figure 2.6, TEM signals, according to the interactions between electrons and samples, can be divided into coherent/incoherent elastic/inelastic scattered electrons and transmitted electrons, which are applied to different characterizations. For example, coherent/incoherent elastic scattered electrons can be used for Scanning Transmission Electron Microscopy (STEM) for compositional analysis of nano-domains, and all of the above electrons can be used for Electron Energy Loss Spectroscopy (EELS). More importantly, High Resolution Transmission Electron Microscope (HRTEM) enables crystal structure analysis through light/dark fringe spacing that should be matched with the spacing between specific crystal planes of a crystalline material.

The structure of TEM (Figure 2.7) is also similar to that of SEM. The main difference is the location of the sample and the placement of the corresponding Lens. SEM detects surface signals, thus the sample is located at the bottom of lenses; while the sample of TEM is located in the upper middle position for collection of transmission electrons.[75, 76]

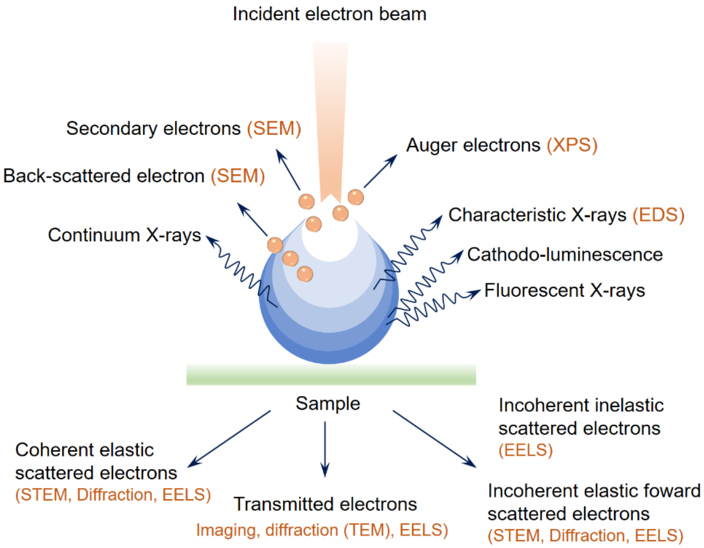

Figure 2.6 Principles of Transmission Electron Microscopy: electron-sample interactions (Electron Energy Loss Spectroscopy, EELS; Scanning Transmission Electron Microscopy, STEM).

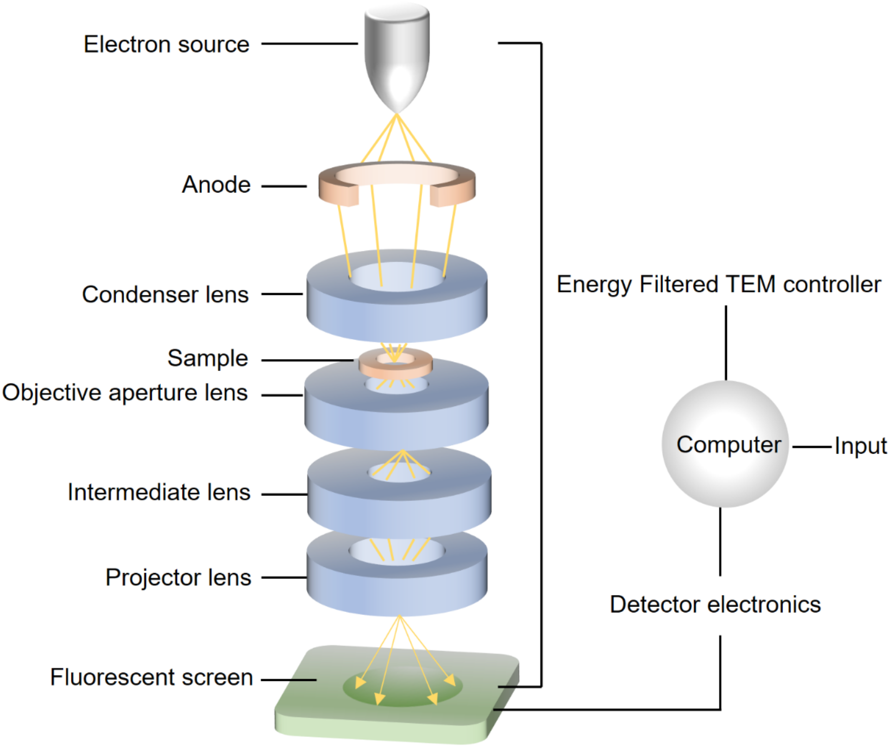

Figure 2.7 Structure of TEM: From high-energy electron beam emission to interaction with the sample, to signal collection and imaging processes.

TEM (Titan 80-300 electron microscope, Thermo Fisher Scientific), especially HRTEM and STEM, is crucial for this thesis. The nanostructures of NiS_x were studied by HRTEM and corresponding crystal structure information was compared with XRD results to make a "mutual confirmation" for their phase structure. STEM was further used to analyze the changes in morphology and composition of NiS_x before and after electrochemical treatment. All TEM measurements were conducted by Dr. Meital Shviro in ER-C2.

The sample preparation processes were as follows: i) ca. 0.1 mg powder sample was ultrasonically dispersed in ca. 2 mL ethanol, and then ii) a very dilute supernatant was dropped on a copper grid, iii) put it into the sample box after drying. The catalyst-coated glassy carbon electrodes were electrochemically treated and then placed in sonication for 10 minutes, and then the dispersion was dropwise deposited on a copper mesh for at least 10-20 drops.

2.3.4 X-ray photoelectron spectroscopy (XPS)

XPS is one of the most important methods for surface composition and chemical valence analysis. It can not only test the chemical composition, but also provide with the chemical coordination environment of elements. The inner electrons of different elements have different binding energies that are also related to chemical environment, which are known as chemical shift.

As shown in Figure 2.8, an X-ray, with energy of hv, bombards the electron and the electron overcomes the work function (W_f), escapes, and continues to move at high speed with the kinetic energy of E_k. Then according to the law of energy conservation, the initial electron binding energy (E_b) is calculated as: $E_b = hv - E_k - W_f$.

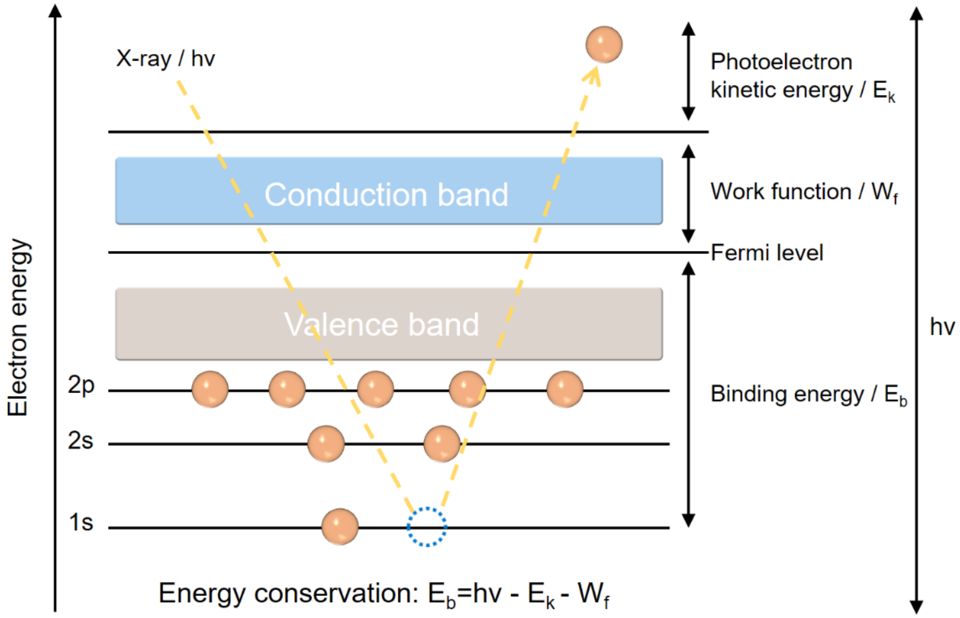

Figure 2.8 Principle of XPS according to the law of energy conservation: high-energy X-ray bombardment, electron detachment, and high-speed motion.

Based on the above, the main principle of XPS is first to excite the inner electrons of the material with ultra-high energy X-rays, then analyze the energy loss of electrons by an energy analyzer (Figure 2.9), thus obtaining the binding energy through the law of energy conservation, and then compare it with the known database. However, considering the complexity of the inner electron and atomic coordination environment, the analysis of XPS spectra, especially for transition metal compounds, is quite complicated. Thus, fine spectra fitting is needed for analysis of the elemental coordination environment.[77]

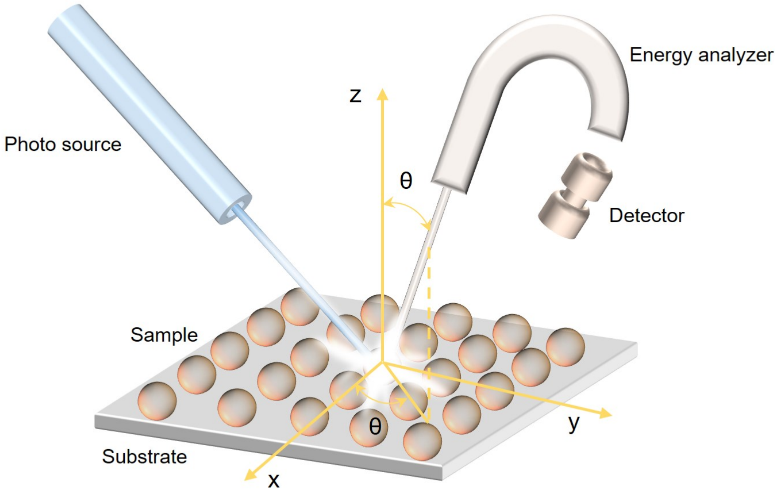

Figure 2.9 Main structure of XPS: from X-ray source, Electron reception and its energy analysis to binding energy.

After analysis by XRD, SEM, TEM, etc., the phase composition and morphological characteristics of NiS_x could be determined, but the chemical states of Ni and S were still unclear. Therefore, XPS was further used to analyze the valence distribution of Ni and the chemical environment of S. Specially, S in the form of (poly)sulfides (e.g. S^{2-}, S_2^{2-}, S_x^{2-}) was leached out during OER tests to form corresponding Ni (oxy)hydroxides, which relies heavily on the fine spectral scan and post-fitting analysis. All XPS measurements were conducted by Dr. Heinrich Hartmann in ZEA-3.

2.3.5 Fourier transform infrared spectroscopy (FTIR)

FTIR is based on a beam of interference light that interacts with the sample and the fast calculation of output-input changes will be conducted by computer to determine the structure of samples for specific molecular vibrations, rotations and transitions, etc. (Figure 2.10). FTIR is powerful for organic materials, and also can be used for organic part of inorganic materials.[78] Thus, it was used for the structure changes of NiS_2/Ni_3S_4 before and after water electrolysis, and the detection of leached product of sulfur, which is highly important for the understanding of the sulfur leaching processes. The FTIR measurements were conducted by Wulyu Jiang in IEK-14.

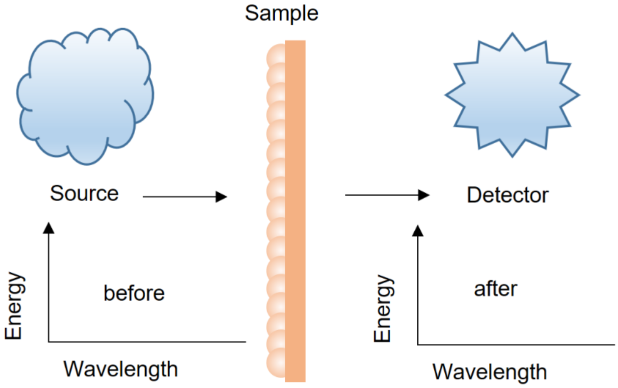

Figure 2.10 Principle of Fourier transform infrared spectroscopy (FTIR).

2.4 Half-cell tests

Above all, the inks in half-cell tests were prepared by dispersing 8 mg of NiS_x catalysts in the solvent of 0.5 mL DI water and 1.5 mL isopropanol with 20 µL 5 wt.% Nafion solution as the binder (Figure 2.11A), thus forming a homogeneous ink suspension with the catalyst concentration of 4 mg mL^{-1}. Then, glassy carbon (GC) electrodes (active area: 0.19625 cm^2) were coated by a drop of 10 µL (ca. 0.04 mg) the above ink suspension to achieve a mass loading of ca. 0.2 mg cm^{-2} (Figure 2.11B).

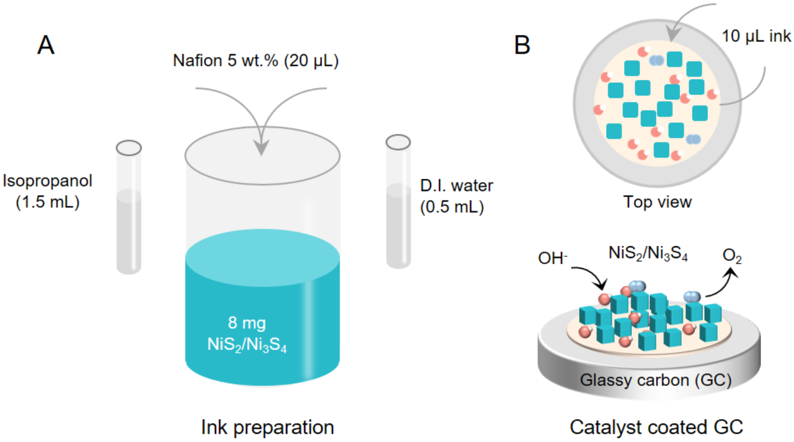

Figure 2.11 Details of ink preparation and catalyst coated glassy carbon (GC).

A rotating disk electrode system (RDE, Pine Research Instrumentation, USA), coupling with an electrochemical workstation (VSP-150, BioLogic Sciences Instruments), was utilized for the catalyst tests in a half cell. Typically, the half cell (Figure 2.12) consisted of i) 1 M KOH as the electrolyte with the volume of 150-200 mL, ii) catalyst coated GC as the working electrode (WE), iii) platinum wire as the counter electrode (CE), and iv) Hg/HgO as the reference electrode (RE).

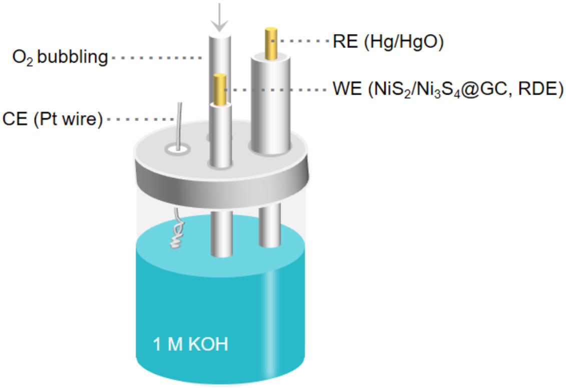

Figure 2.12 Three-electrode system with catalyst coated GC as working electrode (WE), platinum wire as counter electrode (CE), and Hg/HgO as reference electrode (RE) in 1 M KOH saturated with oxygen.

The calibration was achieved by i) (potential (vs. Hg/HgO)+0.926 V), ii) the standardized potential was further compensated by 85% of the IR loss. Linear sweep voltammetry (LSV) curves were utilized to assess the OER activity (@10 mA cm^{-2}) and kinetics (Tafel slope). All the catalyst activation was achieved by cyclic voltammetry (CV) method: i) the potential was scanned in the range of 1.0~1.7 V (100 mV s^{-1}) for ca. 30 cycles, which was denoted as sulfur leaching and the electrolyte was refreshed after activation; ii) then the LSV curves before and after activation were compared in the range of 1.0~1.7 V at 5 mV s^{-1}. The stability of catalysts during continuous OER processes was checked by a chronopotentiometry method at the current density of 10 mA cm^{-2}.

2.5 Materials for single-cell tests

Potassium hydroxide (KOH) for half- and full-cell tests was supplied from EMSURE®. Commercial Ni/NiO nanopowder and iridium black as the benchmark was purchased from

Alfa-Aesar (Thermo Fisher Scientific). Cathode (carbon paper, 350 μm) and anode (nickel fiber, 500 μm) as porous transport electrode (PTE) were received from Toray Industries Inc. (Japan) and NV Bekaert SA (Belgium) respectively. Both carbon paper and nickel fiber were cleaned by isopropanol for 30 min under sonication before use. FAA-3-50 and AF1-HNN8-50 (first generation) as membranes, and FAA-3-SOLUT-10, AP1-HNN8-00-X with the same composition of membrane materials as ionomers were supplied by Fumatech and Aemion+^{TM} (Ionomr Innovations Inc.), respectively. All chemicals/materials were summarized in Table 2.3.

Table 2.3 Materials for the benchmark.

Chemicals/materials	Molar mass	Purity/properties
Electrolyte	KOH	>85.00%
Anode catalyst	Ir black	99.99% Ir
Cathode catalyst	Pt/C	60 wt.% Pt
Anode PTE	Carbon paper	500 μm (2.2 cm*2.3 cm)
Cathode PTE	Nickel fiber	350 μm (2.2 cm*2.3 cm)
Membrane^1	AF1-HNN8-50	2.1~2.5 IEC (meq/g)
Ionomer^1	AP1-HNN8-00-X	-
Membrane^2	FAA-3-50	1.85 IEC (meq/g)
Ionomer^2	FAA-3-SOLUT-10	-

IEC*: Ion exchange capacity from technical data sheet.

2.6 Electrode fabrication via CCS

All electrodes in this thesis were fabricated via a CCS structure, which was achieved by spray coating (Sono-Tek, Figure 2.13A). First, catalyst ink consisted of 25 wt.% ionomer and 75 wt.% catalyst for the cathode, while 20 wt.% ionomer and 80 wt.% catalyst for the anode. Cathode catalyst was composed of 60 wt.% Pt that mixed with 40 wt.% high-surface-area carbon black. Anode catalyst was 100 wt.% synthesized NiS_x without additives. The ionomers used in this thesis were FAA-3-SOLUT-10, and AP1-HNN8-00-X, corresponding to the membranes of FAA-3-50 and AF1-HNN8-50 respectively.

All inks were sonicated for 30 minutes in an ice bath when the above catalyst-ionomer compositions were prepared. The catalyst was then injected into the syringe with a stirrer inside that was continuously stirring to prevent solid-liquid separation. The ink was then connected to a sprinkler by plastic tubes. Before spraying, positioning and pre-spraying were required to make ink more evenly sprayed on electrodes.

The spraying path was carried out in a repeated cross-serpentine manner with the spraying rate of 0.3 mL min^{-1} (Figures 2.13B-C). All sprays were done at 80°C and standard atmosphere mechanical pressure. After that the mass loading was controlled by weighing the mass change of the electrode with an accurate balance to the anode mass loading of 5 mg cm^{-2} and cathode of 0.8 mg cm^{-2}. The achieved CCSs were shown in Figure 2.13D for the anode and Figure 2.13E for the cathode, which were cut into pieces with suitable size of 2.2 cm*2.3 cm for single-cell tests.

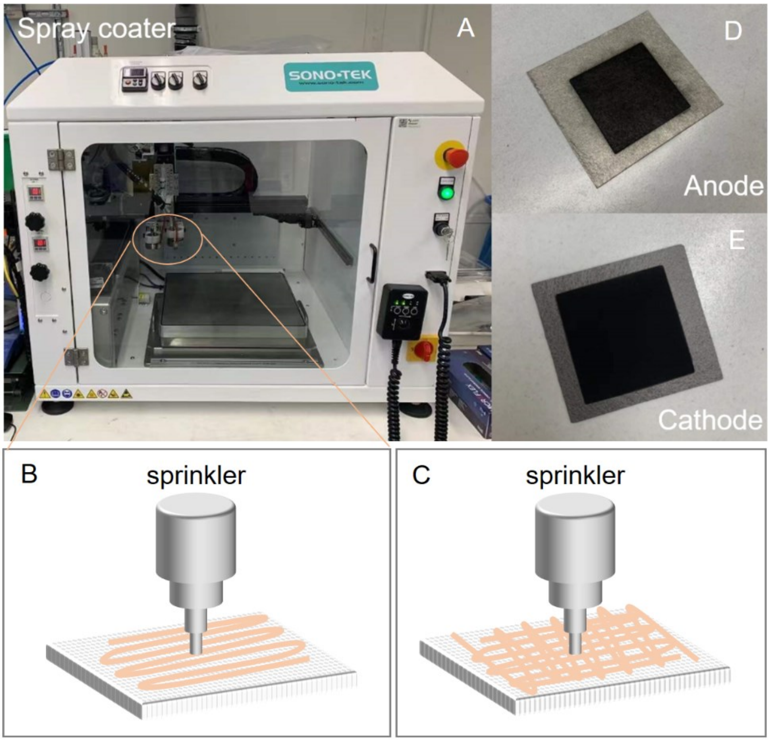

Figure 2.13 (A) Picture of spray coater, (B-C) spraying path and the achieved catalyst-coated (D) anode and (E) cathode.

2.7 Full-cell configuration

The prepared NiS_2/Ni_3S_4 were used as the anode catalyst, which were coated on the Ni fiber substrate with the area and total thickness of 5 cm^2 and 550 μm, respectively. Meanwhile Pt (wt.60%)/C was selected as the cathode catalyst, which was coated on the carbon paper with the area, total thickness of 5 cm^2 and 350 μm, respectively, and the loading of 0.8 mg cm^{-2}.

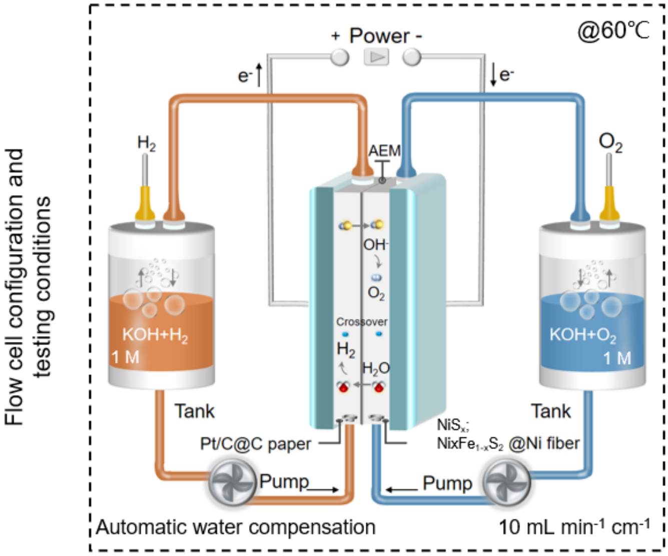

Figure 2.14 Sing-cell configuration and testing conditions.

As shown in Figure 2.14, FAA-3-50 and AF1-HNN8-50 were used as membranes, which were immersed in 1 M KOH for overnight before cell assembly and corresponding same composition ionomers were used as binders. 1 M KOH calibrated by a density tester was used as the electrolyte and its concentration was automatically controlled by a water-level sensor for water compensation. The bottoms of the two electrolyte tanks were connected to ensure balanced concentration. The hydrogen and oxygen produced on the cathode and anode are evacuated by a fume hood from the top of the tanks to prevent from hydrogen leakage and other potential risks. The electrolyte tank and the cells were connected by PTFE pipes fitted with gaskets. Before the test, it was necessary to check the tightness of the pipeline to prevent electrolyte leakage and CO_2 contamination to the electrolyte.

All the single-cell tests were conducted at the constant temperature of 60±1℃. The pumping rate of 50 mL min^{-1} was used for electrolyte flow and torque was fixed at 10.0 N·m for single-cell assembly to ensure repeatability from the perspective of mechanical pressure distribution. The configuration for the NiS_2/Ni_3S_4-based cell is as shown in Figure 2.15A. The initial gaps between polytetrafluoroethylene (PTFE) and both of the anode and cathode will be discussed later in Chapter 7 (Figure 7.1C). Then 2-3 cells were tested (Figures 2.15B-C) to further ensure repeatability. The main characteristics of key materials and corresponding parameters were summarized in Table 2.4. Electrodes that have been aged in water electrolyzers were stored and further analyzed. To compare the changes of the electrodes before and after long-term test of 500 h, the key parts of the MEA were also photographed.

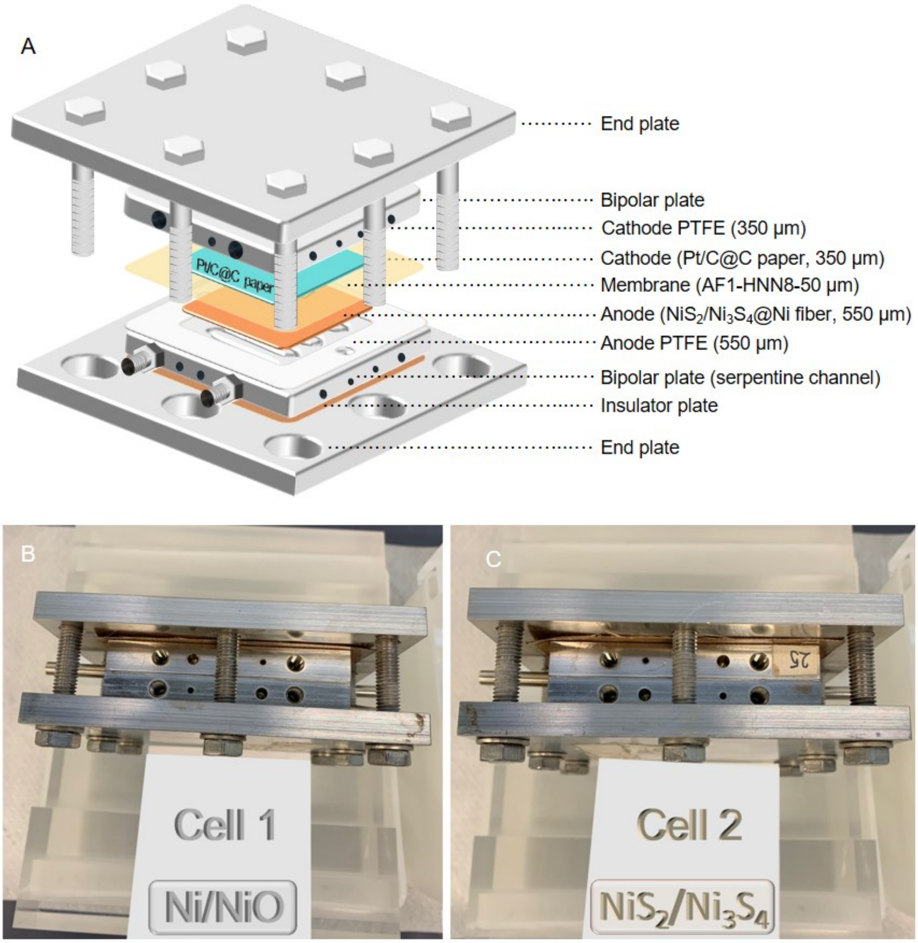

Figure 2.15 (A) Cell configuration and (B-C) parallel AEM water electrolysis cells.

Table 2.4 Characteristics of key materials and corresponding parameters.

Characteristics	Parameters
Cathode	0.8 mg/cm^2 Pt/C
Anode	5 mg/cm^2 TMS [*]
Electrolyte	1 M KOH
Electrode area	2.2 cm*2.3 cm
Flow field	Serpentine-type
Gasket	PTFE (Anode/Cathode: 550/350 μm)
Flow rate	50 mL min^{-1}
Temperature	60±1°C

TMS [*] Transition Metal Sulfides

2.8 Full-cell testing steps

All full-cell tests were carried out by a potentiostatic/galvanostatic station with AC impedance test element (BioLogic, BCS-815). The testing steps was as follows: i) 2 h for temperature stabilization without any operation; ii) electrode activation through sulfur leaching and 6 h conditioning at 1.7 V until the cell voltage was stabilized with the variation <1%, which was the key step for a stabilized and fair comparison among all cells. iii) Polarization curves were recorded by a multi-step galvanostatic method from “charge transfer resistance control”, “mixed control” to “ohmic internal resistance control” current areas (@5 min step^{-1}). The points in the low current density region were set as dense as possible, due to nonlinear changes and large errors, while in the high current region it is relatively sparse, which was already close to the linear variation region. Detailed single-cell testing steps and two parallel cells were shown in Figures 2.16-2.17.

Electrochemical impedance spectroscopy (EIS) was recorded during polarization tests at 10, 300 and 1000 mA cm^{-2} from 10 kHz to 0.1 Hz with amplitude of 10% of applied current density. After that, more than 500 h long-term stability was tested at the constant current density of 1000 mA cm^{-2}.

Finally, the above cells after stability tests were i) disassembled, ii) refreshed with a new membrane, iii) reassembled, and then restarted to test polarization curves that will be used for comparison with its initial performance to determine the stability of the anode.

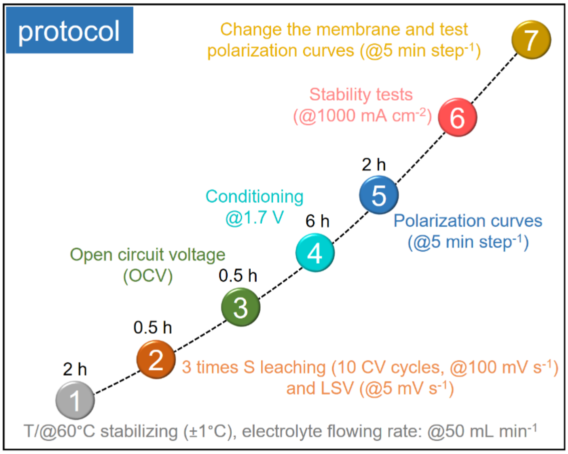

Figure 2.16 Detailed protocol for single cell tests.

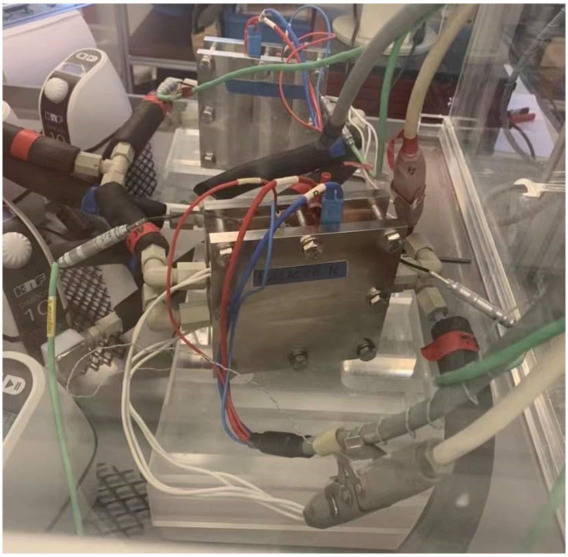

Figure 2.17 Photo of the cell-testing setup with current and voltage input (blue cables for cathode and red for anode, while white for heating and green for temperature monitor).

3 Experimental methods for $Ni_xFe_{1-x}S_2$

3.1 Chemicals

Nickel chloride hexahydrate ($NiCl_2 \cdot 6H_2O$) and ferrous sulfate heptahydrate ($FeSO_4 \cdot 7H_2O$) as cation precursors, sodium sulfide nonahydrate ($Na_2S \cdot 9H_2O$) and sulfur powder (S) as sulfur sources, and sodium hydroxide (NaOH) as the pH controller were all used as received from Sigma-Aldrich without further purification. The molar mass of the above chemicals and their purities were shown in Table 3.1.

Table 3.1 Synthesis information involved in $Ni_xFe_{1-x}S_2$ *based catalysts.*

Chemicals	Molar mass	purity
$NiCl_2\cdot6H_2O$	237.69 g/mol	99.90%
$FeSO_4\cdot7H_2O$	278.01 g/mol	99.00%
NaOH	40.00 g/mol	98.00%
$Na_2S\cdot9H_2O$	240.18 g/mol	98.00%
S	32.07 g/mol	99.98%

3.2 Synthesis of $Ni_xFe_{1-x}S_2$

First, 10 mmol $NiCl_2\cdot6H_2O$ and 5 mmol $FeSO_4\cdot7H_2O$ were fully dissolved in 20 mL deionized (D.I.) water after stirring for 5 min, thus forming a uniform green solution, denoted as the "solution A" (avoid long-term strong sonication to prevent from its hydrolysis). And then 30 mL Na_2S_x solution with the concentration of 0.5 M, prepared by solid-liquid reaction between Na_2S and S supported in NaOH with the molar ratio of Na_2S: S: NaOH=1:1:1 at 80°C for 1 h, was added into the "solution A", thus forming a huge amount of black precipitates. Notably, Na_2S_x solution was cooled and then adjusted to the corresponding concentration, and then precipitated with Ni, Fe precursors. The entire process must be done in a fume hood due to the volatility of Na_2S_x.

After strong stirring for 10 min, the above black products were transferred into a 100 mL Teflon-lined autoclave and kept at 200±1°C in an oven for 2 h. Finally, the resulting black precipitates with different Ni/Fe ratios were marked as NiS_2, $Ni_{0.80}Fe_{0.20}S_2$, $Ni_{0.67}Fe_{0.33}S_2$, $Ni_{0.50}Fe_{0.50}S_2$, $Ni_{0.33}Fe_{0.67}S_2$, FeS_2, which were further washed with deionized (D.I.) water and ethanol for serval times to remove sulfur residues and other soluble impurities until the supernatant became completely clear. Alternate shaking and centrifugation were necessary for better cleaning.

All three dark precipitates/catalysts were dried and ground under same conditions as that of NiS_x. Particularly, $Ni_{0.67}Fe_{0.33}S_2$ catalysts prepared by different reaction time (0.5 h, 1 h) at 200±1°C, together with other $Ni_xFe_{1-x}S_2$, were listed in Table 3.2.

Table 3.2 Synthesis information involved in $Ni_xFe_{1-x}S_2$ (x=0~1) based catalysts.

Catalyst	Cation precursor	Anion precursor	Temperature	Time
$Ni_{0.80}Fe_{0.20}S_2$	Ni^{2+}/Fe^{2+}	S_x^{2-}	200±1°C	2 h
$Ni_{0.67}Fe_{0.33}S_2$	Ni^{2+}/Fe^{2+}	S_x^{2-}	200±1°C	2 h
$Ni_{0.50}Fe_{0.50}S_2$	Ni^{2+}/Fe^{2+}	S_x^{2-}	200±1°C	2 h
$Ni_{0.33}Fe_{0.67}S_2$	Ni^{2+}/Fe^{2+}	S_x^{2-}	200±1°C	2 h
NiS_2	Ni^{2+}	S_x^{2-}	200±1°C	2 h
FeS_2	Fe^{2+}	S_x^{2-}	200±1°C	2 h
$Ni_{0.67}Fe_{0.33}S_2$	Ni^{2+}/Fe^{2+}	S_x^{2-}	200±1°C	1 h
$Ni_{0.67}Fe_{0.33}S_2$	Ni^{2+}/Fe^{2+}	S_x^{2-}	200±1°C	0.5 h

3.3 Material characterizations

3.3.1 Basic XRD, SEM, HRTEM, STEM and XPS

All synthesized $Ni_xFe_{1-x}S_2$ catalysts were characterized according to the experimental methods (XRD, SEM, HRTEM, STEM, XPS etc.) described in Chapter 2.

3.3.2 Inductively Coupled Plasma with Optical Emission Spectroscopy (ICP-OES)

ICP-OES, similar with Inductively Coupled Plasma-Mass Spectrometry (ICP-MS), is a method that can accurately and quickly obtain composition information of materials by using ICP. Compared with SEM-EDX, both ICP-MS and ICP-OES need to destroy the chemical structure of the material by acid, such as hydrochloric (HCl) and nitric acids (HNO_3).

The working principle of them is slightly different. ICP-MS characterize elements by different charge/mass ratios, while ICP-OES distinguishes different elements according to their wavelength of the characteristic spectrum generated. For example, hydrogen atom from excited state 6 to ground state 2 will emit the light with wavelength of 410 nm (Figure 3.1).[79]

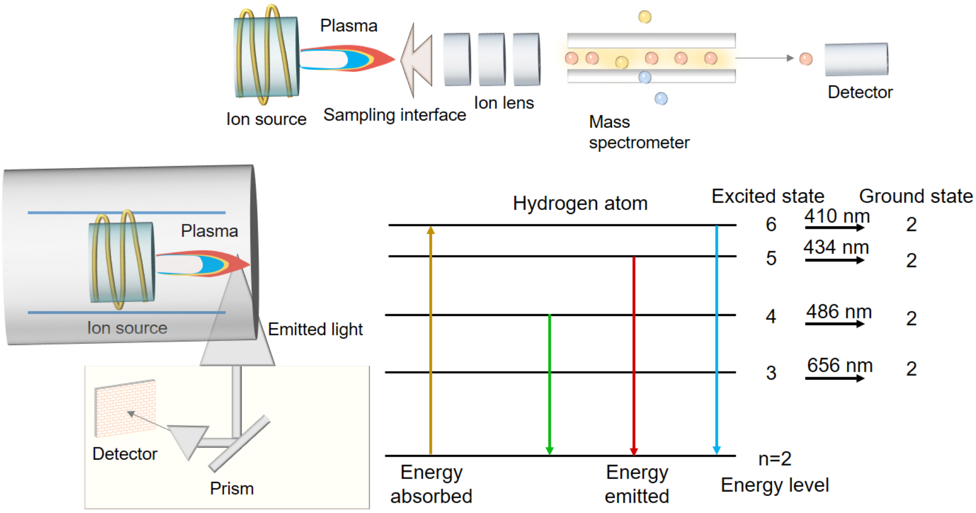

Figure 3.1 The working principle of Inductively Coupled Plasma with Optical Emission Spectroscopy (ICP-OES): source of ion, light emission, spectroscopy, and detector.

ICP-OES is an important analysis method for determining element ratio between Ni and Fe for $Ni_xFe_{1-x}S_2$ to ensure the input-output ratio of precursors and catalyst products, and also for composition analysis of transition metal elements in different catalysts. Sulfur is not in the scope of ICP-OES study due to its instability in strong acids, which volatilizes in the form of hydrogen sulfide.

Specifically, ca. 50 mg sample was dissolved by 3 mL HCl and 3 mL HNO_3 and 4 mL H_2O_2 at 25°C for half an hour, and each solution was made up to 50 mL. After that, 2 replicates of the above solution (100-fold) were analyzed by ICP-OES (iCAP 7600) in ZEA-3. Finally, mass fraction was transferred to atomic fraction with standard deviation.

3.3.3 *In-situ* Raman spectra

Raman spectra is a highly adaptable characterization method with low requirements on the state of samples. It can characterize gas, liquid and solid samples, and achieve in-situ detection by special setups.

In particular, when the laser with the wavelength of λ_{laser} passes through transparent materials, a "frequency change" of wavelength occurs for the light scattered by molecules from λ_{laser} to $\lambda_{scatter}$, which is known as "Raman scattering" and can be divided into three types, namely, i) Stokes ($\lambda_{scatter} > \lambda_{laser}$), Rayleigh ($\lambda_{scatter} = \lambda_{laser}$) and Anti-Stokes ($\lambda_{scatter} < \lambda_{laser}$)

Raman Scattering (Figure 3.2A).[80] Based on this phenomenon, an analytical method called Raman Scattering Spectroscopy (RSS) was developed to analyze corresponding scattering spectrum with different frequencies, thus obtaining information on vibration/rotation etc., such as O-H in H_2O and $Ni(OH)_2$ and -OOH in NiOOH, FeOOH (Figure 3.2B), which is also applied to infer the structure of corresponding materials.

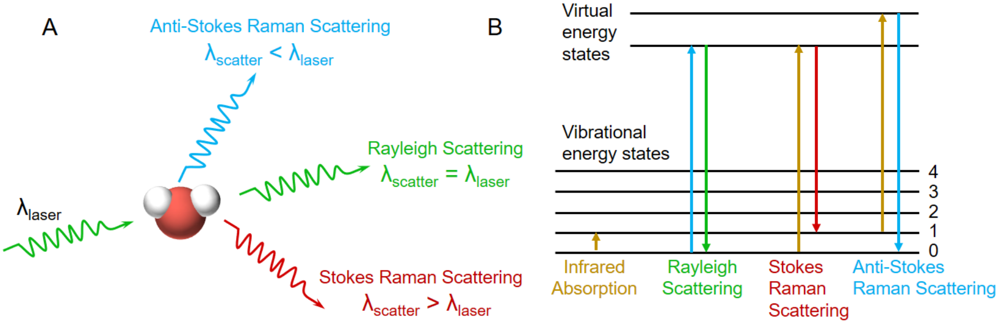

Figure 3.2 Principle of Raman Spectra: (A) The relationship between incident wavelength and the type of scattering, (B) corresponding energy states.

Raman spectra is a highly important method for the detection of real active species of $Ni_xFe_{1-x}S_2$ in catalyzing OER. However, Raman spectroscopy testing needs to be time-sensitive during OER. Therefore, *in-situ* Raman spectroscopy characterization was designed and implemented and is of great importance for determining the real steps of surface reconstruction of $Ni_xFe_{1-x}S_2$ at different potentials (vs. RHE), and the corresponding active species formed during OER processes, which is more powerful than ex-situ tests.

As shown in Figure 3.3, three electrode system was arranged in a small box with the transparent top for the transmission of Raman spectrum to the working electrode. Normally, counter and reference electrodes were set on the left side and a hole for gas bubbling. The box also acted as an electrolyte container and could be easily disassembled for cleaning and replacement of parts.[81]

Trace amount of $Ni_xFe_{1-x}S_2$ catalyst was coated on the working electrode, which was further kept at 1.3-1.7 V with the increment of 0.1 V, respectively. During each potential stage, Raman spectra was applied to the surface of the working electrodes and the curve of between intensity and wavenumber was recorded. All the in-situ Raman spectra during OER were conducted by Dr. Alaa Faid in NTNU.

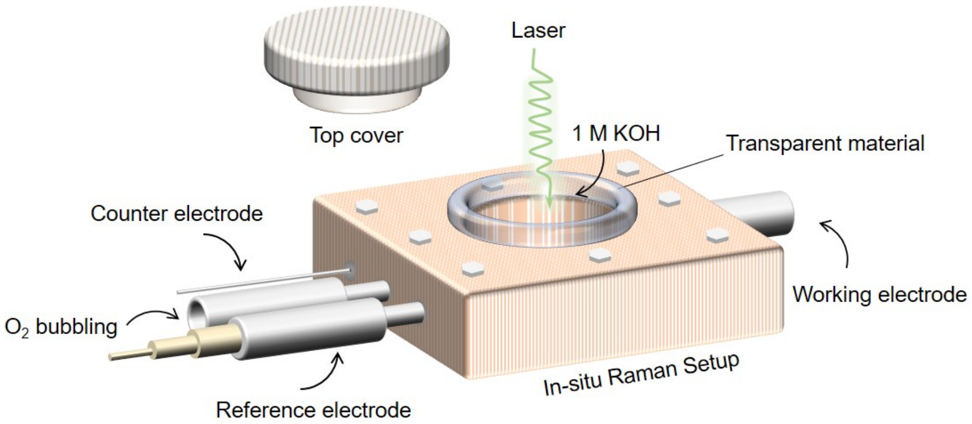

Figure 3.3 Setup for in-situ Raman Spectra with reference electrode, counter electrode and oxygen inlet on the left, while working electrode on the right and 1 M KOH inside (in the central area of the cell, just above the working electrode, a piece of transparent glass was used for the incidence of the laser).

4 Experimental methods for performance optimization

4.1 Materials

As shown in Table 4.1, three anion exchange membranes (Aemion+™, AF1-HNN5-25, AF1-HNN8-50, AF2-HWP8-75) with different thickness, ion exchange capacity (IEC) and conductivity for single cell tests and ionomer (AP1-HNN8-00-X) for the spray coating of CCS were all supplied from Ionomr Innovations Inc (Canada). Additionally, platinum (Pt/C, 60% Pt) as cathode catalyst and iridium black as anode catalyst with Ir content≥99.99%) were used as received without further treatment from Fuel Cell Store and Alfa Aesar respectively.

Table 4.1 Main technical parameters of three type of anion exchange membranes

Membrane	Thickness (μm)	Ion Exchange Capacity [c] (meq $OH^- g^{-1}$)	Conductivity [c] ($mS \cdot cm^{-1}$)
AF1-HNN5-25	25	1.4-1.7	56±1
AF1-HNN8-50	50	2.1-2.5	102±3
AF2-HWP8-75	75	2.3 - 2.6	-

4.2 Electrode preparation

Cathodes and anodes consisted of Pt/C (0.8 mg cm^{-2}) coated on carbon paper, and Ir black (1 mg cm^{-2}) on nickel fiber, all fabricated by the above-mentioned spray coater in Chapter 2 with a constant spraying rate of ca. 0.3 mL min^{-1} at atmospheric pressure and temperature of 80°C. The ionomer mass ratio of cathode and anode was slightly different, 25% (75% cathode catalyst) and 20% (80% anode catalyst) respectively. After spray coating, the catalyst loading of the electrode was measured by a precise balance between the final weight and original weight (Mass loading = (final weight - original weight) / area).

4.3 Mechanical pressure tests

Mechanical pressure tests were achieved in the real cell with different thickness of PTFE with the same electrode thickness of 350 and 550 μm for the cathode and anode respectively.

The only difference lies in that the pressure-sensitive foil (types LLLW, LLW and LW from Fujifilm) will be placed within the anode and cathode without the membrane. Mechanical pressure distribution tracking was implemented by the “color mapping” of three foils, with completely different mechanical pressure sensitivity in three ranges, in the cells assembled by different configuration of PTFE. As shown in Figure 4.1, Δd was defined as “exposed height”, which is the total gap of anode-PTFE$_{anode}$ and cathode-PTFE$_{cathode}$ from 0 to 300 μm with the increment of 100 μm. For convenience, the PTFE-electrode gaps of the cathode and anode are equidistant. Mechanical pressure was tested by Sebastian Holtwerth.

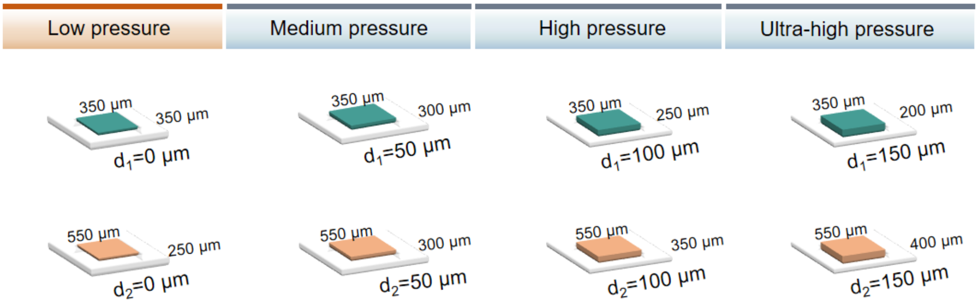

Figure 4.1 Definition of exposed height (Δd) and corresponding mechanical pressure conditions.

As shown in Figure 4.2, after the cell assembly by the above PTFE and electrode configuration with the torque of 10 N·m, the cells were disassembled and the mechanical pressure sensitive foils were taken out and the mechanical pressure distributions were obtained by post scanning and corresponding statistical analysis. To make sure all the cells are under the same imposed stress, a torque controller was utilized and was applied step by step for cell assembly assisted by a stabilizer.

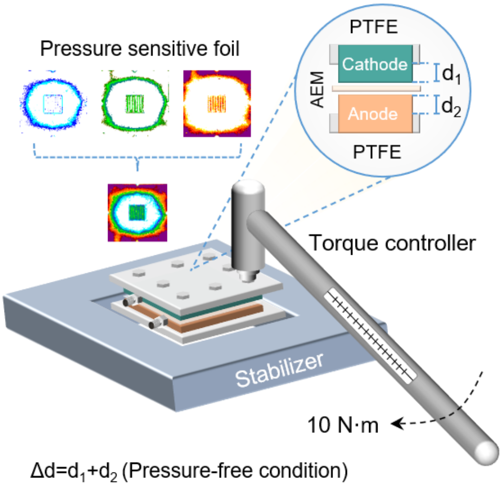

Figure 4.2 control steps for mechanical pressure distribution and corresponding testing method.

4.4 Physical properties

Three main physical properties including electrode thickness, contact resistance, and contact angles were tested. Both anode and cathode after different mechanical pressure assembly such as Δd=0, 100, 200, and 300 etc. were achieved by i) assembling the cell with different initial Δd; ii) opening the cells and the electrodes were taken out for characterizations:

First, the thicknesses of all anodes and cathodes were checked by the thickness tester for serval times at the middle and four corner sites and balanced by error bars.

Then, total resistance, including contact resistance on both sides and the bulk resistance of electrodes was in a simple DC circuit. As shown in Figure 4.3, the overall experimental design for contact resistance was composed of two coppers based (Cu) plates with one anode or cathode in the middle, like a sandwich structure, and this circuit was under an extremely high current of 15 A to outshine the low value of contact resistance, and then calibrated by the resistance of Cu and circuit. It is worth noting that the resistance measured in this way included the contact resistance on both sides and the bulk resistance of the electrode substrate.

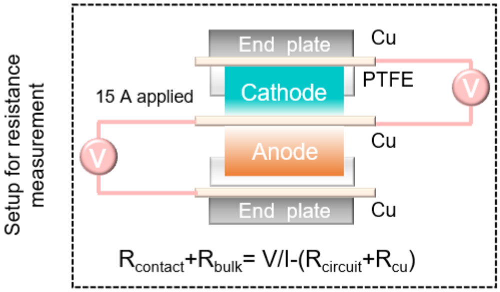

Figure 4.3 Overall experimental design for contact resistance.

And then contact angle of water was further tested by high-speed-camera based instrument (CAT, KRÜSS) from 0 to 30000 ms (30 s). All contact angle tests need to be repeated more than 3 times to verify their authenticity.

4.5 Surface morphology and conductivity

Three-dimensional microscope (VHX-7000, KEYENCE) was used to understand the surface roughness and relative thickness distribution of the pristine Ir-coated anodes. Then optical microscope was applied to disclose the changes of anodes after different compressions, while detailed surface morphologies and pore radius were further captured by a field emission scanning electron microscope (LEO 1550 VP). The roughness and local conductivity were further studied by atomic force microscope (AFM, Asylum Research Cypher S with ORCA holder Nanosensors PPP ContPt cantilever) in air. All the AFM measurements were conducted by Dr. Christian Rodenbücher in IEK-14.

4.6 Single-cell tests

Step for polarization tests were the same as that mentioned in the chapter 2. Single-cell stability was tested at a constant current density of 1000 mA cm^{-2}, and the hydrogen permeation or gas crossover (GC) was tested by a GC system (490, Agilent Technologies). Encouraged by the study of diffusion process in battery fields, we used the galvanostatic intermittent titration technique (GITT) by applying intermittent charging/electrolysis for 300 s at 1000 mA cm^{-2} and then relaxation under open circuit voltage (OCV) for 30 s that are not enough for bubble diffusion (the voltage will continuously increase), thus understanding the voltage increase rate caused by bubble diffusion issues.

5 NiS_2/Ni_3S_4 nano-cubes

5.0 Preface

1. Gap between the literature and Chapter 5:

As summarized in Chapter 1, TMS exhibit great advantages in multi-phase structures, lattice and unique electronic structures, diverse morphologies, and low cost. However, the researches in literature on polysulfide as OER catalysts mainly concentrated on in-situ-grown electrodes on the substrates such as nickel foam, fiber etc. Such electrodes present major challenges for AEMWE cells: i) catalyst loading is difficult to control, ii) catalysts grow on both sides of the electrode, leading to high contact resistance with the bipolar plate, iii) not reproducible (non-uniform distribution and uncontrollable mass loading), iv) low stability in underflow mode (without binder reinforcement, largely washed away). Moreover, the electrochemical behaviors of sulfur and the compositional, morphological evolutions of polysulfides during OER processes, and their remarkable high-rate stability (@1 A cm^{-2}) in electrolyzer cells are still unclear.

In this chapter, a pre-catalyst in the form of NiS_2/Ni_3S_4 nano-cubes in Figure 5.0, was synthesized and sprayed onto the electrode in accordance with a predetermined loading to take advantage of the dispensability of polysulfides and solve the problem of catalyst shedding. Then NiS_2/Ni_3S_4 suffered from sulfur leaching and thanks to the nanostructured $NiS_x/Ni(OH)_2/NiOOH$ derivatives, the electrodes exhibit better bubble diffusivity and lower interfacial resistance than commercial Ni/NiO in high current tests. Most publications focused on half-cell tests, and there are few studies on the high current stability of polysulfides in full cells, thus this chapter can provide some references.

2. The main goals of Chapter 5:

i) Prove the phase structure, surface chemical state and morphology of NiS_2/Ni_3S_4 based nano-cubes and elucidate the reasons for the formation of NiS_2/Ni_3S_4 nano-cubes;

ii) Enhance OER activity via electrochemically assisted sulfur leaching and study the corresponding mechanism behind the reconstruction of NiS_2/Ni_3S_4 nano-cubes for truly active and stabilized species;

iii) Compare the OER performance and stability of NiS_2/Ni_3S_4 nano-cubes with commercial Ni/NiO and synthesized $Ni(OH)_2$ and analyze the "particularity" of the NiS_2/Ni_3S_4 derived catalyst.

iv) Promote the concept of "sulfur leaching" from half to full cells, and test the polarization curves of NiS_2/Ni_3S_4 based single cells with Pt/C as cathode and AF1-HNN8-50 as the membrane and also long-term stability at high current density of 1000 mA cm^{-2}.

v) Summarize the electrochemical behavior of NiS_2/Ni_3S_4 nano-cubes in OER and full-cell water electrolysis and the possibility as a general method for other systems like NiS_2, FeS_2, CoS_2, MoS_2 etc.

Note: Some results of the Chapter 5 were published. [82]

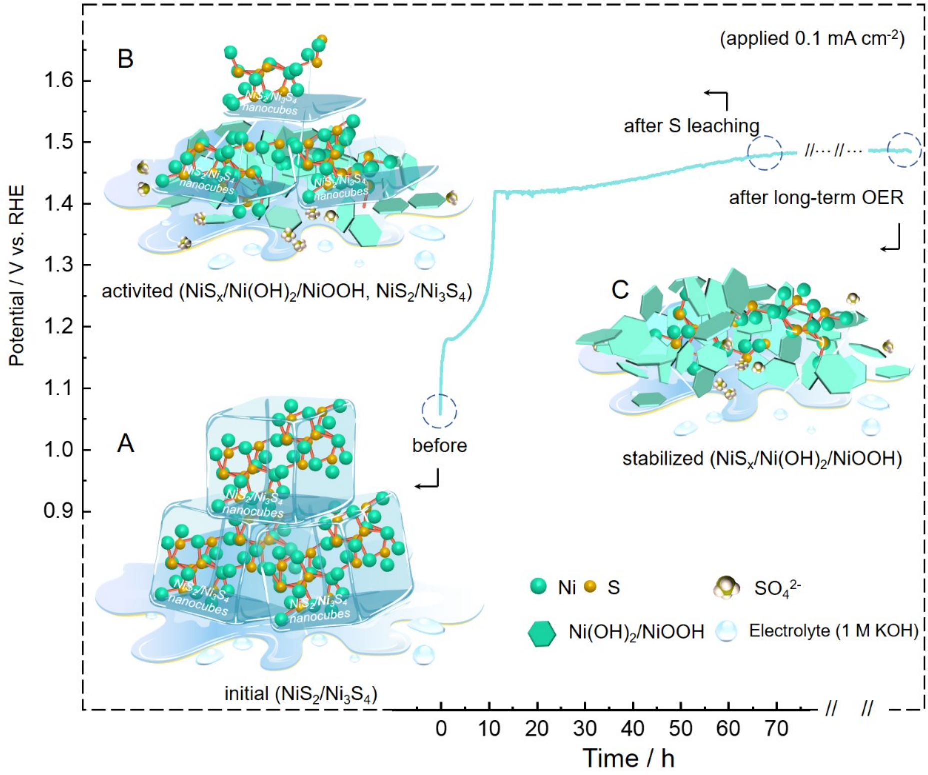

Figure 5.0 Schematic illustrations: (A) initial state of NiS_2/Ni_3S_4 composite nano-cubes as a "pre-catalyst" and corresponding (B) partially activated $NiS_x/Ni(OH)_2/NiOOH$ derivatives and (C) fully activated $NiS_x/Ni(OH)_2/NiOOH$ heterostructure.

5.1 Characterizations of NiS_2/Ni_3S_4

As explained in chapter 2, the synthesis of the NiS_2/Ni_3S_4 nano-cube was achieved by parameter control of vulcanization time to 4 h at 160°C. Its phase structure, chemical composition, the reason behind the formation of NiS_2/Ni_3S_4 nano-cube and corresponding structural changes after sulfur leaching will be included in this part.

5.1.1 Phase, chemical composition and morphology of NiS_2/Ni_3S_4

X-ray diffraction (XRD) was used to study the crystal structure of the Ni (poly)-sulfides. As shown in Figure 5.1, the diffraction peaks at 2θ values corresponds to the typical planes of NiS_2 (JCPDS: 11-0099) with the strongest peak at the (200) plane, [83-85] and (311) plane for Ni_3S_4 (JCPDS: 00-047-1739).[86-88] Meanwhile, the diffraction peaks in the range of ca. 20-25° are corresponding to α-S_8, which is the residue of thioacetamide.[89] Therefore, the phase structure of the synthesized (poly)-sulfide catalyst is composed of NiS_2/Ni_3S_4 with a small amount of impurity α-S_8.

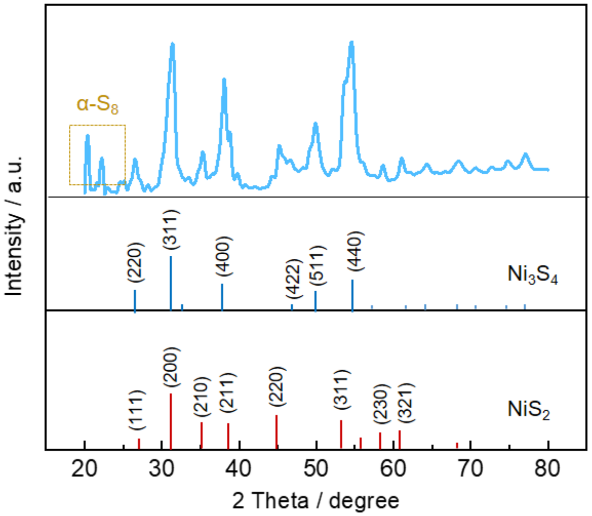

Figure 5.1 XRD patterns of NiS_2/Ni_3S_4 in the range of 20-80° and the standard peaks are corresponding to Ni_3S_4 (blue) and NiS_2 (red).

X-ray photoelectron spectroscopy (XPS) was applied to study the surface chemical state configuration of nickel and sulfur in NiS_2/Ni_3S_4. As shown in Figure 5.2A, the NiS_2/Ni_3S_4 surface mainly contains nickel (Ni), oxygen (O), sulfur (S) and carbon (C). Among them, O and C may come from adsorbed substances such as water molecules and carbon dioxide on the surface. Then the fine spectra of the narrow interval of Ni, S and O are shown in Fig. 5.2B-D.

The Ni 2p spectrum of NiS_2/Ni_3S_4 was fitted into two peaks at ca. 857.8 and 853.7 eV, which are corresponding to Ni^{2+} $2p_{3/2}$ in the sulfate form and Ni^{2+} $2p_{3/2}$ as sulfides respectively (Figure 5.2B),[83] indicating that the pristine NiS_2/Ni_3S_4 is almost fully composed of Ni^{2+}, which could cause relatively low OER performance at the beginning due to poor electrophilicity of adsorbed oxygen.[88, 90, 91] Additionally, the S 2p spectrum (Figure 5.2C) was fitted into three peaks: the peaks at 161.5 and 162.6 eV are attributed to $2p_{3/2}$ and $2p_{1/2}$ of sulfide ions (S^{2-}).[83, 85] The peaks at 162.5 and 163.7 eV are corresponding to $2p_{3/2}$ and $2p_{1/2}$ of disulfide ions (S_2^{2-}).[84, 92, 93] Notably, the peaks at 163.5 and 164.7 eV can be attributed to $2p_{3/2}$ and $2p_{1/2}$ of α-S_8 respectively, which reflect the signal from S impurity that produced from organic sulfur precursor during the sulfurization reaction processes (specifically, the oxidation reaction between S_n^{2-}, O_2 and H^+ due to decreased pH).[83, 94]

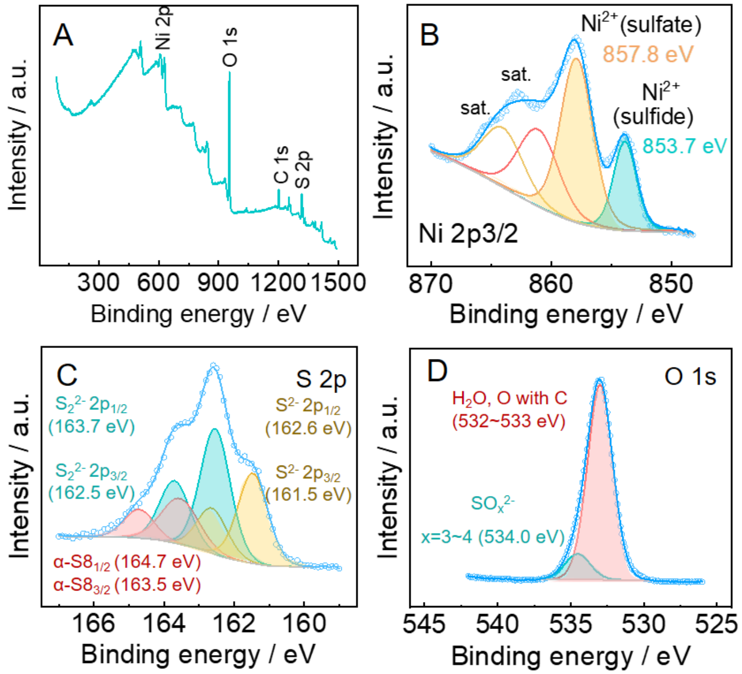

Figure 5.2 XPS of NiS_2/Ni_3S_4: (A) Survey from 100-1500 eV, (B) Ni 2p from 847.5-870 eV, (C) S 2p from 162-168 eV and (D) O 1s regions from 525.0-542.5 eV.

Moreover, the binding energy peaks at ~529 and ~531 eV in O 1s region can be corresponded to NiO and $Ni(OH)_2$, respectively, which were not detected (Figure 5.2D),[95, 96] indicating the surface of the pristine NiS_2/Ni_3S_4 catalyst has no nickel oxides/hydroxides species. Consequently, the NiS_2/Ni_3S_4 surface consists of low-valence nickel, low sulfide state sulfur/disulfide ions (Ni^{2+}, S^{2-}, and S_2^{2-}).

The morphology of NiS_2/Ni_3S_4 was observed by high resolution transmission electron microscopy (HRTEM). It is shown in Figures 5.3A-C that NiS_2/Ni_3S_4 exhibits the cubic morphology with the length of ca. 80±20 nm with some coverage that could be attributed to the S impurity.

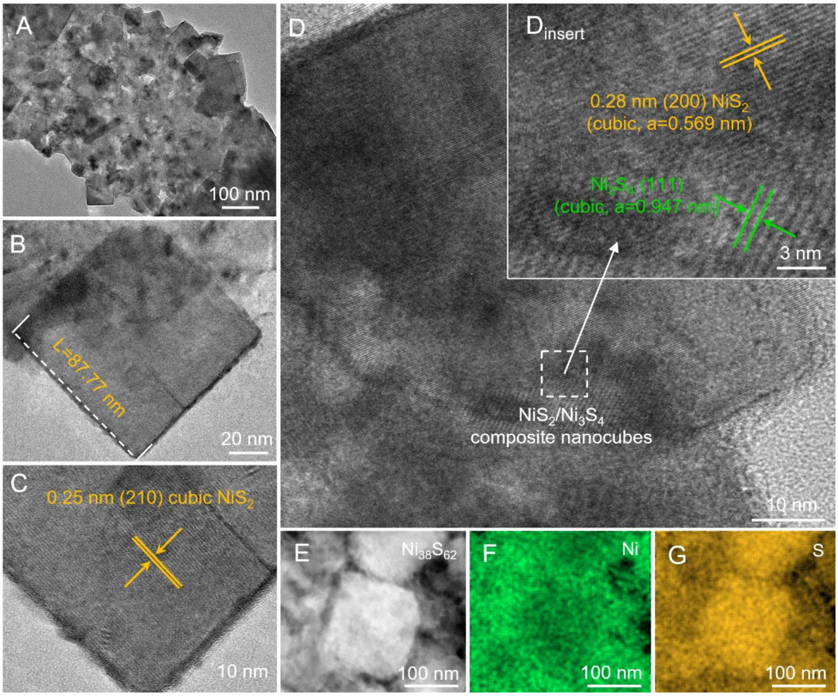

Figure 5.3 TEM, HRTEM images, HAADF-STEM images and corresponding elemental mappings of NiS_2/Ni_3S_4: (A) Low magnification TEM, (B) geometric size of single nano-cube, (C) HRTEM images of the NiS_2 nano-cube, (D) NiS_2/Ni_3S_4 composite nano-cube and (D_{insert}) magnified image, (E) HAADF-STEM image of NiS_2/Ni_3S_4 nano-cube, and (F-G) distribution of Ni and S by EDX mappings.

Such a special structure is achieved by moderate pH during 4 h vulcanization, under which the produced elemental sulfur further reacts with nickel sulfides (NiS) to form NiS_2/Ni_3S_4 polysulfides. As shown in Figures 5.4-5.5, sulfur species (S^{2-}, S_2^{2-}) first suffered from the precipitation with Ni^{2+} ions to form the phase of $NiS/NiS_2/Ni_3S_4$ (after 2 h), namely, hexagonal NiS (JCPDS: 75-0613),[97] NiS_2 (JCPDS: 1-0099) and Ni_3S_4 (JCPDS: 00-047-1739).[83-85, 97] Then extra $NiS/NiS_2/Ni_3S_4$ was transformed to NiS_2/Ni_3S_4 polysulfides by the reaction with elemental S (after 4 h), and then Ni_3S_4 dissolved due to decreased pH to form the phase of NiS/NiS_2 (after 6 h) with H_2S gas releasing.[94]

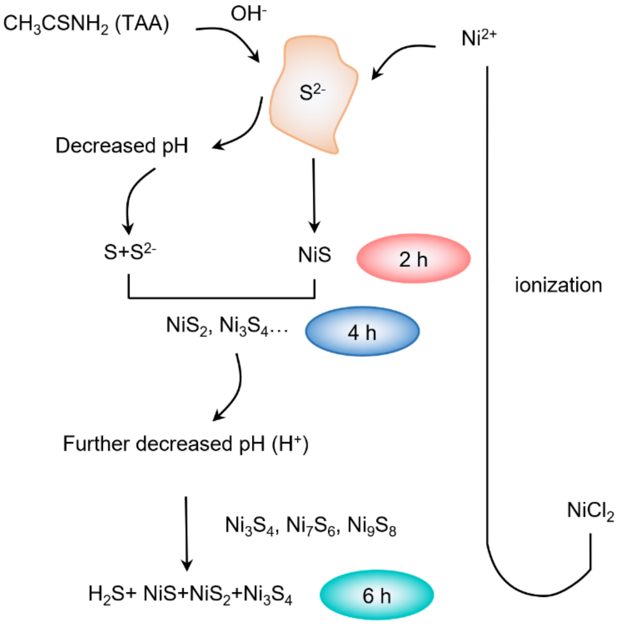

Figure 5.4 Possible reaction pathways with different vulcanization time.

Figure 5.3D shows the HRTEM image with an inter-planar spacing of 0.28 and 0.54 nm between two lattice fringes, which can be attributed to (200) lattice planes of NiS_2 and (111) of Ni_3S_4, respectively, verifying again the crystal structure of NiS_2 and Ni_3S_4 shown by XRD results.[84, 87] As shown in Figures 5.3E-G, the high-angle annular dark-field scanning transmission electron microscopy (HAADF-STEM) image and the corresponding energy dispersive X-ray (EDX) mapping of NiS_2/Ni_3S_4 show the elemental distribution of Ni and S on the surface. Coincidentally, the quantitative EDX analysis of NiS_2/Ni_3S_4 is to be $Ni_{38}S_{62}$, which is also consistent with that of XPS and XRD results analyzed above, confirming the ratio of Ni and S from another perspective.

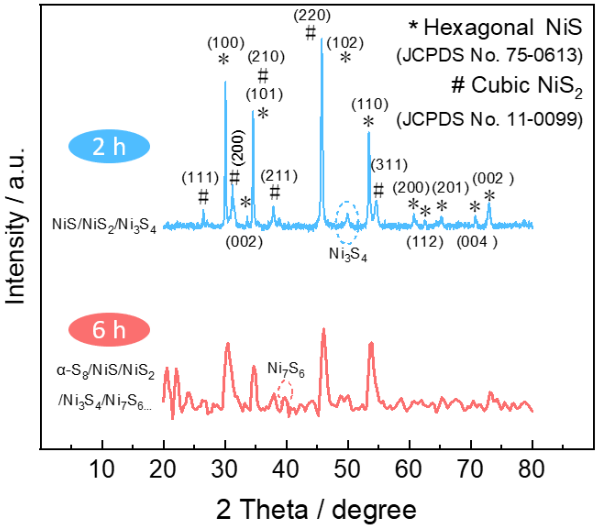

Figure 5.5 X-ray diffraction (XRD) of Ni-S catalysts prepared by different vulcanization time from 2, 4 to 6 h.

5.1.2 Sulfur leaching of NiS_2/Ni_3S_4 in half cells

The electrochemically assisted sulfur leaching of NiS_2/Ni_3S_4 was investigated during the OER process in 1 mol L^{-1} KOH on a glassy carbon (GC) electrode or carbon paper. Surface oxidation/reconstruction occurs with S being leached out into the electrolyte in strong polarization environment, especially assisted by produced oxygen. It was reported that the electrochemically oxidized (oxy)-hydroxides during OER exhibit higher performance than hydrothermally synthesized oxides/hydroxides.[98-100] Therefore, before testing OER activity of NiS_2/Ni_3S_4, the first step was to study the oxidation or sulfur leaching processes at an ultra-low current density of 0.1 mA cm^{-2} slow down and prevent from instant oxidation.

As shown in Figure 5.6A, three potential platforms were recorded during sulfur leaching processes at 1.150-1.170 V for 2 min and 1.350-1.450 V for 21 min, indicating fast structural evolution from initial NiS_2/Ni_3S_4 to $Ni(OH)_2$ in the first stage even if the current density is as low as 0.1 mA cm^{-2}, then to higher-valence NiOOH in the second stage, and then the third stage at 1.480 V represents the continuous OER processes.[101] After the sulfur leaching pretreatment, linear sweep voltammetry (LSV) curves show that the suppression of the overpotential from 365 (initial NiS_2/Ni_3S_4) to 339 mV at 10 mA cm^{-2} leads to ca. 7.12% of reduction, owing to the benefits from in-situ derived catalyst (Figure 5.6B). Meanwhile, only the oxidation peak of $Ni(OH)_2$ to NiOOH remains at ca. 1.381 V, indicating that surface sulfur in NiS_2/Ni_3S_4 was leached out, thus exhibiting no oxidation peaks at 1.313 V.

To support the above electrochemical phenomenon, ex-situ XPS, XRD, Fourier Transform Infrared Spectrometer (FTIR) and STEM-EDX were used to investigate i) the structure evolution before and after sulfur leaching, ii) chemical composition of the leached product in the electrolyte, and iii) the morphology of derived new catalyst.

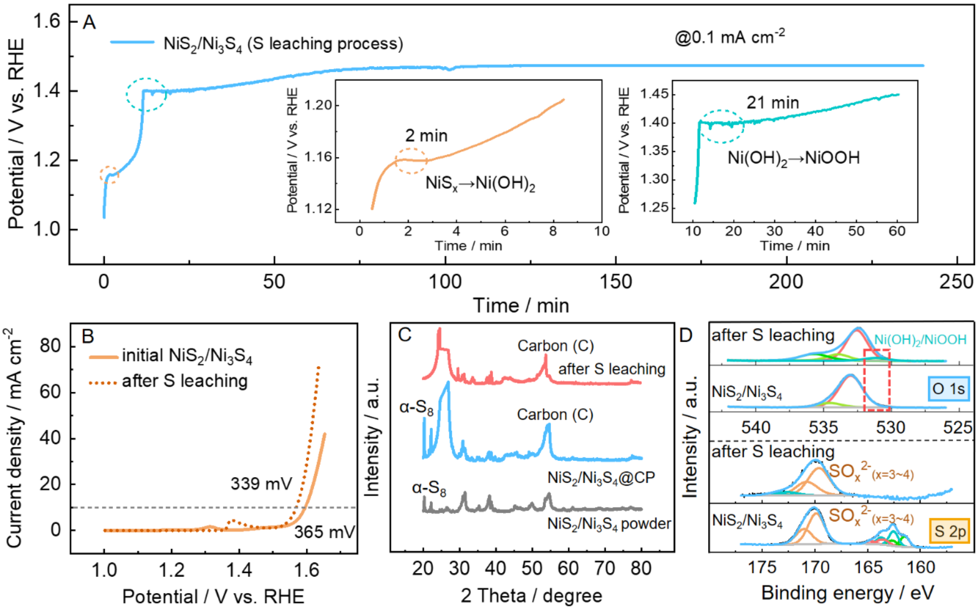

Figure 5.6 (A) Galvanostatic curve of NiS_2/Ni_3S_4 tested at 0.1 mA cm^{-2} for multi-step oxidation processes. (B) LSV curves of NiS_2/Ni_3S_4 before and after sulfur leaching in 1 M KOH at the scan rate of 5 mV s^{-1}. (C-D) XRD patterns and XPS spectra of NiS_2/Ni_3S_4 after sulfur leaching during OER.

The XRD results (Figure 5.6C) show that the diffraction peaks of sulfur impurity (α-S_8) in the range of ca. 20~25° and that of NiS_2/Ni_3S_4 at ca. 35.3°, 45.3° etc. disappeared, indicating surface oxidation of sulfur impurity and bulk polysulfides. The XPS results after sulfur leaching support this observation with the disappeared peaks at the binding energy range of 160~165 eV in the S 2p region (Figure 5.6D) and the emerged peak at ~531.0 eV in the O 1s region of NiS_2/Ni_3S_4, indicating sulfur leaching and the formation of nickel (oxy)hydroxide.

Additionally, FTIR of NiS_2/Ni_3S_4 after potentiostatic activation at 1.350 V for 6 h exhibits a new peak at ca. 3640 cm^{-1}, which is corresponding to the non-hydrogen bonded hydroxide (O-H) in oxidation-derived $Ni(OH)_2$, while the peaks intensity ca. 800-1000 cm^{-1} corresponding to NiS_x (NiS_2, Ni_3S_4) etc. decreases (Figure 5.7A). Therefore, NiS_2/Ni_3S_4 was partially oxidized to $Ni(OH)_2$ at the first oxidation stage.[102]

Meanwhile, FTIR of the NiS_2/Ni_3S_4 after potentiostatic activation at 1.70 V for 6 h exhibits decreased peak intensity at 3640 cm^{-1}, matching well with the conclusion from the literature, which kept $Ni(OH)_2$ under specific voltages such as 1.4, 1.5 V etc. and summarized that the weakened peak intensity was caused by the further electrochemical oxidation of $Ni(OH)_2$ to NiOOH in the potential range of >1.400 V.[103]

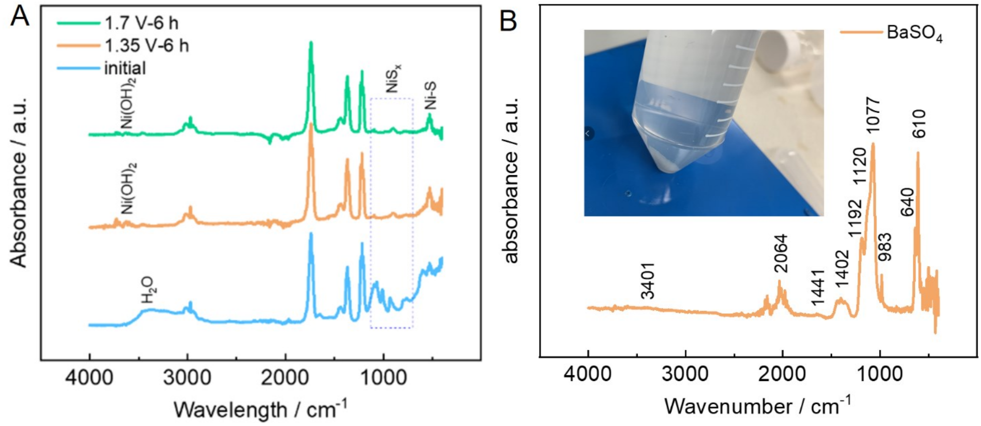

Figure 5.7 (A) FTIR of NiS_2/Ni_3S_4 before and after 6 h OER processes by a potentiostatic method at 1.35 and 1.7 V. (B) Products prepared by Ba^{2+} and unknow anions in the electrolyte and its FTIR curve.

To verify the chemical composition of the leached product, the anions in the electrolyte before and after OER tests was both precipitated by barium (Ba^{2+}) ions from barium chloride ($BaCl_2$), and excluded by hydrochloric (HCl) and nitric acids (HNO_3) for carbonate (CO_3^{2-}) ions. It was found that the electrolyte before the OER test did not produce any precipitates, while the tested one produced a white precipitate (Figure 5.7B, photo) that needs further analysis by FTIR. As shown in Figure 5.7B, the peak positions of the above precipitate are highly matching with the barium sulfate ($BaSO_4$) reported.[104] Moreover, as shown in Figure 5.8, the HAADF images and energy dispersive X-Ray (EDX) mappings of Ni and S show greatly decreased atomic ratios of Ni/S, further proving phase transformation and the loss of cubic morphology caused by the sulfur leaching from NiS_2/Ni_3S_4 nano-cubes.

It is proved by XPS (Figure 5.6 D) that there is no elemental S after electrochemical activation, indicating all sulfur leaching processes are achieved by the fully oxidized sulfur specie (sulfate ion, SO_4^{2-}) that is soluble in the electrolyte. Two possible pathways of sulfur leaching from NiS_2/Ni_3S_4 to SO_4^{2-} are presented in schematic illustration in Figure 5.9 and explained as follows:

The S-S bond in the S impurity (α-S_8, proved by XRD, Figure 5.1) will be oxidized to the S-O bond, then dissolved in electrolyte to form sulfate ions (proved by XPS of S 2p region at ca. 169.0~170.0 eV, Figure 5.6D). The lattice sulfur inside the NiS_2/Ni_3S_4 will be oxidized to the S_x (x=2-8) impurity (S-S) with the formation of $Ni(OH)_2$/NiOOH, Then, the S_x follows the leaching pathway of the α-S_8 to sulfur oxides first, and then sulfate ions. Due to strong polarization condition during OER, multi-step oxidation of S was extremely fast.

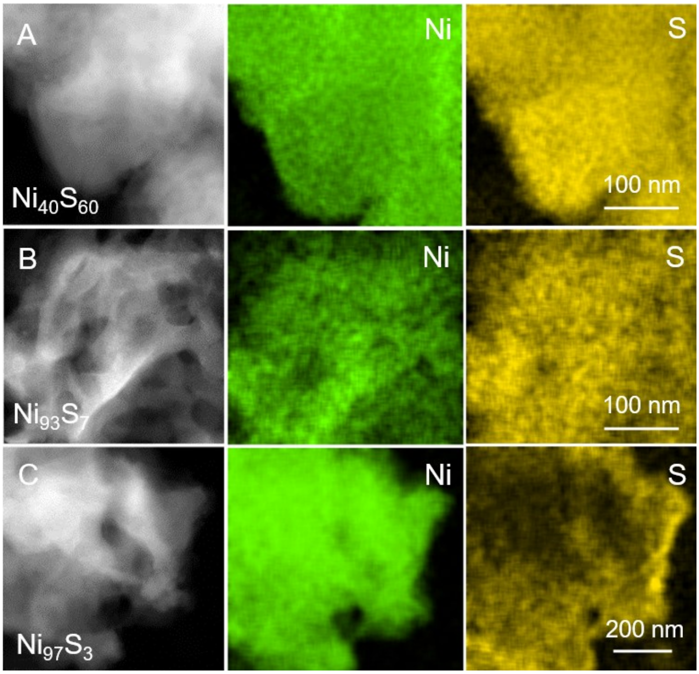

Figure 5.8 HAADF images and energy dispersive X-Ray (EDX) mapping of Ni and S: (A-C) residues and derivatives after sulfur leaching captured at different sites.

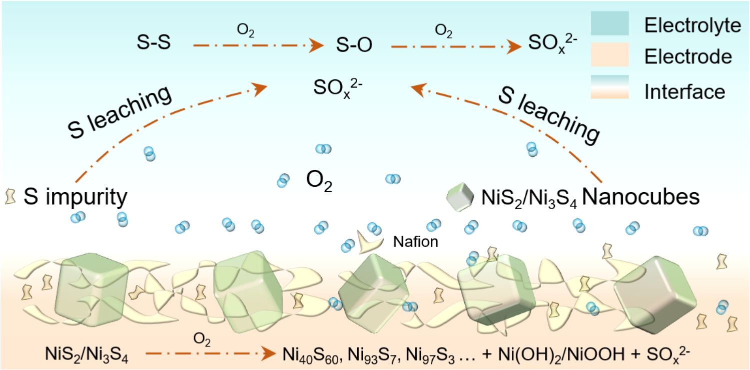

Figure 5.9 Schematic illustration of the possible sulfur leaching pathways from both of the S impurity and lattice S (the squares represent NiS_2/Ni_3S_4 nano-cubes; the balls represent oxygen molecules; the small yellow particles represent S impurities, and the flocs represent Nafion ionomers; the yellow area is the electrode surface, while the blue area is the electrolyte, and the junction is the solid-liquid interface).

Such a method for activity enhancement of NiS_2/Ni_3S_4 by electrochemical assisted sulfur leaching encouraged us to study whether it is applicable for other sulfide-based catalysts. As shown in Figures 5.10A-D, the catalysts ($NiS/NiS_2/Ni_3S_4$, 2 h) and (NiS/NiS_2, 6 h) show enhanced performance after sulfur leaching with the overpotential from 380 to 354 mV (2 h) and 381 to 357 mV (6 h), while a similar trend of Tafel slope from 72.6 to 64.8 mV dec^{-1} (2 h) and 95.9 to 60.5 mV dec^{-1} (6 h), respectively, which however are all worse than the catalyst prepared by 4 h (NiS_2/Ni_3S_4) from 365 to 339 mV and 69.8 to 60.1 mV dec^{-1}.

These performance difference among the above three catalysts can be explained from both morphological and phase compositional perspectives. The HRTEM images exhibit that the catalyst prepared for 2 h is mainly composed of nanoparticles with the average diameter of 20±5 nm (Figures 5.11A-B), while big aggregates with the diameter more than 200 nm were observed for the 6 h-based catalyst ((Figures 5.11C-D).

Additionally, the phase structures of the catalysts prepared for 2-6 h changed with different vulcanization time from mainly $NiS/NiS_2/Ni_3S_4$ (2 h), then to NiS_2/Ni_3S_4 (4 h) and then to NiS/NiS_2 (6 h), which are shown in Figure 5.5. The above phase structures matching well with the previous reports, which explained that after the coprecipitation of Ni^{2+} and S^{2-} (2 h), Ni polysulfides were produced with longer vulcanization time (4 h) due to the polymerization reaction between Ni sulfides and elemental sulfur, then some over-rich polysulfides like Ni_7S_6, Ni_3S_4 etc. were dissolved in the solution with decreased pH (6 h) to form low-sulfur-state NiS/NiS_2.[94]

Consequently, NiS_2/Ni_3S_4 prepared for 4 h, consisting of i) more conductive and active polysulfides with the surface morphology of relatively small-size nano-cubes, exhibits better OER performance than that of the catalysts prepared for 2 h with more “less conductive” NiS phase, while that prepared for 6 h with not only “less conductive” NiS phase but also more large-size aggregates.

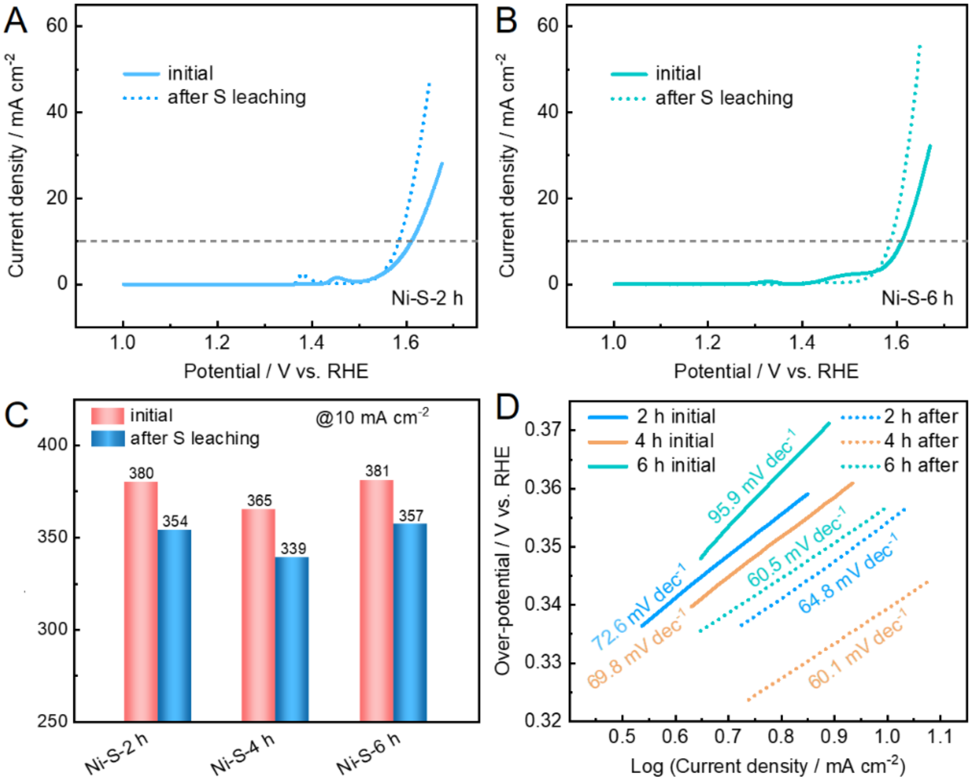

Figure 5.10 LSV curves of (A) Ni-S-2 h with main phases of NiS/NiS$_2$/Ni$_3$S$_4$, (B) Ni-S-6 h with main phases of NiS/NiS$_2$ before and after sulfur leaching recorded in the potential range of 1.0~1.7 V at the scan rate of 5 mV s^{-1}. (C-D) Representative catalytic activity (over-potential at the current density of 10 mA cm^{-2}) and Tafel slope, which also includes the results of Ni-S-4 h with the main phases of NiS$_2$/Ni$_3$S$_4$ from Figure 5.6B.

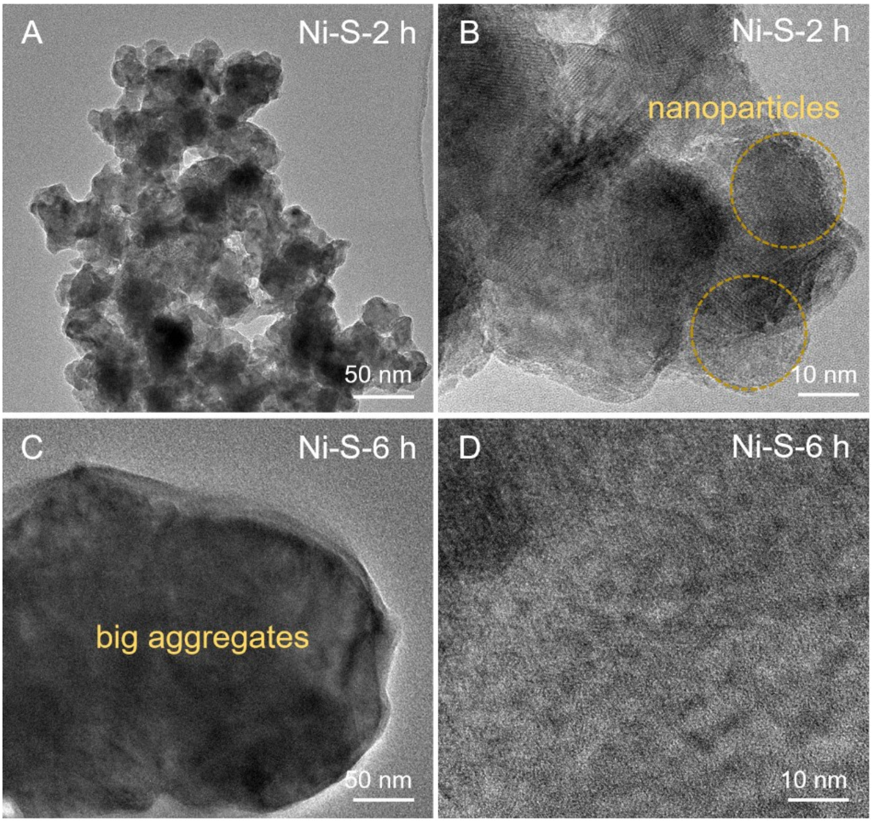

Figure 5.11 HRTEM images of (A-B) the catalyst prepared for 2 h (NiS/NiS_2/Ni_3S_4 based nanoparticles) with the diameter of 20±5 nm and (C-D) 6 h (NiS/NiS_2 based big aggregates) with diameter more than 200 nm.

5.2 Cycling stability of NiS_2/Ni_3S_4 in the half cell

To evaluate the OER activity of the NiS_2/Ni_3S_4 prepared by the optimized condition, its performance and that of commercial Ni/NiO are compared in Figures 5.12A-B. The corresponding onset potentials in Table 5.1, at the beginning of OER, the onset potential of 1.554 V for NiS_2/Ni_3S_4 is similar to that of 1.529 V for Ni/NiO, which is then decreased after sulfur leaching to 1.492 V. After 3000 CVs, the onset potentials of both NiS_2/Ni_3S_4 and Ni/NiO decrease to 1.478 and 1.497 V, respectively. After 10000 CVs, it is found that the cycling stability of NiS_2/Ni_3S_4 is better than that of Ni/NiO with the increase of onset potential of only 0.021 V (while 0.031 V for Ni/NiO) from that of “after 3000 CVs” to “after 10000 CVs”.

Table 5.1 Onset-potential of NiS_2/Ni_3S_4 and Ni/NiO

Catalyst	NiS_2/Ni_3S_4 (V)	Ni/NiO (V)
initial	1.554	1.529
after sulfur leaching	1.492	-
after 3000 CVs	1.478	1.497
after 8000 CVs	1.497	1.524
after 10000 CVs	1.499	1.528

Moreover, the overpotentials at 10 mA cm^{-2} (noted as η_{10}) in Figure 5.12C are compared respectively. The η_{10} of NiS_2/Ni_3S_4 is suppressed from 370 mV to that of "after 3000 CVs" for 305 mV, and then to that of "after 10000 CVs" for 341 mV. Meanwhile the η_{10} of Ni/NiO exhibits the following trend from initial 377 mV to that of "after 3000 CVs" for 339 mV and then to that of "after 10000 CVs" for 428 mV.

One of the trend differences lie in that here is an extra decrease of OER overpotential for NiS_2/Ni_3S_4 before and after sulfur leaching. Another difference lies in that during the decay period from 3000 to 10000 CVs, the overpotential increase of Ni/NiO from 339 to 428 mV is much larger than that of NiS_2/Ni_3S_4 from 305 to 341 mV, indicating better long-term cycling of NiS_2/Ni_3S_4, which is also applicable to the trend of Tafel slope in Figures 5.12D-E and summarized in Figure 5.12F.

Tafel curves of NiS_2/Ni_3S_4 and Ni/NiO show a similar trend as that of η_{10}: from the initial 73.5 mV dec^{-1} to that of "after 3000 CVs" ca. 46.0 mV dec^{-1}, and to that of "after 10000 CVs" ca. 62.3 mV dec^{-1} for NiS_2/Ni_3S_4, while that of Ni/NiO is from initial 69.0 mV dec^{-1} to that of "after 3000 CVs" ca. 67.2 mV dec^{-1}, and to that of "after 10000 CVs" ca. 84.7 mV dec^{-1}. Similarly, here is also an extra improvement for the kinetics of NiS_2/Ni_3S_4 before and after sulfur leaching and surface reconstruction. The above advantages of NiS_2/Ni_3S_4 are owing to the activation of polysulfides to more active $NiS_x/Ni(OH)_2/NiOOH$ and the electrochemical cleaning, redistributing and refining effects during sulfur leaching.[105, 106]

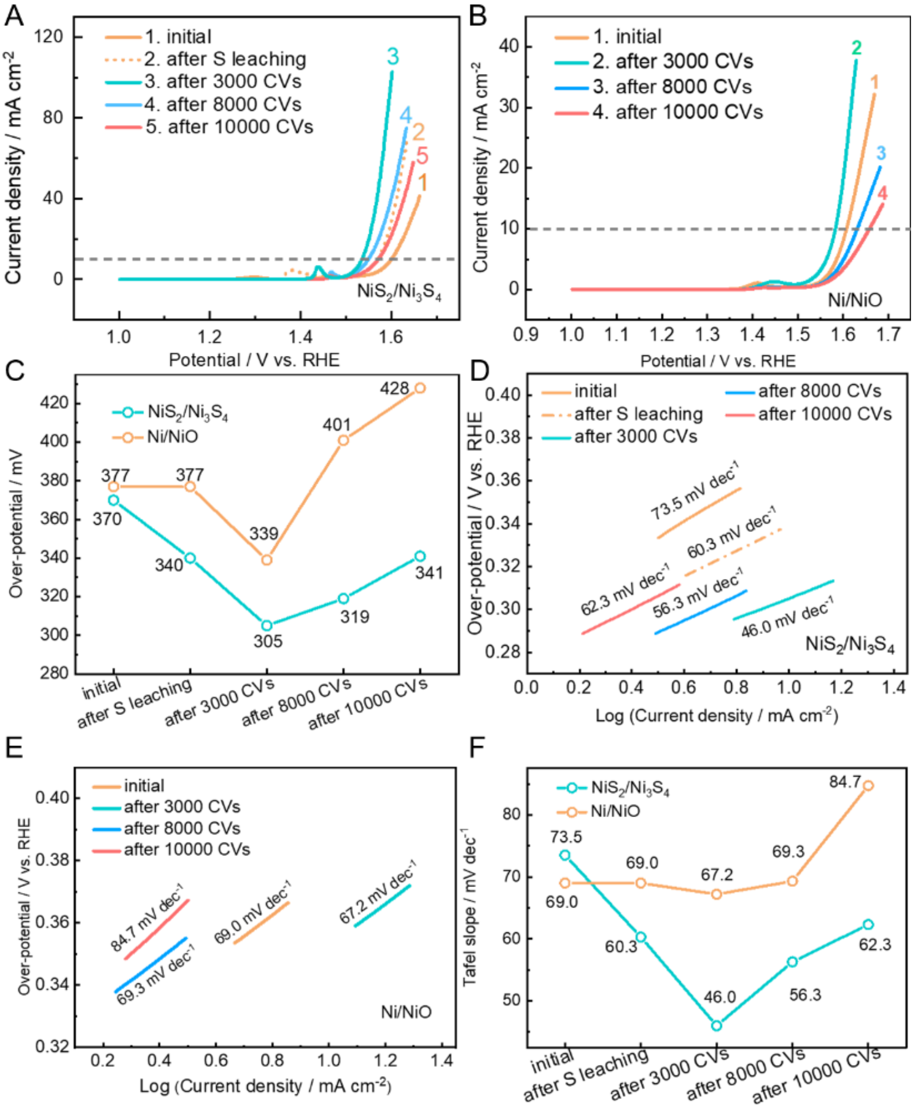

Figure 5.12 (A-B) LSV curves of Ni_3S_4 and Ni/NiO recorded at 5 mV s^{-1} and (C) summarized over-potential at 10 mA cm^{-2} before and after sulfur leaching, 3000, 8000, and 10000 CVs (for Ni/NiO, the performance before and after sulfur leaching is the same). Tafel slopes of (D) Ni_3S_4, (E) Ni/NiO, summarized and compared in (F) before and after sulfur leaching, 3000, 8000, and 10000 CVs.

To understand the cleaning effect of electrochemical sulfur leaching for the NiS_2/Ni_3S_4, electrochemical impedance spectroscopy (EIS) curves of NiS_2/Ni_3S_4 before and after sulfur leaching, Ni/NiO, and $Ni(OH)_2$ were tested by the potentiostatic method at 1.6 V and compared in Figure 5.13. It is clear that all the catalyst coated electrodes exhibit similar internal resistance of ca. 1.2 Ω cm^2 and before sulfur leaching, the charge transfer resistance (R_{ct}) of NiS_2/Ni_3S_4 for ca. 4.8 Ω cm^2 is almost two times as that of 2.3 Ω cm^2 for Ni/NiO and 2.6 Ω cm^2 for $Ni(OH)_2$, while that for NiS_2/Ni_3S_4 after sulfur leaching sharply decreases to 1.1 Ω cm^2. Such a huge jump of R_{ct} can be attributed to the following reasons:

i) The sulfur leaching of surface impurity and absorbed sulfide ions (S_x^{2-}) to sulfate ions (SO_4^{2-}) that exhibits much lower adsorption energy of OH^-;

ii) The formation of highly active polysulfides/hydroxides/(oxy)-hydroxides species ($NiS_x/Ni(OH)_2/NiOOH$).

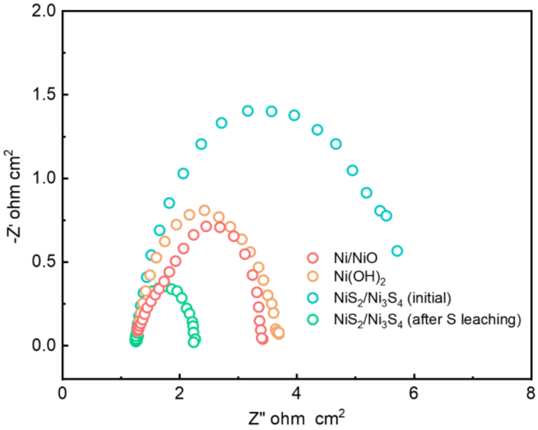

Figure 5.13 Electrochemical impedance spectroscopy (EIS) of NiS_2/Ni_3S_4 before and after sulfur leaching, Ni/NiO, and $Ni(OH)_2$) at 1.6 V.

To support the redistributing and refining effects from sulfur leaching, the electrochemically active surface area (ECSA) of both NiS_2/Ni_3S_4 and Ni/NiO was recorded by the CV method in the potential range of 0.9-1.0 V to avoid side reactions that contribute to the peak current in CV. As shown in Figures 5.14A-D and compared in Figure 5.14E, the ECSA can be reflected by the double-layer capacitance (C_{dl}) values that are related to the slope in “potential” vs. “peak current density” curves.

It is calculated that C_{dl} of the initial NiS_2/Ni_3S_4 is 0.422 (before) and 0.451 mF cm^{-2} after sulfur leaching, which are both as two time as that of Ni/NiO ca. 0.235 mF cm^{-2}, indicating larger ECSA and more active sites exposed to hydroxide ions for NiS_2/Ni_3S_4 than Ni/NiO, thus better OER activity.

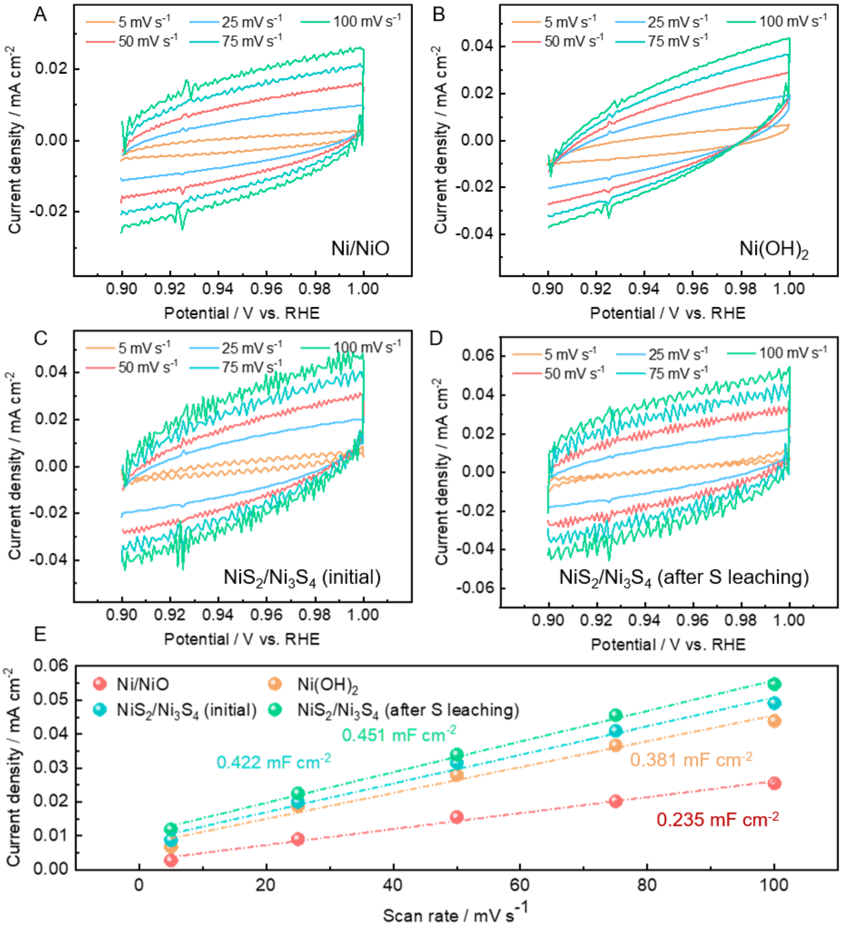

Figure 5.14 Double-layer capacitance (C_{dl}) for the measurements of electrochemically active surface area (ECSA) by CV in the potential range of 0.9~1.0 V vs. RHE at the different scan rates from 5, 25, 50, 75 to 100 mV s^{-1} (A) commercial Ni/NiO, (B) synthesized $Ni(OH)_2$, (C-D) NiS_2/Ni_3S_4 nano-cubes before and after sulfur leaching, and (E) summarized plots of peak current densities vs. scan rate and corresponding slopes: Ni/NiO, $Ni(OH)_2$, NiS_2/Ni_3S_4 before and after sulfur leaching.

It is worth mentioning that the deterioration of NiS_2/Ni_3S_4 derived $NiS_x/Ni(OH)_2/NiOOH$ catalyst in OER performance from that of "after 3000 CVs" to "after 10000 CVs" could be explained as follows:

1) Further sulfur leaching and irreversible phase transformation: as supported by XRD patterns after sulfur leaching, 3000 and 10000 CVs from Figure 5.15, the new peaks occur and are not fully matching with specific phases due to surface amorphous structure.[63] The XPS further supports the continuous formation of $Ni(OH)_2/NiOOH$ from 3000 to 10000 CVs(Figures 5.17A-B). Additionally, SEM-EDX mapping confirms that surface sulfur was almost fully leached out into the electrolyte from "initial (100%)", to that of "after sulfur leaching" (66.7%), "after 3000 CVs (80.6%)", and to that of "after 10000 CVs (96.6%)" (Figure 5.17C), which suggests that the best S content on the surface is ca. 20 wt.%.
2) Microstructure changes: the microstructure changed to nanoparticles after 10000 CVs, supported by HAADF images and EDX mappings (Figure 5.16), which exhibited different OER performance than its initial state.
3) Catalyst shedding: part of the NiS_2/Ni_3S_4 fell off into the electrolyte and caused a direct decrease of catalyst mass loading, which can be inferred from decreased peak intensity of S 2p (S from Nafion, 170-175 eV, Figure 5.17A).
4) Electrolyte poisoning: the electrolyte could be contaminated by carbon dioxide (CO_2) form the air, causing decreased concentration of hydroxide ions, thus lower performance.

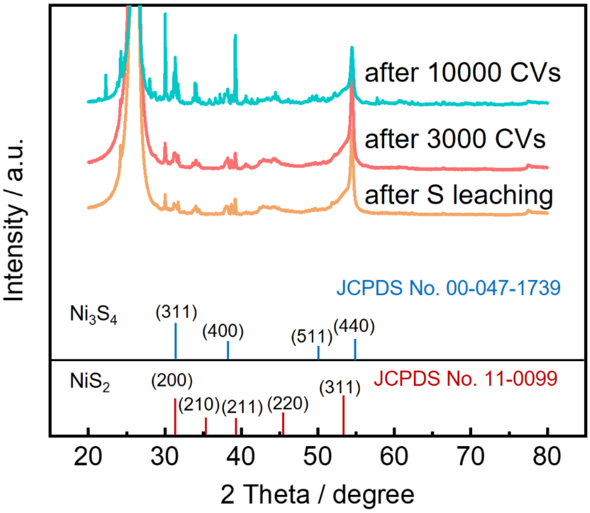

Figure 5.15 XRD of NiS_2/Ni_3S_4 coated on the carbon paper after different electrochemical treatments: i) after sulfur leaching (yellow), ii) after 3000 CVs (red) and after 10000 CVs (bule green) in 1 M KOH.

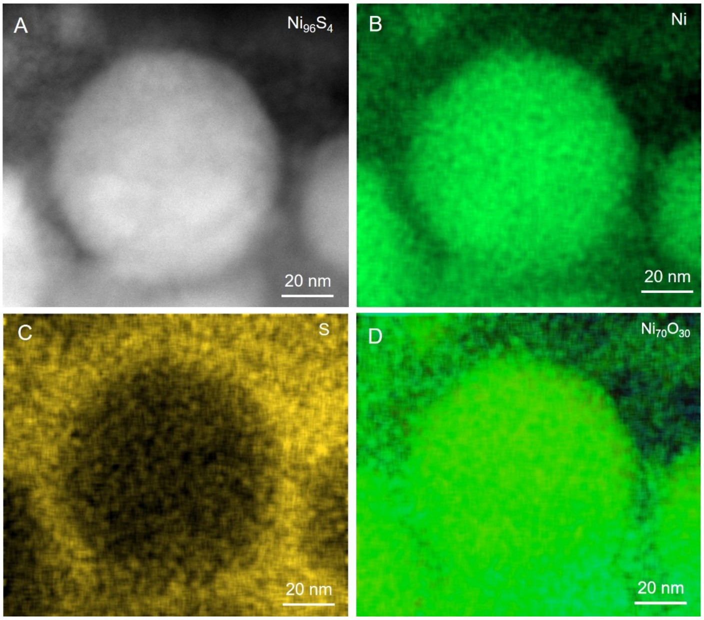

Figure 5.16 (A) The HAADF image and (B-D) EDX mapping of NiS_2/Ni_3S_4 after 10000 CVs.

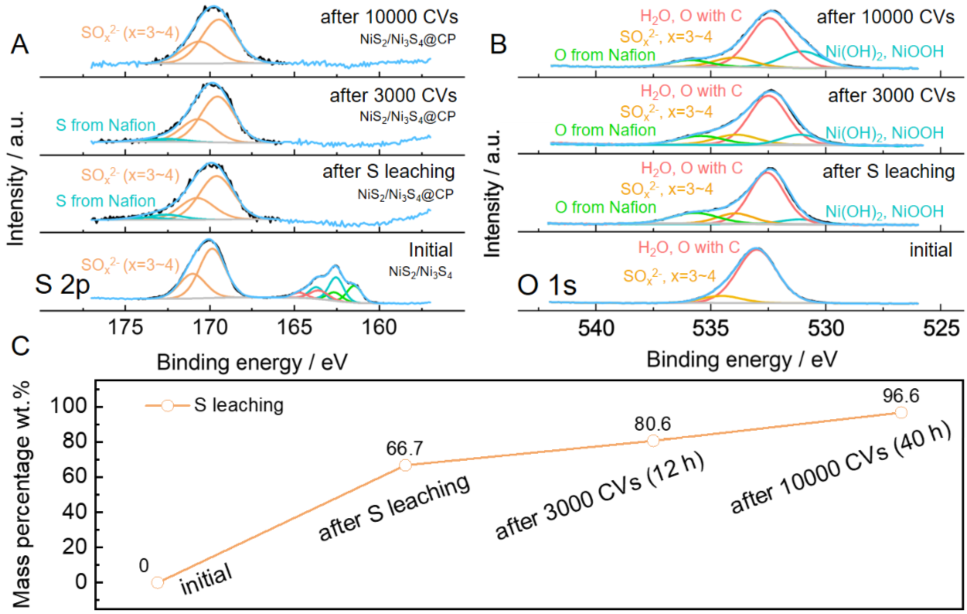

Figure 5.17 XPS spectra of NiS_2/Ni_3S_4 and that coated on the carbon paper (CP) after sulfur leaching, 3000 and 10000 CVs: (A) S 2p and (B) O 1s regions. (C) Mass percentage of surface leached sulfur from NiS_2/Ni_3S_4@CP by SEM-EDX mapping.

Recently, the performance improvement of Ni-based catalysts after electrochemical tests was attributed to iron impurities.[107, 108] Therefore, 1 M NaOH was also used as the electrolyte and corresponding OER performance was compared with that in 1 M KOH (Figures 5.18A-B), which is tabulated in Table 5.2. The NiS_2/Ni_3S_4 catalyst in KOH and NaOH shows almost the same results after sulfur leaching with only 1 mV difference in η_{10} after sulfur leaching, and only 6 mV error after 3000 CVs, indicating Fe impurities are not the determining factor.

From the analysis above, it can be summarized that the sulfur leaching and surface reconstruction of NiS_2/Ni_3S_4 contributes to the performance enhancement of OER activity. The derived $NiS_x/Ni(OH)_2/NiOOH$ structure with more exposed active sites and refined morphology is more efficient and stable than the pristine NiS_2/Ni_3S_4 with α-S_8 impurity, and commercial Ni/NiO.

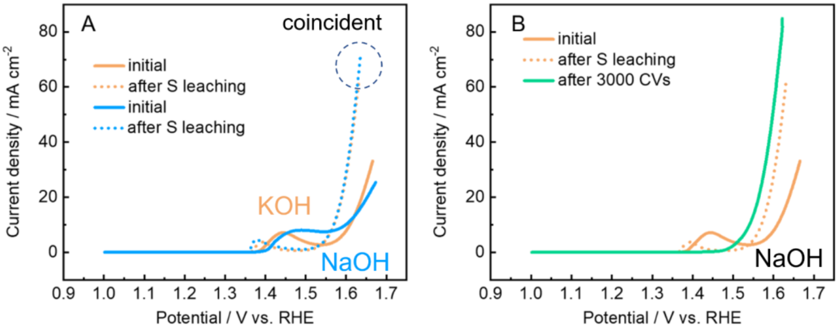

Figure 5.18 LSV curves of NiS_2/Ni_3S_4 in (A) 1 M KOH (yellow) and NaOH (blue) before and after sulfur leaching, (B) the comparison among "initial" and "after 3000 and 10000 CVs" in 1 M NaOH with the scan rate of 5 mV s^{-1}.

Table 5.2 Over-potential from Figure 5.18 at 10 mA cm^{-2}.

Electrolyte	1 M NaOH (mV)	1 M KOH (mV)
before sulfur leaching	380	369
after sulfur leaching	341	340
after 3000 CVs	311	305

5.3 Long-term stability of NiS_2/Ni_3S_4 in half cells

In addition to lower OER overpotential, the NiS_2/Ni_3S_4 also exhibits high stability with the potential increase of 11.0 mV after 65 h at a constant condition of 10 mA cm^{-2}, while 59.9 and 23.8 mV potential increases are recorded for the commercial Ni/NiO and synthesized $Ni(OH)_2$ (Figure 5.19A). Then LSV curves before and after 40 and 65 h are shown in Figures 5.19B-D. The overpotential at 50 mA cm^{-2} (η_{50}) of NiS_2/Ni_3S_4 increases by only ~2 mV (ca. ~0.53%) before and after 65 h, with an average η_{50} of 373.7 mV (the reason to choose 50 mA cm^{-2} as a reference current density is that the oxidation peak disturbs the overpotential at the current density of 10 mA cm^{-2}, as shown in Figure 5.19D). In comparison, the highest current density of Ni/NiO and $Ni(OH)_2$ cannot reach lower than 50 mA cm^{-2} before long-term test, indicating poor charge transfer capability. And the η_{50} of Ni/NiO increases by ~35 mV (ca. ~9.09%) from that of “after 40 h (385 mV)” to “after 65 h (420 mV)”, with an average value of 402.5 mV, while 400.5 mV for $Ni(OH)_2$, indicating the best activity and stability of NiS_2/Ni_3S_4 among three catalysts with the average decreased overpotential of ca. 30 mV at the current density of 50 mA cm^{-2}.

Moreover, Tafel slopes before and after 40 and 65 h show that NiS_2/Ni_3S_4 almost keeps an average value of 53.6 mV dec^{-1} with slight shifting from 52.8 to 54.3 mV dec^{-1}, which is much lower and stable than that of Ni/NiO and $Ni(OH)_2$ ca. 70.5 (from 62.2 to 78.9 mV dec^{-1}) and 77.5 mV dec^{-1} (increasing from 63.1 to 85 mV dec^{-1}) in average, indicating faster and stable kinetics of NiS_2/Ni_3S_4 (Figure 5.19E) during long-term tests and highly unstable kinetics of Ni/NiO and $Ni(OH)_2$. Therefore, the NiS_2/Ni_3S_4 after sulfur leaching, consisting of multi-phase Ni-rich polysulfide, $Ni(OH)_2$ and NiOOH, exhibits excellent stability and high activity retention in half cells with negligible degradation. It is noteworthy that the NiS_2/Ni_3S_4 exhibits less bubble issues and more stable potential curves, indicating excellent surface hydrophilicity and great capability for bubble diffusion.

However, the NiS_2/Ni_3S_4 based three-electrode cell involves a relatively low current density of 10 mA cm^{-2} and the sulfur leaching is highly dependent on the polarization states, which are quite different in strong-polarized full cells from that in half cells with moderate polarizations. Also, the tests under such a moderate condition are less promising for real understanding of its physical and chemical stability and application. Therefore, sulfur leaching under strong polarization needs to be studied to prove the feasibility of TMS based catalysts and high-rate performance, especially stability at high current density of 1000 mA cm^{-2} should be further verified in the full cells of AEMWE.

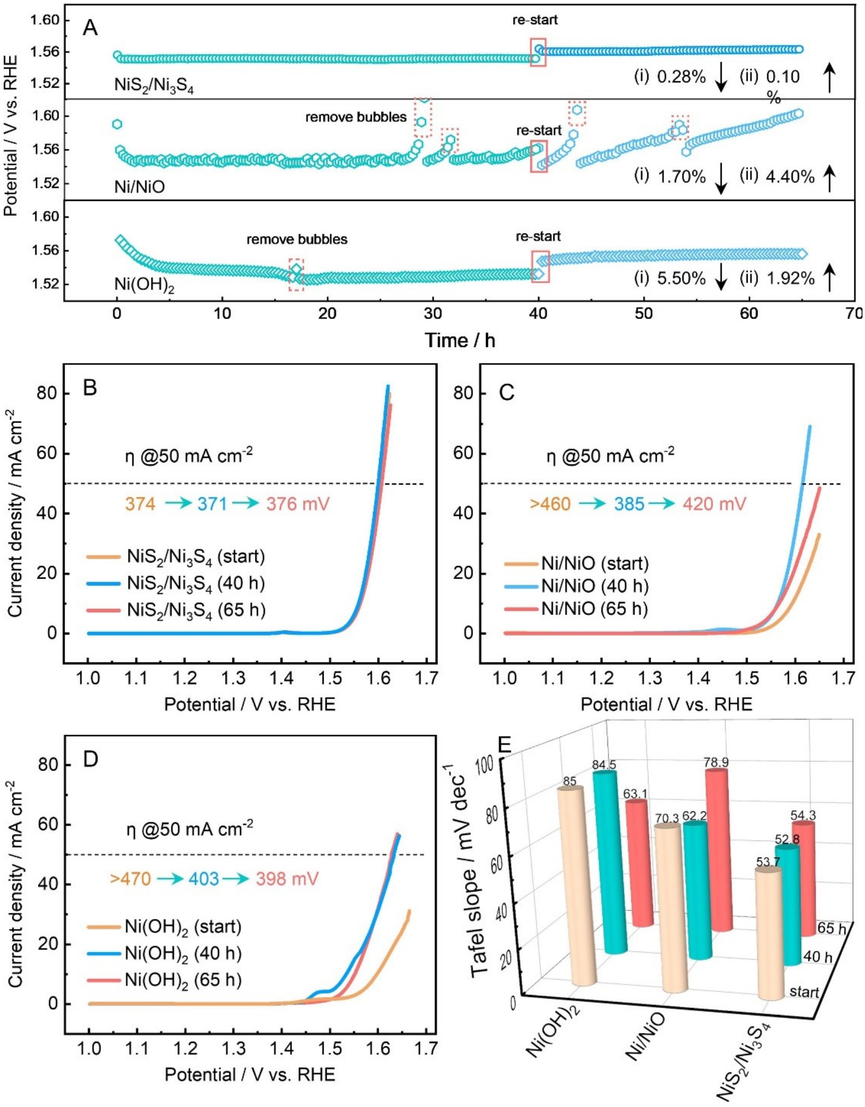

Figure 5.19 (A) Stability curves at 10 mA cm^{-2} for 65 h, and (B-D) corresponding LSV before and after 40 and 65 h of NiS_2/Ni_3S_4, Ni/NiO, $Ni(OH)_2$, respectively, and (E) derived Tafel slopes.

5.4 Sulfur leaching of NiS_2/Ni_3S_4 in full cells

Inspired by the sulfur leaching for boosting OER activity and stability of NiS_2/Ni_3S_4 in half cells, an AEM-based electrolyzer was constructed to study the feasibility of this activation method for full-cell water splitting. The key materials are as follows: Pt/C@C paper (cathode)||FAA-3-50|| NiS_2/Ni_3S_4 or Ni/NiO (anode). Two parallel single cells employ Ni/NiO and NiS_2/Ni_3S_4 as anode catalysts that achieved by the spray coating method and corresponding testing protocol are all explained in Chapter 2 (2.6-2.8).

To keep consistent with the testing protocol in half cells, the sulfur leaching was also achieved by the CV method in the single-cell tests at 100 mV s^{-1} (Figure 5.20A). After sulfur leaching for three times, the NiS_2/Ni_3S_4-based cell performance exhibit same improvement trend with that in half cells with the current density increasing from initial 1152 mA cm^{-2} to 1424 mA cm^{-2} (after the 1st sulfur leaching), then to 1539 mA cm^{-2} (after the 2nd sulfur leaching), and then to1587 mA cm^{-2} (after the 3rd sulfur leaching) at 2.0 V (Figure 5.20C). The improvement of cell performance suggests that the leaching of S from NiS_2/Ni_3S_4 promote the formation of Ni-rich NiS_x and a $NiS_x/Ni(OH)_2/NiOOH$ heterostructure.

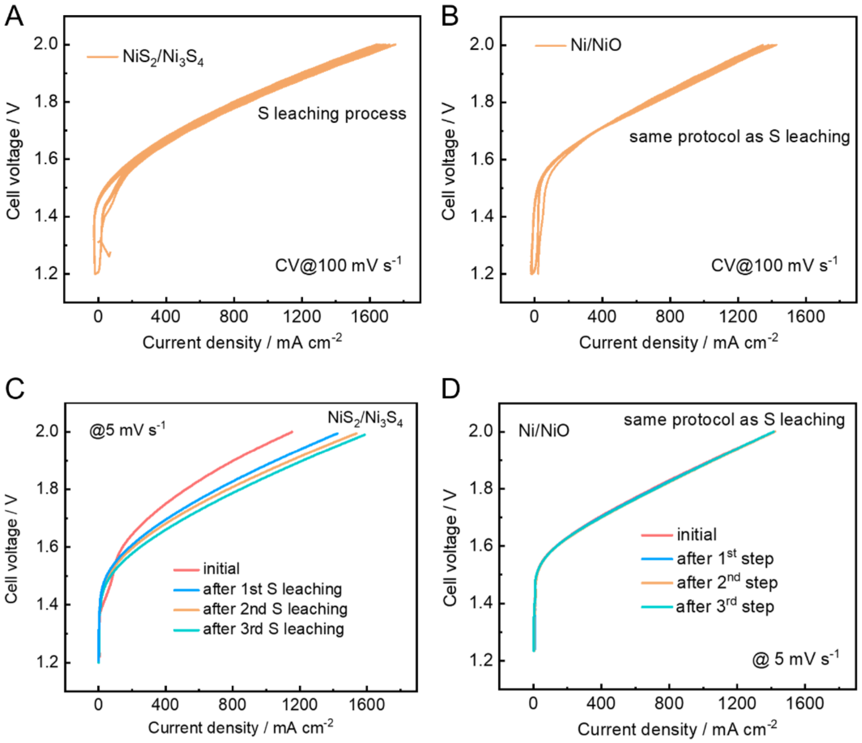

Figure 5.20 (A-B) Sulfur leaching processes of NiS_2/Ni_3S_4 and Ni/NiO based cells (Pt/C@C paper (cathode)||FAA-3-50|| NiS_2/Ni_3S_4 or Ni/NiO (anode)) by the CV method in the voltage range of 1.2-2.0 V at the scan rate of 100 mV s^{-1} (10 cycles for each step sulfur leaching), and (C-D) polarization curves of after 1-3 times of sulfur leaching.

The Ni/NiO-based cells were also cycled under the same protocol for the sulfur leaching step of that NiS_2/Ni_3S_4-based cells (Figure 5.20B, Figure 5.21). After three times of sulfur leaching, the current density of the Ni/NiO-based cells remains unchanged at ca. 1417 (initial), 1419 (after the 1st sulfur leaching), 1421 (after the 2nd sulfur leaching), and 1414 mA cm^{-2} (after the 3rd sulfur leaching) at 2.0 V (Figure 5.20D, Figure 5.21), indicating that sulfur leaching is the crucial contributing factor for the performance improvement of the NiS_2/Ni_3S_4-based cells.

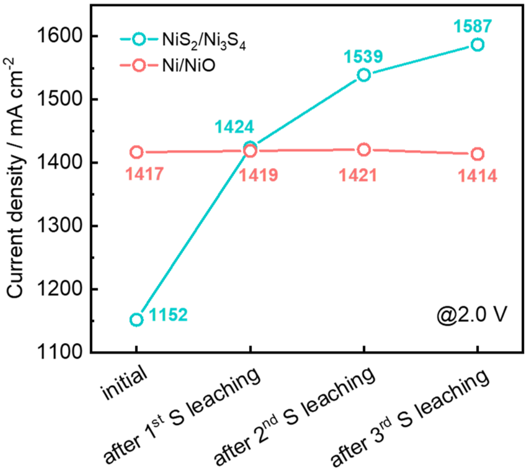

Figure 5.21 Current density at 2.0 V summarized from Figure 5.19C-D.

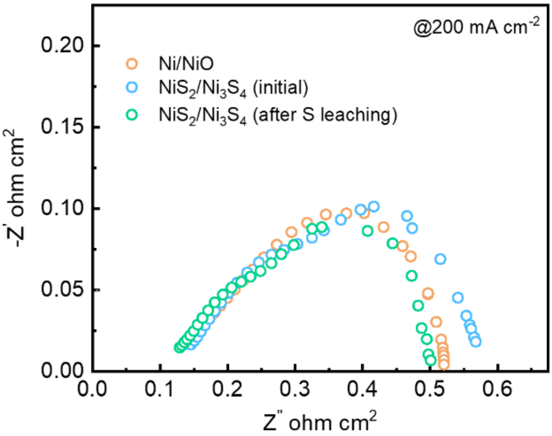

Figure 5.22 EIS of the NiS_2/Ni_3S_4 and Ni/NiO based cells with the configuration as follows: Pt/C@C paper||FAA-3-50|| NiS_2/Ni_3S_4 or Ni/NiO before and after sulfur leaching.

Moreover, the EIS curves show that the internal resistance and charge transfer resistance of NiS_2/Ni_3S_4 based cells are higher than that of Ni/NiO based cells at the beginning, while suppressed and lower than that of Ni/NiO based cells after sulfur leaching (Figure 5.22). This result is similar to that from the half-cell tests (Figure 5.13), suggesting the effects of cleaning, redistributing, refining from sulfur leaching for performance enhancement are also applicable in full cells.

After temperature stabilization for 2 h and sulfur leaching, all Ni/NiO and NiS_2/Ni_3S_4 based cells were kept at a constant voltage of 1.7 V for 6 h, which is for cell conditioning to a stabilized state with a current error less than 1% for reliable polarization curves. During conditioning, the current density of the Ni/NiO-based cell decreases from 400 to 336 mA cm^{-2}, while that of the NiS_2/Ni_3S_4-based cell almost keeps stable at 445 mA cm^{-2}, except for a slight decrease from 469 to 445 mA cm^{-2} during the first 0.5 h due to the activation polarization (Figure 5.24A), indicating better stability of the NiS_2/Ni_3S_4-based cells at the conditioning stage. Then the current density of NiS_2/Ni_3S_4-based cell further increases from 1587 mA cm^{-2} after three times of sulfur leaching to 1738 mA cm^{-2} after conditioning, indicating further performance improvement induced by sulfur leaching of the NiS_2/Ni_3S_4 on the anode side (Figure 5.24B, 5 mV s^{-1}).

From the perspective of side reactions, the Faradaic efficiency is tested by a water displacement method (Figure 5.23). The initial Faradaic efficiency of NiS_2/Ni_3S_4-based cells increases from 92.2% to 94.8% at the beginning and is much lower than that after conditioning ca. 97.4%, indicating side reactions (oxidization of sulfur to sulfate ions) occupied a small amount of current (Figures 5.24C-D).

Figure 5.23 Setup for the test of Faradaic efficiency by water displacement.

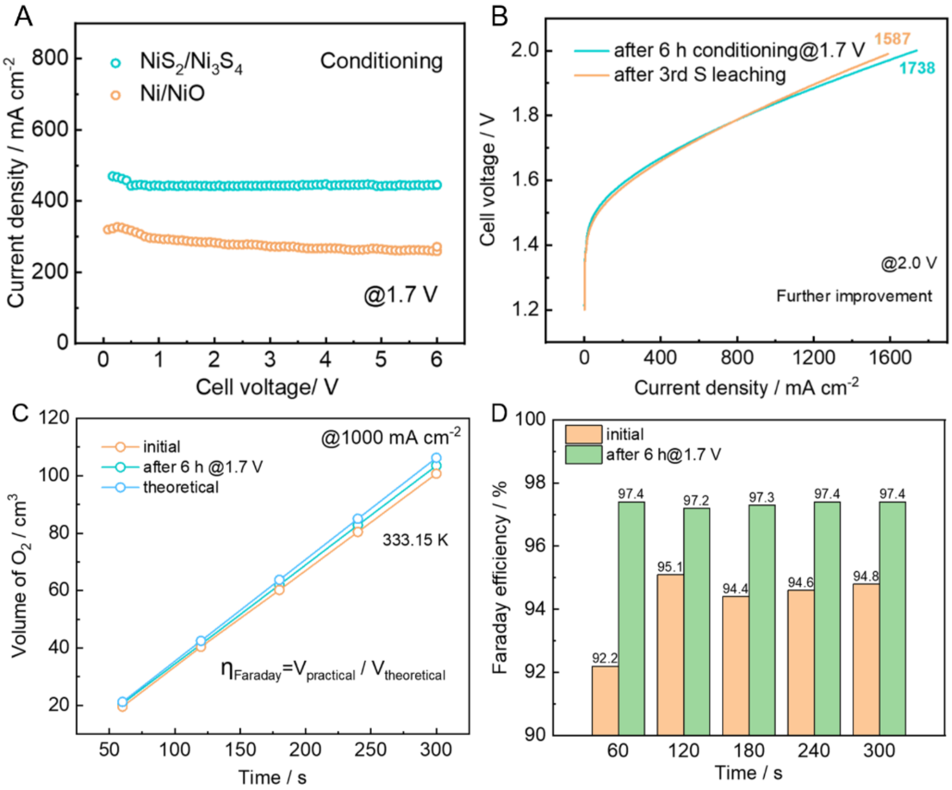

Figure 5.24 (A) Conditioning curves at 1.7 V for 6 h and (B) polarization curves of the NiS_2/Ni_3S_4 based cells (Pt/C@C paper (cathode)||FAA-3-50||NiS_2/Ni_3S_4 or Ni/NiO (anode)) after 3 times of sulfur leaching and conditioning. (C) Calculated and tested volume of O_2 at 1000 mA cm^{-2} before and after conditioning and (D) Faraday efficiency calculated by the ratio of practical/theoretical volume from the graph (C).

After conditioning, polarization performance was tested by a galvanostatic method for the hold of 5 min step^{-1}, which is under steady-state polarization conditions. A typical steady-state polarization curve consists of three stages: i) charge transfer resistance (R_{ct}) controlled stage in very low current range (e.g. ~10 mA cm^{-2}); ii) mix-controlled stage ($R_{\Omega*ct}$) in the middle range (e.g. ~300 mA cm^{-2}); iii) internal resistance (R_{Ω}) controlled stage in the high-current range (e.g. >1000 mA cm^{-2}).

As shown in Figure 5.25, in R_{ct} controlled stage, the initial cell voltage of NiS_2/Ni_3S_4 based cells is ~0.02 V lower than that of Ni/NiO based cells, indicating high charge transfer efficiency. In R_{Ω}-controlled stage, NiS_2/Ni_3S_4 based cells show a higher current density of 1550 mA cm^{-2}

than that of the Ni/NiO-based cells with 900 mA cm^{-2} at 2.0 V, indicating higher catalytic activity of NiS_2/Ni_3S_4 and lower R_Ω than Ni/NiO in full cells.

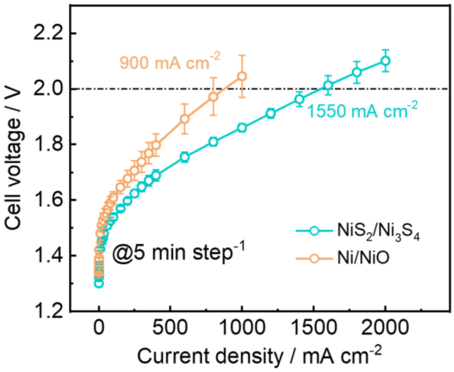

Figure 5.25 Polarization curves of Pt/C@C paper||FAA-3-50||NiS_2/Ni_3S_4 or Ni/NiO.

However, FAA-3-50 membrane is not suitable for long-term stability test due to its poor mechanical stability, especially at high temperature. As shown in Figures 5.26A-B, both NiS_2/Ni_3S_4 and Ni/NiO based cells failed after short-term tests due to the short circuit caused by membrane damage. Additionally, Ni/NiO is unstable and most of the catalyst was printed on the membrane, while NiS_2/Ni_3S_4 is still attached on the Ni fiber, indicating S plays an important role in the stability of Ni based catalysts, which needs to be further tested in a more stable cell with stable membranes.

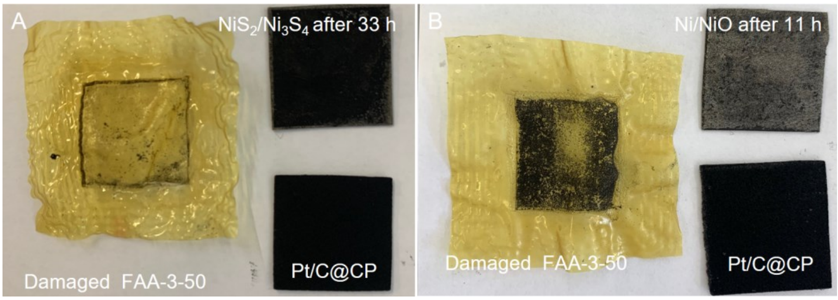

Figure 5.26 Photos of membrane electrode assembly (MEA) after single-cell testing: (A) NiS_2/Ni_3S_4 coated Ni fiber, Pt/C coated carbon paper, and FAA-3-50 membrane after 33 h. (B) Ni/NiO coated Ni fiber, Pt/C coated carbon paper, and FAA-3-50 membrane after 11 h. Note: The above two cells are short-circuited, and cracks around the corner of the electrode edges were captured.

5.5 Long-term stability of NiS_2/Ni_3S_4 in full cells

To test the long-term stability of NiS_2/Ni_3S_4 based cells, a highly stable membrane marked as “AF1-HNN8-50” was utilized as the separator. As shown in Figure 5.27, the AF1-HNN8-50 and NiS_2/Ni_3S_4 based cells exhibit further enhanced current density of 1800 mA cm^{-2} at 2.0 V than that of FAA-3-50 based cells, which is also much higher than that of Ni/NiO based cells at ca. 1067 mA cm^{-2}

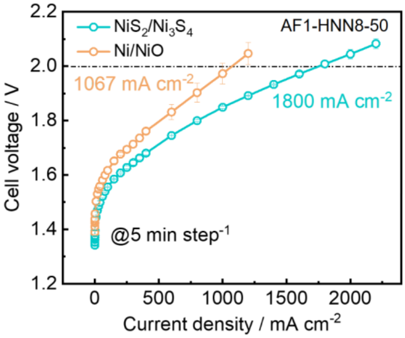

Figure 5.27 (A) Polarization curves of the cell based on Pt/C@C paper||FAA-3-50||NiS_2/Ni_3S_4 after conditioning at 1.7 V for 6 h at 5 min step^{-1}.

Then the long-term test (Figure 5.28) shows that NiS_2/Ni_3S_4 based cells are highly stable, showing an initial cell voltage of 1.84 V and low voltage increase rate of 0.12 mV h^{-1}, while that of Ni/NiO based cells are 2.00 V and 1.7 mV h^{-1} respectively.

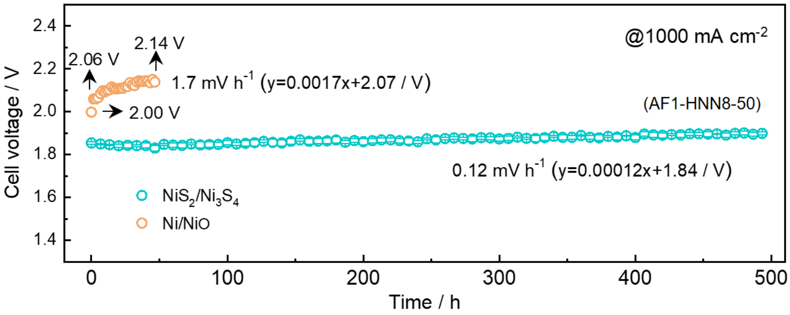

Figure 5.28 Stability of Ni/NiO and NiS_2/Ni_3S_4 based cells with AF1-HNN8-50 as the anion exchange membrane at the current density of 1000 mA cm^{-2} (both stability curves are linearly fitted for the evaluation of its degradation rate).

The degradation of NiS_2/Ni_3S_4 based cells during the long-term testing stage is shown in Figures 5.29A-B. The current density of the above cells at 2.0 V decreases from 1800 (initial), 1600 (after the 185th h), 1512 (after the 310th h), and 1455 (after the 400th h) to 1400 mA cm^{-2} (after the 500th h), while that of Ni/NiO-based cells decreases from 1067 to 890 mA cm^{-2} after only 50 h.

The degradation of NiS_2/Ni_3S_4 based cells is not caused by the R_{ct} increase of the electrodes, but by the increase of the internal resistance, which can be supported by the EIS curves (Figure 5.29C) at 1000 mA cm^{-2} (internal-resistance-dominated stage gradually shifts to the right with stable charge transfer resistance). It is worth mentioning that the increase of membrane resistance mainly focused on the first 200 h, and keeps relatively stable from the 200th to 500th h. Additionally, the degradation of the Ni/NiO-based cells after a short term of 50 h is mainly caused by the increased R_{ct}, while the internal resistance keeps relatively unchanged (Figure 5.29D).

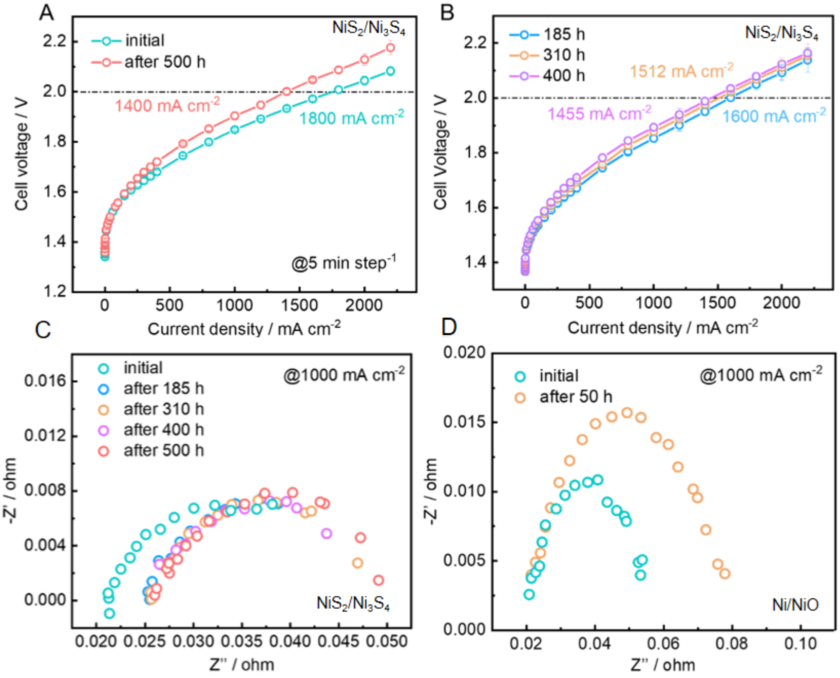

Figure 5.29 (A-B) Polarization curves of the cells Pt/C@C paper||FAA-3-50||NiS_2/Ni_3S_4 from "initial", "after 185 h", "after 310 h", "after 400 h" to "after 500 h" and corresponding EIS curves of (C)NiS_2/Ni_3S_4 and (D) Ni/NiO based cells before and after 500 and 50 h respectively.

After opening the cells, it was found that both anode and cathode catalysts remained on the Ni fiber and carbon paper substrates, and the membrane was fully damaged by high mechanical pressure and temperature (Figures 5.30A-B), while Ni/NiO was washed out entirely, which is the same as the cells with the FAA-3-50 membrane (Figures 5.26A-B).

After only membrane refreshing, with other components and conditions unchanged, the EIS curves were found to be highly consistent with its initial state, indicating restored internal resistance and unchanged R_{ct} (Figure 5.30C).

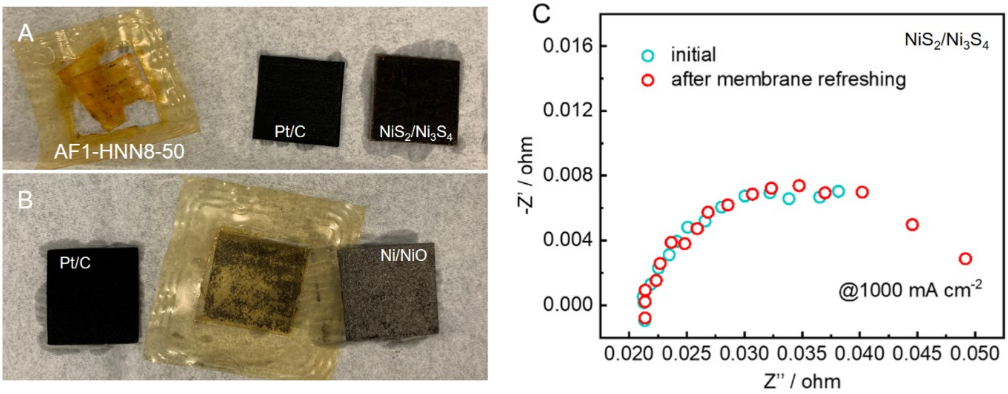

Figure 5.30 (A-B) Photos of AF1-HNN8-50, Pt/C@C paper and NiS_2/Ni_3S_4 and Ni/NiO@Ni fiber, (C) EIS of NiS_2/Ni_3S_4 based cells before test and that after 500 h at 1000 mA cm^{-2} water electrolysis and membrane refreshing.

Then, the polarization curves after 500 h were rechecked and compared with that of its initial state in Figure 5.31. It is clear that the current density of the NiS_2/Ni_3S_4 cells at 2.0 V keeps almost stable from 1800 to 1713 mA cm^{-2} with the degradation rate of only 4.8%, indicating the catalyst is stable and promising for longer-term water electrolysis, and the cells are mainly limited by membrane stability. Notably, the error bar of the polarization curves after 500 h becomes larger than before, which could be caused by i) changes to the electrode interface during cell disassembly/assembly and different sulfur leaching conditions for different catalytic activity.

However, the current density of Ni/NiO-based cells decreases from 1067 to 890 mA cm^{-2} after only 50 h, exhibiting much higher degradation rate of 17%, indicating Ni/NiO is not as active as before. The error bar of Ni/NiO based cells decreases, and the performance is highly repeatable, which could be explained that the Ni/NiO is fully washed out and the substrate is the same Ni fiber, thus good repeatability.

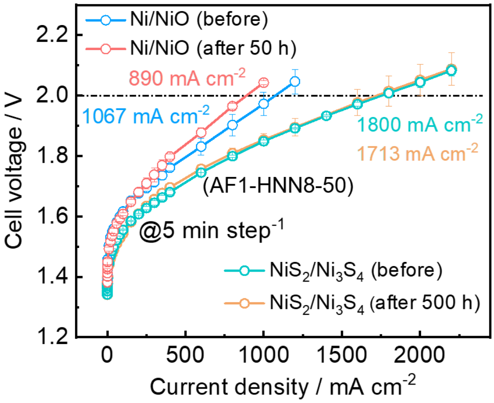

Figure 5.31 Polarization curves of the cells Pt/C@C paper||FAA-3-50||NiS_2/Ni_3S_4 or Ni/NiO before and after stability tests.

The reasons of stability/instability behind the above cells are shown in Figures 5.32A-B. The instability of Ni/NiO-based cells can be attributed to serious bubble issues (also half-cell tests, Figure 5.19A), with the cell voltage increasing from 2.00 to 2.14 V in the stability curve at the current density of 1000 mA cm^{-2} (Figure 5.28), while the voltage in the steady-state polarization curve after 50 h is only 2.04 V at 1000 mA cm^{-2} (Figure 5.31), indicating a high reversible cell voltage of 0.1 V that mainly caused by diffusion issue of bubbles, which greatly increases the interfacial resistance and leads to a continuous voltage increase until a higher voltage equilibrium. When one layer of surface catalyst is washed out, then the gap between the membrane and electrode increases, causing high internal resistance and strong polarization. Then relatively higher voltage and strong polarization further promote catalyst aggregation and degradation and cause extra damage to the membrane and in-depth catalyst layers. Finally, the whole catalyst layer was fully removed from the Ni fiber substrates as shown in Figure 5.30B.

Meanwhile, inferred from Figures 5.19, 5.28, 5.30, and 5.31, the high stability of NiS_2/Ni_3S_4 based cells is owing to the suppressed bubble issues due to electrochemical refining and redistributing effects of sulfur leaching for the formation of the $NiS_x/Ni(OH)_2/NiOOH$ structure with more active sites and higher surface area. More active sites mean higher activity and thus relatively lower average cell voltage (moderate polarization), thus relieving the bubble issue and catalyst aggregation. Meanwhile, higher surface area is conducive to ion adsorption and bubble desorption, thus reducing mass transfer resistance during electrolysis, suppressing reversible degradation and preventing the cell from continuous voltage increase.

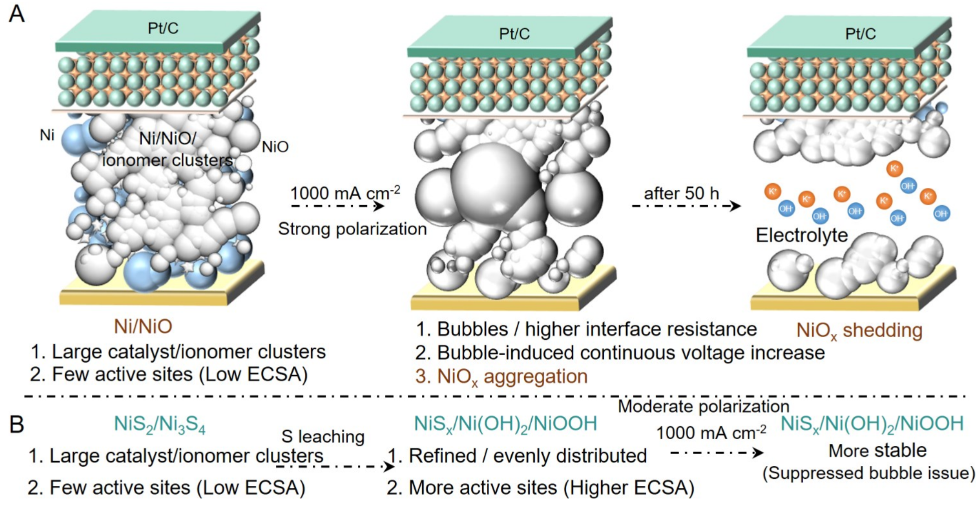

Figure 5.32 Degradation analysis of the Ni/NiO catalyst and reasons behind high stability of NiS_2/Ni_3S_4- based cells

As shown in Figures 5.33A-D initial NiS_2/Ni_3S_4 coated Ni fiber mainly consists of big ionomer/catalyst clusters with the size of 1-10 μm, while that after 500 h tests is mainly composed of stabilized Ni (oxy)-hydroxides from XPS results in Figures 5.34A-B and its morphology is nanosheet with the size of ca. 300-500 nm, which is more stable than Ni/NiO that was fully washed out after only 50 h continuous water electrolysis without tuning effects from sulfur leaching. This comparison indicates the assistance of sulfur leaching is highly helpful for the catalyst to achieve self-adaptation to strong polarization conditions by the formation of porous structures, defect-rich nanosheets, and sulfate-adsorbed surface, thus suppressing cell voltage.

Additionally, the stability of the catalyst is dependent on its activity: relatively higher activity means lower polarization/average cell voltage, which in turn means more moderate condition at the same current density, thus better stability. Conversely, lower activity not only cause relatively higher polarization/average cell voltage, but also put extra damage on the membrane, the electrolyte, the catalyst layers and the interface among them (e.g. contact resistance of electrode and bipolar plate was enhanced). All sorts of side reactions (e.g. CO_2

with KOH and even its reduction on the cathode) were greatly boosted, thus the less-active catalyst also suffered from low stability at high current density.

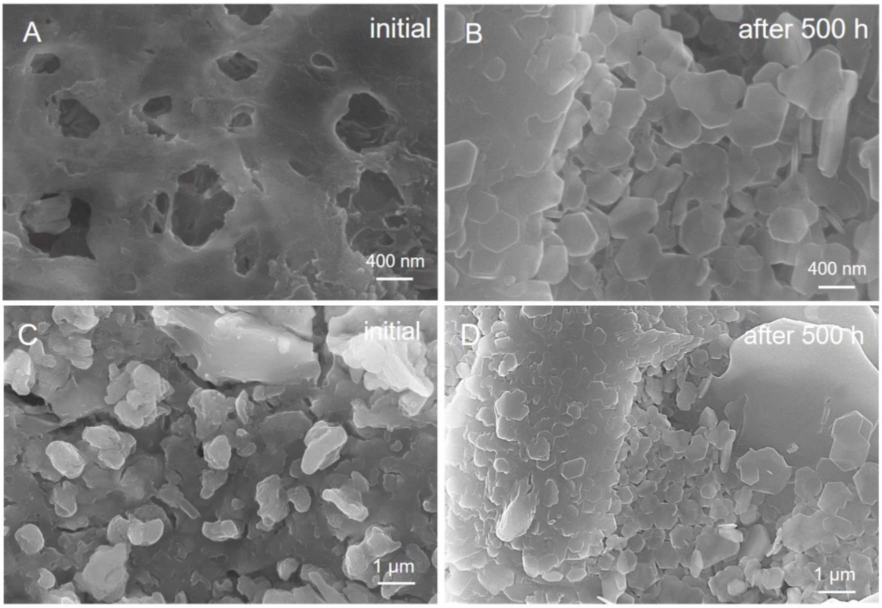

Figure 5.33 SEM images of (A, C) initial NiS_2/Ni_3S_4 coated on Ni fiber, which is covered with catalyst/ionomer clusters due to ink dispersion issue and 5 mg cm^{-2} mass loading (B, D) NiS_2/Ni_3S_4 coated Ni fiber after 500 h long-term cell testing at 1000 mA cm^{-2}, consisting of nickel (poly)-sulfides and (oxy)-hydroxides.

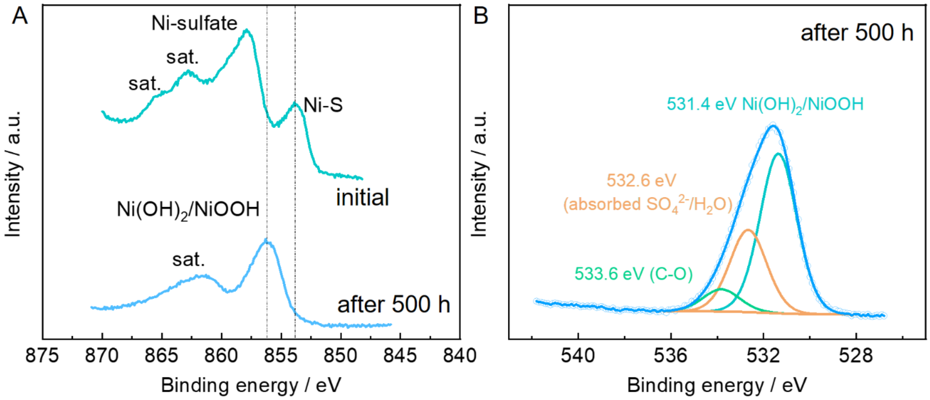

Figure 5.34 XPS of NiS_2/Ni_3S_4 after 500 h single-cell tests: (A) Ni 2p, (B) O 1s regions.

5.6 Summary of NiS_2/Ni_3S_4 based catalyst

NiS_2/Ni_3S_4 nano-cubes are synthesized by well-controlled vulcanization time between Ni^{2+} and sulfide/polysulfide ions, showing small size of 80±20 nm, which are further stabilized by a multi-step sulfur leaching process from NiS_2/Ni_3S_4 composite nano-cubes to more active $NiS_x/Ni(OH)_2/NiOOH$ heterostructure as intrinsic species for OER with higher ECSA/activity and stability than both Ni/NiO, and $Ni(OH)_2$. Moreover, the NiS_2/Ni_3S_4 exhibits better cycling stability during 10000 CVs at 100 mV s^{-1} than Ni/NiO and $Ni(OH)_2$.

More importantly, the stabilized $NiS_x/Ni(OH)_2/NiOOH$ catalyst from NiS_2/Ni_3S_4 exhibits stable performance for not only 65 h@10 mA cm^{-2} in a half cell, but also 500 h stability at a high current density 1000 mA cm^{-2} in full cells with negligible degradation rate, which supports that TMS could be promising as the anode catalyst for AEMWE.

The present work provides fundamental understanding and a specific approach to making full use of TMS and promotes the advancement of AEMWE by highly stabilized, low-cost OER catalysts. Sulfur leaching is highly promising as a general method for activation of other catalysts like NiS_2, FeS_2, CoS_2, MoS_2, etc., and can be further extended to phosphide, boride, nitride, etc.

6 $Ni_{0.67}Fe_{0.33}S_2$ nano-octahedrons

6.0 Preface

1. The research gap between Chapter 5 and Chapter 6:

Monometallic sulfides/polysulfides (NiS_2/Ni_3S_4) are synthesized via organic S precursor (thioacetamide, TAA), which is unfriendly to the environment. Additionally, NiS_2/Ni_3S_4 is advantageous in phase/interface engineering but very poor in charge and electron transfer processes due to their semiconductor nature, resulting in high R_{ct} and R_{Ω} during water electrolysis. (Chapter 5) Therefore, NiS_2/Ni_3S_4 needs further improvements: i) the synthesis method should be modified and ii) through bimetallic nanostructured sulfides/polysulfides, the metallicity can be improved, thus suppressing R_{ct} and R_{Ω} and enhancing cell performance.[85]

However, great challenges need to be addressed in the synthesis of nanostructured bimetallic sulfides/polysulfides: i) morphology control into nanostructures is much more complicated than that of monometallic ones, which are mainly achieved by template method from organometallic framework in the literature.[70] In this way, the catalysts always suffered from low production rate (<100 mg) and organic residues/pollutants.

In this chapter, a novel, additive-free method by two steps of coprecipitation and recrystallization was utilized to synthesize nanostructured $Ni_xFe_{1-x}S_2$ (x=0-1) with the production rate of 5 g. Then the $Ni_xFe_{1-x}S_2$ based catalysts suffered from sulfur leaching and owing to the ultra-fined $NiFeS_x$/$NiFe(OH)_2$/NiFeOOH derivatives to 2-5 nm, the derived catalyst exhibits 10 times higher ECSA and superhydrophilicity, excellent bubble diffusivity and lower interfacial resistance than NiS_2/Ni_3S_4 and commercial iridium black as well.

Consequently, the Chapter 5 involves a traditional synthesis method for NiS_2/Ni_3S_4 by organic S source as the precursor and focuses on fundamental study of monometallic sulfides/polysulfides for the concept of sulfur leaching and its effects on both half- and full-cell performance. On this basis, Chapter 6 optimizes the synthesis method under the premise that the particle size of $Ni_xFe_{1-x}S_2$ is below 100 nm, and with the Fe doping, the catalyst activity is greatly enhanced from ~340 to 286 mV@10 mA cm^{-2} and single cell performance from 1800 to 2200 mA cm^{-2} at 2.0 V.

2. The main goals of Chapter 6:

i) Achieve green synthesis of nanostructured single-phase $Ni_xFe_{1-x}S_2$ (x=0-1) without using organic thioacetamide precursor.

ii) Enhance OER activity via electrochemically assisted sulfur leaching and study the corresponding mechanism behind the reconstruction of representative $Ni_{0.80}Fe_{0.20}S_2$ and $Ni_{0.67}Fe_{0.33}S_2$ nano-octahedrons for truly active and stabilized species by in-situ Raman spectra (Figure 6.0);

iii) Prove the surface chemical state and morphology changes before and after sulfur leaching by XPS and HRTEM.

iv) Screen the best strategy for OER activity among i) monometallic heterostructure with two phases (NiS_2/Ni_3S_4), ii) bimetallic heterostructure with two phases (NiS_2/FeS_2) and iii) bimetallic heterostructure with a single phase ($Ni_xFe_{1-x}S_2$), meanwhile the best composition ratio of Ni/Fe to be 2:1 in $Ni_{0.67}Fe_{0.33}S_2$ for achieving comprehensive performance (activity and stability).

v) Extend $Ni_{0.67}Fe_{0.33}S_2$ from half to full cells, and test the polarization curves of the cells with Pt/C as cathode and AF1-HNN8-50 as the membrane and also long-term stability at high current density of 1000 mA cm^{-2}.

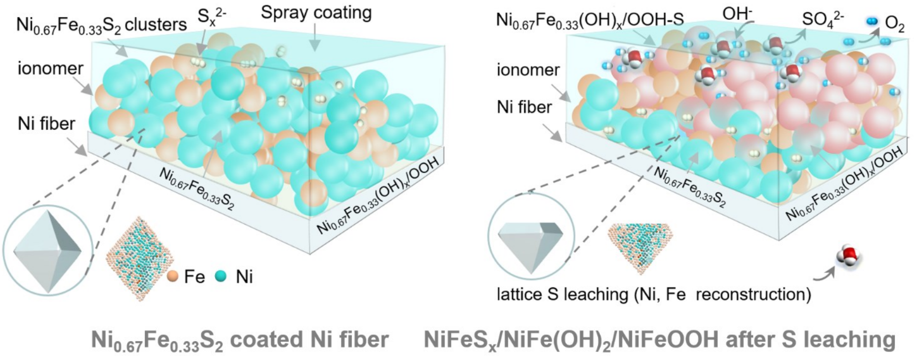

Figure 6.0 Sulfur leaching of $Ni_{0.67}Fe_{0.33}S_2$ coated on Ni fiber and its derivatives $NiFeS_x/NiFe(OH)_2/NiFeOOH/SO_4^{2-}$ for refined morphology and redistributed compositions.

6.1 Characterizations of $Ni_{0.67}Fe_{0.33}S_2$ nano-octahedrons

As explained in chapter 2, the synthesis of the $Ni_{0.67}Fe_{0.33}S_2$ nano-octahedrons was achieved by two-step synthesis of coprecipitation at room temperature by Ni^{2+}/Fe^{2+} and Na_2S_2 and recrystallization at 200°C. Its phase structure, morphology, chemical composition and surface states and corresponding morphology/structural changes after sulfur leaching will be discussed in this part.

6.1.1 Phase, chemical composition and morphology of $Ni_xFe_{1-x}S_2$ (x=0-1)

To understand phase compositions of obtained Ni based (poly)-sulfides, X-ray diffraction (XRD) was used to study their crystal structures. As shown in Figure 6.1A, diffraction peaks at 2θ values corresponds to typical planes of monometallic NiS_2 (JCPDS: 11-0099),[83-85] and FeS_2 (JCPDS: 42-1340) with the strong peak at (200) plane.[109] Meanwhile, the diffraction peaks of bimetallic $Ni_xFe_{1-x}S_2$ (x=0.33, 0.67, 0.50, 0.80) catalysts are all between that of pure NiS_2/FeS_2 and with higher content of Ni or Fe, the peaks shift to corresponding NiS_2 or FeS_2 side, indicating successful phase control of $Ni_xFe_{1-x}S_2$ (x=0-1). Particularly, the $Ni_{0.50}Fe_{0.50}S_2$ with equal proportions of Ni and Fe agrees well with the standard peaks (JCPDS: 02-0850),[109] which are coincidentally located in the middle of the peaks from NiS_2/FeS_2. The catalyst power was refined manually and from the exterior appearance, only the $Ni_{0.33}Fe_{0.67}S_2$ is brown, while other compositions are all dark (Figure 6.1B).

Overall, the $Ni_xFe_{1-x}S_2$ (x=0-1) catalysts after aging at 200°C are fully recrystallized, indicating this temperature is sufficient for crystallization, and all exhibit one similar set of diffraction peaks with only slight shifts, indicating isomorphism between all the above sulfides with different Fe/Ni doping rate. Specifically, with one third of the Ni doping in FeS_2, the diffraction peaks (2θ) move about 0.3° towards NiS_2. Similarly, with one-fifth of the Fe doping in NiS_2, the diffraction peaks (2θ) move about 0.3° towards FeS_2 (Figure 6.1C). And other catalyst compositions also follow the rule of “higher doping rate, more peak shifts”. Therefore, the phase structures of the synthesized (poly)-sulfide catalysts are determined to be $Ni_xFe_{1-x}S_2$ (x=0-1), which can be described as the crystal structures in Figure 6.2 A.

It is worth noting that the peak intensity difference between “the strongest (I_1)” and “the second strongest (I_2)” peaks change with different Ni/Fe ratios. For example, I_1 of pure NiS_2 is much stronger than I_2, while the I_1 of pure FeS_2 is almost equal to I_2, indicating more planes of (200) are exposed for NiS_2. Similarly, with the Ni/Fe ratios of 2:1 and 4:1, the I_1 is also stronger than I_2. When further increase the amount of Fe, this phenomenon will diminish, indicating orientation preference in Fe doped NiS_2 with Fe: Ni≤0.33.

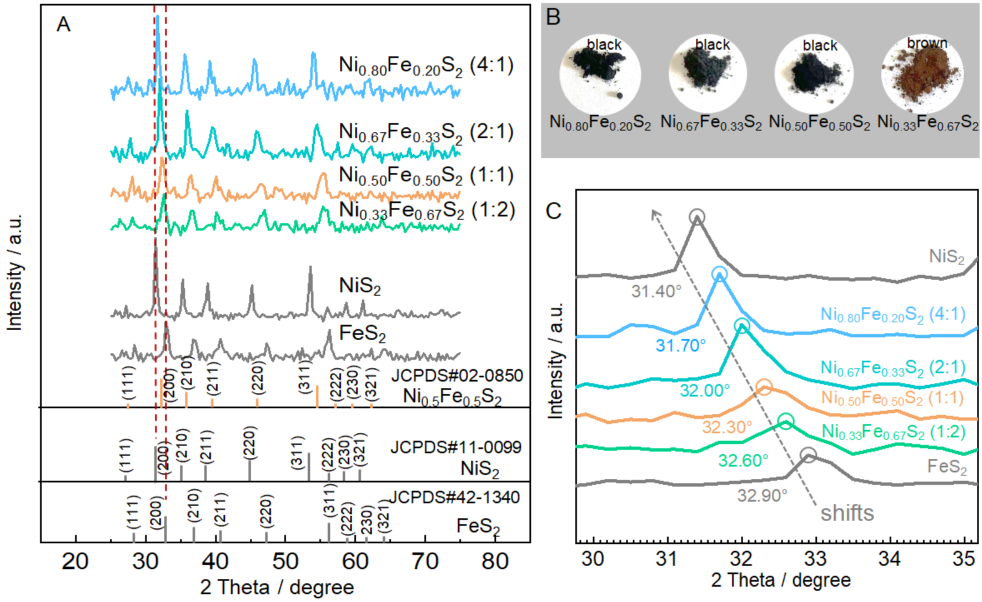

Figure 6.1 (A) XRD patterns of $Ni_xFe_{1-x}S_2$ (x=0-1), (B) photos of bimetallic disulfide catalysts, and (C) partially magnified interval.

The output ratios between Ni and Fe tested by inductively coupled plasma-optical emission spectrometry (ICP-OES) and elemental mapping via SEM equipped energy dispersive X-Ray analysis (SEM-EDX) are shown in Figure 6.2B. The results tested by two methods are highly similar and output compositions of $Ni_xFe_{1-x}S_2$ (x=0.33-0.80) slightly shift compared with input Ni/Fe ratios.

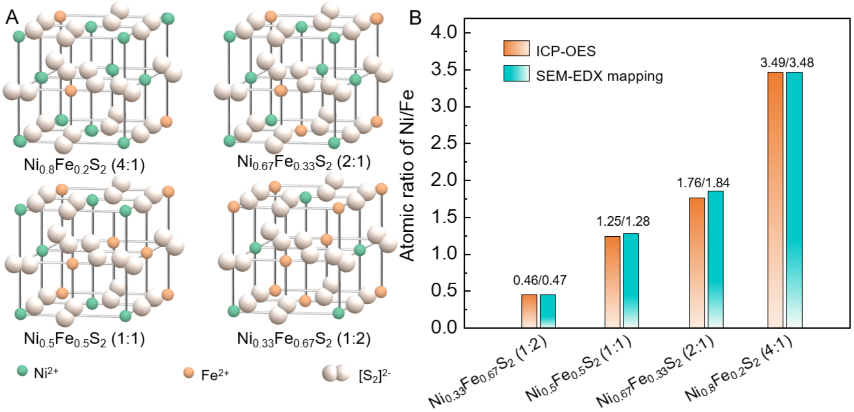

Figure 6.2 (A) Crystal structures of disulfide catalysts with the composition from Ni/Fe=4:1, 2:1, 1:1 to 1:2, (B) inductively coupled plasma-optical emission spectrometry (ICP-OES) and elemental mapping by SEM equipped energy dispersive X-Ray analysis (SEM-EDX).

Then, X-ray photoelectron spectroscopy (XPS) was applied to study the surface chemical state configuration of nickel and sulfur in $Ni_xFe_{1-x}S_2$ (x=0.33-0.80). As shown in Figure 6.3A, The Fe 2p spectra of $Ni_xFe_{1-x}S_2$ were fitted into peaks at ca. i) 706.3 and 718.4 eV corresponding to $2p_{3/2}$ and $2p_{1/2}$ of Fe^{2+} in Fe^{2+}-S; ii) 707.3 and 720.2 eV attributed to the $2p_{3/2}$ and $2p_{1/2}$ of Fe^{2+}-S_2; iii) 708.6 and 721.5 eV corresponding to the $2p_{3/2}$ and $2p_{1/2}$ of Fe^{2+}-S_x;[110] iv) 710.6 and 724.2 eV attributed to the $2p_{3/2}$ and $2p_{1/2}$ of Fe^{2+}; v) 712.8 and 726.4 eV corresponding to $2p_{3/2}$ and $2p_{1/2}$ of Fe^{3+}; vi) 716.2 and 732.5 eV attributed to satellite peaks.[109, 111] Thus, the surface Fe on the $Ni_xFe_{1-x}S_2$ (x=0.33-0.80) is composed of Fe^{2+}-S, Fe^{2+}-S_2, Fe^{2+}-S_x, Fe^{2+}, and Fe^{3+}. It is noteworthy that the content of Fe^{3+} increases with the increasing of Ni/Fe ratios, which facilitates the formation of FeOOH.

Meanwhile, the peaks fitted in the Ni 2p region as shown in Figure 6.3B shows that the Ni 2p spectra of $Ni_xFe_{1-x}S_2$ were fitted into peaks at ca. i) 853.5 and 870.7 eV corresponding to the $2p_{3/2}$ and $2p_{1/2}$ of Ni^{2+} in Ni^{2+}-S_2; ii) 854.4 and 871.8 eV attributed to the $2p_{3/2}$ and $2p_{1/2}$ of Ni^{2+}-S_x;[83, 97, 112-114] iii) 856.2 and 874.4 eV corresponding to $2p_{3/2}$ and $2p_{1/2}$ of Ni^{2+}; iv) 857.5 and 876.2 eV attributed to the $2p_{3/2}$ and $2p_{1/2}$ of Ni^{3+}; v) 862.2 and 879.9 eV are attributed to satellite peaks.[109, 112] Thus, the surface Ni on the $Ni_xFe_{1-x}S_2$ (x=0.33-0.80) consists of Ni^{2+}-S_2, Ni^{2+}-S_x, Ni^{2+}, and Ni^{3+}. Similarly, the content of Ni^{3+} increases with the increasing of Ni/Fe ratios, which facilitates the formation of NiOOH.

Additionally, the peaks fitted in the S 2p region as shown in Figures 6.4A-D shows that the S 2p spectra of $Ni_xFe_{1-x}S_2$ were fitted into peaks at ca. i) 161.7 and 162.9 eV corresponding to $2p_{3/2}$ and $2p_{1/2}$ of S^{2-};[86, 87] ii) 162.8 and 164.0 eV attributed to $2p_{3/2}$ and $2p_{1/2}$ of S_2^{2-};[93, 115] iii) 163.7 and 164.8 eV corresponding to $2p_{3/2}$ and $2p_{1/2}$ of S_x;[84, 97, 114, 115] iv) 165.7 and 166.9 eV attributed to $2p_{3/2}$ and $2p_{1/2}$ of the S-O bond; v) 169.2 and 170.4 eV attributed to SO_x^{2-}, with x=3-4.[86, 87] Thus, the surface S on the $Ni_xFe_{1-x}S_2$ (x=0.33-0.80) consists of S^{2-}, S_2^{2-}, S_x^{2-}, S-O, SO_3^{2-} and SO_4^{2-}. With higher ratio of Ni/Fe, the percentage of polysulfide species (S_x^{2-}) increased from ca. 13.67% to 33.20%, indicating nickel promotes the formation of polysulfides, while iron is more inclined to form low-vulcanized FeS, FeS_2, etc. Such a trend can be explained by the return reaction between Fe^{3+} with strong oxidative property and S^{2-}/S_2^{2-} ions as strong reduction agent to form FeS/FeS_2.

The $Ni_xFe_{1-x}S_2$ surface consists of complex chemical states with not only low-valence Ni and Fe sulfides, disulfides and polysulfides, but also absorbed Ni^{2+}/Ni^{3+} and Fe^{2+}/Fe^{3+} etc. With higher amount of Ni, the content of polysulfides and trivalent Ni^{3+} ions will increase significantly, indicating Ni^{3+} is more stable than Fe^{3+} with less extent of reaction with S^{2-}/S_2^{2-}. Therefore, adjusting the ratio of Ni/Fe will greatly change the chemical compositions and states of the catalyst surface. With higher ratio of Ni/Fe, the percentage of Fe^{2+}-S_x increased from 3.89% to 18.51%, which agrees well with S 2p regions that excessive iron is more inclined to form FeS_2. Meanwhile, the percentage of Fe^{3+} also increased much from 10.47% to 29.22%, indicating higher content of Ni promotes the formation of Fe^{3+}.

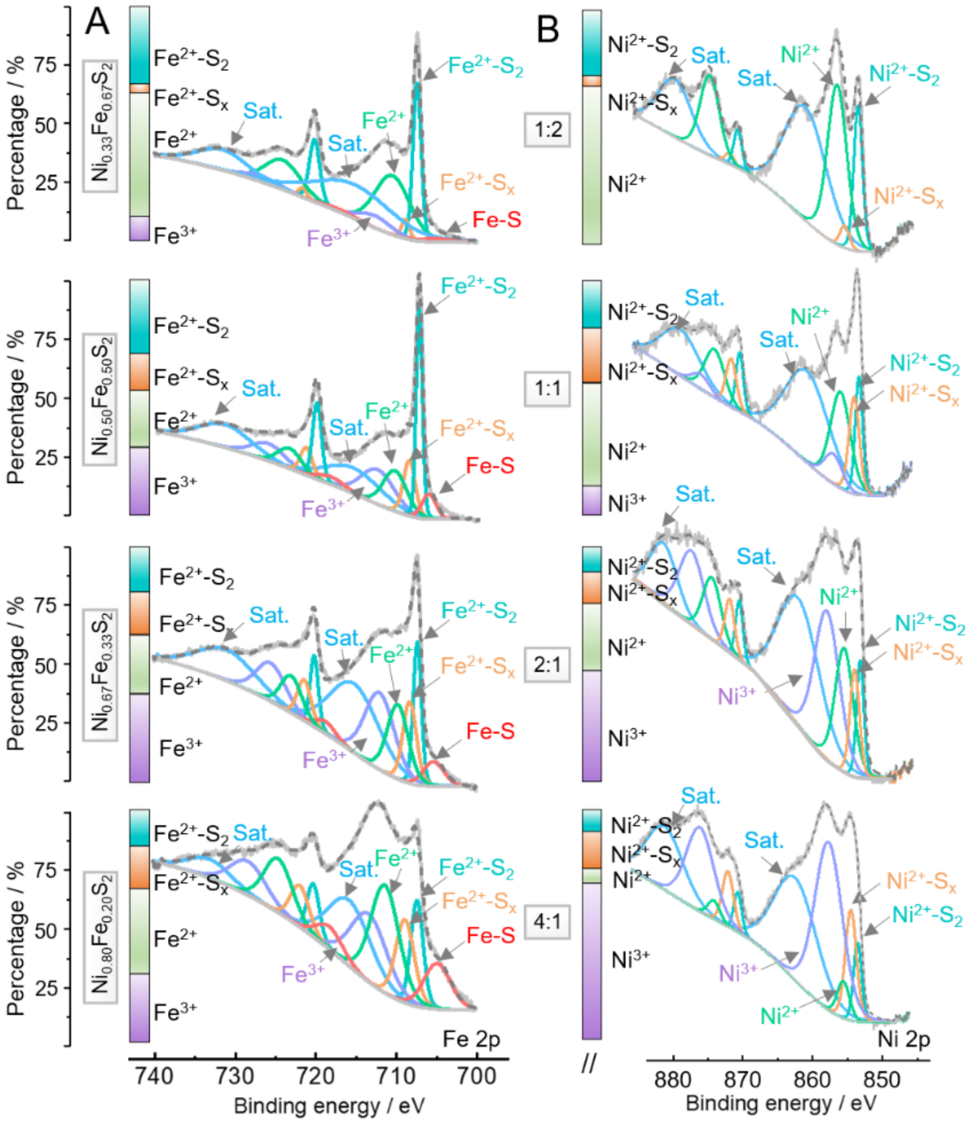

Figure 6.3 (A) X-ray photoelectron spectroscopy (XPS) of bimetallic disulfide catalysts with the composition from Ni/Fe=4:1, 2:1, 1:1 to 1:2 in Fe 2p and (B) Ni 2p regions.

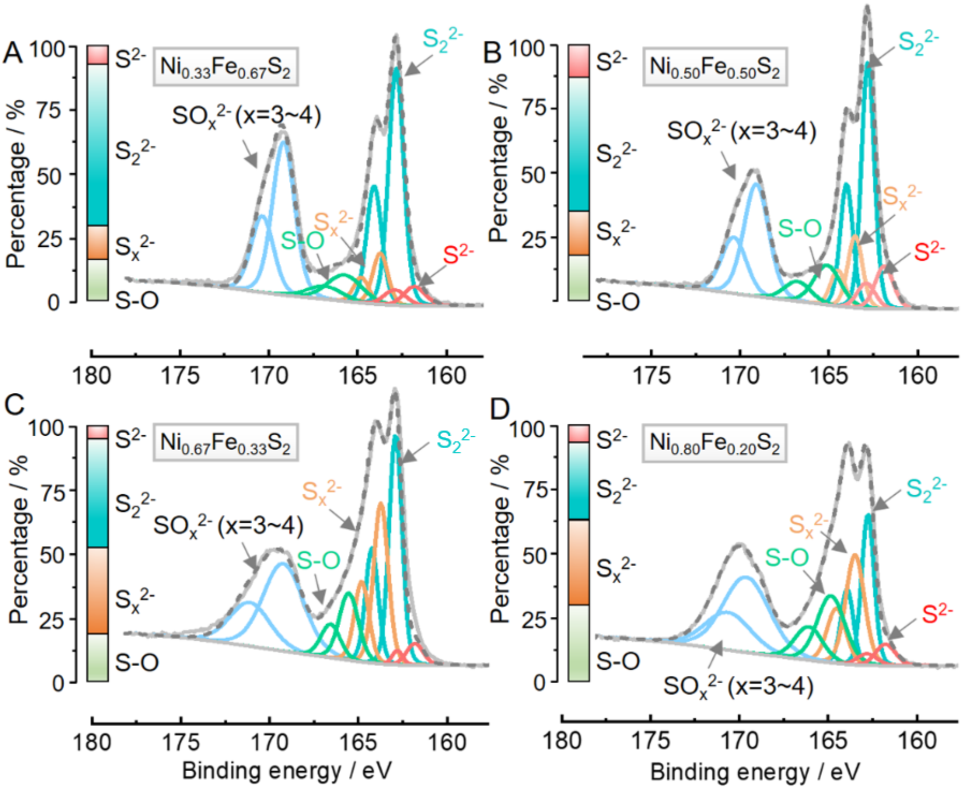

Figure 6.4 (A-D) XPS of bimetallic disulfide catalysts with the composition from Ni/Fe=4:1, 2:1, 1:1 to 1:2 in the S 2p region.

The morphologies of representative $Ni_{0.80}Fe_{0.20}S_2$ and $Ni_{0.67}Fe_{0.33}S_2$ were observed by high resolution transmission electron microscopy (HRTEM). It is shown in Figures 6.5B-C that $Ni_{0.80}Fe_{0.20}S_2$ exhibits the morphology of nano-octahedrons (one captured octahedron with the size of ca. 75.5*70.0 nm, long axis*short axis). Then Figure 6.5C shows the HRTEM image with an inter-planar spacing of 0.32 nm two lattice fringes, which can be attributed to the (111) lattice plane of $Ni_{0.80}Fe_{0.20}S_2$, verifying again the crystal structure of $Ni_{0.80}Fe_{0.20}S_2$ shown by XRD results.[84, 109] As shown in Figures 6.5A and D, the high-angle annular dark-field scanning transmission electron microscopy (HAADF-STEM) image and the corresponding energy dispersive X-ray (EDX) mappings show the elemental distribution of Ni, Fe and S on the surface of $Ni_{0.80}Fe_{0.20}S_2$. It is noteworthy that Ni and S are uniformly distributed, while Fe is more concentrated on the catalyst surface. Coincidentally, the quantitative EDX analysis of

$Ni_{0.80}Fe_{0.20}S_2$ is to be in average of Ni/Fe=3.27 and (Ni+Fe)/S_2=0.51, which is also consistent with that from ICP-OES and SEM-EDX mapping and XRD results analyzed above, confirming the ratio among Ni Fe and S from another perspective. Similarly, it is shown in Figures 6.5F-G that $Ni_{0.67}Fe_{0.33}S_2$ also exhibits the morphology of nano-octahedrons (one captured octahedron with the size of ca. 93.0*61.2 nm, long axis*short axis). Then Figure 6.5G shows the HRTEM image with an inter-planar spacing of 0.28 nm two lattice fringes, which can be attributed to (111) lattice planes of $Ni_{0.67}Fe_{0.33}S_2$, which is also mutually confirmed with the crystal structure shown by XRD results.[109] As shown in Figures 6.5E and H, the HAADF-STEM image and the corresponding EDX mappings show the elemental distribution of Ni, Fe and S on the surface of $Ni_{0.67}Fe_{0.33}S_2$. It is noteworthy that the distribution of Ni, Fe, S are similar with that of $Ni_{0.80}Fe_{0.20}S_2$ with more Fe concentrated on the catalyst surface. Coincidentally, the quantitative EDX analysis of $Ni_{0.67}Fe_{0.33}S_2$ is to be in average of Ni/Fe=1.75 and (Ni+Fe)/S_2=0.52, which is also consistent with that from ICP-OES and SEM-EDX mapping and XRD results analyzed above, confirming the ratio among Ni, Fe and S in $Ni_{0.67}Fe_{0.33}S_2$.

To understand the special distribution of surface Fe, $Ni_{0.67}Fe_{0.33}S_2$ prepared for 1 h was compared with that for 2 h in Figures 6.6A-B. Such a special structure is achieved by i) the nucleation of FeS/FeS_2, ii) Ni replaces Fe and iii) the diffusion of Ni and Fe with the Fe/Ni ratio gradually increases from 34.6, 3.74 to 2.03 that captured by EDX mapping. Then with further aging for 2 h, Fe was fully replaced by Ni to an equilibrium state, with the ratio of Fe/Ni further increasing to 0.57 that is close to the input ratio of 0.50. The first nucleation of FeS/FeS_2 can be explained by the preferential precipitation of iron with sulfur than that with Ni due to faster kinetics. While the Ni substitution of Fe can be attributed to their similar atomic sizes and isomorphism between NiS_2 and FeS_2 with the same crystal structure proved by XRD. Surface Fe distribution can be revealed by the different atomic diffusivity of Ni and Fe.

The pure phases of NiS_2 and FeS_2 were also synthesized and their HAADF images are shown in Figure 6.7. It is clear that both NiS_2 and FeS_2 exhibit the morphology of nanoflowers with a lot of hollow spaces for mutual doping with each other. The size of FeS_2 is much larger than that of NiS_2, and its distribution is not uniform, which shows that Ni plays an important role in controlling the size of $Ni_{0.67}Fe_{0.33}S_2$ catalysts. During the redistribution of Ni and Fe, FeS/NiS in the low-sulfur-state was converted into FeS_2/NiS_2 by the reaction between FeS/NiS and S_x^{2-}. Due to the limited amount of S and specific temperature of ~200°C, it is not conducive to the formation of polysulfides FeS_x/NiS_x. Then FeS_2 and NiS_2 can form a homogeneous solid solution $Ni_xFe_{1-x}S_2$ and the higher content of Ni is, the larger inter-planar spacing will be, which also explains the peaks shifts to the left from FeS_2 to NiS_2 due to enlarged inter-planar spacing with more Ni inside.

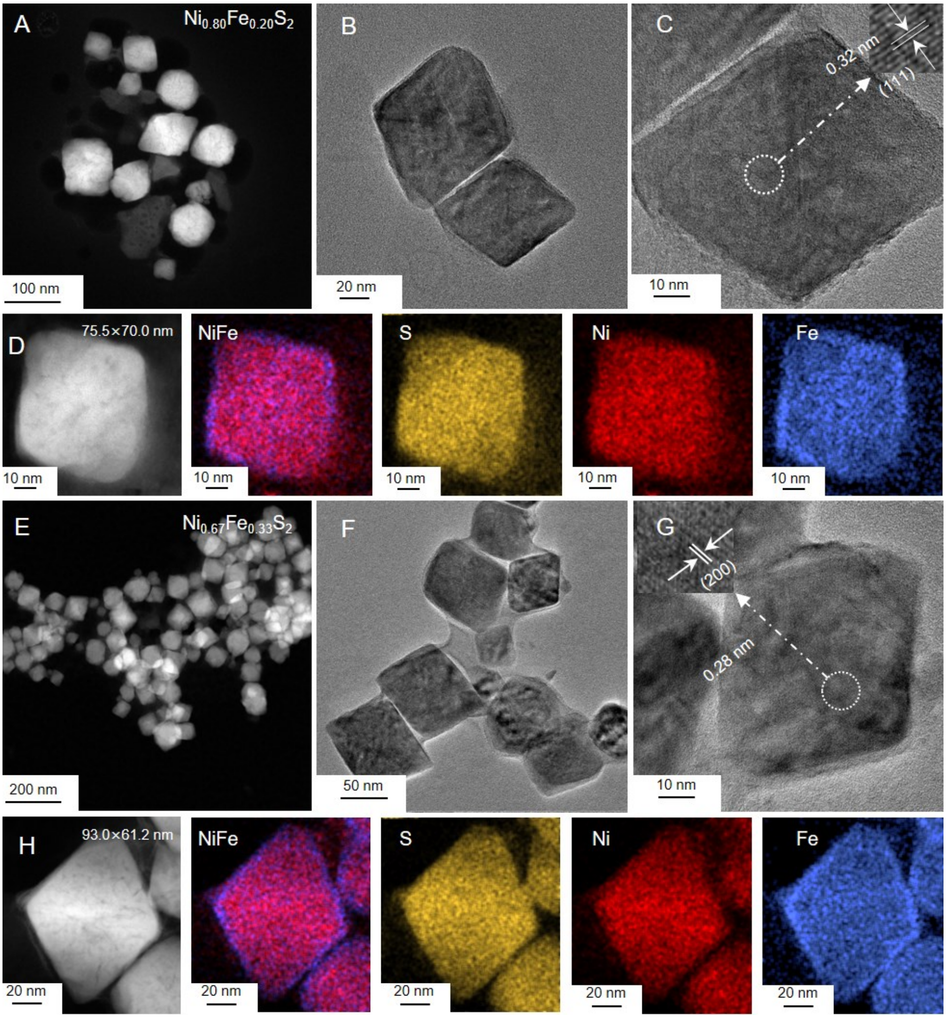

Figure 6.5 (A) HAADF image, and (B, C) HRTEM of $Ni_{0.80}Fe_{0.20}S_2$. *(D) HAADF image and corresponding elemental mapping of NiFe, S, Ni, and Fe of* $Ni_{0.80}Fe_{0.20}S_2$. *(E) HAADF image, and (F, G) HRTEM of* $Ni_{0.67}Fe_{0.33}S_2$. *(H) HAADF image and corresponding elemental mapping of NiFe, S, Ni, and Fe of* $Ni_{0.67}Fe_{0.33}S_2$.

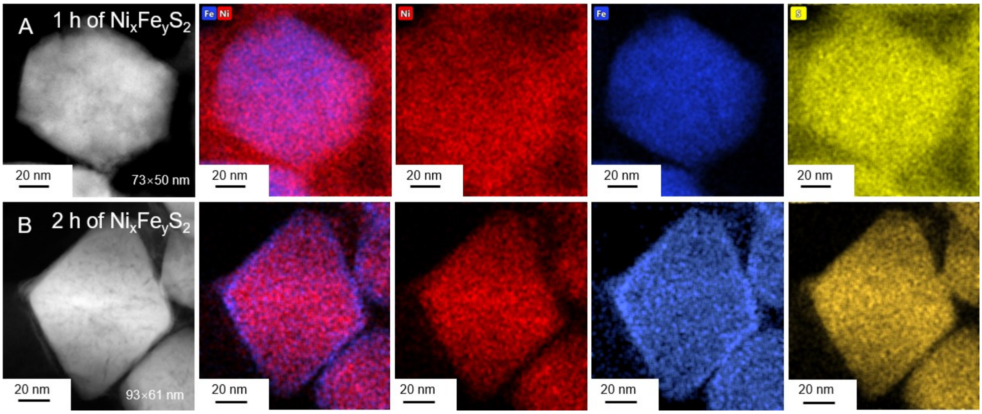

Figure 6.6 High-angle annular dark-field imaging (HAADF) images and corresponding elemental mapping of bimetallic disulfide catalysts with the composition of Ni/Fe=4:1 prepared by different reaction hours (h): (A) 1 h, (B) 2 h.

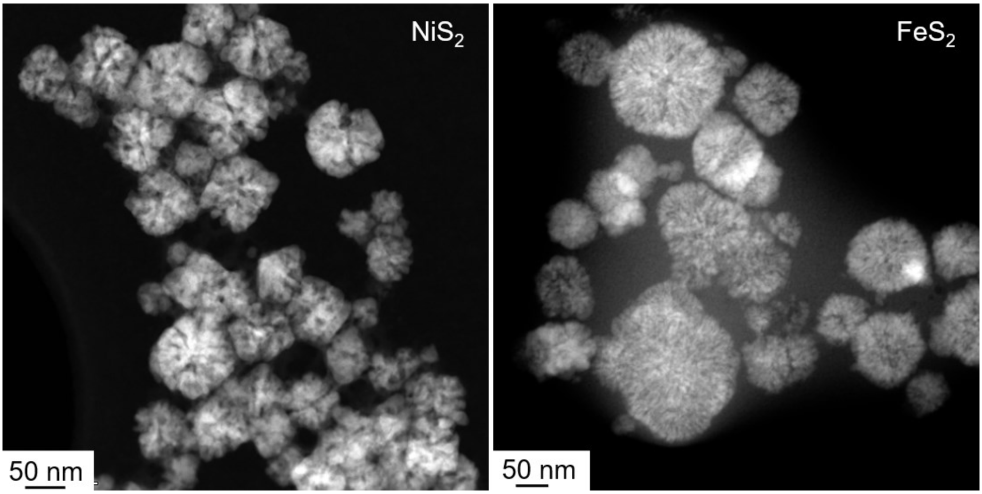

Figure 6.7 HAADF images of monometallic disulfide catalysts NiS_2 and FeS_2 prepared by the same method as that of $Ni_xFe_{1-x}S_2$ (x=0.33-0.80) but different precursors.

6.1.2 Sulfur leaching of $Ni_xFe_{1-x}S_2$ (x=0-1) in half cells

After fundamental understanding of the formation of $Ni_xFe_{1-x}S_2$ (x=0-1), it is time to study their sulfur leaching behavior. As shown in Figure 6.8A, with the same operation steps as that for the activation of NiS_2/Ni_3S_4, the $Ni_{0.67}Fe_{0.33}S_2$ after three times of sulfur leaching by CVs at 100 mV s^{-1}, exhibits continuous performance enhancement from the 1st, 2nd, 10th and 20th cycles. It is clear that 20 CVs are enough for a basic stabilization for $Ni_{0.67}Fe_{0.33}S_2$. Meanwhile, the commercial Ni-Fe alloy was also used as the OER catalyst and scanned for 20 CVs, which shows no performance improvement, indicating sulfur leaching also plays role in the bimetallic Ni/Fe disulfide-based catalysts.

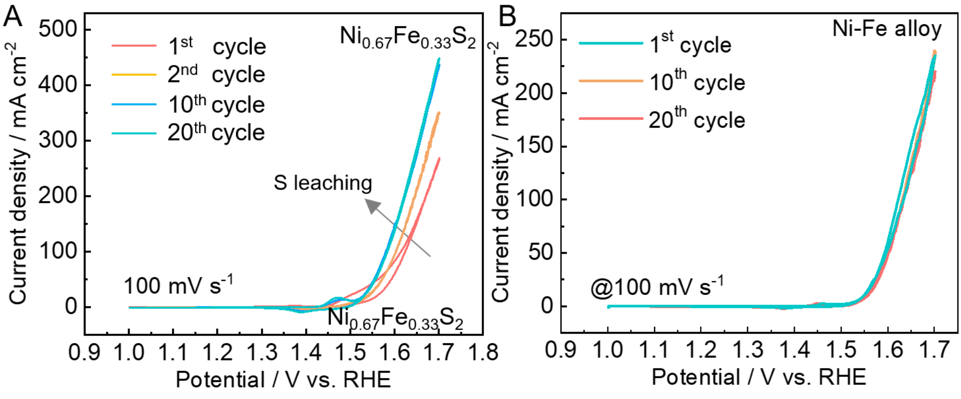

Refer “after 30 CVs” as “after S leaching”

Figure 6.8 (A) Cyclic voltammetry (CV) of $Ni_{0.67}Fe_{0.33}S_2$ at 100 mV s^{-1} for the first, second, 10th, 20th cycles. (B) Electrochemical active surface area (ECSA) of bimetallic disulfide catalysts with the composition of Ni/Fe=4:1, 2:1, 1:1, and 1:2 before and after sulfur leaching, and (C) corresponding overpotential summarized from Figure 6.8. (D) LSV curves of $Ni_{0.67}Fe_{0.33}S_2$ at a scan rate of 5 mV s^{-1} before and after 10000 CVs. (E) Stability test of $Ni_{0.67}Fe_{0.33}S_2$ coated on the nickel fiber ($Ni_{0.67}Fe_{0.33}S_2$@NF) at 1.6 V for 100 h. (F) LSV curves of $Ni_{0.67}Fe_{0.33}S_2$@NF at 5 mV s^{-1} before and after 100 h.

To understand the time-dependent structural evolutions, $Ni_{0.80}Fe_{0.20}S_2$ and $Ni_{0.67}Fe_{0.33}S_2$ were monitored by in-situ Raman spectra (the setup is shown in Chapter 3). As shown in Figure 6.9, in-situ Raman results of $Ni_{0.80}Fe_{0.20}S_2$ and $Ni_{0.67}Fe_{0.33}S_2$ at different voltages (from 1.3 to 1.7 V and back to 1.3 V with the increment of 0.1 V) show that the structural evolutions during OER processes. For example, at a relatively low voltage of 1.3/1.4 V, the recorded peak at ~386 cm^{-1} is attributed to the pristine pyrite structure of metal-S_2,[109] and the peaks at 450 and 500 cm^{-1} correspond to the $Ni(OH)_2$. Then with higher voltage of 1.6-1.7 V, two emerging bands at

~475 and ~555 cm^{-1} indicate the conversion of the Ni(OH)$_2$ into NiOOH.[81] When the voltage is scanned back, the peak positions move relatively to the left, indicating the derived NiOOH is partially reduced to Ni(OH)$_2$.

Both of the Ni$_{0.80}$Fe$_{0.20}$S$_2$ and Ni$_{0.67}$Fe$_{0.33}$S$_2$ are unstable under strong-polarization conditions in alkaline electrolytes and not the real active species for OER, while the newly derived NiOOH and Fe doped NiOOH is highly active for catalyzing OER processes. Thus, all Ni$_x$Fe$_{1-x}$S$_2$ (x=0-1) catalysts follow the rule of sulfur leaching from sulfur-rich disulfides to nickel-rich hydroxides and then (oxy)-hydroxides.

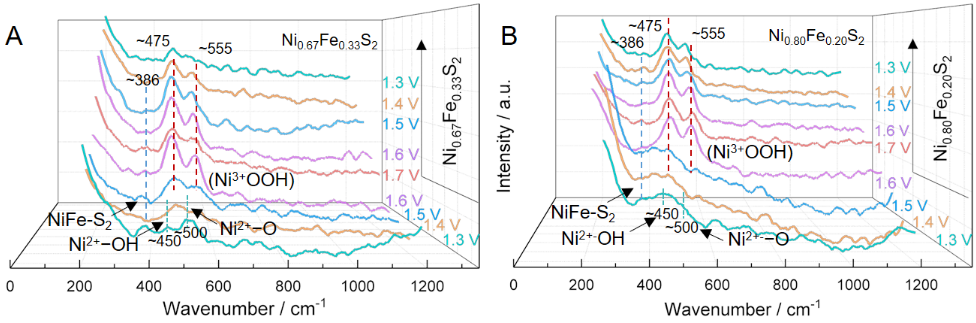

Figure 6.9 In-situ Raman spectra of bimetallic disulfide catalysts with the composition of Ni/Fe=4:1 and 2:1 during OER processes in 1 M KOH recorded at the voltage of 1.3 to 1.7 V and then back to 1.3 V with the increment of 0.1 V: (A) Ni$_{0.80}$Fe$_{0.20}$S$_2$, (B) Ni$_{0.67}$Fe$_{0.33}$S$_2$.

In-situ Raman is powerful in the determination of the products from Ni$_x$Fe$_{1-x}$S$_2$ after sulfur leaching, but cannot monitor detailed processes of sulfur leaching. Therefore, XPS was further used to characterize the ex-situ evolution of surface chemical states of O and S in Ni$_{0.67}$Fe$_{0.33}$S$_2$. As shown in Figure 6.10A, the binding energy peaks at ~529 and ~531 eV in O 1s region are corresponding to NiFe-O and Ni/Fe(OH)$_x$ respectively, which however were not detected in initial Ni$_{0.67}$Fe$_{0.33}$S$_2$,[90, 91] indicating the surface of the pristine catalyst has almost no nickel oxides/hydroxides. Then the Ni$_{0.67}$Fe$_{0.33}$S$_2$ catalyst after sulfur leaching exhibits an emerged peak at ~531 eV attributed to Ni/Fe(OH)$_x$, consistent with the in-situ Raman spectra on the first stage. When long-term CVs were applied, the Ni$_{0.67}$Fe$_{0.33}$S$_2$ catalyst exhibits decreased peak at ~529 eV, which can be attributed to the lattice O in Ni/FeOOH,[95, 96] agreeing well with in-situ Raman results on the second stage. And the peaks at ~528 eV can be attributed to S-O bond in sulfur oxides. In addition, the evolution of the peaks in S 2p regions show that the sulfur is leached out by the following steps: i) Polymerization of low-sulfur-state sulfides to form polysulfides; ii) oxidation of polysulfides to sulfur oxides, and iii) oxidation of sulfur oxides to sulfate ions. Thus, the sulfur is leached out step by step with the formation of multiphase heterostructures.

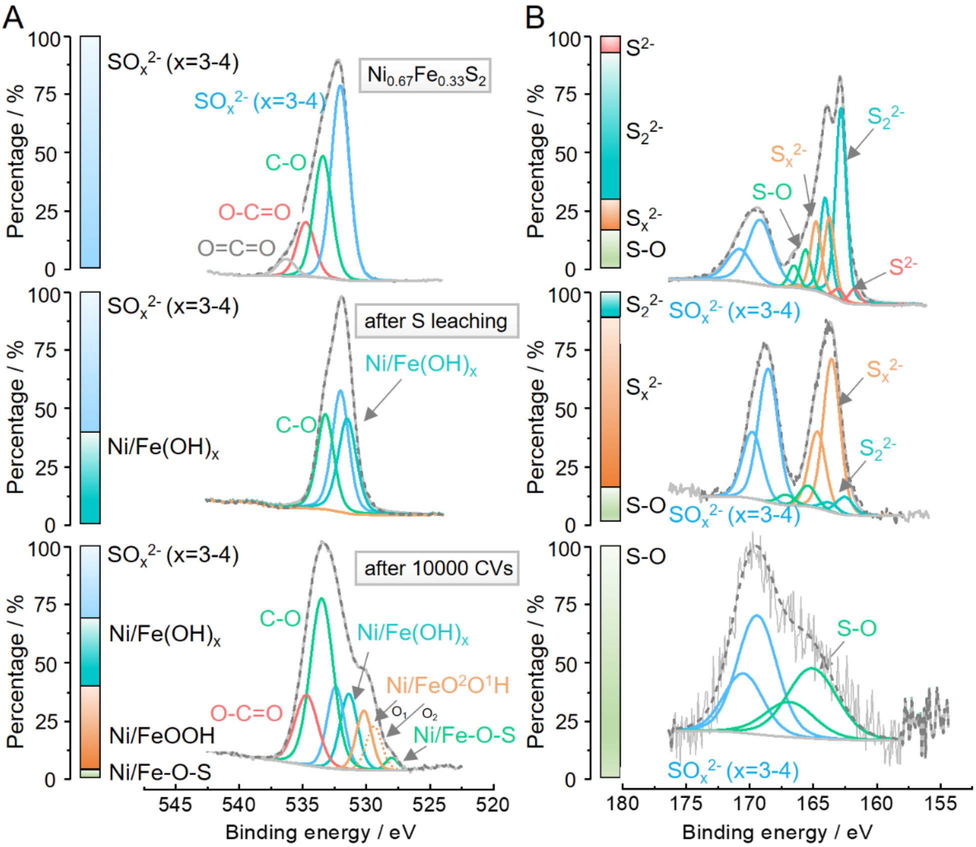

Figure 6.10 XPS of bimetallic disulfide catalysts with the composition of Ni/Fe=4:1 before and after sulfur leaching, and 10000 CVs in (A) O 1s and (B) S 2p regions.

6.1.3 Activity of $Ni_xFe_{1-x}S_2$ (x=0-1) in half cells

As shown in Figure 6.11, the LSV curves show that the performance of all $Ni_xFe_{1-x}S_2$ (x=0-1) catalysts, except for FeS_2, exhibits enhancement after sulfur leaching, indicating the electrochemically assisted sulfur leaching is also applicable to bimetallic sulfides. Additionally, FeS_2 is highly unstable and can survive for only ~100 CVs, indicating sulfur leaching deteriorates the performance of FeS_2.

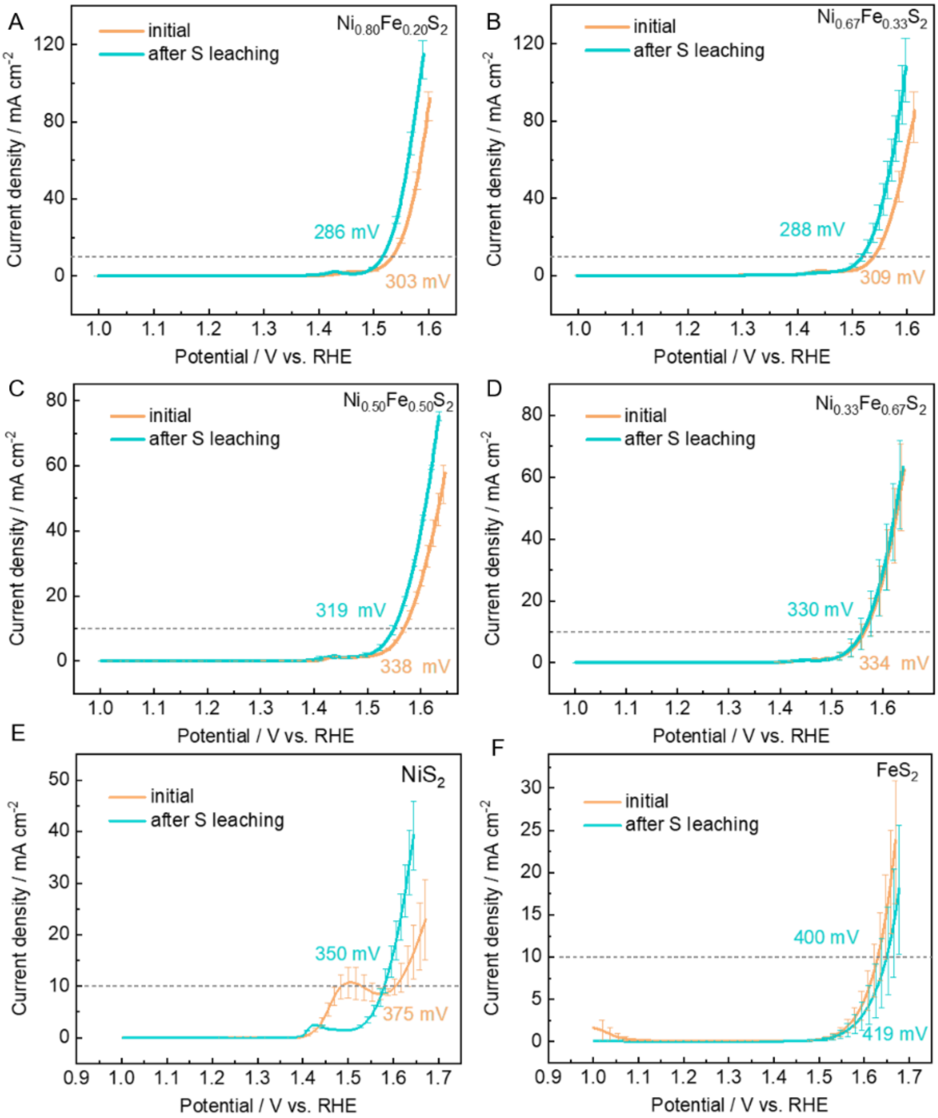

Figure 6.11 Linear sweep voltammetry (LSV) curves of $Ni_xFe_{1-x}S_2$ with different compositions before and after sulfur leaching: (A) x=0.80, (B) x=0.67, (C) x=0.50, (D) x=0.33, (E) x=1, (F) x=0 in 1 M KOH at 5 mV s^{-1}.

The overpotentials at 10 mA cm^{-2} and Tafel slopes of the above sulfides are summarized in Figures 6.12A-B. Notably, i) the best configuration of Ni/Fe ratios is ca. 2.0-4.0. ii) The higher content of Ni is, the stronger the effect of sulfur leaching will be. For example, $Ni_{0.67}Fe_{0.33}S_2$ exhibits enhanced performance after sulfur leaching from 309 to 288 mV with the drop of 21 mV. Similarly, NiS_2 exhibits enhanced performance after sulfur leaching from 375 to 350 mV with the potential drop of 25 mV, while FeS_2 shows decreased performance from 400 to 419 mV with the potential increase of 19 mV.

The OER performance improvement caused by surface reconstruction can be analyzed by the differences in R_Ω, R_{ct} and ECSA. As shown in Figure 6.12C (take $Ni_{0.67}Fe_{0.33}S_2$ as an example), the EIS of $Ni_{0.67}Fe_{0.33}S_2$ exhibits that both R_Ω and R_{ct} are suppressed after sulfur leaching, which is consistent with the conclusion from NiS_2/Ni_3S_4. Also, the ECSA of $Ni_{0.80}Fe_{0.20}S_2$ and $Ni_{0.67}Fe_{0.33}S_2$ (Figure 6.12D, supported by Figures 6.13A-D) is as 10 times as before, while that of $Ni_{0.50}Fe_{0.50}S_2$ and $Ni_{0.33}Fe_{0.67}S_2$ is slightly increased, which supports the trends of overpotentials at 10 mA cm^{-2} and Tafel slopes for $Ni_xFe_{1-x}S_2$ (x=0-1).

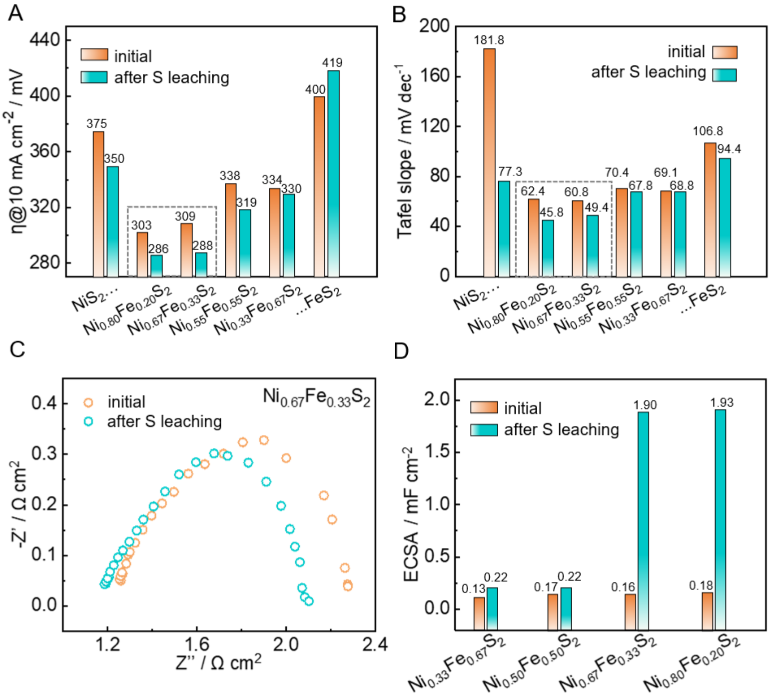

Figure 6.12 (A) Overpotential at 10 mA cm^{-2}, (B) Tafel slopes summarized for Figure 6.11, (C) EIS of $Ni_{0.67}Fe_{0.33}S_2$, and ECSA of $Ni_xFe_{1-x}S_2$ (x=0.80, 0.67).

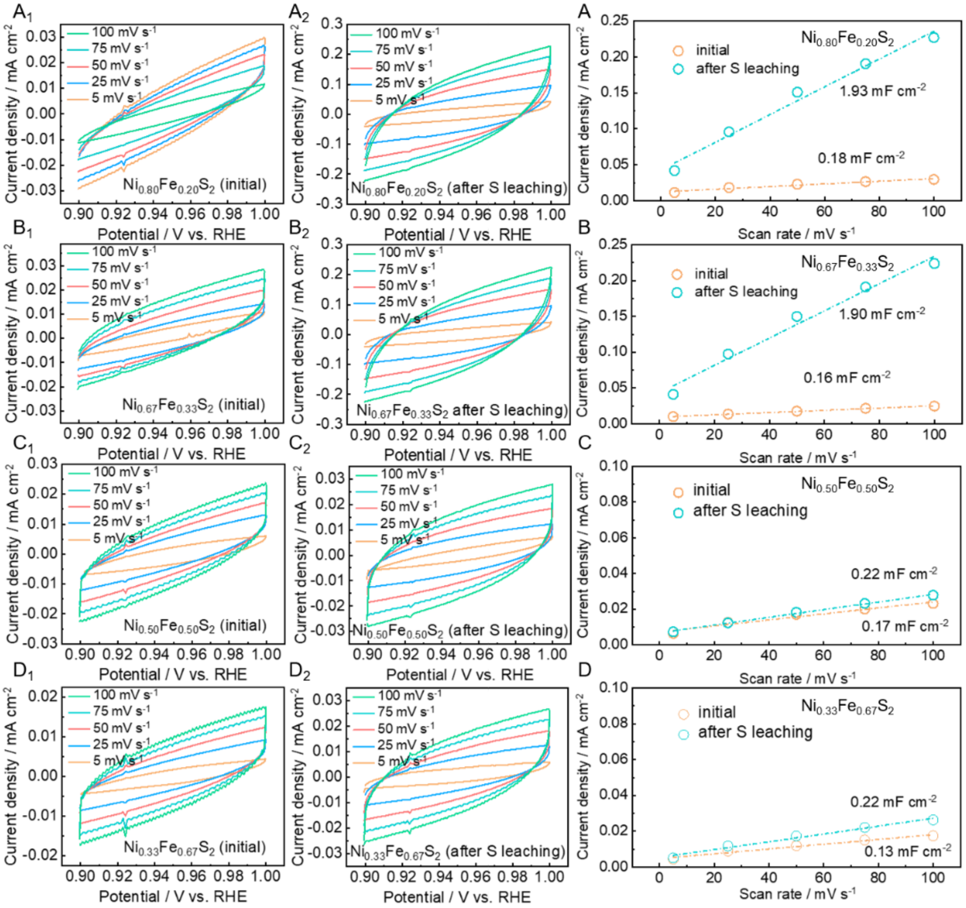

Figure 6.13 ECSA of $Ni_xFe_{1-x}S_2$ in the potential range of 0.9-1.0 V vs. RHE at the scan rate of 5, 25, 50, 75, 100 mV s^{-1}: (A_1-D_1) before and (A_2-D_2) after S leaching, and (A-D) corresponding slopes with peak current density vs. scan rate.

To verify the increased effective area of the catalyst, HRTEM images of $Ni_{0.67}Fe_{0.33}S_2$ after sulfur leaching at 1.7 V for 1 h were captured. As shown in Figures 6.14A-C, after electrochemical activation, its octahedral morphology sacrifices into nanoparticles with the diameter of ca. 2-5 nm, accompanied by a large number of amorphous spacer regions, which agrees well with the greatly enhanced ECSA. However, it is hard to determine the inter-planar spacing of the derived catalysts (e.g. 0.16, 0.18, 0.19 nm) due to the similarity of transition metal sulfides, hydroxides and multiplicity of crystal planes.

According to the XRD results in Figure 6.15, the $Ni_{0.67}Fe_{0.33}S_2$ after sulfur leaching exhibits no extra peaks, indicating the (oxy)-hydroxides are amorphous, which agrees well with the reported literature that concluded the in-situ oxidized bimetallic OER catalyst formed amorphous NiOOH/FeOOH layers. Thus, in our case, the above inter-planar spacing could be more inclined to the sulfides that after partial sulfur leaching and still in the form of crystals. Such crystalline/amorphous interfaces also favor the OER process.

The OER performance enhancement after sulfur leaching can be attributed to i) suppressed R_Ω (internal resistance is compensated) and R_{ct} for better charge transfer efficiency, ii) greatly enhanced ECSA (10 times higher) for fully exposed active sites, iii) crystalline/amorphous interfaces with rich defects and absorbed SO_4^{2-} for better OH^- adsorption and the formation of more active NiOOH with Fe doping and sulfur residues for the best activity at each site.

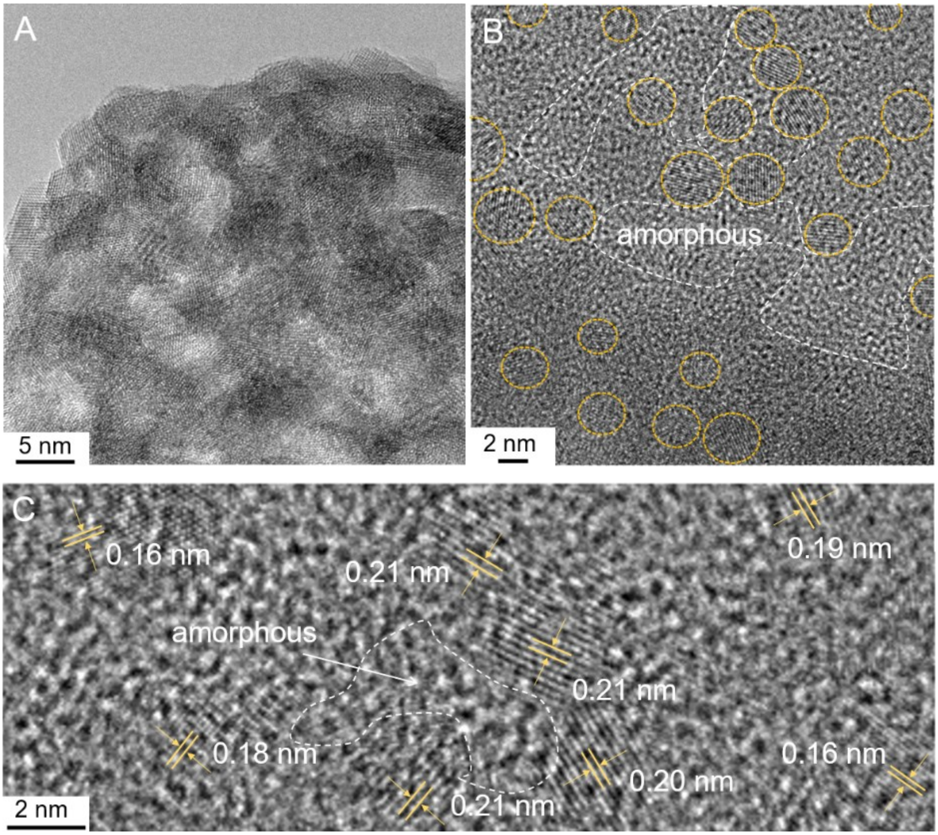

Figure 6.14 (A-C) HRTEM of $Ni_{0.67}Fe_{0.33}S_2$ after electrochemically assisted sulfur leaching at 1.7 V for 1 h.

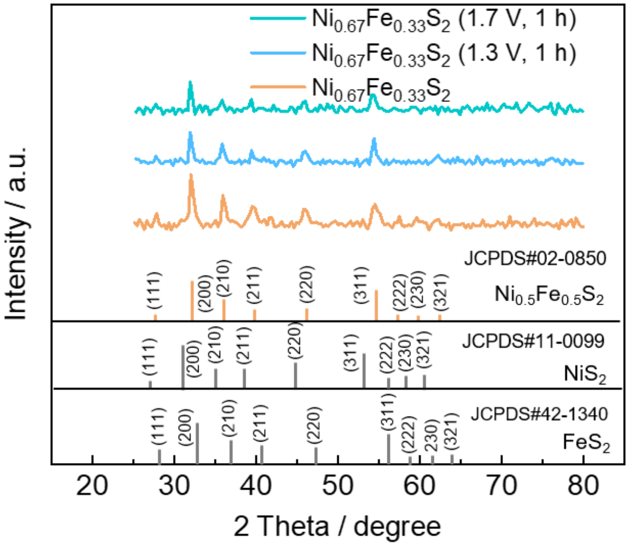

Figure 6.15 XRD of $Ni_{0.67}Fe_{0.33}S_2$ *before and after electrochemically assisted sulfur leaching at the cell voltage of 1.7 V for 1 h.*

After activity control by adjusting cation ratios, the anions were further optimized. As can be seen in Figure 6.16A, Na_2S, Na_2S_2, Na_2S_3, Na_2S_4 (stoichiometric ratio, not pure solutions of polysulfides, which always keep equilibrium among S^{2-}, S_2^{2-}, S_3^{2-}, S_4^{2-}, S_5^{2-}…) were prepared by dissolving Na_2S into D.I. water and its polymerization with elemental sulfur.[94] Then the $NiFeS_x$ with the Ni/Fe ratio of 2:1 was prepared by co-precipitation with among Ni^{2+}, Fe^{2+} and S_x^{2-} ions, and then 2 h hydrothermal treatment for crystallization and purification. Figure 6.16B shows the XRD patterns of $NiFeS_x$ prepared by different polysulfide precursors. It is found that with lower sulfur content (Na_2S_2), there will be completely distinctive phases. Meanwhile that prepared by polysulfides (Na_2S_3-Na_2S_4) all consist of the phase structure of $Ni_{0.67}Fe_{0.33}S_2$.

Higher S content not change the main outputs but the morphology, crystallinity etc., which affect OER performance. As shown in Figures 6.16C-F, i) the performance of the catalyst prepared by Na_2S before and after sulfur leaching is quite close, and the charge transfer resistance keeps almost unchanged; ii) The performance after sulfur leaching is lower than that of initial state, with increased charge transfer resistance; iii) The performance after sulfur leaching is also lower than that of initial state, with further increased charge transfer resistance.

Here are two reasons behind the above performance: i) The ink for that prepared by Na_2S_2 is very uniform and stable (like a thin film) on glass carbon electrode just comparable with Pt/C, while other three catalysts are extremely poor in distribution with aggregation and large particles; ii) The chemical and phase structures differences cause distinctive surface reconstructions.

Therefore, too much sulfur hinders the charge transfer process, while too little sulfur causes the low crystallinity and different phase compositions, and Na_2S_2 is the best anion precursor.

To support the positive effect of Fe doping, the performance of NiS_2/FeS_2 by mechanical mixing of pure NiS_2 and FeS_2 with the same ratio of 2:1 as $Ni_{0.67}Fe_{0.33}S_2$ was compared. As shown in Figure 6.17, the NiS_2/FeS_2 (2:1) exhibits improved performance with the overpotential of 323 mV@10 mA cm^{-2} than that of pure NiS_2 (350 mV) and FeS_2 (419 mV), indicating the strategy of phase engineering of $NiS_x/Ni(OH)_2/NiOOH$ in Chapter 5 is applicable in bimetallic catalyst. And the NiS_2/FeS_2 (2:1) derived $NiS_x/FeS_x/Ni(OH)_2/Fe(OH)_3/NiOOH/FeOOH$ is better in OER performance with the formation of Fe-doped NiOOH, thus higher performance (323 mV) than that of $NiS_x/Ni(OH)_2/NiOOH$ (339 mV). However, the Fe doping in two-phase NiS_2/FeS_2 (2:1) derived catalyst is much less than that from bimetallic, single-phase $Ni_{0.67}Fe_{0.33}S_2$. Therefore, its performance (323 mV) is lower than $Ni_{0.67}Fe_{0.33}S_2$ (288 mV) that was fully pre-doped with Fe in the pre-catalyst.

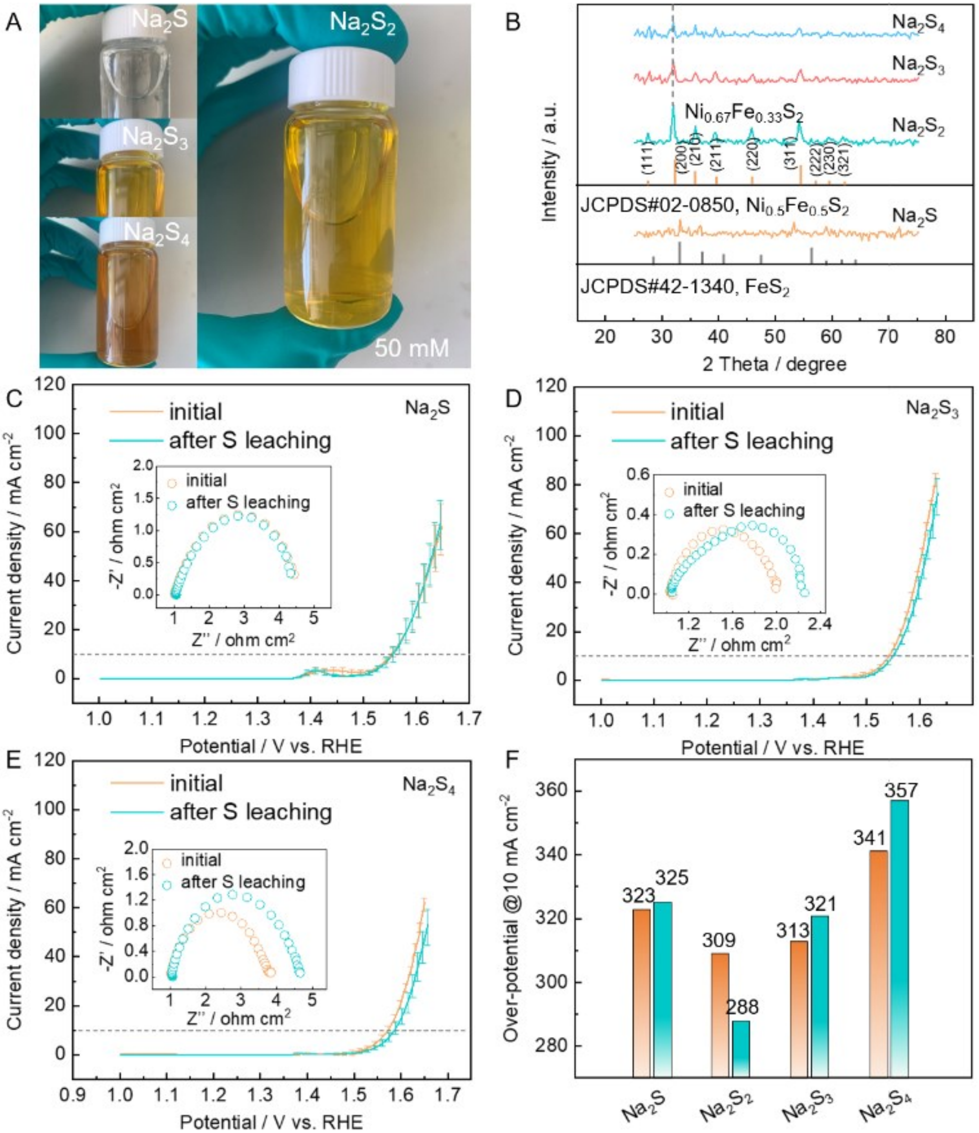

Figure 6.16 (A) Photos of sulfur precursors of Na_2S_x (x=1-4), and XRD results of corresponding Ni_xFe_{1-x} based sulfide compounds prepared by Na_2S_x (x=1-4) (B) XRD of $Ni_{0.67}Fe_{0.33}S_x$ catalysts prepared by the above sulfur precursors. (C) LSV curves and EIS results of the catalyst prepared by (C) Na_2S, (D) Na_2S_2 (E) Na_2S_4, and (F) summarized over-potentials at the current density of 10 mA cm^{-2}.

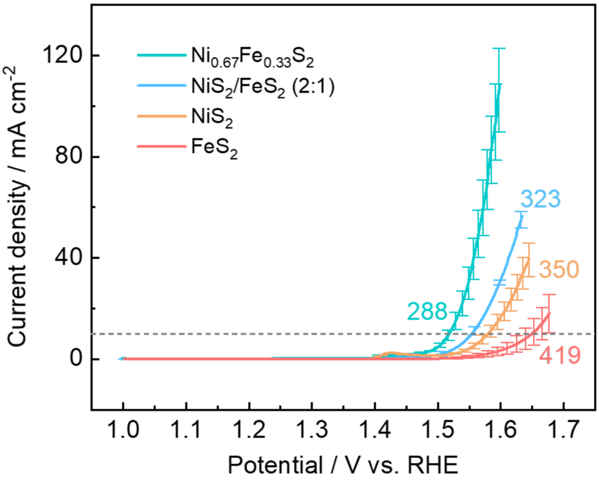

Figure 6.17 LSV of NiS_2/FeS_2 by mechanical mixing of pure NiS_2 and FeS_2 with the same ratio of 2:1 as $Ni_{0.67}Fe_{0.33}S_2$, NiS_2, FeS_2, and single-phase $Ni_{0.67}Fe_{0.33}S_2$.

6.1.4 Stability of $Ni_{0.67}Fe_{0.33}S_2$ in half cells

To screen the best catalyst with high activity and stability within $Ni_{0.80}Fe_{0.20}S_2$ and $Ni_{0.67}Fe_{0.33}S_2$, the LSV curves after sulfur leaching and 3000 CVs of the above two catalysts were compared in Figures 6.18A-B. The $Ni_{0.80}Fe_{0.20}S_2$ exhibits decreased performance from 290 mV after sulfur leaching to 300 mV after 1000 CVs, and further decreases to 308 mV after 3000 CVs, while that of $Ni_{0.67}Fe_{0.33}S_2$ performs much better from 293, 291, to 285 mV after sulfur leaching, 1000 and 3000 CVs, respectively. Moreover, the $Ni_{0.67}Fe_{0.33}S_2$ can further keep stable for 10000 CVs, as shown in Figure 6.19, without degradation. The degradation of $Ni_{0.80}Fe_{0.20}S_2$ can be attributed to the relatively higher solubility of $Ni_{0.80}Fe_{0.20}OOH$ than $Ni_{0.67}Fe_{0.33}OOH$ caused by the local pH changes during OER processes.

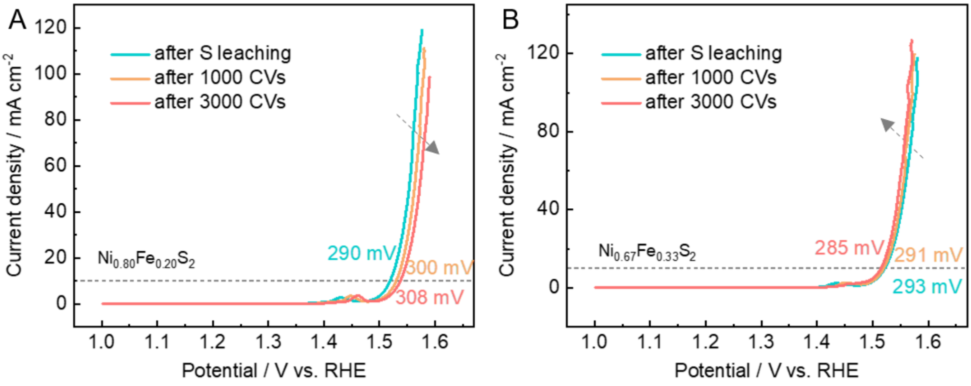

Figure 6.18 LSV curves of (A) $Ni_{0.80}Fe_{0.20}S_2$ and (B) $Ni_{0.67}Fe_{0.33}S_2$ before and after 1000 and 3000 CVs.

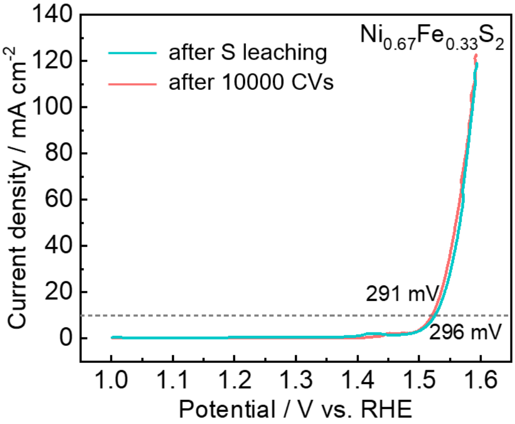

Figure 6.19 LSV curves of $Ni_{0.67}Fe_{0.33}S_2$ before and after sulfur leaching and 10000 CVs.

Therefore, the $Ni_{0.67}Fe_{0.33}S_2$ is screened as the best catalyst with the highest comprehensive performance due to the optimized cation and anion configurations. However, the half-cell performance is far from application, thus it should be further examined in the full cells for sulfur leaching, polarization curves and more importantly, stability tests under high current density of 1000 mA cm^{-2}.

6.2 Sulfur leaching of $Ni_{0.67}Fe_{0.33}S_2$ in full cells

The $Ni_{0.67}Fe_{0.33}S_2$ underwent sulfur leaching in the full cells. After temperature stabilization for 2 h and sulfur leaching, both iridium black and $Ni_{0.67}Fe_{0.33}S_2$ based cells were kept at a constant voltage of 1.7 V for 6 h, which is for cell conditioning to a stabilized state with a current error less than 1% for reliable polarization curves. During conditioning, the current density of the iridium black-based cell decreases from ca. 380 to 280 mA cm^{-2}, while that of the $Ni_{0.67}Fe_{0.33}S_2$ based cell increases from 550 to 700 mA cm^{-2} (Figure 6.20A), indicating better stability of the $Ni_{0.67}Fe_{0.33}S_2$ based cells at the conditioning stage. Then the current density of $Ni_{0.67}Fe_{0.33}S_2$ based cell further increases from 1326 mA cm^{-2} after 3 times of sulfur leaching to 2045 mA cm^{-2} after conditioning, indicating further performance improvement induced by the sulfur leaching of $Ni_{0.67}Fe_{0.33}S_2$ catalyst (Figure 6.20B, 5 mV s^{-1}).

As for side reactions, the Faradaic efficiency was tested by a water displacement method (Figures 6.20C-D). The initial Faradaic efficiency of $Ni_{0.67}Fe_{0.33}S_2$ based cells increases from 93.2% to 97.4% at the beginning and is much lower than that after conditioning ca. 97.7%, indicating side reactions of the sulfur leaching to sulfate ions occupied a small amount of current.

6.3 Long-term stability of $Ni_{0.67}Fe_{0.33}S_2$ in full cells

Before long-term test the $Ni_{0.67}Fe_{0.33}S_2$ was compared with iridium black (with same mass loading of 1 mg cm^{-2}) in single cells for their preliminary comparison of stability. The relatively short-term test (Figure 6.21A) shows that $Ni_{0.67}Fe_{0.33}S_2$ based cells are highly stable, showing an initial cell voltage of 1.79 V and low voltage increase rate of 0.20 mV h^{-1} for 20 h, while that of iridium-based cells are 2.00 V and 0.43 mV h^{-1} for 10 h, respectively. The iridium is highly unstable and was fully washed out into the electrolyte with almost no residue on the electrode surface (Figure 6.21 B), while $Ni_{0.67}Fe_{0.33}S_2$ is still attached on the electrode, indicating much better stability of $Ni_{0.67}Fe_{0.33}S_2$.

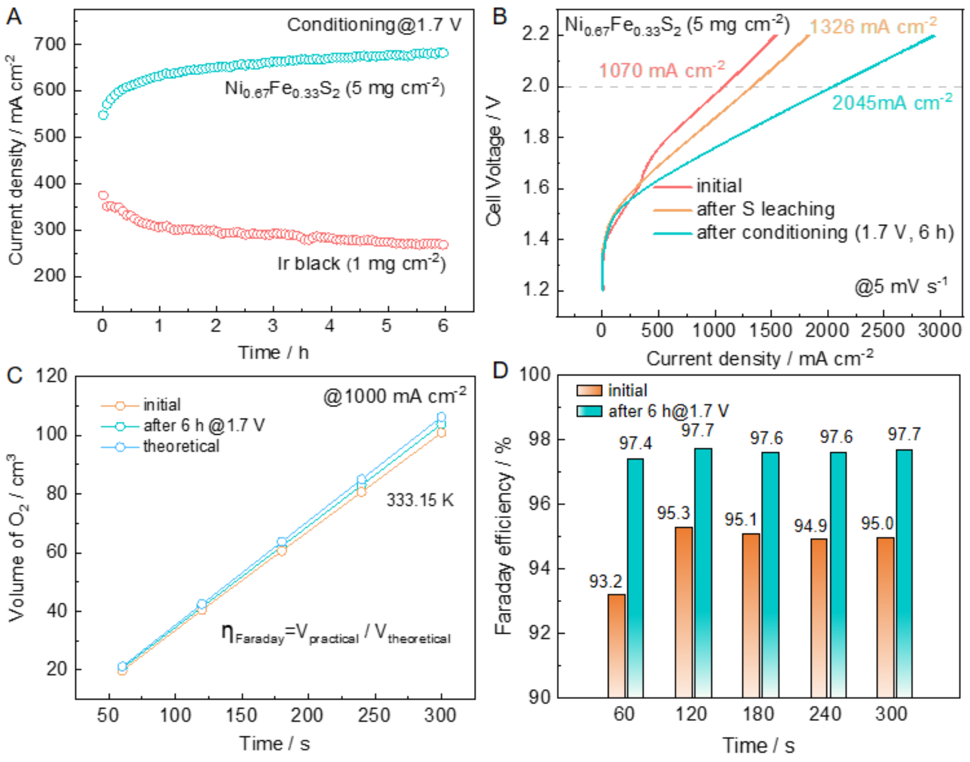

Figure 6.20 (A) Conditioning curves at 1.7 V for 6 h and (B) polarization curves of the NiS_2/Ni_3S_4 based cells Pt/C@C paper (cathode)||FAA-3-50||NiS_2/Ni_3S_4 or Ni/NiO (anode) after 3 times of sulfur leaching and conditioning. (C) Calculated and tested volume of O_2 at the current density of 1000 mA cm^{-2} before and after conditioning and (D) Faraday efficiency calculated by the ratio of practical/theoretical volume from the graph (C).

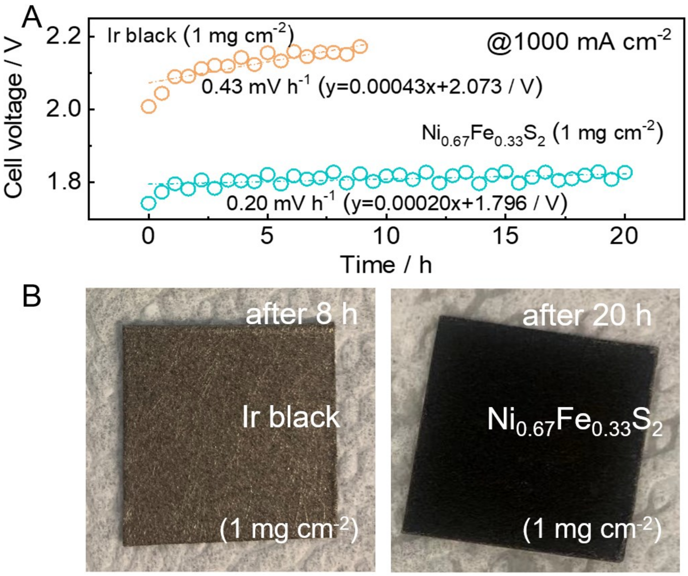

Figure 6.21 (A) Short-term stability curves of iridium black and $Ni_{0.67}Fe_{0.33}S_2$ based cells with the mass loading of 1 mg cm^{-2} at 1000 mA cm^{-2}. (B) Photos of iridium black and $Ni_{0.67}Fe_{0.33}S_2$ coated on the Ni fiber.

Considering the low cost of $Ni_{0.67}Fe_{0.33}S_2$, we improved its mass loading to 5 mg cm^{-2} for long-term stability tests. As shown in Figure 6.22A, $Ni_{0.67}Fe_{0.33}S_2$ based cells are highly stable, showing an initial cell voltage of 1.79 V (1.84 V for NiS_2/Ni_3S_4-based cells) and low voltage increase rate of 0.12 mV h^{-1} for 550 h. The polarization curves before and after 550 h are shown in Figure 6.22B, the current density of $Ni_{0.67}Fe_{0.33}S_2$ based cell decreases from 2000 mA cm^{-2} to 1600 mA cm^{-2}.

After membrane refreshing, the performance recovered to 1914 mA cm^{-2} (Figure 6.22C), which is similar as that in NiS_2/Ni_3S_4 based cells caused by increased membrane resistance. Then the cell was opened and it is found that the membrane was fully damaged by mechanical pressure and high temperature, while $Ni_{0.67}Fe_{0.33}S_2$ was still stable (Figure 6.22D), also supported by the SEM images after 550 h (Figure 6.23).

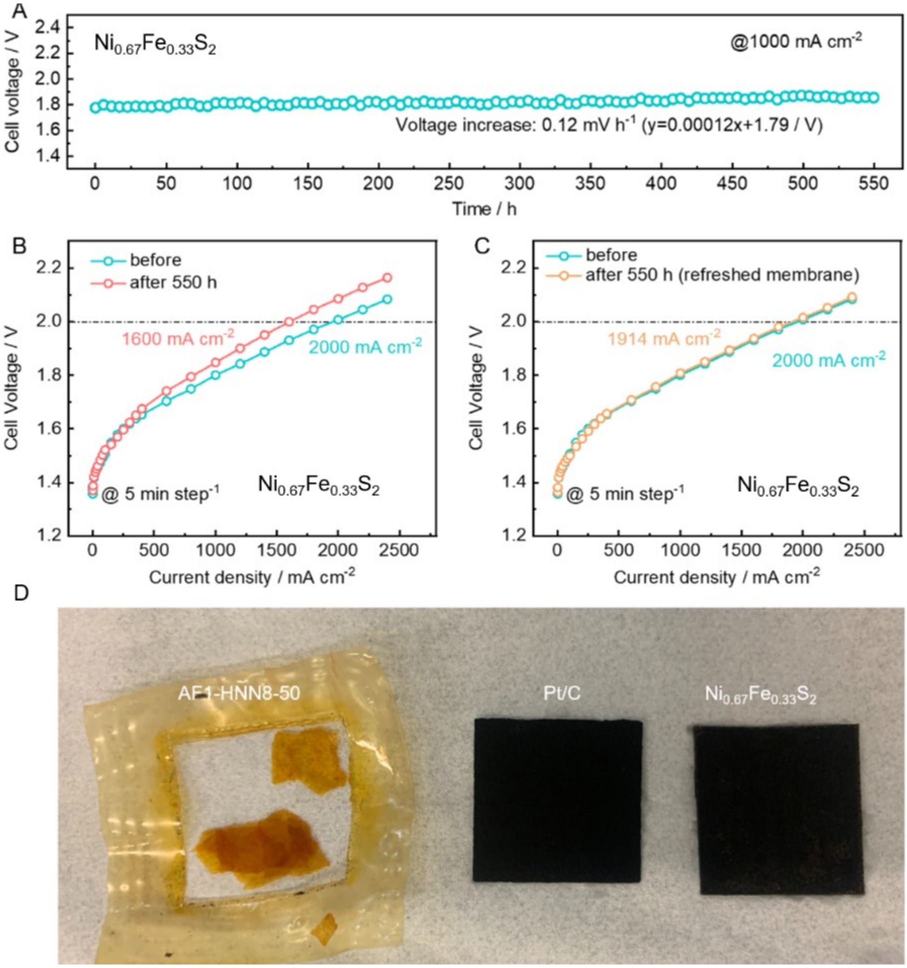

Figure 6.22 (A) Stability curves of $Ni_{0.67}Fe_{0.33}S_2$ based cells at 1000 mA cm^{-2} for 550 h with the mass loading of 5 mg cm^{-2}. (B) Polarization curves before and after 550 h, and (C) after membrane refreshing. (C) Photos of the AF1-HNN8-50 membrane, Pt/C, and $Ni_{0.67}Fe_{0.33}S_2$ coated on the Ni fiber after 550 h.

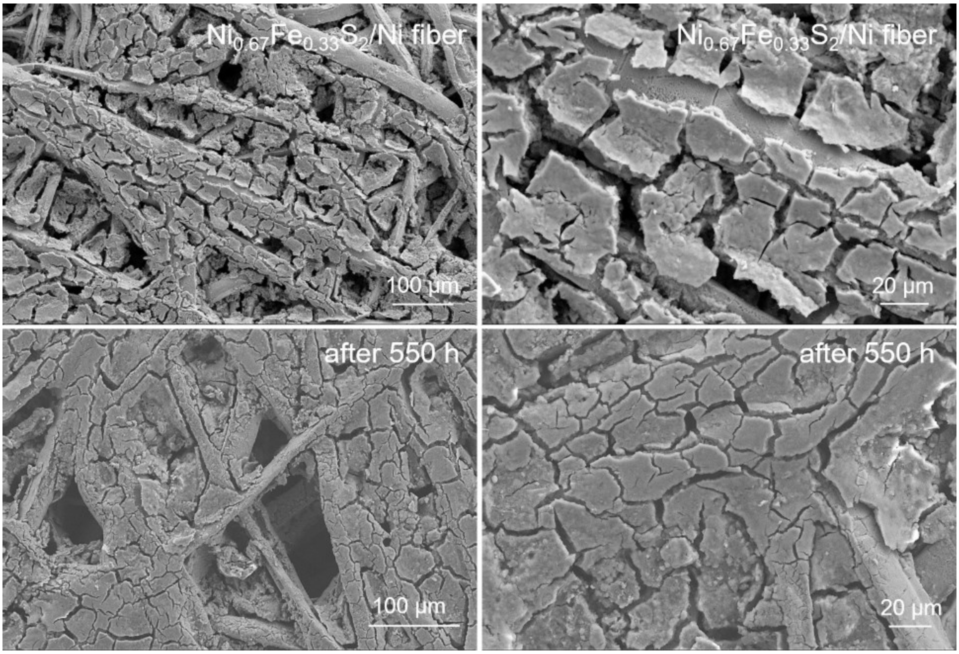

Figure 6.23 SEM of $Ni_{0.67}Fe_{0.33}S_2$@Ni fiber before and after 550 h at 1000 mA cm^{-2} with different magnifications.

The stability of $Ni_{0.67}Fe_{0.33}S_2$ based cell is quite similar to that of NiS_2/Ni_3S_4 based cells. Therefore, here could be some other intrinsic reasons for performance degradation: i) both electrode and membrane are still working independently, but the membrane-electrode interface could be poisoned by by-products like $K_2CO_3/KHCO_3$ (produced by CO_2 reacting with KOH in long-term run, the solubility of which in 1 M KOH is quite low, thus precipitating as particles), which increased the internal resistance (we mistakenly believe that this is an increase in the internal resistance of the membrane). When we refreshed the membrane, the interface was also renewed, and then the cell performance recovered. However, the membrane was always broken into small pieces, or even particles, which was hard for characterization to support the interface damage.

Therefore, future work should be focused on the comprehensive analysis of the degradation of cell performance, especially interests in the membrane electrode assembly (MEA) interfaces and electrolyte contamination.

6.4 Summary of $Ni_{0.67}Fe_{0.33}S_2$ based catalyst

$Ni_{0.67}Fe_{0.33}S_2$ nano-octahedrons were synthesized by a two-step of precipitation and recrystallization method with well-controlled cation and anion configurations. It was proved that Fe preferentially precipitated with sulfur and was gradually replaced by Ni, and finally formed a nanooctahedral structure through atomic diffusion. Then the $Ni_{0.67}Fe_{0.33}S_2$ was further stabilized by a multi-step sulfur leaching process to more active $NiFeS_x/NiFe(OH)_x/NiFeOOH$ heterostructure as intrinsic species for OER with 10 times higher ECSA and greatly enhanced activity of 288 mV at 10 mA cm^{-2}, and 10000 CVs cycling stability, which is much better than $NiS_x/Ni(OH)_2/NiOOH$ heterostructure derived from NiS_2/Ni_3S_4.

More importantly, the stabilized $NiFeS_x/NiFe(OH)_x$ catalyst from $Ni_{0.67}Fe_{0.33}S_2$ exhibits stable performance for not only 100 h@1.6 V in a half cell, but also 550 h@1000 mA cm^{-2} in full cells with lower initial voltage of 1.79 V than that of $NiS_x/Ni(OH)_2/NiOOH$ (1.84 V) with also negligible degradation rate, which further boosts TMS as promising anode catalysts for AEMWE.

The present work provides a better method for additive-free and large-scale synthesis of single-phase, bimetallic TMS catalysts, which better enhance OER performance than two-phase monometallic (NiS_2/Ni_3S_4) and bimetallic (NiS_2/FeS_2, 2:1) ones. And sulfur leaching was further extended from monometallic to bimetallic systems, which is highly universal and promising for activation and stabilization of TMS and also can be further extended to phosphide, boride, and nitride etc.

7 Optimization of single-cell performance

7.0 Preface

1. The research gap between Chapter 5-6 and Chapter 7:

Cell-configuration optimization and operation modes/testing conditions also have great impacts on the cell performance. For example, Niaz et al. tested the cells based on $NiFe_2O_4$//Sustainion X37-50//NiFeCo alloy//1 M KOH in short and long periods, concluding that long-term operation is beneficial to stability.[116] Moreover, the mechanical pressure imposed on the electrochemical devices is one of decisive factors for their performance, which has been confirmed in lithium-ion batteries, fuel cells and redox flow batteries.[117-120]

Unfortunately, most of the literature related to AEMWE hardly mentioned the mechanical pressure imposed on the cell, which however directly affects crucial steps such as R_{Ω}, R_{md} and R_{ct} etc., thus posing remarkable effects on the cell performance (e.g. polarization curves, stability, hydrogen permeation and even short circuit etc.). Even though a few papers mentioned the potential effects of mechanical pressure, there is no in-depth study of the mechanical pressure effects on the changes of electrodes and the relationship of cell assembly, mechanical pressure distribution and cell performance. For example, by removing the gasket from the cathode, Xu et al. found that the potential of both anode and cathode changed, and this linkage was attributed to the change of internal mechanical pressure.[121] However, the authors did not deeply study the effects of mechanical pressure on the properties of electrodes such as thickness, morphologies, hydrophilicity, resistance and corresponding full-cell stability. Additionally, a big difference occurs in cell performance among different research groups even with the same benchmark materials, caused by incomparable conditions like unquantified mechanical pressure. Moreover, PTFE-electrode thickness gaps and the corresponding quantified mechanical pressure have hardly been provided, yet non-negligible details for mechanical pressure distributions. Therefore, an in-depth understanding of the mechanical pressure effect on the performance of AEMWE is urgently needed.

In this chapter, mechanical pressure is quantified by converting imposed torque (N·m) into mechanical pressure distribution through an in-situ tracking method to describe the mechanical pressure acting on the central area of the MEA. Afterwards, the "thickness gap" between PTFE and electrodes (Δd) that works together with mechanical pressure is also discussed to provide researchers with references for MEA sealing. Moreover, mechanical pressure-dependent cell performance based on three membranes with different thickness is comprehensively studied to elucidate the effects of mechanical pressure on contact resistance, mass and charge transfer processes, and gas crossover etc. (Figure 7.0), thus maximizing the polarization performance, and ensuring the safety (<2% H_2 in O_2) and stability as well. Ultimately, an overall better option of cell assembly was recommended to achieve the best comprehensive performance. This chapter provides researchers, practitioners with a reference to build up benchmarks and to optimize cell performance.

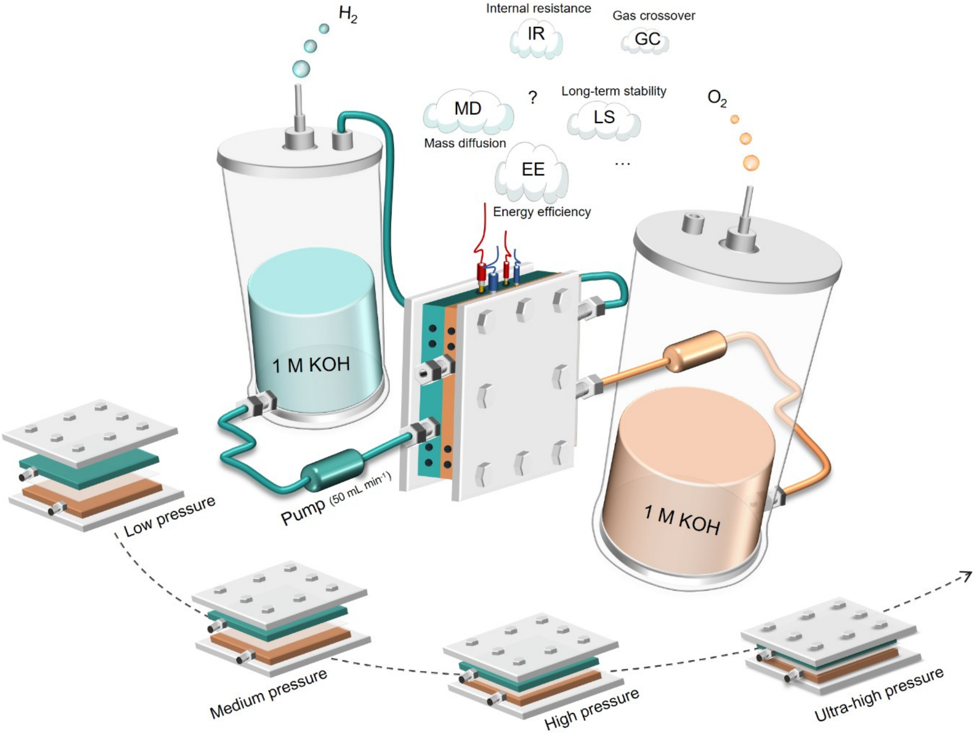

Figure 7.0 Schematic illustration of main effects of "mechanical pressure" from low, medium, and high to ultra-high mechanical pressure on cell performances in 1 M KOH, including internal resistance (IR), mass diffusion (MD), long-term stability (LS), gas crossover (GC), and energy efficiency (EE) etc.

It is worth mentioning that all the cell tests in Chapter 5-6 are operated under mechanical pressure-free conditions, which means zero thickness gap (Δd) between the electrode and the gasket of poly-tetra-fluoroethylen (PTFE) that causes high internal resistance, which needs further enhancement by optimization of mechanical pressure (Chapter 7).

2. The main goals of Chapter 7:

i) Control and quantify mechanical pressure imposed on the cells via adjustment of Δd and a well-designed "mechanical pressure tracking" method.

ii) Discuss the effect of mechanical pressure on internal resistance and charge transfer resistance of the cells, and the structural changes of porous electrode before and after mechanical pressure treatment.

iii) Benchmark and optimize the thickness gap (Δd) between the electrode and PTFE for achieving the best comprehensive cell performance with standard all commercial materials: Pt/C (cathode)//AEM//Ir black (anode).

iv) Discuss the interaction between membrane thickness and different mechanical pressure, and corresponding cell performance. Also, study the influence of mechanical pressure on hydrogen crossover, stability and mass diffusion processes.

v) Extend from standard anode catalyst (Ir black) to synthesized $Ni_{0.67}Fe_{0.33}S_2$ for optimized cell performance.

Overall, the main storyline follows: i) the control, quantification of mechanical pressure; ii) mechanical pressure effects on physical properties of electrodes; iii) corresponding cell performances of compressed electrodes, including steady-state polarization, stability, mass diffusion, gas crossover etc.; iv) summary of recommended parameters for cell assembly and its application for $Ni_{0.67}Fe_{0.33}S_2$ based cells.

7.1 Control and quantification of mechanical pressure

The first step is to control and quantify the mechanical pressure distribution. As shown in Figure 7.1A, the cell is fixed by a stabilizer, and the specific mechanical pressure imposed by torque controller (up to10 N·m) on eight screws is highly related to the PTFE-electrode gaps (top right, cross section of the cell). Therefore, their initial values are denoted as d_1 (cathode) and d_2 (anode), and the total gap from both sides is denoted as $\Delta d= d_1+d_2$, which is in the range of 0-300 μm with the increment of 100 μm. To simplify the control conditions, d_1 and d_2 are set as "equal" ($d_1=d_2$). It is noteworthy that the definition of initial Δd refers to the total gaps under "mechanical pressure-free" conditions, facilitating the reproduction of cell assemblies, which will decrease after compression but not affect the repeatability.

The cell for mechanical pressure tracking is assembled in accordance with the above Δd configuration and the torque of 10 N·m by step-by-step mechanical pressure application to the diagonal screws. Then, the footprint of mechanical pressure will be recorded by three thin foils in MEA zone with sensitivity to different mechanical pressure ranges (0-10 MPa), and then their distributions can be obtained after post-scanning, -fitting and analysis. With Δd increasing from 0 to 300 μm, the corresponding cell conditions are denoted as low mechanical pressure (Δd=0 μm), medium (Δd=100 μm), high (Δd=200 μm), and ultra-high (Δd =300 μm), respectively (Figure 7.1B).

Then the tracked mechanical pressure distributions are presented in Figure 7.1C with color mapping in three ranges. It is clear that the area with the highest mechanical pressure is concentrated on the outside of the screw (up to 10.0 MPa), and the lowest lies in junction zones around MEA-PTFE borders (hollow area) with mechanical pressure ca. 0 MPa caused by electrode-PTFE gaps, indicating cell assembly by crews causes stress concentration and uneven distributions. The mechanical pressure decreases with increasing distance from the screw and presents the characteristic of annular distribution. The mechanical pressure exerted on the MEA is also not evenly distributed due to non-planar contact between electrodes and bipolar plate with electrolyte channels. The mechanical pressure in the solid region of the channels is much greater than that in the hollow parts. Thus, the mechanical pressure in the solid region is considered as the real mechanical pressure on MEA for convenience, while that on hollow region can be used for the description of electrode invasion.

Notably, Δd plays a decisive role in mechanical pressure and its distribution in single cells. Due to the non-uniformity of mechanical pressure distribution, it is estimated with a rough range, but Δd do have a significant effect as follows: $P_{\Delta d=0\ \mu m}$ (~0 MPa) < $P_{\Delta d=100\ \mu m}$ (0~0.5 MPa) < $P_{\Delta d=200\ \mu m}$ (1.0~2.0 MPa) < $P_{\Delta d=300\ \mu m}$ (5.0~6.0 MPa).

First, the cell assembled by Δd=0 μm shows negligible mechanical pressure on the central zone due to zero contact space and incompressibility of PTFE. In this case, low contact rate between the electrode and the bipolar plate may result in large contact resistance, while extended range of diffusion ions to the catalyst surface may also result in high charge transfer resistance, which will be proved in single-cell tests.

Second, with Δd=100 μm, the mechanical pressure increases to ca. 0~0.5 MPa and also not uniformly distributed, which may be caused by the uneven distribution of electrode thickness that will be proved by surface roughness distribution of the electrode in the physical characterization parts. Therefore, the electrode should be fully cleaned and smoothed to remove surface absorbed particles or oxidized species. Also, it is necessary to preload and reload the torque (first assemble the cell, then open the cell, and then reassemble the cell) to alleviate the roughness effects of the electrodes for better mechanical pressure distribution.

Thirdly, with Δd=200 μm the mechanical pressure increases to ca. 1.0~2.0 MPa and the mechanical pressure is fully printed on the foils, with the mechanical pressure of ca.1.0 MPa. The mechanical pressure exhibits a regular alternating distribution from solids to channels, which is determined by the geometry of the serpentine flow channels, indicating that the electrode is in close contact with the bipolar plate. In this case, the electrodes slightly intrude into the interior of the channel, causing a small stress concentration.

Then, the mechanical pressure further increases with increasing Δd from 200 to 300 μm, following a non-linear relationship with sharply increased mechanical pressure from 1.0~2.0 to 5.0~6.0 MPa. When Δd=300 μm, the mechanical pressure of the solid part increases to 5.0~6.0 MPa, which is close to the mechanical pressure on the outer layer around the screw. Meanwhile the mechanical pressure of channel areas (green) keeps stable but more continuous at ca. 1.0 MPa, indicating that electrode invades more into electrolyte channels than that with lower mechanical pressure (Δd=200 μm). High electrode intrusion rate reduces mass transfer efficiency and causes serious bubble issues especially at high current density, which will be further clarified in cell testing parts.

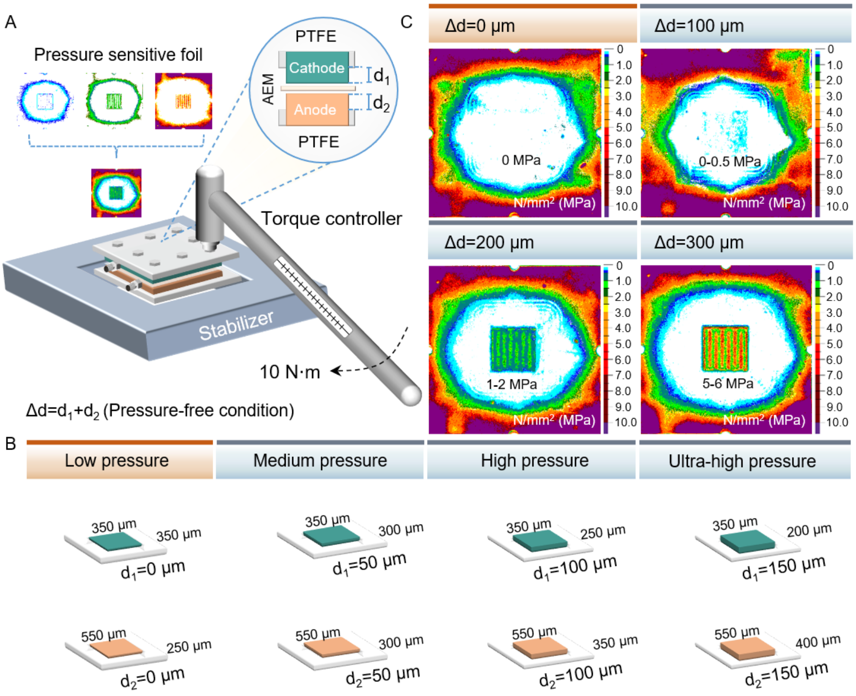

Figure 7.1 (A) Cell assembly by 10 N·m for each screw applied by torque controller, and the total difference in thickness between PTFE-anode (d_1) and PTFE-cathode (d_2) is denoted as $\Delta d=d_1+d_2$. (B) Correspondence between relative mechanical pressure and Δd: low mechanical pressure (Δd=0 μm), medium mechanical pressure (Δd=100 μm), high mechanical pressure (Δd=200 μm), and ultra-high mechanical pressure (Δd=300 μm). (C) Practical mechanical pressure distribution around the electrodes/flow channels and screws with color bar prepared by Δd from 0, 100, 200, to 300 μm.

7.2 Mechanical pressure effects on physical properties

After compression above, the physical properties of the electrodes have undergone great changes. First, the electrode thickness decreases by 2.86% (cathode) and 8.35% (anode), indicating Ni-based anode substrate is more sensitive to mechanical pressure than carbon-based cathode substrate (Figure 7.2A). Another possible reason could be that the total thickness of anode is 200 μm greater than that of the cathode, which has more space for compression. The error bars for both thickness variations decrease with increasing mechanical pressure due to surface roughness and decreased space for thickness variation.

Then the (bulk+contact) resistance (R_{b+c}) was tested in a sandwich-like cell configuration (cupper plate/electrode/cupper plate) with the applied current of 15 A to outshine the undetectable voltage, which is described in Chapter 4 in detail. Since the bulk resistance of the electrode is also affected by the mechanical pressure and all of the resistance has an impact on the cell performance, we consider it and the contact resistance as a whole, which will not affect the trend of the resistance.

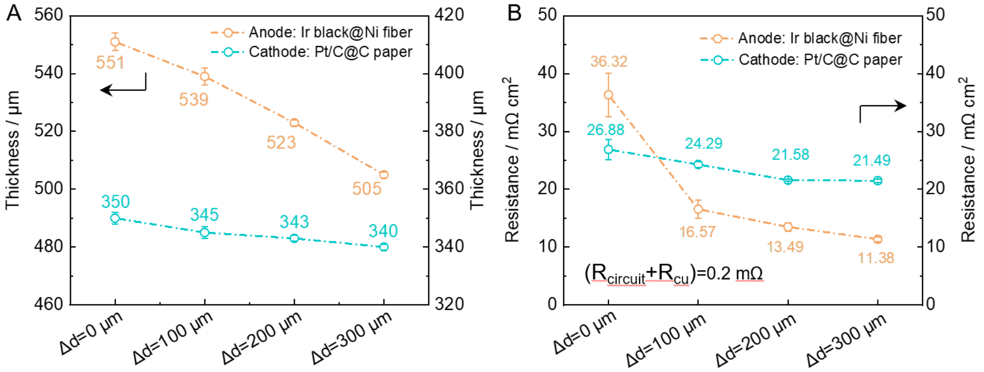

Figure 7.2 (A) Thickness changes of anodes (yellow dotted line, left, with 1 mg cm^{-2} Ir coated on nickel fibers) and cathodes (green dotted line, right, with 0.8 mg cm^{-2} Pt on carbon papers) after cell assembly with Δd from 0, 100, 200, to 300 μm. (B) Bulk and contact resistance (BCR) of both anodes and cathodes calculated by Ohm's Law and calibrated by internal resistance of circuit and Cu.

Similarly, the R_{b+c} of anode is also more sensitive than cathode to mechanical pressure effects, with a total decrease rate of 68.3% and 20.1% from Δd=0 to 300 μm, respectively. The R_{b+c} of the anode (Ir@Ni fiber) drops sharply by 54.4% from Δd=0 to 100 μm, while that of cathode (Pt/C@C paper) decreases only by 9.6%, indicating the type of substrate material and its thickness are key factors in the response to mechanical pressure (Figure 7.2B). The error bar of R_{b+c} follows the same rule of thickness, namely, continuous decrease with increasing mechanical pressure, caused by decreased surface roughness (Figure 7.3, the roughness decreases from 1200-1400 to 700-900 nm), which agrees well with uneven mechanical pressure distribution results (Δd=0, 100 μm). The surface conductivity of the electrode by atomic force microscope (AFM) shows that the improvement (Δd=0, 300 μm) is negligible (Figure 7.4), indicating the influence of mechanical pressure on contact resistance is much higher than that on surface area resistance. This is mainly caused by low conductivity of ionomer, and the difference of the electrode before and after compression is ignorable.

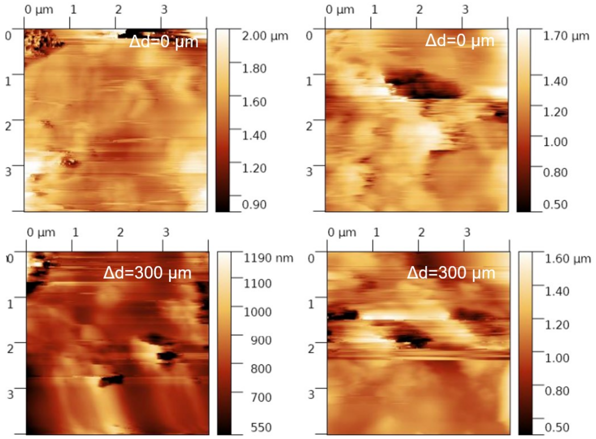

Figure 7.3 Atomic Force Microscope (AFM) images of surface roughness distribution of the electrodes prepared by Δd= 0 and 300 μm.

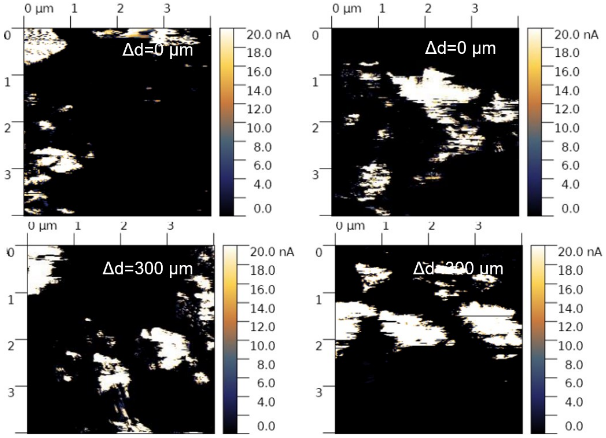

Figure 7.4 Surface conductivity distribution of the electrodes prepared by Δd= 0 and 300 μm.

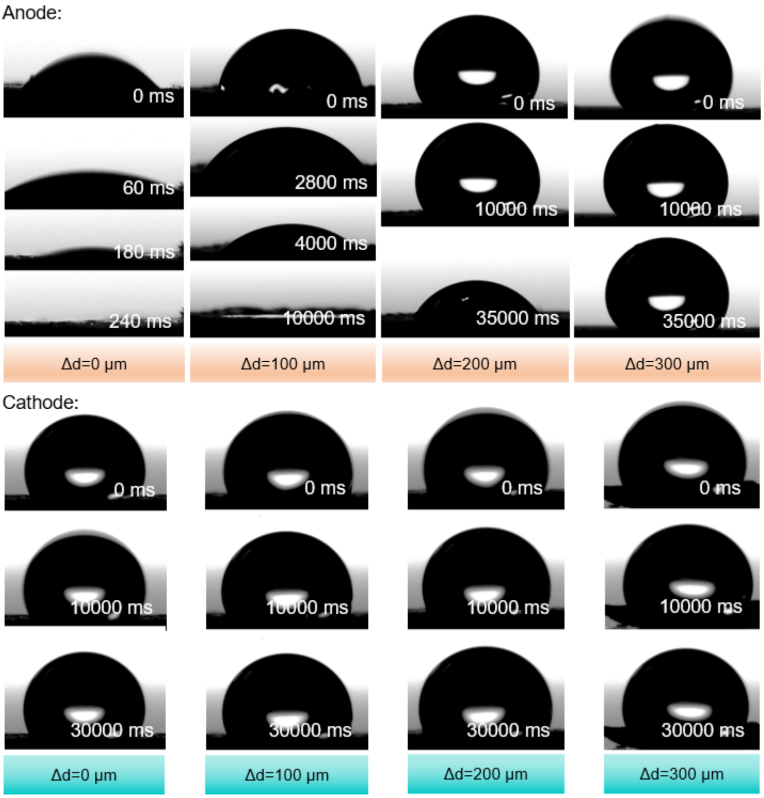

Figure 7.5 Water contact angle of anodes with Ir coated on the Ni fiber and cathodes with Pt/C coated on the carbon fiber, captured at different time.

In addition, the surface water contact behavior on the anode is also more sensitive than that on the cathode to mechanical pressure, which can be supported by contact angles before and after compression (Figure 7.5). The initial contact angles of the cathode and anode are 130±5°, 30±10°, respectively, indicating anode is more hydrophilic than cathode. The hydrophilicity of the anode decreases sharply from Δd=0 (240 ms, full wetting) to 300 μm (35000 ms, unwetting), while the cathode shows negligible difference, indicating the surface microstructure of anodes may change much more than cathode after different compressions. Therefore, considering the above results, we will focus more on anodes in the following discussion.

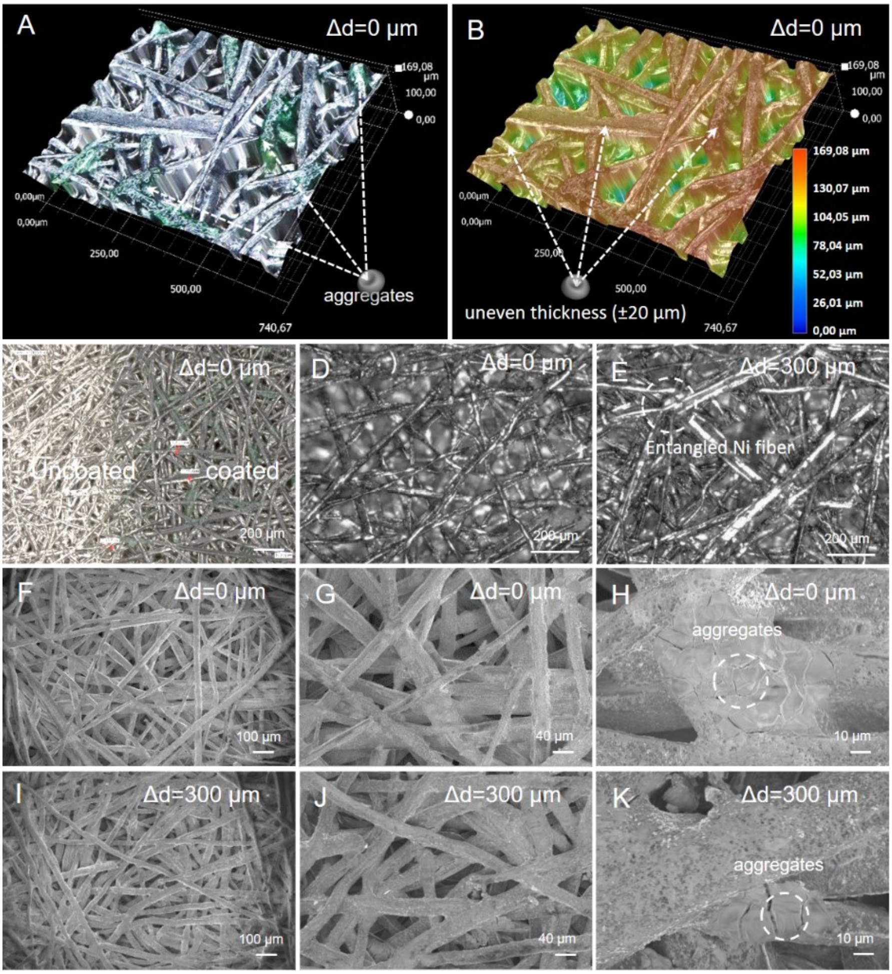

Figure 7.6 Digital microscope images of Ir coated nickel fiber prepared by Δd= 0 μm: (A) 3D surface morphology of ionomer and catalyst with the roughness distribution, (B) surface roughness with thickness distribution, and (C) 2D morphology comparison between coated and uncoated electrodes. Optical microscope images: (D-E) anodes prepared by Δd=0 and 300 μm, and SEM images: (F-H) anodes prepared by Δd=0 μm, and (I-K) Δd=300 μm with three different magnifications.

To understand the surface microstructure of the anode, its initial 3D profile was captured by a digital microscope. As shown in Figures 7.6A-B, Ir black and ionomer are unevenly distributed, with numerous of aggregates. Also, the surface of pristine Ir coated anode is extremely rough, the roughness of which changes from relatively thicker to thinner areas with an error bar of ±20 μm. Therefore, both catalyst-ionomer aggregates and large surface roughness could be highly sensitive to compression.

Then the microstructures of the anodes before and after compression were further captured by optical microscope and scanning electron microscope (SEM). After compression, some Ni fibers entangle together (Figures 7.6C-E) and the porosity decreases, thus increasing the bulk conductivity of the electrode.

Meanwhile, some catalyst-ionomer aggregates with large thickness on the surface are compressed or even crushed (Figures 7.6F-K), thus suppressing the contact resistance and hydrophilicity. Consequently, the microstructure changes of the anodes before and after compression, such as condensed and entangled Ni fibers and compressed catalyst-ionomer aggregates, provide explanations for sharp decreases of thickness/R_{b+c}/hydrophilicity.

7.3 Mechanical pressure effects on single-cell performance

After understanding mechanical pressure effects on the physical properties of electrodes, it is time to study their impacts on single-cell performance. Since AEMs retain in different thicknesses, we selected typical membranes with three different thicknesses (25, 50, 75 μm) to study the specific effects of mechanical pressure, namely AF1-HNN5-25, AF1-HNN8-50 and AF2-HWP8-75 in Table 1. Among them, AF1-HNN5-25 exhibits the lowest conductivity of 56±1 ($mS\cdot cm^{-1}$), while that of AF1-HNN8-50 (102±3 $mS\cdot cm^{-1}$) and AF2-HWP8-75 reinforced by polyolefin (close to 102±3 $mS\cdot cm^{-1}$) is nearly doubled.

Table 7.1 Properties of three anion exchange membranes involved in this study.

Membrane	Thickness (μm)	Ion Exchange Capacity [c] (meq OH^- g^{-1})	Reinforcement	Conductivity ($mS\cdot cm^{-1}$)
AF1-HNN5-25	25	1.4-1.7	no	56±1
AF1-HNN8-50	50	2.1-2.5	no	102±3
AF2-HWP8-75	75	2.3-2.6	polyolefin reinforced	-

7.3.1 Mechanical pressure effects on AF1-HNN5-25 based cells

Cell testing results based on AF1-HNN5-25 with different compression are shown in Figure 7.7. The polarization curves and specific current densities (Figures 7.7A-B) show that the current density of the cells with Δd=0 μm is only 219 mA cm^{-2} at 1.8 V and 509 mA cm^{-2} at 2.0 V, while the current density of the cells with Δd=100 μm is 401 mA cm^{-2} at 1.8 V, and 1017 mA cm^{-2} at 2.0 V. Electrochemical impedance spectroscopies (EIS) at three current densities of 10, 300 and 1000 mA cm^{-2} (Figure 7.7D-F) show that the AF1-HNN5-25 based cells are highly sensitive to mechanical pressure, and the enhanced performance is mainly caused by suppressed R_{Ω} and slightly decreased R_{ct}.

With further increased Δd=200 μm, the cell failed due to the membrane damage caused by electrode intrusion, which is also confirmed by a multimeter with nearly 0 V open-circuit cell voltage. To ensure the safety, hydrogen permeation/gas crossover (GC) was recorded during a short-term stability test at 1000 mA cm^{-2} (Figure 7.7C). With continuous increased voltage that caused by catalyst attenuation, GC of the cell is stabilized at 1.48%, indicating normal condition of the membrane and guaranteed safety for the cell (H_2 in O_2<2%).

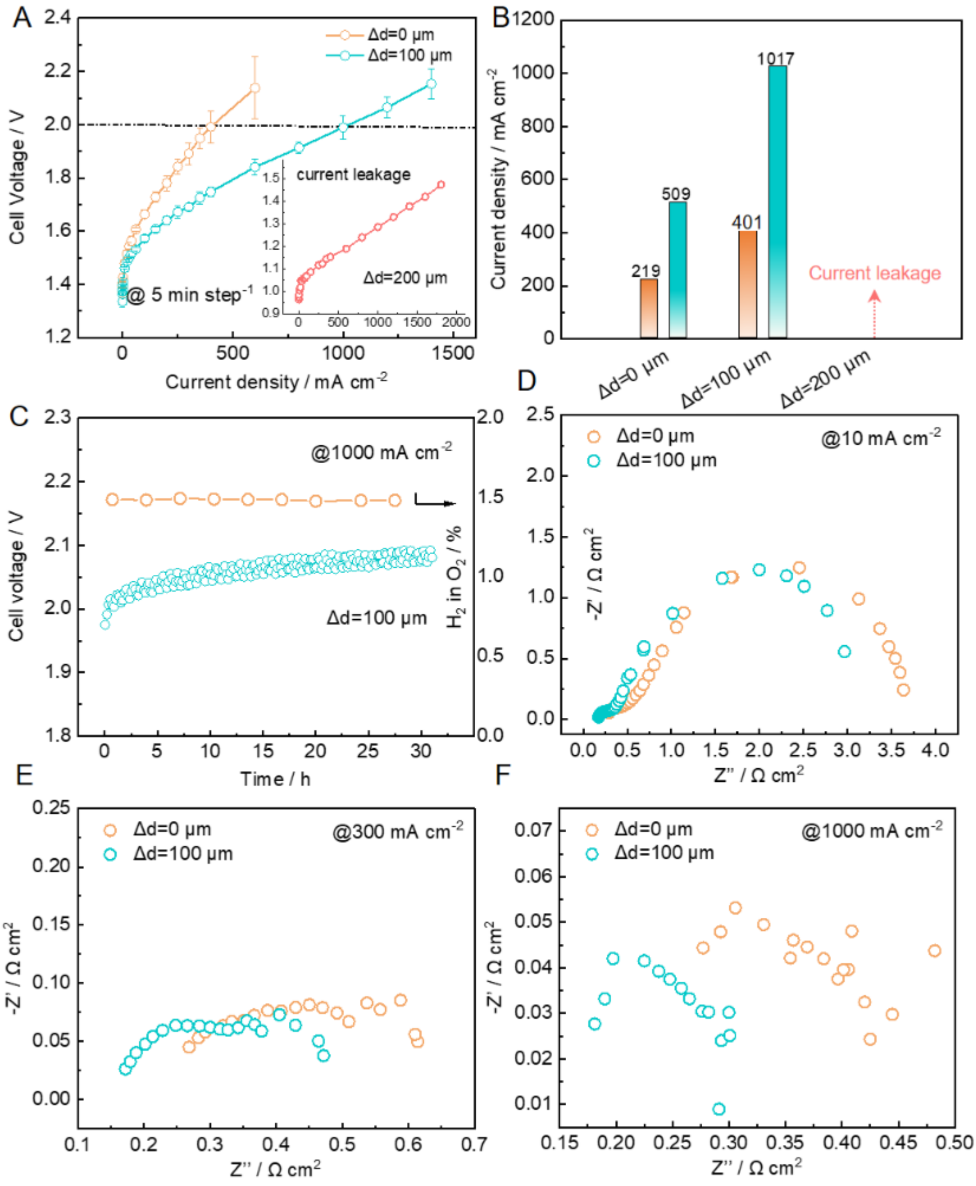

Figure 7.7 (A) Polarization curves of the cells based on Pt/C||AF1-HNN5-25||Ir black assembled by Δd=0, 100, and 200 μm (inset graph) for 5 min step^{-1}, (B) corresponding current density at 1.8 and 2.0 V derived from (A), (C) durability at 1000 mA cm^{-2} (green scatter, left) for 31 h and hydrogen concentration in oxygen (yellow dotted line, right), and (D-F) EIS curves at 10, 300 and 1000 mA cm^{-2}.

7.3.2 Mechanical pressure effects on AF1-HNN8-50 based cells

Then, the AF1-HNN8-50 membrane is further used to check effects of higher mechanical pressure (Δd=200, 300 μm) on the cell performance. As shown in Figures 7.8A-B, the current density of the cells exhibits similar improvement trends with Δd=0 increasing to Δd=100 μm, namely, 668 and 843 mA cm^{-2} at 1.8 V (1200 and 1640 mA cm^{-2} at 2.0 V). However, why the AF1-HNN8-50 based cells show lower performance improvements and seem less sensitive than AF1-HNN5-25 to mechanical pressure? It is due to much lower basic conductivity of the membrane of AF1-HNN5-25 than AF1-HNN8-50 (Table 1), causing much lower initial performance and thus providing space for improvements.

When further increasing the Δd to 200 μm, it is found that the cell performance is stabilized at ca. 1636 mA cm^{-2} without further improvements, which is attributed to the stabilized R_{Ω}/R_{ct}. With higher Δd from 200 to 300 μm, the cell performance decreases from 1636 mA cm^{-2} to 1500 mA cm^{-2}, which can be explained by sharply increased mechanical pressure from 1.0-2.0 to 5.0-6.0 MPa, resulting in poor gas/ions diffusion and much higher R_{md}. However, why the EIS results exhibit no big difference *(*Figures 7.8D-F) corresponding to distinctive polarization curves? It is because the EIS was tested after full relaxation, while each stage of polarization curves should be kept at constant current density for 5 min with more than 2 h (much higher bubble resistance) for each completed curve, which means EIS results are not the in-situ impedance spectrum corresponding to polarization curves.

To better distinguish the effect of different mechanical pressures on R_{md} and stability, we further kept cells at a high current density of 1000 mA cm^{-2} for 88 h. As shown in Figure 7.8C, mechanical pressure-free cells (Δd=200 μm) exhibit higher initial voltage (1.939 V) due to the highest R_{Ω}/R_{ct} among all conditions, but it is interesting that its voltage fluctuation is the lowest due to lower R_{md}, while all compressed cells exhibit lower gradually decreased initial voltage, namely, 1.856, 1.854 and 1.851 V due to the decreasing trend in R_{Ω}/R_{ct}. However, the voltage increase rates of the cells based on Δd=200 and 300 μm are much higher than that of the cells based on Δd=0 and 100 μm, indicating much higher "accumulated" bubble issues and hence high R_{md}.

Overall, the effect of mechanical pressure on cell performance not follow a single promoting trend: moderate mechanical pressure (Δd=100 μm) is beneficial to polarization via suppressing R_{Ω}/R_{ct} without promoting R_{md}, while excessive pressure (Δd=200/300 μm) greatly enhances R_{md}, thus reducing the stability.

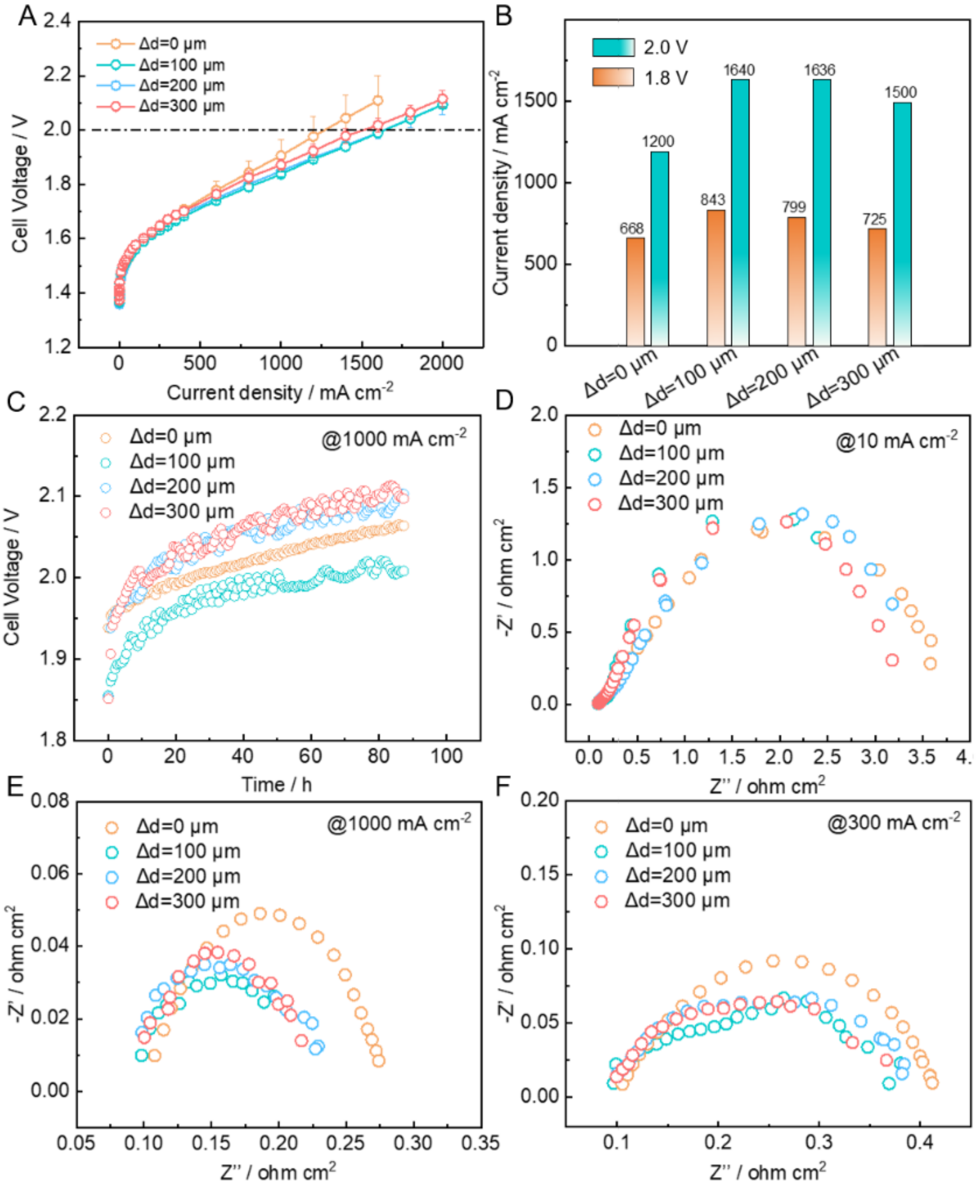

Figure 7.8 (A) Polarization curves of the cells based on Pt/C||AF1-HNN8-50||Ir black assembled by Δd from 0, 100, 200, to 300 μm by a galvanostatic method for 5 min step^{-1}, (B) corresponding current density at 1.8 and 2.0 V, (C) durability at 1000 mA cm^{-2} for 88 h, and (D-F) EIS curves at 10, 300 and 1000 mA cm^{-2}.

7.3.3 Mechanical pressure effects on AF2-HWP8-75 based cells

Thereafter, we move to the effect of mechanical pressure on AF2-HWP8-75 based cells, focusing on torque-caused effects from 5, 7, to 10 N·m. As shown in Figures 7.9A-B, the current density of the cells exhibits a slight improvement with the torque increasing from 5 to 7 N·m, namely, 625 and 776 mA cm^{-2} at 1.8 V (1205 and 1460 mA cm^{-2} at 2.0 V), while no further enhancement was observed with the torque increasing to 10 N·m, indicating 7 N·m is enough for suppressing R_{Ω}/R_{ct}.

To distinguish reversible degradation caused by accumulated bubble issues (R_{md}) and irreversible degradation caused by MEA attenuation (R_{Ω}/R_{ct}), the cells after polarization curves are further tested at 1000 mA cm^{-2} for ~14 h first, then stopped for 1 h under open circuit voltage, and then restarted and kept for ~10 h. The reversible and irreversible degradation are defined as (V_2-V_3), (V_3-V_1) respectively, which are described in detail in Figure 7.9D and corresponding summary in Figure 7.9E. Notably, 10 N·m is unsuitable for long-term stability test due to severe bubble issues and doubled reversible and irreversible degradation than that of "5 N·m-based" cells, while 7 N·m is a compromised choice for comprehensively higher energy efficiency. Hydrogen permeation (Figure 7.9C) of the above cells was also detected during stability test, showing a trend from 0.341% (5 N·m), 0.393% (7 N·m), to 0.677% (10 N·m) H_2 in O_2, which affects the stability from another perspective.

To examine the effect of mechanical pressure on the diffusion of bubbles in more detail, the galvanostatic intermittent titration technique (GITT) curves for the cells assembled by torques from 5-10 N·m were obtained through intermittent electrolysis/relaxation. As shown in Figure 7.9F, the voltage fluctuation continuously increases with higher torques, and "5 N·m" causes a relatively high internal resistance", while "10 N·m" greatly sacrifices stability as three times of the voltage increase rate (0.025 V h^{-1}) as that of "5 N·m" (0.008 V h^{-1}). Also, the pumping rates (Figure 7.10A) through both anode and cathode sides decrease with increasing mechanical pressure and corresponding images of anodes after cells testing with Δd=100 and 300 μm, further supporting the mass transport issues in cells with high mechanical pressure, as shown in Figures 7.10B-C.

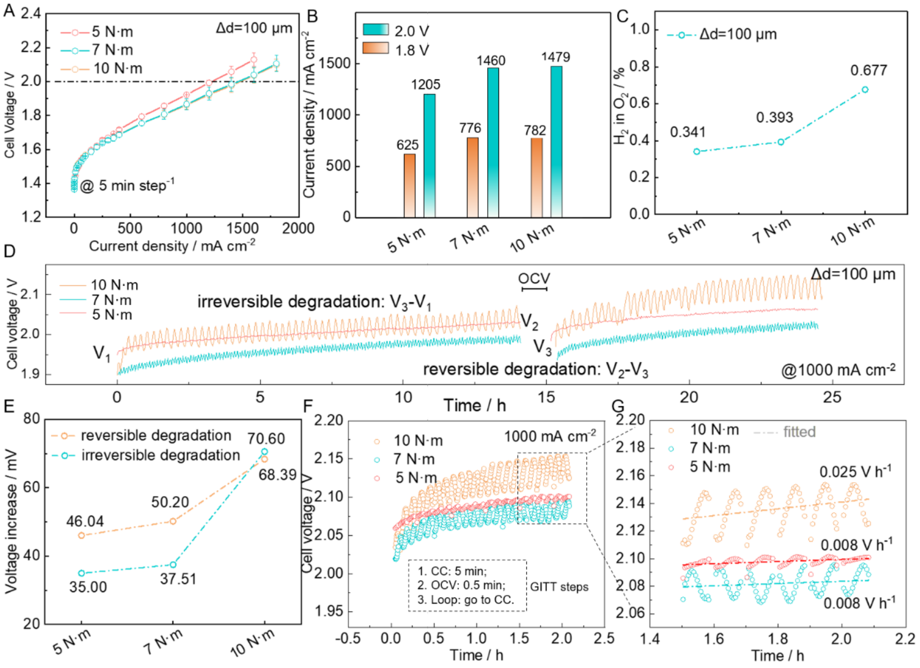

Figure 7.9 (A) Polarization curves of the cells based on Pt/C||AF2-HWP8-75||Ir black assembled by Δd=100 μm with different force arms (5, 7, 10 N·m), (B) current density at the cell voltage of 1.8/2.0 V, and (C) gas crossover. (D) Stability test with 1 h gap under the condition of open-circuit voltage (OCV) after 14 h, and (E) voltage increase), (F) GITT, and (G) detailed results from (F).

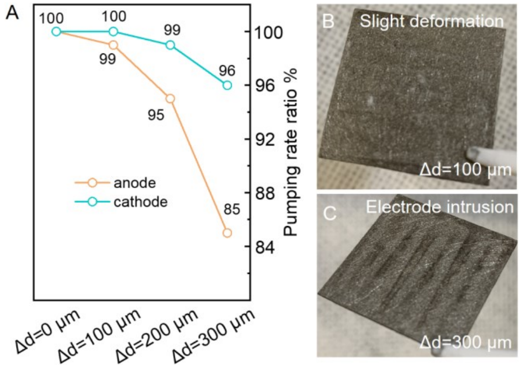

Figure 7.10 (A) Pumping rates through the anode and cathode with different Δd and (B, C) images of anodes after cells testing with Δd=100 and 300 μm respectively.

Thus, different torques also have a significant effect on cell performance, especially hydrogen permeation and cell stability. Low mechanical pressure (5 N·m) results in high average voltage, while excessive mechanical pressure (10 N·m) increases both reversible and irreversible decay. Thus, optimized mechanical pressure (7 N·m) is considered as a compromise, from the perspective of both energy efficiency and stability.

7.4 Summary of the mechanical pressure effects and recommendations

After considering the pros (R_{Ω}/R_{ct}) and cons (R_{md}, GC, stability, short circuit) of mechanical pressure effects comprehensively (Figure 7.11A), the followings details are highly recommended (Figure 7.11B):

i) Δd=100 µm and 7 N·m for cell assembly are good options for suppressing R_{Ω}/R_{ct} and relieve R_{md},

ii) Step-by-step pressurization by torque (3, 5, 7 N·m) is preferred for preventing from “stress concentration”;

iii) Relatively higher membrane thickness (≥50 µm) to prevent from high GC and even short circuit;

iv) Better contact can be achieved by using a sheet of PTFE with the same thickness as the membrane to “pre-assemble” the cell, and then open and reassemble with membranes.

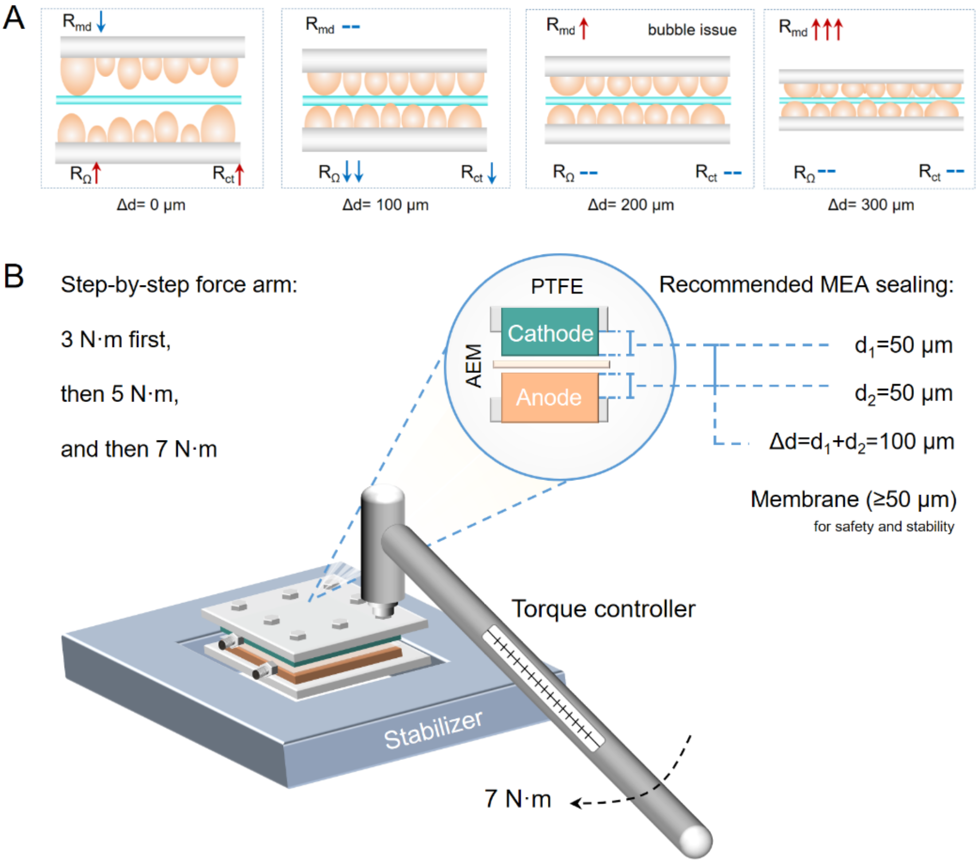

Figure 7.11 (A) Summary of trends in ohmic (R_{Ω}), charge transfer (R_{ct}), and mass diffusion resistance (R_{md}) with Δd increasing from 0, 100, 200, to 300 μm. (B) Recommended relative thickness between PTFE and electrodes, membrane thickness ($\geq 50\mu m$) for safety and stability, and step-by-step force arm from 3, 5, to 7 N·m for cell assembly.

7.5 Performance optimization for $Ni_{0.67}Fe_{0.33}S_2$ based cells

After cell performance optimization with standard catalyst (Pt/Ir), the above optimal conditions (Δd=100 μm and 7 N·m) for cell assembly are applied for the $Ni_{0.67}Fe_{0.33}S_2$ based cells. As shown in Figure 7.12, mechanical pressure-optimized cells exhibit an average current density of 2515 mA cm^{-2}, which is 315 mA cm^{-2} higher than mechanical pressure-free cells with the current density of 2200 mA cm^{-2} at 2.0 V. It is noteworthy that both the starting cell voltage at very low current density and that at high current density (>1000 mA cm^{-2}) of mechanical pressure-optimized cells are lower than mechanical pressure-free cells, indicating faster charge transfer and lower internal resistance.

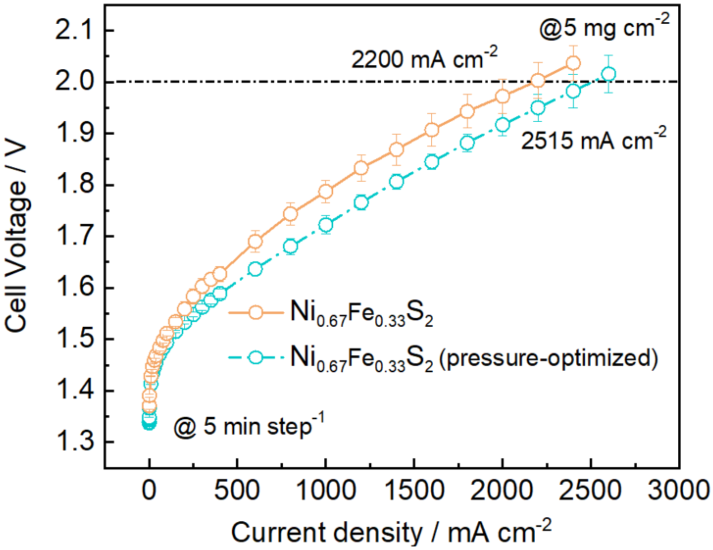

Figure 7.12 polarization curves of $Ni_{0.67}Fe_{0.33}S_2$ *based cells with Pt/C as cathode catalyst and AF1-HNN8-50 as the separator before and after mechanical pressure optimization.*

From the above conclusions, it can be seen that under the premise of only changing the anode catalyst, the optimal mechanical pressure conditions can still be applicable, and the current density at 2.0V is increased by about 15%, indicating that mechanical pressure optimization is an extremely low-cost and effective cell performance optimization method. Since AEMWE is still in the laboratory stage, research on the influence of mechanical pressure on cell performance should be emphasized. The results of this chapter also provide a reference for PhD students or technicians for cell assembly.

However, since we used an integrated method for the pressure of the central MEA, it was not possible to separate the mechanical pressure on both sides. Therefore, more detailed mechanical pressure control requires further studies and “how the cathode and anode are respectively affected by mechanical pressure and the interaction between both sides” needs to be further explored.

8 Overall discussion

Anion exchange membrane water electrolysis (AEMWE) has been attracting increasing interests in its scalability and low cost. Transitional metal sulfides (TMS) acting as anode catalysts for oxygen evolution reaction (OER) exhibit great morphological controllability on nanoscale (<100 nm), higher conductivity than oxides/hydroxides and unique electrochemical behavior due to its structural reconstruction for in-situ derived sulfides/(oxy)hydroxides. However, i) researches of sulfides are mainly focused on in-situ grown catalysts on substrates, while substrate-free 3D nanostructured TMS are urgently needed. ii) The synthesis of nanostructured sulfides is concentrated on template-assisted methods that involves organic impurities. iii) The TMS catalysts are mainly tested in half cells at a relatively low current density of below 200 mA cm^{-2} and rarely used in AEMWE full cells. iv) The stability of TMS under high current density (~1000 mA cm^{-2}) is still unknown, which is crucial for industry applications.

In this thesis, a facile “sulfur leaching” method was demonstrated during OER steps from monometallic sulfides (NiS_2/Ni_3S_4) that were prepared by organic precursor to sulfides/hydroxides heterostructures. The mechanism of sulfur leaching from NiS_2/Ni_3S_4 to sulfate (SO_4^{2-}) is proposed and the catalyst morphologies, structures, and compositions before and after sulfur leaching are fully characterized. After electrochemically assisted sulfur leaching, NiS_2/Ni_3S_4 exhibits more excellent performance, which was attributed to the composite NiS_x/$Ni(OH)_2$/NiOOH catalyst produced by surface reconstruction. In addition to activity, the derived NiS_x/$Ni(OH)_2$/NiOOH exhibits high stability in half cells for 65 h at 10 mA cm^{-2} and 500 h at 1000 mA cm^{-2} in full cells. However, the main concerns for this catalyst are i) the extra phase of impurity (α-S_8) from organic precursor (Thioacetamide, TAA), and ii) relatively lower kinetics (high R_{ct}) and conductivity (high R_{Ω}) compared with bimetallic sulfides.

To address the above two issues, a two-step coprecipitation and recrystallization method was used to synthesize bimetallic $Ni_{0.67}Fe_{0.33}S_2$ nano-octahedrons. It is proved that there is no extra phase of the impurity, and $Ni_{0.67}Fe_{0.33}S_2$ exists in the form of isomorphism with same crystal structures of NiS_2 and FeS_2 but only different inter-planar spacing and unit cell volume. After sulfur leaching, the $Ni_{0.67}Fe_{0.33}S_2$ sacrifices its nano-octahedron morphology but transforms into an even more refined $Ni_{0.67}Fe_{0.33}S_x$/NiFe(OH)x/NiFeOOH heterostructure with the size <10 nm, which greatly improves electrochemical active surface (ECSA) and suppresses the R_{ct} and R_{Ω}, thus enhancing the performance of NiS_2/Ni_3S_4 from 340 to 288 mV. Similarly, the $Ni_{0.67}Fe_{0.33}S_2$ also keeps stable for more than 500 h in Pt/C and AF1-HNN8-50 based cells but lower cell voltage (1.79 V, initial) than that of NiS_2/Ni_3S_4 (1.84 V). However, the above all mentioned cells are assembled under mechanical pressure-free conditions with zero thickness gap between the gaskets and electrodes, which means high contact resistance (R_c) between electrodes and bipolar plates, relatively longer ion diffusion distance, and thus higher R_{ct}.

To suppress R_c and R_{ct}, total thickness gap between the gaskets and electrodes (Δd) are optimized and corresponding mechanical pressure is quantified by tracking foils. It is clear that the mechanical pressure has great effects on physical properties on the porous electrodes, such as decreased thickness, roughness, hydrophilicity and contact resistance. Moreover, moderate mechanical pressure with $\Delta d = 100$ μm is sufficient for greatly improved cell performance without sacrificing stability, while higher mechanical pressure with $\Delta d = 200\text{-}300$ μm greatly enhances mass transfer resistance (R_m). Additionally, the torque for cell assembly is optimized to 7 N·m for the best overall performance. Then, the benchmarked parameters are used in $Ni_{0.67}Fe_{0.33}S_2$ based cells, which exhibit improved performance of 2515 mA cm^{-2} than that under mechanical pressure-free conditions with the current density of 2200 mA cm^{-2} at 2.0 V.

Consequently, Chapter 5 of the NiS_2/Ni_3S_4 catalyst provides a basic understanding of TMS and its stability in both half and full cells, while Chapter 6 of the $Ni_{0.67}Fe_{0.33}S_2$ catalyst addresses the synthesis issues and enhances the OER performance. Then Chapter 7 is for a further improvement by a cost-free method via mechanical pressure optimization. The whole story proves the mechanism of sulfur leaching, and verifies the possibility for TMS to be used in alkaline water electrolysis cells, especially its high-current stability for at least 550 h.

As for the industry application, the $Ni_{0.67}Fe_{0.33}S_2$ catalyst is still in its infancy for much less duration compared with commercialization standard. To date, IrO_2/Pt/C in PEM water electrolyzers can survive on the order of 50000-100000 h, while most of AEM electrolyzers, no matter what catalysts involved, are tested less than 1000 h due to limitation of test station or instability of membrane electrode assembly (MEA), especially the membrane issue. As shown in Figures 8.1A-B, the lab-scale single cells are almost tested under relatively low current density of ≤500 mA cm^{-2} and the average duration is even below 500 h.[122] Although Liu et al. and Masel et al. used a current density of 1000 mA cm^{-2} for 1000-2000 h, the cell voltage is above 1.9 V and even 2.2 V, causing low energy efficiency.[64, 123]

In addition to the duration, the real stability of the cells is also a challenge. As shown in Figure 8.2, more than half of the literature reported a relatively high cell voltage increase rates from 0.5-2.5 mV h^{-1}, which are caused by not only the instability of MEA, but also the electrolyte pollutants such as potassium carbonate (K_2CO_3) and potassium bicarbonate ($KHCO_3$) through the reaction between CO_2 and KOH.

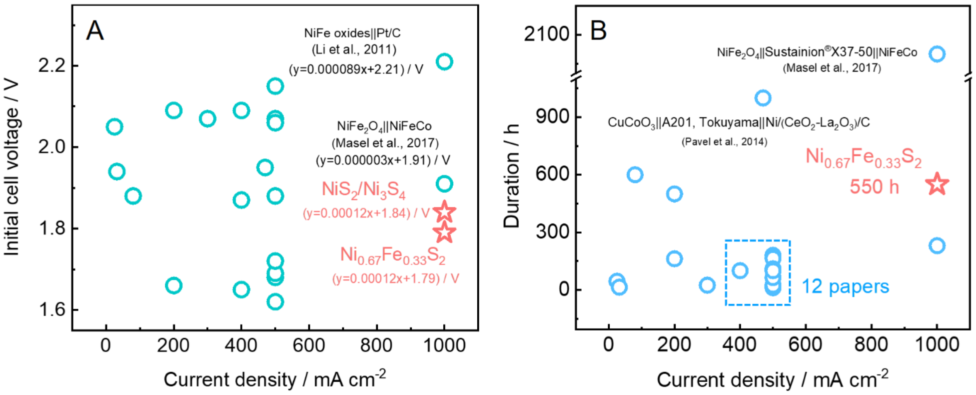

Figure 8.1 The initial voltage of reported cells and duration operated at different current densities (red star represents "this work" with Pt/C and AF1-HNN8-50 as cathode catalyst and membrane, and key information of all cells are summarized in appendix).

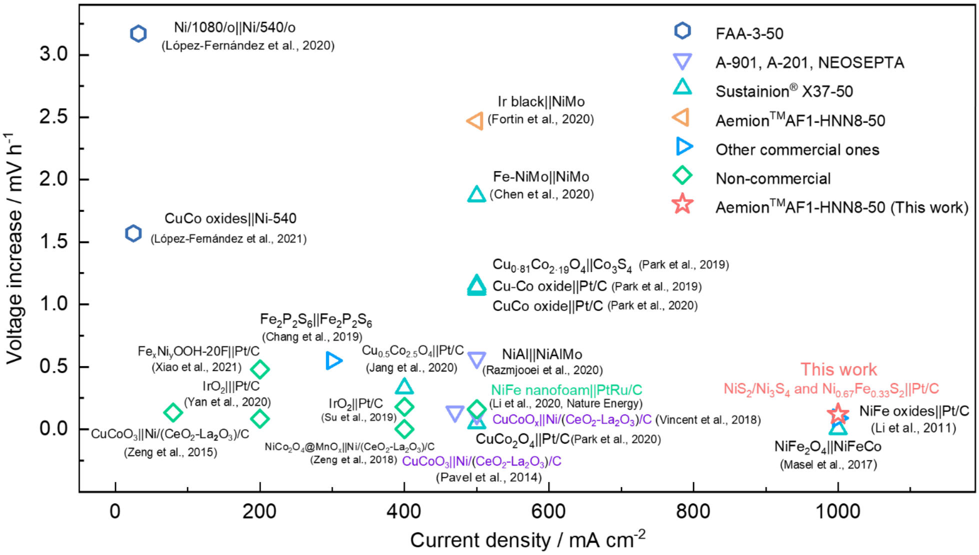

Figure 8.2 Stability (voltage increase rate) of AEMWE cells at different current densities (key information of all cells are summarized in appendix).

Therefore, the overall stability of AEMWE cells needs to be further optimized in the future, especially i) the electrolyte contamination, ii) chemical and mechanical stability of the membrane. The stability of the electrolyte can be improved by inert-gas protection, which still needs more practice, and the stability of the membrane at high temperature and high concentration is of crucial importance. On the basis of the optimization of all key materials, the duration can be extended to 10000-100000 h for ultra-long-term cell tests with sulfide-derived heterostructures as anode catalysts, thus promoting the commercialization of AEMWE.

9 Conclusion and outlook

9.1 Conclusion

This thesis develops nanostructured transitional metal sulfides (e.g. NiS_2/Ni_3S_4, and $Ni_xFe_{1-x}S_2$ with x=0-1) as OER catalysts, which are activated by an electrochemically assisted sulfur leaching method and corresponding derived sulfides/hydroxides heterostructures with refined particle ad enhanced electrochemical active surface area (ECSA) acts as intrinsic active species. Among them, bimetallic $Ni_{0.67}Fe_{0.33}S_2$ is screened as the most promising sulfide catalyst and its cell performance and durability are compared with iridium-based cells. What's more, $Ni_{0.67}Fe_{0.33}S_2$ based cell performance can be further boosted by optimized mechanical pressure. The main conclusions of this thesis are as follows:

i) Monometallic NiS_2/Ni_3S_4 nano-cubes with the size of 80±20 nm are synthesized by one-step vulcanization between Ni^{2+} and sulfide/polysulfide ions for 4 h, which are activated and stabilized by a multi-step sulfur leaching method from NiS_2/Ni_3S_4 to $NiS_x/Ni(OH)_2/NiOOH$ with the performance improved from 365 to 340 mV at the current density of 10 mA cm^{-2}. The derived $NiS_x/Ni(OH)_2/NiOOH$ exhibits better cycling stability during 10000 CVs at 100 mV s^{-1} than Ni/NiO and $Ni(OH)_2$ and is also stable for not only 65 h@10 mA cm^{-2} in a half cell, but also 500 h stability at 1000 mA cm^{-2} in full cells with negligible degradation, providing fundamental understanding of sulfur leaching to make full use of TMS.

ii) Bimetallic $Ni_{0.67}Fe_{0.33}S_2$ nano-octahedrons are synthesized by an additive-free method by two steps of coprecipitation and recrystallization. Then the $Ni_{0.67}Fe_{0.33}S_2$ catalyst suffered from sulfur leaching and the derived catalyst exhibits 10 times higher ECSA and 288 mV at 10 mA cm^{-2} and 10000 CVs stability without degradation, owing to ultra-fine, stabilized $NiFeS_x/NiFe(OH)_2/NiFeOOH$ derivatives with the size of 2-5 nm. With Fe doping, the single cell performance is boosted from 1800 (NiS_2/Ni_3S_4) to 2200 mA cm^{-2} ($Ni_{0.67}Fe_{0.33}S_2$) at 2.0 V.

iii) The mechanical pressure of the cells is optimized to <0.5 MPa with the total thickness gap between gaskets and electrodes of Δd=100 μm and the torque is to be 7 N·m for cell assembly, thus suppressing internal resistance, charge transfer resistance and mass diffusion resistance. The performance for $Ni_{0.67}Fe_{0.33}S_2$ based cells is optimized from 2200 to 2500 mA cm^{-2}

9.2 Outlook

The two-step precipitation and recrystallization synthesis of novel shaped sulfide nanostructures provide a new inside for an additive-free method, which can be extended to other nanostructured materials prepared by templates. This thesis also provides a universal strategy by electrochemical pretreatment of transition metal sulfides, phosphides, nitrides, borides, etc. (X-ides) to leach out anions for highly active reconstructed surface structures. The activation of monometallic and bimetallic sulfides provides references for all these electrochemical systems and can be further derived to trimetallic or even high-entropy X-ides with 5-10 metals inside for higher performance. Such a method can be used not only in the field of water electrolyzers but also in other energy storage and conversion devices (e.g. CO_2 reduction, polysulfide-based alkaline redox flow battery).

10 References

1. Van Hoecke, L.; Laffineur, L.; Campe, R.; Perreault, P.; Verbruggen, S. W.; Lenaerts, S., Challenges in the Use of Hydrogen for Maritime Applications. *Energy & Environmental Science* **2021,** *14* (2), 815-843.

2. Ju, H.; Badwal, S.; Giddey, S., A Comprehensive Review of Carbon and Hydrocarbon Assisted Water Electrolysis for Hydrogen Production. *Applied Energy* **2018,** *231*, 502-533.

3. Hodges, A.; Hoang, A. L.; Tsekouras, G.; Wagner, K.; Lee, C. Y.; Swiegers, G. F.; Wallace, G. G., A High-Performance Capillary-Fed Electrolysis Cell Promises More Cost-Competitive Renewabl Hydrogen. *Nature Communications* **2022,** *13* (1), 1304.

4. Mohan, M.; Sharma, V. K.; Kumar, E. A.; Gayathri, V., Hydrogen Storage in Carbon Materials -- A Review. *Energy Storage* **2019,** *1* (2).

5. Andersson, J.; Grönkvist, S., Large-Scale Storage of Hydrogen. *International Journal of Hydrogen Energy* **2019,** *44* (23), 11901-11919.

6. Boretti, A.; Banik, B. K., Advances in Hydrogen Production from Natural Gas Reforming. *Advanced Energy and Sustainability Research* **2021,** *2* (11).

7. Mansoor, R.; Tahir, M., Recent Developments in Natural Gas Flaring Reduction and Reformation to Energy-Efficient Fuels: A Review. *Energy & Fuels* **2021,** *35* (5), 3675-3714.

8. Oni, A. O.; Anaya, K.; Giwa, T.; Di Lullo, G.; Kumar, A., Comparative Assessment of Blue Hydrogen from Steam Methane Reforming, Autothermal Reforming, and Natural Gas Decomposition Technologies for Natural Gas-Producing Regions. *Energy Conversion and Management* **2022,** *254*.

9. Henkensmeier, D.; Najibah, M.; Harms, C.; Žitka, J.; Hnát, J.; Bouzek, K., Overview: State-of-the-Art Commercial Membranes for Anion Exchange Membrane Water Electrolysis. *Journal of Electrochemical Energy Conversion and Storage* **2021,** *18* (2).

10. Lindquist, G. A.; Xu, Q.; Oener, S. Z.; Boettcher, S. W., Membrane Electrolyzers for Impure-Water Splitting. *Joule* **2020,** *4* (12), 2549-2561.

11. Miller, H. A.; Bouzek, K.; Hnat, J.; Loos, S.; Bernäcker, C. I.; Weißgärber, T.; Röntzsch, L.; Meier-Haack, J., Green Hydrogen from Anion Exchange Membrane Water Electrolysis: A Review of Recent Developments in Critical Materials and Operating Conditions. *Sustainable Energy & Fuels* **2020,** *4* (5), 2114-2133.

12. Vincent, I.; Bessarabov, D., Low Cost Hydrogen Production by Anion Exchange Membrane Electrolysis: A Review. *Renewable and Sustainable Energy Reviews* **2018,** *81*, 1690-1704.

13. Gernaat, D. E. H. J.; de Boer, H. S.; Daioglou, V.; Yalew, S. G.; Müller, C.; van Vuuren, D. P., Climate Change Impacts on Renewable Energy Supply. *Nature Climate Change* **2021,** *11* (2), 119-125.

14. Pletcher, D.; Li, X., Prospects for Alkaline Zero Gap Water Electrolysers for Hydrogen Production. *International Journal of Hydrogen Energy* **2011,** *36* (23), 15089-15104.

15. Lamy, C.; Millet, P., A Critical Review on the Definitions Used to Calculate the Energy Efficiency Coefficients of Water Electrolysis Cells Working under Near Ambient Temperature Conditions. *Journal of Power Sources* **2020,** *447*.

16. Chen, P.; Hu, X., High-Efficiency Anion Exchange Membrane Water Electrolysis Employing Non-Noble Metal Catalysts. *Advanced Energy Materials* **2020,** *10* (39).

17. Vincent, I.; Kruger, A.; Bessarabov, D., Development of Efficient Membrane Electrode Assembly for Low Cost Hydrogen Production by Anion Exchange Membrane Electrolysis. *International Journal of Hydrogen Energy* **2017,** *42* (16), 10752-10761.

18. Amstutz, V.; Toghill, K. E.; Powlesland, F.; Vrubel, H.; Comninellis, C.; Hu, X.; Girault, H. H., Renewable Hydrogen Generation from a Dual-Circuit Redox Flow Battery. *Energy & Environmental Science* **2014,** *7* (7), 2350-2358.

19. Buttler, A.; Spliethoff, H., Current Status of Water Electrolysis for Energy Storage, Grid Balancing and Sector Coupling via Power-to-Gas and Power-to-Liquids: A Review. *Renewable and Sustainable Energy Reviews* **2018,** *82*, 2440-2454.

20. Wan, L.; Xu, Z.; Wang, P.; Lin, Y.; Wang, B., H_2SO_4-Doped Polybenzimidazole Membranes for Hydrogen Production with Acid-Alkaline Amphoteric Water Electrolysis. *Journal of Membrane Science* **2021,** *618*.

21. Oener, S. Z.; Twight, L. P.; Lindquist, G. A.; Boettcher, S. W., Thin Cation-Exchange Layers Enable High-Current-Density Bipolar Membrane Electrolyzers via Improved Water Transport. *ACS Energy Letters* **2020,** *6* (1), 1-8.

22. Mayerhöfer, B.; McLaughlin, D.; Böhm, T.; Hegelheimer, M.; Seeberger, D.; Thiele, S., Bipolar Membrane Electrode Assemblies for Water Electrolysis. *ACS Applied Energy Materials* **2020,** *3* (10), 9635-9644.

23. Xu, J.; Amorim, I.; Li, Y.; Li, J.; Yu, Z.; Zhang, B.; Araujo, A.; Zhang, N.; Liu, L., Stable Overall Water Splitting in an Asymmetric Acid/Alkaline Electrolyzer Comprising a Bipolar Membrane Sandwiched by Bifunctional Cobalt-Nickel Phosphide Nanowire Electrodes. *Carbon Energy* **2020,** *2* (4), 646-655.

24. Carmo, M.; Fritz, D. L.; Mergel, J.; Stolten, D., A Comprehensive Review on PEM Water Electrolysis. *International Journal of Hydrogen Energy* **2013,** *38* (12), 4901-4934.

25. Vincent, I., Hydrogen Production by Water Electrolysis with an Ultrathin Anion-Exchange Membrane (AEM). *International Journal of Electrochemical Science* **2018**, 11347-11358.

26. Feng, Q.; Yuan, X. Z.; Liu, G.; Wei, B.; Zhang, Z.; Li, H.; Wang, H., A Review of Proton Exchange Membrane Water Electrolysis on Degradation Mechanisms and Mitigation Strategies. *Journal of Power Sources* **2017,** *366*, 33-55.

27. Kraglund, M. R.; Carmo, M.; Schiller, G.; Ansar, S. A.; Aili, D.; Christensen, E.; Jensen, J. O., Ion-Solvating Membranes as a New Approach towards High Rate Alkaline Electrolyzers. *Energy & Environmental Science* **2019,** *12* (11), 3313-3318.

28. Arges, C. G.; Zhang, L., Anion Exchange Membranes' Evolution toward High Hydroxide Ion Conductivity and Alkaline Resiliency. *ACS Applied Energy Materials* **2018,** *1* (7), 2991-3012.

29. Jin, H.; Ruqia, B.; Park, Y.; Kim, H. J.; Oh, H. S.; Choi, S. I.; Lee, K., Nanocatalyst Design for Long-Term Operation of Proton/Anion Exchange Membrane Water Electrolysis. *Advanced Energy Materials* **2020,** *11* (4).

30. Liu, C.; Carmo, M.; Bender, G.; Everwand, A.; Lickert, T.; Young, J. L.; Smolinka, T.; Stolten, D.; Lehnert, W., Performance Enhancement of PEM Electrolyzers through Iridium-Coated Titanium Porous Transport Layers. *Electrochemistry Communications* **2018,** *97*, 96-99.

31. Liu, C.; Wippermann, K.; Rasinski, M.; Suo, Y.; Shviro, M.; Carmo, M.; Lehnert, W., Constructing a Multifunctional Interface between Membrane and Porous Transport Layer for Water Electrolyzers. *ACS Applied Materials Interfaces* **2021,** *13* (14), 16182-16196.

32. Wang, M.; Wang, Z.; Gong, X.; Guo, Z., The Intensification Technologies to Water Electrolysis for Hydrogen Production -- A Review. *Renewable and Sustainable Energy Reviews* **2014,** *29*, 573-588.

33. Babic, U.; Suermann, M.; Büchi, F. N.; Gubler, L.; Schmidt, T. J., Critical Review -- Identifying Critical Gaps for Polymer Electrolyte Water Electrolysis Development. *Journal of The Electrochemical Society* **2017,** *164* (4), F387-F399.

34. Alia, S. M.; Ha, M.-A.; Ngo, C.; Anderson, G. C.; Ghoshal, S.; Pylypenko, S., Platinum-Nickel Nanowires with Improved Hydrogen Evolution Performance in Anion Exchange Membrane-Based Electrolysis. *ACS Catalysis* **2020,** *10* (17), 9953-9966.

35. Hagesteijn, K. F. L.; Jiang, S.; Ladewig, B. P., A Review of the Synthesis and Characterization of Anion Exchange Membranes. *Journal of Materials Science* **2018,** *53* (16), 11131-11150.

36. Aili, D.; Kraglund, M. R.; Tavacoli, J.; Chatzichristodoulou, C.; Jensen, J. O., Polysulfone-Polyvinylpyrrolidone Blend Membranes as Electrolytes in Alkaline Water Electrolysis. *Journal of Membrane Science* **2020,** *598*.

37. Konovalova, A.; Kim, H.; Kim, S.; Lim, A.; Park, H. S.; Kraglund, M. R.; Aili, D.; Jang, J. H.; Kim, H.-J.; Henkensmeier, D., Blend Membranes of Polybenzimidazole and an Anion Exchange Ionomer (FAA3) for Alkaline Water Electrolysis: Improved Alkaline Stability and Conductivity. *Journal of Membrane Science* **2018,** *564*, 653-662.

38. Kraglund, M. R.; Aili, D.; Jankova, K.; Christensen, E.; Li, Q.; Jensen, J. O., Zero-Gap Alkaline Water Electrolysis Using Ion-Solvating Polymer Electrolyte Membranes at Reduced KOH Concentrations. *Journal of The Electrochemical Society* **2016,** *163* (11), F3125-F3131.

39. Li, H.; Kraglund, M. R.; Reumert, A. K.; Ren, X.; Aili, D.; Yang, J., Poly(Vinyl Benzyl Methylpyrrolidinium) Hydroxide Derived Anion Exchange Membranes for Water Electrolysis. *Journal of Materials Chemistry A* **2019,** *7* (30), 17914-17922.

40. de Groot, M. T.; Vreman, A. W., Ohmic Resistance in Zero Gap Alkaline Electrolysis with a Zirfon Diaphragm. *Electrochimica Acta* **2021,** *369*.

41. Trinke, P.; Haug, P.; Brauns, J.; Bensmann, B.; Hanke-Rauschenbach, R.; Turek, T., Hydrogen Crossover in PEM and Alkaline Water Electrolysis: Mechanisms, Direct Comparison and Mitigation Strategies. *Journal of The Electrochemical Society* **2018,** *165* (7), F502-F513.

42. Schalenbach, M.; Lueke, W.; Stolten, D., Hydrogen Diffusivity and Electrolyte Permeability of the Zirfon PERL Separator for Alkaline Water Electrolysis. *Journal of The Electrochemical Society* **2016,** *163* (14), F1480-F1488.

43. Shirvanian, P.; van Berkel, F., Novel Components in Proton Exchange Membrane (PEM) Water Electrolyzers (PEMWE): Status, Challenges and Future Needs. A Mini Review. *Electrochemistry Communications* **2020,** *114*.

44. Motealleh, B.; Liu, Z.; Masel, R. I.; Sculley, J. P.; Richard Ni, Z.; Meroueh, L., Next-generation Anion Exchange Membrane Water Electrolyzers Operating for Commercially Relevant Lifetimes. *International Journal of Hydrogen Energy* **2021,** *46* (5), 3379-3386.

45. Jang, M. J.; Yang, J.; Lee, J.; Park, Y. S.; Jeong, J.; Park, S. M.; Jeong, J.-Y.; Yin, Y.; Seo, M.-H.; Choi, S. M.; Lee, K. H., Superior Performance and Stability of Anion Exchange

Membrane Water Electrolysis: pH-Controlled Copper Cobalt Oxide Nanoparticles for the Oxygen Evolution Reaction. *Journal of Materials Chemistry A* **2020,** *8* (8), 4290-4299.

46. Cao, L. M.; Hu, Y. W.; Tang, S. F.; Iljin, A.; Wang, J. W.; Zhang, Z. M.; Lu, T. B., Fe-CoP Electrocatalyst Derived from a Bimetallic Prussian Blue Analogue for Large-Current-Density Oxygen Evolution and Overall Water Splitting. *Advanced Science (Weinh)* **2018,** *5* (10), 1800949.

47. Kwon, C. Y.; Jeong, J. Y.; Yang, J.; Park, Y. S.; Jeong, J.; Park, H.; Kim, Y.; Choi, S. M., Effect of Copper Cobalt Oxide Composition on Oxygen Evolution Electrocatalysts for Anion Exchange Membrane Water Electrolysis. *Frontier Chemistry* **2020,** *8*, 600908.

48. Xi, W.; Yan, G.; Lang, Z.; Ma, Y.; Tan, H.; Zhu, H.; Wang, Y.; Li, Y., Oxygen-Doped Nickel Iron Phosphide Nanocube Arrays Grown on Ni Foam for Oxygen Evolution Electrocatalysis. *Small* **2018,** *14* (42), e1802204.

49. Li, X.; Walsh, F. C.; Pletcher, D., Nickel Based Electrocatalysts for Oxygen Evolution in High Current Density, Alkaline Water Electrolysers. *Physical Chemistry Chemical Physics* **2011,** *13* (3), 1162-7.

50. Cossar, E.; Oyarce Barnett, A.; Seland, F.; Baranova, E. A., The Performance of Nickel and Nickel-Iron Catalysts Evaluated As Anodes in Anion Exchange Membrane Water Electrolysis. *Catalysts* **2019,** *9* (10).

51. Phillips, R.; Gannon, W. J. F.; Dunnill, C. W., Chapter 2. Alkaline Electrolysers. In *Electrochemical Methods for Hydrogen Production*, 2019; pp 28-58.

52. Prats, H.; Chan, K., The Determination of the HOR/HER Reaction Mechanism from Experimental Kinetic Data. *Physical Chemistry Chemical Physics* **2021,** *23* (48), 27150-27158.

53. Zhang, Y.; Lei, H.; Duan, D.; Villota, E.; Liu, C.; Ruan, R., New Insight into the Mechanism of the Hydrogen Evolution Reaction on MoP(001) from First Principles. *ACS Applied Materials Interfaces* **2018,** *10* (24), 20429-20439.

54. Hu, C.; Zhang, L.; Gong, J., Recent Progress Made in the Mechanism Comprehension and Design of Electrocatalysts for Alkaline Water Splitting. *Energy & Environmental Science* **2019,** *12* (9), 2620-2645.

55. Song, J.; Wei, C.; Huang, Z. F.; Liu, C.; Zeng, L.; Wang, X.; Xu, Z. J., A Review on Fundamentals for Designing Oxygen Evolution Electrocatalysts. *Chemical Society Review* **2020,** *49* (7), 2196-2214.

56. Zhang, K.; Zou, R., Advanced Transition Metal-Based OER Electrocatalysts: Current Status, Opportunities, and Challenges. *Small* **2021,** *17* (37), e2100129.

57. Chang, J.; Wang, G.; Belharsa, A.; Ge, J.; Xing, W.; Yang, Y., Stable $Fe_2P_2S_6$ Nanocrystal Catalyst for High-Efficiency Water Electrolysis. *Small Methods* **2019,** *4* (6).

58. Busacca, C.; Zignani, S. C.; Di Blasi, A.; Di Blasi, O.; Lo Faro, M.; Antonucci, V.; Aricò, A. S., Electrospun $NiMn_2O_4$ and $NiCo_2O_4$ Spinel Oxides Supported on Carbon Nanofibers as Electrocatalysts for the Oxygen Evolution Reaction in an Anion Exchange Membrane-Based Electrolysis Cell. *International Journal of Hydrogen Energy* **2019,** *44* (38), 20987-20996.

59. Campagna Zignani, S.; Lo Faro, M.; Trocino, S.; Aricò, A. S., Investigation of NiFe-Based Catalysts for Oxygen Evolution in Anion-Exchange Membrane Electrolysis. *Energies* **2020,** *13* (7).

60. Chen, N.; Paek, S. Y.; Lee, J. Y.; Park, J. H.; Lee, S. Y.; Lee, Y. M., High-Performance Anion Exchange Membrane Water Electrolyzers with a Current Density of 7.68 A cm^{-2} and a Durability of 1000 Hours. *Energy & Environmental Science* **2021,** *14* (12), 6338-6348.

61. López-Fernández, E.; Gil-Rostra, J.; Escudero, C.; Villar-García, I. J.; Yubero, F.; de Lucas Consuegra, A.; González-Elipe, A. R., Active Sites and Optimization of Mixed Copper-Cobalt Oxide Anodes for Anion Exchange Membrane Water Electrolysis. *Journal of Power Sources* **2021,** *485*.

62. Thangavel, P.; Ha, M.; Kumaraguru, S.; Meena, A.; Singh, A. N.; Harzandi, A. M.; Kim, K. S., Graphene-Nanoplatelets-Supported NiFe-MOF: High-Efficiency and Ultra-Stable Oxygen Electrodes for Sustained Alkaline Anion Exchange Membrane Water Electrolysis. *Energy & Environmental Science* **2020,** *13* (10), 3447-3458.

63. Thangavel, P.; Kim, G.; Kim, K. S., Electrochemical Integration of Amorphous NiFe (Oxy)Hydroxides on Surface-Activated Carbon Fibers for High-Efficiency Oxygen Evolution in Alkaline Anion Exchange Membrane Water Electrolysis. *Journal of Materials Chemistry A* **2021,** *9* (24), 14043-14051.

64. Liu, Z.; Sajjad, S. D.; Gao, Y.; Yang, H.; Kaczur, J. J.; Masel, R. I., The Effect of Membrane on an Alkaline Water Electrolyzer. *International Journal of Hydrogen Energy* **2017,** *42* (50), 29661-29665.

65. Pavel, C. C.; Cecconi, F.; Emiliani, C.; Santiccioli, S.; Scaffidi, A.; Catanorchi, S.; Comotti, M., Highly Efficient Platinum Group Metal Free Based Membrane-Electrode Assembly for Anion Exchange Membrane Water Electrolysis. *Angewandte Chemie International Edition* **2014,** *53* (5), 1378-81.

66. Zeng, L.; Zhao, T. S., Integrated Inorganic Membrane Electrode Assembly with Layered Double Hydroxides as Ionic Conductors for Anion Exchange Membrane Water Electrolysis. *Nano Energy* **2015,** *11*, 110-118.

67. Zeng, L.; Zhao, T. S.; Zhang, R. H.; Xu, J. B., $NiCo_2O_4$ Nanowires@MnO_x Nanoflakes Supported on Stainless Steel Mesh with Superior Electrocatalytic Performance for Anion Exchange Membrane Water Splitting. *Electrochemistry Communications* **2018,** *87*, 66-70.

68. Razmjooei, F.; Farooqui, A.; Reissner, R.; Gago, A. S.; Ansar, S. A.; Friedrich, K. A., Elucidating the Performance Limitations of Alkaline Electrolyte Membrane Electrolysis: Dominance of Anion Concentration in Membrane Electrode Assembly. *ChemElectroChem* **2020,** *7* (19), 3951-3960.

69. Xiao, J.; Oliveira, A. M. Wang, L.; Zhao, Y.; Wang, T.; Wang, J.; Setzler, B. P.; Yan, Y., Water-Fed Hydroxide Exchange Membrane Electrolyzer Enabled by a Fluoride-Incorporated Nickel-Iron Oxyhydroxide Oxygen Evolution Electrode. *ACS Catalysis* **2020,** *11* (1), 264-270.

70. Yin, J.; Jin, J.; Lin, H.; Yin, Z.; Li, J.; Lu, M.; Guo, L.; Xi, P.; Tang, Y.; Yan, C. H., Optimized Metal Chalcogenides for Boosting Water Splitting. *Advanced Science (Weinh)* **2020,** *7* (10), 1903070.

71. Khan, H.; Yerramilli, A. S.; D'Oliveira, A.; Alford, T. L.; Boffito, D. C.; Patience, G. S., Experimental Methods in Chemical Engineering: X-ray Diffraction Spectroscopy -- XRD. *The Canadian Journal of Chemical Engineering* **2020,** *98* (6), 1255-1266.

72. Bunaciu, A. A.; Udristioiu, E. G.; Aboul-Enein, H. Y., X-ray Diffraction: Instrumentation and Applications. *Critical Reviews in Analytical Chemistry* **2015,** *45* (4), 289-99.

73. Zhu, F. Y.; Wang, Q. Q.; Zhang, X. S.; Hu, W.; Zhao, X.; Zhang, H. X., 3D Nanostructure Reconstruction Based on the SEM Imaging Principle, and Applications. *Nanotechnology* **2014,** *25* (18), 185705.

74. Oatley, C. W., The Eearly History of the Scanning Electron Microscope. *Journal of Applied Physics* **1982,** *53* (2), R1-R13.

75. Winey, M.; Meehl, J. B.; O'Toole, E. T.; Giddings, T. H., Jr., Conventional Transmission Electron Microscopy. *Molecular Biology of the Cell* **2014,** *25* (3), 319-23.

76. Schorb, M.; Haberbosch, I.; Hagen, W. J. H.; Schwab, Y.; Mastronarde, D. N., Software Tools for Automated Transmission Electron Microscopy. *Nature Methods* **2019,** *16* (6), 471-477.

77. Bagus, P. S.; Ilton, E. S.; Nelin, C. J., TheInterpretation of XPS Spectra: Insights into Materials Properties. *Surface Science Reports* **2013,** *68* (2), 273-304.

78. Bacsik, Z.; Mink, J.; Keresztury, G., FTIR Spectroscopy of the Atmosphere. I. Principles and Methods. *Applied Spectroscopy Reviews* **2004,** *39* (3), 295-363.

79. Morrison, C.; Sun, H.; Yao, Y.; Loomis, R. A.; Buhro, W. E., Methods for the ICP-OES Analysis of Semiconductor Materials. *Chemistry of Materials* **2020,** *32* (5), 1760-1768.

80. Bumbrah, G. S.; Sharma, R. M., Raman Spectroscopy -- Basic Principle, Instrumentation and Selected Applications for the Characterization of Drugs of Abuse. *Egyptian Journal of Forensic Sciences* **2016,** *6* (3), 209-215.

81. Zhu, K.; Zhu, X.; Yang, W., Application of In Situ Techniques for the Characterization of NiFe-Based Oxygen Evolution Reaction (OER) Electrocatalysts. *Angewandte Chemie International Edition* **2019,** *58* (5), 1252-1265.

82. Xia, L.; Jiang, W.; Hartmann, H.; Mayer, J.; Lehnert, W.; Shviro, M., Multistep Sulfur Leaching for the Development of a Highly Efficient and Stable $NiS_x/Ni(OH)_2/NiOOH$ Electrocatalyst for Anion Exchange Membrane Water Electrolysis. *ACS Applied Materials Interfaces* **2022**, 14, 19397-19408.

83. Zhao, G.; Zhang, Y.; Yang, L.;Jiang, Y.; Zhang, Y.; Hong, W.; Tian, Y.; Zhao, H.; Hu, J.; Zhou, L.; Hou, H.; Ji, X.; Mai, L., Nickel Chelate Derived NiS_2 Decorated with Bifunctional Carbon: An Efficient Strategy to Promote Sodium Storage Performance. *Advanced Functional Materials* **2018,** *28* (41).

84. Zeng, L.; Liu, Z.; Sun, K.; Chen, Y.; Zhao, J.; Chen, Y.; Pan, Y.; Lu, Y.; Liu, Y.; Liu, C., Multiple Modulations of Pyrite Nickel Sulfides via Metal Heteroatom Doping Engineering for Boosting Alkaline and Neutral Hydrogen Evolution. *Journal of Materials Chemistry A* **2019,** *7* (44), 25628-25640.

85. Huang, S.; Li, Y.; Chen, S.; Wang, Y.; Wang, Z.; Fan, S.; Zhang, D.; Yang, H. Y., Regulating the Breathing of Mesoporous $Fe_{0.95}S_{1.05}$ Nanorods for Fast and Durable Sodium Storage. *Energy Storage Materials* **2020,** *32*, 151-158.

86. He, Y.; Zhang, X.; Wang, S.; Meng, J.; Sui, Y.; Wei, F.; Qi, J.; Meng, Q.; Ren, Y.; Zhuang, D., Rubik's Cube-Like Ni_3S_4/CuS_2 Nanocomposite for High-Performance Supercapacitors. *Journal of Alloys and Compounds* **2020,** *847.*

87. Zhang, Y.; Sun, W.; Rui, X.; Li, B.; Tan, H. T.; Guo, G.; Madhavi, S.; Zong, Y.; Yan, Q., One-Pot Synthesis of Tunable Crystalline Ni_3S_4@Amorphous MoS_2 Core/Shell Nanospheres for High-Performance Supercapacitors. *Small* **2015,** *11* (30), 3694-702.

88. Wan, K.; Luo, J.; Zhou, C.; Zhang, T.; Arbiol, J.; Lu, X.; Mao, B. W.; Zhang, X.; Fransaer, J., Hierarchical Porous Ni_3S_4 with Enriched High-Valence Ni Sites as a Robust Electrocatalyst for Efficient Oxygen Evolution Reaction. *Advanced Functional Materials* **2019,** *29* (18).

89. S, N.; A, J. C. M.; G, M., Facile Microwave-Hydrothermal Synthesis of NiS Nanostructures for Supercapacitor Applications. *Applied Surface Science* **2018,** *449*, 485-491.

90. Wang, H.-Y.; Hsu, Y.-Y.; Chen, R.; Chan, T.-S.; Chen, H. M.; Liu, B., $Ni3^+$-Induced Formation of Active NiOOH on the Spinel Ni-Co Oxide Surface for Efficient Oxygen Evolution Reaction. *Advanced Energy Materials* **2015,** *5* (10).

91. Tahir, M.; Pan, L.; Zhang, R.; Wang, Y.-C.; Shen, G.; Aslam, I.; Qadeer, M. A.; Mahmood, N.; Xu, W.; Wang, L.; Zhang, X.; Zou, J.-J., High-Valence-State NiO/Co_3O_4 Nanoparticles on Nitrogen-Doped Carbon for Oxygen Evolution at Low Overpotential. *ACS Energy Letters* **2017,** *2* (9), 2177-2182.

92. Dai, W.; Pan, Y.; Ren, K.; Zhu, Y.-a.; Lu, T., Heteroatom Ni Alloyed Pyrite-Phase FeS_2 as a Pre-Catalyst for Enhanced Oxygen Evolution Reaction. *Electrochimica Acta* **2020,** *355*.

93. Ma, Q.; Hu, C.; Liu, K.; Hung, S.-F.; Ou, D.; Chen, H. M.; Fu, G.; Zheng, N., Identifying the Electrocatalytic Sites of Nickel Disulfide in Alkaline Hydrogen Evolution Reaction. *Nano Energy* **2017,** *41*, 148-153.

94. Alexey Kamyshny, A. G., Jenny Gun, Dan Rizkov, and Ovadia Lev, Equilibrium Distribution of Polysulfide Ions in Aqueous Solutions at 25°C: A New Approach for the Study of Polysulfides' Equilibria. *Environmental Science & Technology* **2004,** *38* (24), 6633-6644.

95. Wang, R.; Xu, C.; Lee, J.-M., High Performance Asymmetric Supercapacitors: New NiOOH Nanosheet/Graphene Hydrogels and Pure Graphene Hydrogels. *Nano Energy* **2016,** *19*, 210-221.

96. Xiao, M.; Tian, Y.; Yan, Y.; Feng, K.; Miao, Y., Electrodeposition of $Ni(OH)_2$/NiOOH in the Presence of Urea for the Improved Oxygen Evolution. *Electrochimica Acta* **2015,** *164*, 196-202.

97. Wang, L.; Zhu, Y.; Li, H.; Li, Q.; Qian, Y., Hydrothermal Synthesis of NiS Nanobelts and NiS_2 Microspheres Constructed of Cuboids Architectures. *Journal of Solid State Chemistry* **2010,** *183* (1), 223-227.

98. Jin, S., Are Metal Chalcogenides, Nitrides, and Phosphides Oxygen Evolution Catalysts or Bifunctional Catalysts? *ACS Energy Letters* **2017,** *2* (8), 1937-1938.

99. Mabayoje, O.; Shoola, A.; Wygant, B. R.; Mullins, C. B., The Role of Anions in Metal Chalcogenide Oxygen Evolution Catalysis: Electrodeposited Thin Films of Nickel Sulfide as "Pre-Catalysts". *ACS Energy Letters* **2016,** *1* (1), 195-201.

100. Lee, M.; Oh, H.-S.; Cho, M. K.; Ahn, J.-P.; Hwang, Y. J.; Min, B. K., Activation of a Ni Electrocatalyst through Spontaneous Transformation of Nickel Sulfide to Nickel Hydroxide in an Oxygen Evolution Reaction. *Applied Catalysis B: Environmental* **2018,** *233*, 130-135.

101. Fan, K.; Zou, H.; Lu, Y.; Chen, H.; Li, F.; Liu, J.; Sun, L.; Tong, L.; Toney, M. F.; Sui, M.; Yu, J., Direct Observation of Structural Evolution of Metal Chalcogenide in Electrocatalytic Water Oxidation. *ACS Nano* **2018,** *12* (12), 12369-12379.

102. Kaspar, J.; Bazarjani, M. S.; Schitco, C.; Gurlo, A.; Graczyk-Zajac, M.; Riedel, R., Electrochemical Study of NiO Nanosheets: toward the Understanding of Capacity Fading. *Journal of Materials Science* **2017,** *52* (11), 6498-6505.

103. Yavuz, A.; Ozdemir, N.; Erdogan, P. Y.; Zengin, H.; Zengin, G.; Bedir, M., Nickel-Based Materials Electrodeposited from a Deep Eutectic Solvent on Steel for Energy Storage Devices. *Applied Physics A* **2019,** *125* (8).

104. Sivakumar, S.; Soundhirarajan, P.; Venkatesan, A.; Khatiwada, C. P., Spectroscopic Studies and Antibacterial Activities of Pure and Various Levels of Cu-doped $BaSO_4$ Nanoparticles. *Spectrochimica Acta, Part A: Molecular and Biomolecular Spectroscopy* **2015,** *151*, 895-907.

105. Chen, W.; Wang, H.; Li, Y.; Liu, Y.; Sun, J.; Lee, S.; Lee, J. S.; Cui, Y., In Situ Electrochemical Oxidation Tuning of Transition Metal Disulfides to Oxides for Enhanced Water Oxidation. *ACS Central Science* **2015,** *1* (5), 244-51.

106. Xu, X.; Song, F.; Hu, X., A Nickel Iron Diselenide-Derived Efficient Oxygen-Evolution Catalyst. *Nature Communications* **2016,** *7*, 12324.

107. Michael, J. D.; Demeter, E. L.; Illes, S. M.; Fan, Q.; Boes, J. R.; Kitchin, J. R., Alkaline Electrolyte and Fe Impurity Effects on the Performance and Active-Phase Structure of NiOOH Thin Films for OER Catalysis Applications. *The Journal of Physical Chemistry C* **2015,** *119* (21), 11475-11481.

108. Klaus, S.; Cai, Y.; Louie, M. W.; Trotochaud, L.; Bell, A. T., Effects of Fe Electrolyte Impurities on $Ni(OH)_2/NiOOH$ Structure and Oxygen Evolution Activity. *The Journal of Physical Chemistry C* **2015,** *119* (13), 7243-7254.

109. Ni, B.; He, T.; Wang, J. O.; Zhang, S.; Ouyang, C.; Long, Y.; Zhuang, J.; Wang, X., The Formation of (NiFe)S_2 Pyrite Mesocrystals as Efficient Pre-Catalysts for Water Oxidation. *Chemical Science* **2018,** *9* (10), 2762-2767.

110. Boursiquot, S.; Mullet, M.; Ehrhardt, J.-J., XPS Study of the Reaction of Chromium (VI) with Mackinawite (FeS). *Surface and Interface Analysis* **2002,** *34* (1), 293-297.

111. Ke, W.; Zhang, Y.; Imbault, A. L.; Li, Y., Metal-organic Framework Derived Iron-Nickel Sulfide Nanorods for Oxygen Evolution Reaction. *International Journal of Hydrogen Energy* **2021,** *46* (40), 20941-20949.

112. Thangasamy, P.; Maruthapandian, V.; Saraswathy, V.; Sathish, M., Supercritical Fluid Processing for the Synthesis of NiS_2 Nanostructures as Efficient Electrocatalysts for Electrochemical Oxygen Evolution Reactions. *Catalysis Science & Technology* **2017,** *7* (16), 3591-3597.

113. Luo, R.; Luo, M.; Wang, Z.; Liu, P.; Song, S.; Wang, X.; Chen, M., The Atomic Origin of Nickel-Doping-Induced Catalytic Enhancement in MoS_2 for Electrochemical Hydrogen Production. *Nanoscale* **2019,** *11* (15), 7123-7128.

114. Yang, Y.; Kang, Y.; Zhao, H.; Dai, X.; Cui, M.; Luan, X.; Zhang, X.; Nie, F.; Ren, Z.; Song, W., An Interfacial Electron Transfer on Tetrahedral NiS_2/$NiSe_2$ Heterocages with Dual-Phase Synergy for Efficiently Triggering the Oxygen Evolution Reaction. *Small* **2020,** *16* (1), e1905083.

115. Lu, Y.; Li, X.; Liang, J.; Hu, L.; Zhu, Y.; Qian, Y., A Simple Melting-Diffusing-Reacting Strategy to Fabricate S/NiS_2-C for Lithium-Sulfur Batteries. *Nanoscale* **2016,** *8* (40), 17616-17622.

116. Niaz, A. K.; Akhtar, A.; Park, J.-Y.; Lim, H.-T., Effects of the Operation Mode on the Degradation Behavior of Anion Exchange Membrane Water Electrolyzers. *Journal of Power Sources* **2021,** *481*.

117. Banerjee, R.; Bevilacqua, N.; Mohseninia, A.; Wiedemann, B.; Wilhelm, F.; Scholta, J.; Zeis, R., Carbon Felt Electrodes for Redox Flow Battery: Impact of Compression on Transport Properties. *Journal of Energy Storage* **2019,** *26*.

118. Ali, M. Y.; Lai, W.-J.; Pan, J., Computational Models for Simulations of Lithium-ion Battery Cells under Constrained Compression Tests. *Journal of Power Sources* **2013,** *242*, 325-340.

119. Cannarella, J.; Liu, X.; Leng, C. Z.; Sinko, P. D.; Gor, G. Y.; Arnold, C. B., Mechanical Properties of a Battery Separator under Compression and Tension. *Journal of The Electrochemical Society* **2014,** *161* (11), F3117-F3122.

120. Gor, G. Y.; Cannarella, J.; Prévost, J. H.; Arnold, C. B., A Model for the Behavior of Battery Separators in Compression at Different Strain/Charge Rates. *Journal of The Electrochemical Society* **2014,** *161* (11), F3065-F3071.

121. Xu, Q.; Oener, S. Z.; Lindquist, G.; Jiang, H.; Li, C.; Boettcher, S. W., Integrated Reference Electrodes in Anion-Exchange-Membrane Electrolyzers: Impact of Stainless-Steel Gas-Diffusion Layers and Internal Mechanical Pressure. *ACS Energy Letters* **2020,** *6* (2), 305-312.

122. Jiang, W., Faid, A. Y., Gomes, B. F., Galkina, I., Xia, L., Lobo, C. M. S., Desmau, M., Borowski, P., Hartmann, H., Maljusch, A., Besmehn, A., Roth, C., Sunde, C., Lehnert, W., Shviro, M., Composition-Dependent Morphology, Structure, and Catalytical Performance of Nickel-Iron Layered Double Hydroxide as Highly-Efficient and Stable Anode Catalyst in Anion Exchange Membrane Water Electrolysis. Advanced Functional Materials **2022**, 32, 2203520.

123. Kaczur, J. J.; Yang, H.; Liu, Z.; Sajjad, S. D.; Masel, R. I., Carbon Dioxide and Water Electrolysis Using New Alkaline Stable Anion Membranes. *Frontier Chemistry* **2018,** *6*, 263.

11 Appendix

Re.	Membrane (thickness/μm)	Ionomer	Anodic&cathodic catalysts	Electrolyte& T/°C	At 1.8/2.0 V (mA cm^{-2})	Duration
This work	FAA-3-**50**	FAA-3	Ni/NiO&Pt/C	1 M KOH/60	400/900 @step-wise (5 min step^{-1})	<100 h@1000 mA cm^{-2}
This work	FAA-3-**50**	FAA-3	NiS_2/Ni_3S_4&Pt/C	1 M KOH/60	800/1550 @step-wise (5 min step^{-1})	<100 h@1000 mA cm^{-2}
[1]	FAA-3-PK-**130**	FAA-3-PK-130	$Ce_{0.2}MnFe_{1.8}O_4$&Ni	D.I. water/25	250/- @1 mV s^{-1}	100 h@~220 mA cm^{-2}
[2]	FAA3-**40**	I_2	Acta 3030&Acta-4030	1% K_2CO_3/60	210/600 @unknown	31 h@500 mA cm^{-2}
[2]	FAA3-PP-**75**	I_2	Acta 3030&Acta-4030	1% K_2CO_3/60	140/410 @unknown	200 h@500 mA cm^{-2}
[3]	FAA-3-PE-**30**	FAA-3-SOLUT-10	Ir black&NiMo/X72	1 M KOH/50	680/1370 @unknown	-
[4]	FAA-3-**50**	-	Ni foam&Ni foam	10 wt% (~2 M) KOH/60	20/30 (0-2 A) @20 mA s^{-1}	-
[5]	FAA-3-PK-**75**	PTFE	IrO_2 &Pt/C	0.5 M KOH/50	520/880 @20 mV s^{-1}	-
[6]	FAA-3-**50**	-	IrO_2 &Pt/C	1 M KOH/60	320/620 1.35 to 2.15 V (interval 0.05 V)	-
[6]	FAA-3-**50**	-	g-CN-CNF-800&Pt/C	1 M KOH/60	480/980 1.35 to 2.15 V (interval 0.05 V)	-
[7]	FAA-3-**130**	FAA-3	$NiCoO_x$:Fe&Pt/C	D.I. water/50	110/360 @step wise (3 min step^{-1})	-
[8]	FAA3-**50**	PTFE	$NiMn_2O_4$&Pt/C	D.I. water/50	10/40 @10 mV s^{-1}	

Re.	Membrane (thickness/μm)	Ionomer	Anodic&cathodic catalysts	Electrolyte& T/°C	At 1.8/2.0 V (mA cm^{-2})	Duration
[8]	FAA3-**50**	PTFE	$NiMn_2O_4$&Pt/C	6 M KOH/50	130/- @10 mV s^{-1}	-
[9]	FAA-3-**25**	Poly-arylimidazoliums	Pt/C&Pt/C	1 M KOH/60	20@2.2 V V-t curve at 20 mA cm^{-2}	10 h@20 mA cm^{-2}
[10]	FAA-3-**50**	FAA3-Br	IrO_2 &Pt/C	1 M KOH/70	1150/1830 @2 mV s^{-1}	-
[11]	FAA-3-**50**	FAA-3	$NiMn_2O_4$/C&Pt/C	1 M KOH/50	180/380 @5 mV s^{-1}	-
[12]	FAA-3-**50**	-	Ni/1080/o&Ni/540/o	1 M KOH/40	20/50 @5 mV s^{-1}	14 h@20 mA cm^{-2}
[13]	FAA-3-**50**	-	CuCoO& Ni/540/o	1 M KOH/40	42/94 @5 mV s^{-1}	45 h@25 mA cm^{-2}

Key information for Figures 8.1-8.2

Re.	Membrane (thickness/μm)	Anodic&cathodic catalysts	Electrolyte& T/°C	Initial voltage (V)	Increase rate (mV h^{-1})	Duration
This work	AF1-HNN8-**50**	NiS_2/Ni_3S_4||Pt/C	1 M KOH/60	1.84	0.12	500 h@1000 mA cm^{-2}
This work	AF1-HNN8-**50**	$Ni_{0.67}Fe_{0.33}S_2$||Pt/C	1 M KOH/60	1.79	0.12	500 h@1000 mA cm^{-2}
[14]	AF1-HNN8-**50**	Ir black||Pt/C	0.1 M KOH/50	1.70	3.21	17 h@500 mA cm^{-2}
[15]	A201, Tokuyama	$CuCoO_3$||Ni/CeO_2-La_2O_3/C	1.0 wt.% $K_2CO_3/KHCO_3$/43	1.95	0.14	1000 h@470 mA cm^{-2}
[16]	A901, Tokuyama	$CuCoO_x$||Ni/CeO_2-La_2O_3/C	1.0 wt.% K_2CO_3/50	2.13	0.12	180 h@500 mA cm^{-2}
[17]	NEOSEPTA, Astom	NiAl||NiAlMo	1 M KOH/65	1.88	0.57	112 h@500 mA cm^{-2}

Sustainion® X37-50:

[18]	Sustainion® X37-**50**	$Cu_{0.5}Co_{2.5}O_4$||Pt/C	1 M KOH/45	1.65	0.33	100 h@400 mA cm^{-2}
[19]	Sustainion® X37-**50**	Fe-NiMo||NiMo	1 M KOH/20	1.68	1.87	25 h@500 mA cm^{-2}
[20]	Sustainion® X37-**50**	Cu-Co oxide||Pt/C	1 M KOH/50	1.62	1.14	100 h@500 mA cm^{-2}
[21]	Sustainion® X37-**50**	CE-CCO||Pt/C	1 M KOH/45	1.69	1.12	12 h@500 mA cm^{-2}
[22]	Sustainion® X37-**50**	$Cu_{0\cdot81}Co_{2\cdot19}O_4$||$Co_3S_4$	1 M KOH/45-48	2.07	1.16	12 h@500 mA cm^{-2}
[23]	Sustainion® X37-**50**	$CuCo_2O_4$||Pt/C	1 M KOH/45	1.72	0.05	12 h@500 mA cm^{-2}

Re.	Membrane (thickness/μm)	Anodic&cathodic catalysts	Electrolyte& T/°C	Initial voltage (V)	Increase rate (mV h^{-1})	Duration
[24]	Sustainion® X37-**50**	$NiFe_2O_4$||NiFeCo	1 M KOH/60	1.91	0.02	2000 h@1000 mA cm^{-2}
Others:						
[25]	YAB, Foma Corporation	$Fe_2P_2S_6$||$Fe_2P_2S_6$	1 M KOH/50	2.07	0.55	24 h@300 mA cm^{-2}
[26]	AEM from ITM Power plc, UK	NiFe oxides||Pt/C	4 M NaOH/60	2.21	0.089	240 h@1000 mA cm^{-2}
[27]	Mg/Al LDH	$CuCoO_3$||Ni/CeO_2-La_2O_3/C	0.1 M NaOH/60	1.88	0.135	600 h@80 mA cm^{-2}
[28]	PAP-TP-85	Fe_xNi_yOOH-20F||Pt/C	Pure water/80	1.66	0.48	160 h@200 mA cm^{-2}
[29]	QMter-co-Mpi	IrO_2||Pt/C	1 M KOH/50	2.09	0.085	500 h@200 mA cm^{-2}
[30]	QAPPO-CF	$NiCo_2O_4$@MnO_x||Ni/CeO_2-La_2O_3/C	D.I. water/60	1.86	0.002	100 h@200 mA cm^{-2}
[31]	SEBS-Pi	IrO_2||Pt/C	1 M KOH/50	2.09	0.18	105 h@400 mA cm^{-2}
[32]	HTMA-DAPP	NiFe nanofoam||PtRu/C	D.I. water/60	2.06	0.16	170 h@200 mA cm^{-2}

12 References in Appendix

1. Pandiarajan, T.; John Berchmans, L.; Ravichandran, S., Fabrication of Spinel Ferrite Based Alkaline Anion Exchange Membrane Water Electrolysers for Hydrogen Production. *RSC Advances* **2015,** *5* (43), 34100-34108.

2. Vincent, I.; Kruger, A.; Bessarabov, D., Development of Efficient Membrane Electrode Assembly for Low-Cost Hydrogen Production by Anion Exchange Membrane Electrolysis. *International Journal of Hydrogen Energy* **2017,** *42* (16), 10752-10761.

3. Faid, A.; Oyarce Barnett, A.; Seland, F.; Sunde, S., Highly Active Nickel-Based Catalyst for Hydrogen Evolution in Anion Exchange Membrane Electrolysis. *Catalysts* **2018,** *8* (12).

4. Lee, N.; Duong, D. T.; Kim, D., Cyclic Ammonium Grafted Poly (Arylene Ether Ketone) Hydroxide Ion Exchange Membranes for Alkaline Water Electrolysis with High Chemical Stability and Cell Efficiency. *Electrochimica Acta* **2018,** *271*, 150-157.

5. Marinkas, A.; Strużyńska-Piron, I.; Lee, Y.; Lim, A.; Park, H. S.; Jang, J. H.; Kim, H.-J.; Kim, J.; Maljusch, A.; Conradi, O.; Henkensmeier, D., Anion-Conductive Membranes Based on 2-Mesityl-Benzimidazolium Functionalised Poly (2,6-Dimethyl-1,4-Phenylene Oxide) and Their Use in Alkaline Water Electrolysis. *Polymer* **2018,** *145*, 242-251.

6. Park, J. E.; Kim, M.-J.; Lim, M. S.; Kang, S. Y.; Kim, J. K.; Oh, S.-H.; Her, M.; Cho, Y.-H.; Sung, Y.-E., Graphitic Carbon Nitride-Carbon Nanofiber as Oxygen Catalyst in Anion-Exchange Membrane Water Electrolyzer and Rechargeable Metal-Air Cells. *Applied Catalysis B: Environmental* **2018,** *237*, 140-148.

7. Xu, D.; Stevens, M. B.; Cosby, M. R.; Oener, S. Z.; Smith, A. M.; Enman, L. J.; Ayers, K. E.; Capuano, C. B.; Renner, J. N.; Danilovic, N.; Li, Y.; Wang, H.; Zhang, Q.; Boettcher, S. W., Earth-Abundant Oxygen Electrocatalysts for Alkaline Anion-Exchange-Membrane Water Electrolysis: Effects of Catalyst Conductivity and Comparison with Performance in Three-Electrode Cells. *ACS Catalysis* **2018,** *9* (1), 7-15.

8. Busacca, C.; Zignani, S. C.; Di Blasi, A.; Di Blasi, O.; Lo Faro, M.; Antonucci, V.; Aricò, A. S., Electrospun $NiMn_2O_4$ and $NiCo_2O_4$ Spinel Oxides Supported on Carbon Nanofibers as Electrocatalysts for the Oxygen Evolution Reaction in an Anion Exchange Membrane-Based Electrolysis Cell. *International Journal of Hydrogen Energy* **2019,** *44* (38), 20987-20996.

9. Fan, J.; Willdorf-Cohen, S.; Schibli, E. M.; Paula, Z.; Li, W.; Skalski, T. J. G.; Sergeenko, A. T.; Hohenadel, A.; Frisken, B. J.; Magliocca, E.; Mustain, W. E.; Diesendruck, C. E.; Dekel, D. R.; Holdcroft, S., Poly (Bis-Arylimidazoliums) Possessing High Hydroxide Ion Exchange Capacity and High Alkaline Stability. *Nature communications* **2019,** *10* (1), 2306.

10. Park, J. E.; Kang, S. Y.; Oh, S.-H.; Kim, J. K.; Lim, M. S.; Ahn, C.-Y.; Cho, Y.-H.; Sung, Y.-E., High-Performance Anion-Exchange Membrane Water Electrolysis. *Electrochimica Acta* **2019,** *295*, 99-106.

11. Carbone, A.; Zignani, S. C.; Gatto, I.; Trocino, S.; Aricò, A. S., Assessment of the FAA3-50 Polymer Electrolyte in Combination with a $NiMn_2O_4$ Anode Catalyst for Anion Exchange Membrane Water Electrolysis. *International Journal of Hydrogen Energy* **2020,** *45* (16), 9285-9292.

12. López-Fernández, E.; Gil-Rostra, J.; Espinós, J. P.; González-Elipe, A. R.; de Lucas Consuegra, A.; Yubero, F., Chemistry and Electrocatalytic Activity of Nanostructured Nickel Electrodes for Water Electrolysis. *ACS Catalysis* **2020,** *10* (11), 6159-6170.

13. López-Fernández, E.; Gil-Rostra, J.; Escudero, C.; Villar-García, I. J.; Yubero, F.; de Lucas Consuegra, A.; González-Elipe, A. R., Active Sites and Optimization of Mixed Copper-Cobalt Oxide Anodes for Anion Exchange Membrane Water Electrolysis. *Journal of Power Sources* **2021,** *485*.

14. Fortin, P.; Khoza, T.; Cao, X.; Martinsen, S. Y.; Oyarce Barnett, A.; Holdcroft, S., High-Performance Alkaline Water Electrolysis Using Aemion™ Anion Exchange Membranes. *Journal of Power Sources* **2020,** *451*.

15. Pavel, C. C.; Cecconi, F.; Emiliani, C.; Santiccioli, S.; Scaffidi, A.; Catanorchi, S.; Comotti, M., Highly Efficient Platinum Group Metal Free Based Membrane-Electrode Assembly for Anion Exchange Membrane Water Electrolysis. *Angew Chem Int Ed Engl* **2014,** *53* (5), 1378-81.

16. Vincent, I., Hydrogen Production by Water Electrolysis with an Ultrathin Anion-Exchange Membrane (AEM). *International Journal of Electrochemical Science* **2018**, 11347-11358.

17. Razmjooei, F.; Farooqui, A.; Reissner, R.; Gago, A. S.; Ansar, S. A.; Friedrich, K. A., Elucidating the Performance Limitations of Alkaline Electrolyte Membrane Electrolysis: Dominance of Anion Concentration in Membrane Electrode Assembly. *ChemElectroChem* **2020,** *7* (19), 3951-3960.

18. Jang, M. J.; Yang, J.; Lee, J.; Park, Y. S.; Jeong, J.; Park, S. M.; Jeong, J.-Y.; Yin, Y.; Seo, M.-H.; Choi, S. M.; Lee, K. H., Superior Performance and Stability of Anion Exchange Membrane Water Electrolysis: pH-Controlled Copper Cobalt Oxide Nanoparticles for the Oxygen Evolution Reaction. *Journal of Materials Chemistry A* **2020,** *8* (8), 4290-4299.

19. Chen, P.; Hu, X., High-Efficiency Anion Exchange Membrane Water Electrolysis Employing Non-Noble Metal Catalysts. *Advanced Energy Materials* **2020,** *10* (39).

20. Kwon, C.-Y.; Jeong, J.-Y.; Yang, J.; Park, Yoo Sei.; Jeong J.; Park, H.; Kim, Y.; Moon, K.-S. and Choi. S. M. Effect of Copper Cobalt Oxide Composition on Oxygen Evolution Electrocatalysts for Anion Exchange Membrane Water Electrolysis. *Frontiers in Chemistry* **2020,** *8,* 600908.

21. Park, Y. S.; Yang, J.; Lee, J.; Jang, M. J.; Jeong, J.; Choi, W.-S.; Kim, Y.; Yin, Y.; Seo, M. H.; Chen, Z.; Choi, S. M., Superior Performance of Anion Exchange Membrane Water Electrolyzer: Ensemble of Producing Oxygen Vacancies and Controlling Mass Transfer Resistance. *Applied Catalysis B: Environmental* **2020,** *278*.

22. Park, Y. S.; Lee, J. H.; Jang, M. J.; Jeong, J.; Park, S. M.; Choi, W.-S.; Kim, Y.; Yang, J.; Choi, S. M., Co_3S_4 Nanosheets on Ni foam via Electrodeposition with Sulfurization as Highly Active Electrocatalysts for Anion Exchange Membrane Electrolyzer. *International Journal of Hydrogen Energy* **2020,** *45* (1), 36-45.

23. Park, Y. S.; Jang, M. J.; Jeong, J.; Park, S. M.; Wang, X.; Seo, M. H.; Choi, S. M.; Yang, J., Hierarchical Chestnut-Burr Like Structure of Copper Cobalt Oxide Electrocatalyst Directly Grown on Ni Foam for Anion Exchange Membrane Water Electrolysis. *ACS Sustainable Chemistry & Engineering* **2020,** *8* (6), 2344-2349.

24. Liu, Z.; Sajjad, S. D.; Gao, Y.; Yang, H.; Kaczur, J. J.; Masel, R. I., The Effect of Membrane on an Alkaline Water Electrolyzer. *International Journal of Hydrogen Energy* **2017,** *42* (50), 29661-29665.

25. Chang, J.; Wang, G.; Belharsa, A.; Ge, J.; Xing, W.; Yang, Y., Stable $Fe_2P_2S_6$ Nanocrystal Catalyst for High-Efficiency Water Electrolysis. *Small Methods* **2019,** *4* (6).

26. Li, X.; Walsh, F. C., and Pletcher, D., Nickel Based Electrocatalysts for Oxygen Evolution in High Current Density Alkaline Water Electrolysers. *Physical Chemistry Chemical Physics* **2011**, *13*, 1162–1167.

27. Zeng, L.; Zhao, T. S., Integrated Inorganic Membrane Electrode Assembly with Layered Double Hydroxides as Ionic Conductors for Anion Exchange Membrane Water Electrolysis. *Nano Energy* **2015,** *11*, 110-118.

28. Xiao, J.; Oliveira, A. M.; Wang, L.; Zhao, Y.; Wang, T.; Wang, J.; Setzler, B. P.; Yan, Y., Water-Fed Hydroxide Exchange Membrane Electrolyzer Enabled by a Fluoride-Incorporated Nickel-Iron Oxyhydroxide Oxygen Evolution Electrode. *ACS Catalysis* **2020,** *11* (1), 264-270.

29. Yan, X.; Yang, X.; Su, X.; Gao, L.; Zhao, J.; Hu, L.; Di, M.; Li, T.; Ruan, X.; He, G., Twisted Ether-Free Polymer Based Alkaline Membrane for High-Performance Water Electrolysis. *Journal of Power Sources* **2020,** *480.*

30. Zeng, L.; Zhao, T. S.; Zhang, R. H.; Xu, J. B., $NiCo_2O_4$ Nanowires@MnO_x Nanoflakes Supported on Stainless Steel Mesh with Superior Electrocatalytic Performance for Anion Exchange Membrane Water Splitting. *Electrochemistry Communications* **2018,** *87*, 66-70.
31. Su, X.; Gao, L.; Hu, L.; Qaisrani, N. A.; Yan, X.; Zhang, W.; Jiang, X.; Ruan, X.; He, G., Novel Piperidinium Functionalized Anionic Membrane for Alkaline Polymer Electrolysis with Excellent Electrochemical Properties. *Journal of Membrane Science* **2019,** *581*, 283-292.
32.Li, D.; Park, E. J.; Zhu, W.; Shi, Q.; Zhou, Y.; Tian, H.; Lin, Y.; Serov, A.; Zulevi, B.; Baca, E. D.; Fujimoto, C.; Chung, H. T.; Kim, Y. S., Highly Quaternized Polystyrene Ionomers for High Performance Anion Exchange Membrane Water Electrolysers. *Nature Energy* **2020,** *5* (5), 378-385.

List of Abbreviations

anion exchange membrane	(AEM)
oxygen evolution reactions	(OER)
hydrogen evolution reaction	(HER)
transition metal sulfides	(TMS)
three-dimensional	(3D)
electrochemical active surface area	(ECSA)
solid oxide electrolysis	(SOEC)
alkaline water electrolysis	(AWE)
proton exchange membrane	(PEM)
anion exchange membrane	(AEM)
platinum group metal	(PGM)
transition metal	(TM)
transition metal sulfides	(TMS)
polytetrafluoroethylenes	(PTFE)
membrane electrode assembly	(MEA)
catalyst-coated membrane	(CCM)
catalyst-coated substrate	(CCS)
porous transport electrode	(PTE)
water dissociation theory	(WDT)
hydrogen binding energy theory	(HBET)
interface water/anion transfer theory	(IW/AT)
adsorbate evolution mechanism	(AEM*)
lattice-oxygen-mediated mechanism	(LOM)
transmission electron microscopy	(TEM)
high-resolution transmission electron microscopy	(HRTEM)
scanning transmission electron microscopy	(STEM)
high-angle annular dark-field scanning transmission electron microscopy	(HAADF-STEM)
electron energy loss spectroscopy	(EELS)
X-ray diffraction	(XRD)

deionized water	(D.I. water)
thioacetamide	(TAA)
joint committee on powder diffraction standards	(JCPDS)
X-ray photoelectron spectroscopy	(XPS)
energy dispersive spectroscopy	(EDS)
scanning electron microscopy	(SEM)
fourier transform infrared spectroscopy	(FTIR)
glassy carbon	(GC)
rotating disk electrode	(RDE)
working electrode	(WE)
counter electrode	(CE)
reference electrode	(RE)
linear sweep voltammetry	(LSV)
cyclic voltammetry	(CV)
electrochemical impedance spectroscopy	(EIS)
inductively coupled plasma with optical emission spectroscopy	(ICP-OES)
inductively coupled plasma-mass spectrometry	(ICP-MS)
atomic force microscope	(AFM)
galvanostatic intermittent titration technique	(GITT)
open circuit voltage	(OCV)
double-layer capacitance	(C_{dl})
charge transfer resistance	(R_{ct})
contact resistance	(R_c)
internal resistance	(R_Ω)
mass diffusion	(MD)
mass diffusion resistance	(R_{md})
long-term stability	(LS)
gas crossover	(GC)
energy efficiency	(EE)
bulk and contact resistance	(BCR, R_{b+c})

Acknowledgements

First and foremost, I would like to show great appreciation to my PhD supervisor, Prof. Werner Lehnert, offering me professional guidance in every doctoral seminar and valuable advice in personal meetings. I gained a lot of knowledge from him for my research such as properties of porous electrodes, degradation of catalysts etc. Due to great help and support from him, I finished my PhD thesis in IEK-14 at Forschungszentrum Jülich (FZJ) and RWTH Aachen University in Germany. I really appreciate our discussion of work, life and future, and wish him a wonderful further.

Also, I would like to say “thanks a lot” to my daily supervisor Dr. Meital Shviro. During my PhD, she has been in deep communication with me for novel shaped catalysts and providing me with great help for all the transmission electron microscope (TEM) tests. I was also impressed by her meticulous professionalism, who instructed me how to make to-do lists to the maximum of efficiency, interpret experimental phenomena and present scientific results in a smooth logic flow. Moreover, I would like to thank her for contacting collaborators to do very important characterizations such as in-situ Raman (ISR), and in-situ inductively coupled plasma mass spectrometry (IS-ICP-MS) etc. I believe that in the future we will further keep contact and have fun in the world of science.

Additionally, I want to express my gratitude to my colleagues Chang Liu, Cinar Karacan, Irina Galkina, Yingzhen Chen, Yanpeng Suo, Prof. Dr. Osmando Ferreira Lopes, Ilias Stamatelos, Birgit Schumacher, Andreas Everwand, Christian Rodenbücher, Daniel Holtz, Denise Beate Günther in IEK-14, Dr. Heinrich Hartmann in ZEA-3, and Dr. Alla Faid in NTNU, who were very helpful in my experiments. And I would like to say “special thanks” to Wulv Jiang who helped me with X-ray diffraction (XRD), Fourier-transform infrared spectroscopy (FTIR) and shared me with a lot of experience in catalysts characterizations.

Personally, I also thank my wife Jingyu Yang who gave birth to our baby girl at 2020! She always stays together with me and encourages that “Lu, only you! You are the best!” so that I could face all difficulties bravely. It is worth mentioning that her cooking skills are extremely good and she has made delicious food for me. Of course, she is also the holder of my bank card, helping me manage the Euro (€) well. Last but not the least, I would like to thank my daughter, Anlai Xia, for being so brave. I'm sorry I didn't have the best childhood time with her. I do hope Corona ends soon and then we meet right away.

Schriften des Forschungszentrums Jülich
Reihe Energie & Umwelt / Energy & Environment

Band / Volume 583
Machine learning for monitoring groundwater resources over Europe
Y. Ma (2022), viii, 125 pp
ISBN: 978-3-95806-638-0

Band / Volume 584
Mechanical properties of single and dual phase proton conducting membranes
W. Zhou (2022), IV, VI, 133 pp
ISBN: 978-3-95806-645-8

Band / Volume 585
Improvements to gravity wave physics from an observational perspective
M. Geldenhuys (2022), vii, 136 pp
ISBN: 978-3-95806-647-2

Band / Volume 586
Impact of severe convection on the water vapor mixing ratio in the extra-tropical stratosphere
D. Khordakova (2022), ii, 136 pp
ISBN: 978-3-95806-648-9

Band / Volume 587
Effects of salt precipitation during evaporation on porosity and permeability of porous media
J. Piotrowski (2022), xxvii, 139 pp
ISBN: 978-3-95806-650-2

Band / Volume 588
IEK-14 Report 2022
Forschung für die Energiewende und den Wandel im Rheinischen Revier
B. Emonts (Hrsg.) (2022)
ISBN: 978-3-95806-652-6

Band / Volume 589
Oxidation of monoterpenes studied in atmospheric simulation chambers
L. L. Hantschke (2022), 188 pp
ISBN: 978-3-95806-653-3

Band / Volume 590
NiFe Layered Double Hydroxide Catalysts for Oxygen Evolution Reaction in Alkaline Water Electrolysis
W. Jiang (2022), 165 pp
ISBN: 978-3-95806-658-8

Schriften des Forschungszentrums Jülich
Reihe Energie & Umwelt / Energy & Environment

Band / Volume 591
Optimizing Cross-linked Infrastructure for Future Energy Systems
L. Welder (2022), xxiii, 360 pp
ISBN: 978-3-95806-659-5

Band / Volume 592
Evaluation von Reaktorkonzepten für die CO_2-basierte Methanolsynthese aus Wasserstoff und Kohlendioxid mithilfe von CFD-Simulationen
S. Weiske (2022), x, 369 pp
ISBN: 978-3-95806-661-8

Band / Volume 593
Spectral Induced Polarization of Biochar in Soil
Z. Gao (2022), XXVI, 155 pp
ISBN: 978-3-95806-662-5

Band / Volume 594
Eignung von nickelhaltigen Katalysatorsystemen in sauren Medien zur Nutzung im Betrieb von Brennstoffzellen
A. Karaca (2022), iv, 249 pp
ISBN: 978-3-95806-663-2

Band / Volume 595
Seasonal Comparison of the Chemical Composition and Source Apportionment of Aerosols during the Year-Long JULIAC Campaign
L. Liu (2022), VIII, 189 pp
ISBN: 978-3-95806-668-7

Band / Volume 596
Nanoscale Understanding and Control of Metal Exsolution in Perovskite Oxides
M. L. Weber (2022), ix, 160 pp
ISBN: 978-3-95806-669-4

Band / Volume 597
Nanostructures of Transition Metal Sulfides for Anion Exchange Membrane Water Electrolysis
L. Xia (2022), 161 pp
ISBN: 978-3-95806-670-0

Weitere ***Schriften des Verlags im Forschungszentrum Jülich*** unter
http://wwwzb1.fz-juelich.de/verlagextern1/index.asp

Energie & Umwelt / Energy & Environment
Band / Volume 597
ISBN 978-3-95806-670-0

Mitglied der Helmholtz-Gemeinschaft

JÜLICH
Forschungszentrum